ADVANCED MICROSTRUCTURED SEMICONDUCTOR NEUTRON DETECTORS: DESIGN, FABRICATION, AND PERFORMANCE

by

STEVEN LAWRENCE BELLINGER

B.S., Kansas State University, 2006

AN ABSTRACT OF A DISSERTATION

submitted in partial fulfillment of the
requirements for the degree

DOCTOR OF PHILOSOPHY

Department of Mechanical and Nuclear Engineering
College of Engineering

KANSAS STATE UNIVERSITY
Manhattan, Kansas

2011

ABSTRACT

The microstructured semiconductor neutron detector (MSND) was investigated and previous designs were improved and optimized. In the present work, fabrication techniques have been refined and improved to produce three-dimensional microstructured semiconductor neutron detectors with reduced leakage current, reduced capacitance, highly anisotropic deep etched trenches, and increased signal-to-noise ratios. As a result of these improvements, new MSND detection systems function with better gamma-ray discrimination and are easier to fabricate than previous designs. In addition to the microstructured diode fabrication improvement, a superior batch processing backfill-method for ^{6}LiF neutron reactive material, resulting in a nearly-solid backfill, was developed. This method incorporates a LiF nano-sizing process and a centrifugal batch process for backfilling the nanoparticle LiF material. To better transition the MSND detector to commercialization, the fabrication process was studied and enhanced to better facilitate low cost and batch process MSND production.

The research and development of the MSND technology described in this work includes fabrication of variant microstructured diode designs, which have been simulated through MSND physics models to predict performance and neutron detection efficiency, and testing the operational performance of these designs in regards to neutron detection efficiency, gamma-ray rejection, and silicon fabrication methodology. The highest thermal-neutron detection efficiency reported to date for a solid-state semiconductor detector is presented in this work. MSNDs show excellent neutron to gamma-ray (n/γ) rejection ratios, which are on the order of 10^{6}, without significant loss in thermal-neutron detection efficiency. Individually, the MSND is intrinsically highly sensitive to thermal neutrons, but not extrinsically sensitive because of their small size. To improve upon this, individual MSNDs were tiled together into a 6x6-element array on a single silicon chip. Individual elements of the array were tested for thermal-neutron detection efficiency and for the n/γ reject ratio. Overall, because of the inadequacies and costs of other neutron detection systems, the MSND is the premier technology for many neutron detection applications.

ADVANCED MICROSTRUCTURED SEMICONDUCTOR NEUTRON DETECTORS: DESIGN, FABRICATION, AND PERFORMANCE

by

STEVEN LAWRENCE BELLINGER

B.S., Kansas State University, 2006

A DISSERTATION

submitted in partial fulfillment of the
requirements for the degree

DOCTOR OF PHILOSOPHY

Department of Mechanical and Nuclear Engineering
College of Engineering

KANSAS STATE UNIVERSITY
Manhattan, Kansas

2011

Approved by:

Major Professor
Douglas S. McGregor

COPYRIGHT

STEVEN L. BELLINGER

2011

All rights reserved. No part of the material protected by this copyright notice may be reproduced or utilized in any form or by any means, electronic or mechanical, including photocopying, recording or by any information storage and retrieval system, without written permission from the author.

Abstract

The microstructured semiconductor neutron detector (MSND) was investigated and previous designs were improved and optimized. In the present work, fabrication techniques have been refined and improved to produce three-dimensional microstructured semiconductor neutron detectors with reduced leakage current, reduced capacitance, highly anisotropic deep etched trenches, and increased signal-to-noise ratios. As a result of these improvements, new MSND detection systems function with better gamma-ray discrimination and are easier to fabricate than previous designs. In addition to the microstructured diode fabrication improvement, a superior batch processing backfill-method for ^{6}LiF neutron reactive material, resulting in a nearly-solid backfill, was developed. This method incorporates a LiF nano-sizing process and a centrifugal batch process for backfilling the nanoparticle LiF material. To better transition the MSND detector to commercialization, the fabrication process was studied and enhanced to better facilitate low cost and batch process MSND production.

The research and development of the MSND technology described in this work includes fabrication of variant microstructured diode designs, which have been simulated through MSND physics models to predict performance and neutron detection efficiency, and testing the operational performance of these designs in regards to neutron detection efficiency, gamma-ray rejection, and silicon fabrication methodology. The highest thermal-neutron detection efficiency reported to date for a solid-state semiconductor detector is presented in this work. MSNDs show excellent neutron to gamma-ray (n/γ) rejection ratios, which are on the order of 10^{6}, without significant loss in thermal-neutron detection efficiency. Individually, the MSND is intrinsically highly sensitive to thermal neutrons, but not extrinsically sensitive because of their small size. To improve upon this, individual MSNDs were tiled together into a 6x6-element array on a single silicon chip. Individual elements of the array were tested for thermal-neutron detection efficiency and for the n/γ reject ratio. Overall, because of the inadequacies and costs of other neutron detection systems, the MSND is the premier technology for many neutron detection applications.

Table of Contents

List of Figures viii

List of Tables viii

List of Acronyms xxii

Acknowledgements xxiii

Dedication xxiv

CHAPTER 1 *Introduction* 1
- 1.1 Motivation for the Thesis ... 1
- 1.2 Contribution to MSND Science and Technology ... 4
- 1.3 Organization of Thesis ... 5

CHAPTER 2 *Background* 7
- 2.1 The Neutron ... 7
- 2.2 Common Neutron Detectors in Review ... 13

CHAPTER 3 *Microstructured Semiconductor Neutron Detector: Device Design* 20
- 3.1 MSND Design Features ... 20
- 3.2 MSND Simulation Model Design ... 26
- 3.3 Simulated Reaction Product Ion-Energy Deposition Spectra ... 34
- 3.4 Simulated Neutron Detection Efficiency ... 36
- 3.5 Discussion ... 42

CHAPTER 4 *Microstructured Semiconductor Neutron Detector: Fabrication Methodology* 43
- 4.1 Micromachining of Silicon ... 44
- 4.2 Backfilling of Neutron Reactive Material into Si Microstructures ... 64
- 4.3 MSND Fabrication ... 82
- 4.4 Prototypical Individual MSND Counting Electronics ... 84
- 4.5 Dual-Integrated Stacked MSND Fabrication ... 85
- 4.6 Large-Area Individual and Stacked MSND Designs ... 87
- 4.7 Dual-Integrated 6x6-Arrayed MSND Design ... 88
- 4.8 Foundry Services ... 91

CHAPTER 5 *Microstructured Semiconductor Neutron Detector: Neutron Sensitivity Testing* 93
5.1 MSND Electronic Characteristics 93
5.2 MSND Thermal-Neutron Efficiency Measurements 101
5.3 Moderated and Unmoderated ^{252}Cf Response 134

CHAPTER 6 *Conclusions and Future Work* 145
6.1 Contribution to the Science of Solid-State Neutron Detection 145
6.2 Applications for the MSND Technology 147
6.3 Future Work 152

List of Publications (November 2011) 157
Refereed: 157
Conference Proceedings: 158
Patents: 159

References 161

Appendix A - MSND Model Detail
A. 1 Empirical Fits for ^{6}LiF Ion Data .... - 1 -
A. 2 Gaussian Averaging of the Simulated Spectra .... - 6 -
A. 3 MSND Neutron-Response Model Simulation *MatLab*™ Code .... - 8 -

Appendix B - MSND Fabrication Detail
B. 1 MSND Fabrication Process Detail: Single Sided Device .... - 1 -
B. 2 MSND Fabrication Process Detail: Dual Sided Device .... - 4 -
B. 3 MSND Fabrication Process *Run Card*: Dual Sided Device .... - 9 -

Appendix C - *Silvaco* Model Input Code
C. 1 *Silvaco* TCAD Potential Model Input Code .... - 1 -
C. 2 *Silvaco* TCAD Single Event Upset Model Input Code .... - 2 -

Appendix D - KSU ^{252}Cf Source Detail
D. 1 Californium-252 Radiological Specifications[†] .... - 1 -
D. 2 KSU ^{252}Cf Assay[†] .... - 4 -

LIST OF FIGURES

Figure 2.1: The fine-structure of the free neutron decay. (left) A free neutron will decay into three particles: a proton, an electron, and an antineutrino. (right) A Feynman diagram is depicted describing the free neutron beta decay via an intermediate heavy W^- boson. 8

Figure 2.2: X-ray image of two ^{3}He gas-filled neutron detectors. The active regions of the detectors, when disregarding the field-tubes and insulators, are (left-detector) 5.5 cm by 4 cm diameter and (right-detector) 8 cm by 5.25 cm diameter. These detectors were used for the KSU diffracted thermal-neutron beam flux calibration [70]. 14

Figure 2.3: Basic illustration of thin-film coated semiconductor neutron detector design. It should be noted that some neutron-conversion films have more than one decay chain, therefore convoluting the ion energy-deposition optimization in the bulk semiconductor which is correlated to the film thickness. Additionally, notice that the film thickness is limited by the longest reaction-product range because of self-absorption. 18

Figure 2.4: A graph of ideal approximate radiation-stimulated current in a 1 mm thick silicon diode. The calculated induced current assumes complete charge collection (no losses), radiation interaction charge-production at 3.6 eV per electron-hole pair, an approximate average charge mobility of 5×10^6 cm s^{-1} at 1000 V applied bias [85]. 19

Figure 3.1: Shown is an illustration of the reaction-product charge particle variable energy deposition track through the microstructured semiconductor diode. It should be noted that some neutron-conversion materials have more than one decay chain, therefore convoluting the ion energy-deposition optimization which is correlated to the microstructure pattern size and shape specification in the semiconductor material. 21

Figure 3.2: The mass attenuation coefficient, μ / ρ, as a function of photon energy for elemental silicon, data source [87]. Note that the total interaction cross-section, σ_T, is just the multiplication of μ / ρ by the atomic molar mass divided by Avogadro's number. 23

Figure 3.3: Illustration of angular response from neutron streaming paths through a cylindrical-hole and sinusoidal trench microstructured detector designs, source [48]. 25

Figure 3.4: (left) The "trench design," composed of etched grooves backfilled with neutron reactive material, showing a unit cell as defined for calculations and modeling. (right) Neutron detection efficiency is increased, and streaming minimized, by stacking a 2nd detector off-set from the 1st. Note that the 2200 m/s neutron absorption cross-section of silicon is small, $\sigma_{Si,a}$ = 0.171 b [62]. 25
Figure 3.5: (left) Shown is the "trench design," composed of etched grooves backfilled with neutron reactive material, where a uniform parallel thermal-neutron beam is normally incident as defined for calculations and modeling. (right) An illustration of a center-orientated uniform neutron field configuration used by other groups [28]. In practical designs, the detector dimensions "L" are much larger than the microstructure depths "D". 29
Figure 3.6: (left) Illustration of the stacked detector configuration for the straight trench microstructure design. (right) Notice in the top-side view that the straight trench pattern is completely opaque to normal incident streaming neutrons. 31
Figure 3.7: Shown are depictions of the neutron flux image transfer operations for the straight trench pattern with the trench width the same as the semiconductor fin width. Shown is the (left) neutron transmission image for the top detector where the center portion is the ^{6}LiF-filled trench region, (center) the shifted neutron flux image of neutrons that passed through the top detector so as to align with the bottom detector, and (right) the neutron absorption image for neutrons that interacted in the bottom detector. Note from the left and center images, some neutrons passed through the ^{6}LiF material. 33
Figure 3.8: Shown are depictions of the neutron flux image transfer operations for the straight trench pattern with the trench width much larger than the semiconductor fin width. Shown is the (left) neutron transmission image for the top detector where the center portion is the ^{6}LiF-filled trench region, (center) the shifted neutron flux image of neutrons that passed through the top detector so as to align with the bottom detector, and (right) the neutron absorption image for neutrons that interacted in the bottom detector. Note from the left and center images, some neutrons passed through the ^{6}LiF material. Because the trench is much wider than the semiconductor fin, more neutrons are absorbed in the top detector than the bottom detector. 33

Figure 3.9: Straight trench ^{6}LiF-backfilled silicon microstructured stacked detector calculated ion spectra for four cases. Shown in (A) and (C) are cases in which the trenches and semiconductor fins are both 25 microns wide for depths of (A) 100 microns and (C) 250 microns. Shown in (B) and (D) are cases in which the trench and semiconductor fins are unequal, with the trenches being 14 microns wide and the semiconductor fins being 6 microns wide, for depths of (B) 100 microns and (D) 250 microns. 35

Figure 3.10: Predicted ^{6}LiF backfilled straight trench microstructured detector neutron detection efficiencies as a function of the LLD setting for cases in which the cell dimensions are (A) 50 microns with the trench feature size of 25 microns and (B) 20 microns with the trench feature size of 14 microns, with both microstructures 250 microns deep. The observed efficiency from the stacked MSNDs decreases as the LLD is increased. 37

Figure 4.1: Shown are SEM pictures of microstructure patterns etched into a silicon substrate, showing detail of the circular hole, and straight, chevron, and sinusoidal trench, patterns. Sourced from [27], copyright © 2009, IEEE. 45

Figure 4.2: Shown are SEM pictures of microstructure patterns etched into a silicon substrate, showing detail of the straight trench, sinusoidal trench, and column (pillar) patterns. 46

Figure 4.3: Microstructure patterns etched into a silicon substrate, showing detail of the horizontal scalloping (lateral etching) of the silicon microstructure sidewall because of the alternating etch-deposit process. 48

Figure 4.4: Microstructure patterns etched into a silicon substrate, showing detail of the etched microstructure vertical striations from mask edge failure. 49

Figure 4.5: (left) Standard (110) crystal plane-orientation projection for silicon; showing the rhombic pattern alignment of (111) planes normal to the surface (110) plane. The normal (111) traces do not meet each other at 90°, but instead at 70.53° and 109.47° [86, 100]. Also, the wafer will easily cleave along the (111) planes. (right) Severe undercut of SiO_2 mask because of improper pattern alignment with (111) planes. 50

Figure 4.6: Images of wet-etched straight and chevron trench microstructures. The upper left shows above-view of straight trench microstructure, the upper right shows a cleaved

side-view of high-selectivity deep-etched trenches, and the two bottom pictures show an above-view and side-view of chevron trench microstructures, moving left to right. 51

Figure 4.7: Images of wet-etched straight trench microstructures. The upper left shows an above-view of trench microstructure, and the upper right shows a cleaved side view of etched trenches. The middle left picture displays visible words behind a through-etched wafer, and the middle right picture shows a magnified view of the fully-perforated wafer. The bottom left picture is a SEM image of the through trenches, and the bottom right picture displays an above-view of the silicon fins warping because of the lack of a lateral support structure. 52

Figure 4.8: An illustration of a pn junction diode (left) in a fabricated solid-state structure and (right) electronic device schematic representation. 53

Figure 4.9: An illustration of a pn junction diode in thermodynamic equilibrium with (left) two dopant type regions in separation and (right) when the two different regions are brought together in thermodynamic contact (after Lutz [95]). 54

Figure 4.10: Diagrams of (a) a bare n-type silicon wafer, (b) thermal oxide layer, (c) application photoresist masking layer, (d) lithography imaging of the selective diode area, (e) wafer after development, (f) SiO_2 removal, (g) photoresist removal, (h) cleaned and p-type dopant diffusion, (i) pn junction formed from degenerate doping of silicon, (j) wafer after developed liftoff lithography and evaporated metallization, and (k) the completed pn junction diode with a metal contact. 55

Figure 4.11: (left) Applied dry-etching photoresist mask on bare silicon. (right) Side-view of applied liftoff photoresist patterning, commonly used for selective material layering through photoresist removal by lifting the topologically deposited material layers (i.e., metal contacts). It is essential to have an undercut of the photoresist for a liftoff, where the deposited film will not encase the masking photoresist, and the solvent can thereby remove the underlying photoresist. 59

Figure 4.12: Pictured is the S.M.A.R.T. Lab metrology station. Included equipment are (a) a high voltage source measure unit system, (b) a 1MHz C-V plotter system, (c) a 4-point resistivity measuring system, (d) a single point probing station, (e) a digital multimeter, (f) an oscilloscope, (g) a 1100 Source Meter, (h) a NIM Bin, (i) an EM-shielded dark box, and (j) a computer with LabVIEW interface card and VI communication software. ... 63

Figure 4.13: Pictures of micron-sized LiF is typical of commercially available or solution made material. Note the varying particle sizes of the cubic crystals, ranging from sub-micron to tens of microns. 66

Figure 4.14: Solution-precipitated LiF powder backfilled into straight trench microstructures that are (left) 212 microns deep and (right) 250 microns deep. Notice that the coarse material loosely packs into the microstructures, leaving large packing fraction voids. 67

Figure 4.15: Electron beam evaporation of LiF material onto silicon microstructures with 30 μm diameter by 20 μm deep cylindrical holes. Notice that the holes close as the LiF builds-up at the top perimeter of the hole opening, therefore limiting its use as a backfilling method. 67

Figure 4.16: Melting of LiF material into microstructured silicon. The samples have been cleaved to investigate the fill composition of (left) cylindrical holes and (right) straight trenches. 68

Figure 4.17: A schematic view of the LPC system, partially broken away, which can provide dynamic, low-temperature, 200 - 500°C, LiF condensation filling of Si microstructures. 70

Figure 4.18: A more detailed schematic of the transport physics of the LPC system. The surface of the silicon wafer is held at a constant temperature from a cold chuck, such that a thermal gradient from the front to the back of the wafer is developed because of the radiant and convective energy transport from the furnace. 70

Figure 4.19: Representative pictures of initial experimentations of LPC depositing LiF material in 30 μm wide by 200 μm deep trench silicon microstructures with a low argon carrier-gas flow rate (1 - 3 sccm) and 880°C furnace temperature. The complete LPC process time was eight hours and the surface temperature of the silicon was ~200°C. Notice that the openings of the trench microstructures have sealed closed and the bulk of the LiF material has been deposited on the surface of the silicon wafer. 71

Figure 4.20: Representative pictures of experimentations of improved LPC depositing LiF material in 30 μm diameter by 100 μm deep cylindrical silicon microstructures with a low argon carrier-gas flow rate of 3 sccm and 1100°C furnace temperature. The complete LPC process time was ten hours and the surface temperature of the silicon

was 575°C. (right) Notice that the sample has been cleaved to investigate the fill composition of the holes and showing columns of slightly porous material. 72

Figure 4.21: Representative pictures of experimentations of improved LPC depositing LiF material in 30 μm dia. by 50 μm deep cylindrical silicon microstructures with a higher argon carrier-gas flow rate of 10 sccm and furnace temperatures of 950°C/1100°C/1000°C, for the nearest-to-wafer heating zone to the farthest heating zone, respectively, with the surface temperature of the silicon at 380°C. Because of the gas-flow rate increase and zonal temperature gradient adjustments, the LPC coalesced particle size was reduced. (left) Shown is the condensation of solid material at the bottom of the holes to be more prevalent at a process time of 8 hrs. (right) Shown is the same LPC recipe as (left), but for a longer process duration time of 14 hrs........................ 73

Figure 4.22: (left) Micron-sized ^{6}LiF is typical of commercially available or solution made material. Note the varying particle sizes of the cubic crystals, ranging from sub-micron to several microns. (right) Nanoparticle ^{6}LiF material that was produced via the vapor-condensation method. 74

Figure 4.23: A schematic of the LiF nano-sizing system. LiF is loaded into a carbon crucible under an argon atmosphere and is heated to just below the boiling point to control the evaporation rate of the LiF vapor. The nanoparticle vapor electrostatically condenses on the stainless steel rod and cylinder preferentially because of the applied electric field between the two anodes. The deposited nanoparticle powder LiF material is then physically removed from the electrodes. 75

Figure 4.24: Fractals of LiF-agglomerated nanoparticles produced via LiF vapor condensation. (top) The nanoparticle material has collected into a series of small spheres through electrostatic forces and then agglomerated spheres form into fractal agglomerates of varying dimension. (bottom) With increased carrier-gas flow, the LiF nanoparticle material is given less time to coalesce into spheres and, therefore, the size of the LiF-agglomerated nanoparticles are coherently reduced. Sourced from [112], copyright © 2011, IEEE... 76

Figure 4.25: EDS spectrum of the LiF nanoparticles showing the dominate presences of the element fluorine. Lithium X-ray response is not present because of X-ray absorption in the EDS detector window. Sourced from [112], copyright © 2011, IEEE. 78

Figure 4.26: A progressive illustration of centrifugal LiF deposition in semiconductor microstructures via LiF nanoparticle powder colloidal-suspension in isopropyl alcohol. This method offers a vast improvement for mass production over physically pressing the LiF nanoparticle powder into the microstructures. The size of the diode inside the bottle has been exaggerated for effect. 79

Figure 4.27: SEM pictures of centrifugally backfilled MSNDs with LiF nanoparticle powder in high aspect-ratio wet-etched straight trench microstructures. (top-left and bottom-left) Shown are 225 µm and 100 µm deep trenches filled with nanoparticle LiF material, respectively. (top-right) Pictured is a top-slant view of the MSND represented in the top-left picture; notice fine nanoparticle powder coating layer, characteristic of centrifugal deposition, where the smallest particles fall last because of particle drag forces. (bottom-right) Shown is a top-view of the filled 100 µm deep trenches. Sourced from [21], copyright © 2010, IEEE. 81

Figure 4.28: Cross-section illustration of a fabricated MSND with conformally-diffused diode structure. 83

Figure 4.29: Shown are 6-mm diameter and square MSNDs with an assembled 4-pin readout metal-enclosure header used for single MSND neutron testing. 84

Figure 4.30: Shown (left) are dual-integrated packaged MSNDs with preamplifying circuitry, (top-right) a cut-section illustration of the stacked MSND arrangement of the dual-integrated MSND, and (bottom-right) a picture of the detector package and motherboard. The motherboard provides an adjustable detector bias, bias-current compensation, pulse shaping and gain, an analog output for pulse-height analysis, and a "digital" output from a discriminator. Sourced from [21], copyright © 2010, IEEE. 86

Figure 4.31: Diagram of the dual-integrated stacked MSND's basic readout circuit for pulse amplification, adjustable detector bias, bias current compensation, pulse shaping and gain, analog output for pulse-height analysis, and digital output from a discriminator. 87

Figure 4.32: Shown are (left) the 4-cm^2, large-area, dual-integrated, stacked, MSND package with preamplifying circuitry and (right) a picture of the detector package and motherboard. The motherboard provides an adjustable detector bias, bias-current compensation, pulse shaping and gain, an analog output for pulse-height analysis, and a digital output from a discriminator. 88

Figure 4.33: Shown (left) is a disassembled dual-integrated 6x6-element MSND array (1-cm^2 elements) with amplifying circuitry, adjustable detector bias, bias current compensation, pulse shaping and gain, an analog output for pulse-height analysis, and a digital output from a discriminator. Two 6x6-element MSND arrays are mounted back to back, where both sides of the mounting board are shown in the lower half of the picture. Pictured (right) is the assembled dual-integrated 6x6-arrayed MSND, with a characteristic aluminum housing for assembling many 6x6-element MSND arrays into a large detector panel array. 89

Figure 4.34: Illustration of a cut-section assembly of the dual-integrated 6x6-element MSND array with preamplifier board, stacked MSND array mounting board, and summed-amplifying/digitizing circuitry board. For simplicity and ease of view, only 3 MSNDs are shown, and the MSND scale is enlarged.. 90

Figure 4.35: A diagram representing the 6x6-element MSND array basic readout circuit schematic for pulse amplification, adjustable detector bias, pulse shaping and gain, analog output for pulse-height analysis, and digital output from a discriminator. 91

Figure 5.1: Leakage-current comparison of a planar-diffused detector and conformally-diffused MSNDs with 200 μm and 250 μm deep straight-trenches. All square MSNDs were 1-cm^2. 95

Figure 5.2: Capacitance comparison of a planar-diffused detector and conformally-diffused MSNDs with 200 μm and 250 μm deep straight-trenches. All square MSNDs were 1-cm^2. 96

Figure 5.3: Leakage-current comparison of a planar-diffused detector and conformally-diffused MSND with 200 μm deep straight-trenches. All square MSND areas were 4-cm^2. 98

Figure 5.4: Capacitance comparison of a planar-diffused detector and conformally-diffused MSND with 200 μm deep straight-trenches. All square MSND areas were 4-cm^2. 99

Figure 5.5: ^{241}Am alpha particle response of a conformally-diffused MSND with 200 μm deep straight trenches. The alpha source was placed at the diagonally-opposite corner of the MSND probing point placement on the diode. The square MSND area was 4-cm^2. 100

Figure 5.6: Illustration of KSU TRIGA Mark II Reactor radial-beam-port diffractometer setup for the MSND and the ^{3}He detector in the diffracted thermal-neutron beam line..... 102
Figure 5.7: Pulse-height spectra for 50 μm deep sinusoidal etched pattern backfilled with ^{6}LiF coarse powder. At an LLD = 300 keV (channel 260), the measured thermal-neutron detection efficiency was $7.00 \pm 0.02\%$. Sourced from [38], copyright © 2008, IEEE. 104
Figure 5.8: Pulse-height spectra for 100 μm deep sinusoidal etched pattern backfilled with ^{6}LiF coarse powder. At an LLD = 300 keV (channel 230), the measured thermal-neutron detection efficiency was $11.94 \pm 0.03\%$. Sourced from [38], copyright © 2008, IEEE. 104
Figure 5.9: Pulse-height spectra for 150 μm deep sinusoidal etched pattern backfilled with ^{6}LiF coarse powder. At an LLD = 300 keV (channel 90), the measured thermal-neutron detection efficiency was $13.11 \pm 0.03\%$. 105
Figure 5.10: Pulse-height spectra comparison of a selectively diffused and a conformally-diffused 100 μm deep sinusoidal etched pattern backfilled with ^{6}LiF coarse powder. At an LLD = 300 keV (channel 230), the selectively and conformally-diffused MSND measured thermal-neutron detection efficiencies were $8.96 \pm 0.06\%$ and $11.94 \pm 0.03\%$, respectively. 105
Figure 5.11: Pulse-height spectra for 245 μm deep sinusoidal etched pattern backfilled with ^{6}LiF coarse powder. At an LLD = 160 keV (channel 10), the measured thermal-neutron detection efficiency was $20.40 \pm 0.05\%$. Sourced from [25], copyright © 2009, IEEE..... 106
Figure 5.12: Pulse-height spectra comparison of a selectively diffused and a conformally-diffused 100 μm deep sinusoidal etched pattern backfilled with ^{6}LiF coarse powder. At an LLD = 300 keV (channel 18), the selectively and conformally-diffused MSND measured thermal-neutron detection efficiencies were $4.03 \pm 0.06\%$ and $11.94 \pm 0.08\%$, respectively. Both MSNDs were measured in the thermal-neutron beam for 300 seconds and both have an active area of 28 mm^2.. 107
Figure 5.13: Normalized angular response of circular hole and sinusoidal trench MSNDs compared against the angular response of a thin-film planar detector. The data is fit with spline-interpolated lines. Sourced from [26], copyright © 2007, IEEE. 109

Figure 5.14: Pulse-height spectra for dual-integrated 113 μm deep sinusoidal etched pattern backfilled with ^{6}LiF coarse powder. At an LLD = 15 Chn, the measured thermal-neutron detection efficiency was 21.0 ± 0.04%. Sourced from [25], copyright © 2009, IEEE. 110
Figure 5.15: Pulse-height spectrum from conformal-diffused diode dual-integrated detector with 250 μm deep straight trench microstructures, showing response with and without (Cd shutter closed) neutrons. The preamplifier electronic signal integration time was set at 2 μs. At an LLD = 11 Chn (375 keV), the measured thermal-neutron detection ε_{tn} was 34%. 112
Figure 5.16: Modeled electric potential solution within conformally-diffused 100 μm deep trench MSND. Each plot key describes the electric potential gradient within the Si fin for (a) -1 V, (b) -4 V, (c) -10 V, and (d) -50 V of applied bias........ 114
Figure 5.17: Modeled electric potential solution within conformally-diffused 250 μm deep trench MSND. Each plot key describes the electric potential gradient within the Si fin for (a) -1 V, (b) -4 V, (c) -10 V, and (d) -50 V of applied bias........ 115
Figure 5.18: Modeled electric potential solution within conformally-diffused 350 μm deep trench MSND. Each plot key describes the electric potential gradient within the Si fin for (a) -1 V, (b) -4 V, (c) -10 V, and (d) -50 V of applied bias........ 116
Figure 5.19: Modeled transient solution of current versus time within 100-μm, 250-μm, and 350-μm deep straight trench MSNDs. The silicon fin is 25 μm in width and is the same modeled geometry and potential field as shown in Figures 5.16, 5.17, and 5.18. 118
Figure 5.20: Pulse-height spectra comparison of the previous 2-μs charge integration-time preamplifier old design versus the improved 10-μs charge integration-time preamplifier new design for the dual-integrated 250 μm deep straight trench microstructure backfilled with ^{6}LiF. At an LLD = 15 Chn (300 keV), the measured thermal-neutron detection ε_{tn} was 42% for the 10 μs charge integration-time preamplifier design. Sourced from [21], copyright © 2010, IEEE. 120
Figure 5.21: Measured ^{137}Cs gamma-ray irradiation (Ω_F = 3.18 x 10^{-5}) and neutron irradiation pulse-height spectral features for the dual-integrated neutron detector with the 10-μs signal integration time design. 123

Figure 5.22: Comparison of the measured neutron detection efficiency, the measured ^{137}Cs gamma-ray detection efficiency, and the n/γ rejection ratio of the stacked 1-cm^2 MSND. 123

Figure 5.23: Pulse-height spectra for the individual 4-cm^2 MSND with 200 μm deep, straight trench microstructures backfilled with ^{6}LiF. At an LLD = 25 Chn, the measured thermal-neutron detection was 16.3% and at an LLD = 32 Chn, the measured thermal-neutron detection was 15.9% 125

Figure 5.24: Pulse-height spectra comparison for the individual and stacked 4-cm^2 MSND with 200 μm deep, straight trench microstructures backfilled with ^{6}LiF. At an LLD = 18 Chn, the measured thermal-neutron detection efficiency was 32.4%, and at an LLD = 28 Chn the measured thermal-neutron detection efficiency was 29.0%. 126

Figure 5.25: Measured ^{137}Cs gamma-ray irradiation (Ω_F = 1.27 x 10^{-4}) and neutron irradiation pulse-height spectral features for the dual-integrated neutron detector with the 10-μs signal integration time design. 127

Figure 5.26: Measured ^{137}Cs gamma-ray irradiation (Ω_F = 1.27 x 10^{-4}) and neutron irradiation pulse-height spectral features for the dual-integrated 4-cm^2 MSND with the 10-μs signal integration time design. 128

Figure 5.27: Comparison of the measured neutron detection efficiency, the measured ^{137}Cs gamma-ray detection efficiency, and the n/γ rejection ratio of the stacked 4-cm^2 MSND. 129

Figure 5.28: Pulse-height spectra for the 6x6-arrayed MSND with 60 μm deep, straight trench microstructures backfilled with ^{6}LiF. At an LLD = 20 Chn, the measured thermal-neutron detection was 7.03%. The large number of counts in channel 58 is attributed to amplifier clipping of large pulses. 132

Figure 5.29: Measured ^{137}Cs gamma-ray irradiation (Ω_F = 1.07 x 10^{-3}) and thermal-neutron irradiation pulse-height spectral features for the dual-integrated 6x6-arrayed MSND. The large number of counts in channel 58 is attributed to amplifier clipping of large pulses. 133

Figure 5.30: Energy spectrum of prompt neutrons produced from the fission of fissionable nuclei as calculated by Walsh [125]. Results for ^{233}U, ^{235}U, and ^{239}Pu are for thermal-neutron-induced fission, results for ^{232}Th and ^{238}U are for fast-neutron (2 MeV)-

induced fission, and results for ^{252}Cf are for spontaneous fission. Figure from [90] with permission. 134

Figure 5.31: Pictures of the KSU Californium source. ^{252}Cf spontaneously fissions, providing a source of high-energy neutrons. (left) The Cd encased D_2O sphere at the top of the irradiator is in place to provide a neutron energy spectrum similar to the neutron energy in a nuclear reactor. The spectrum permits calibrating neutron dose rate-meters for use in a nuclear reactor environment, as well as various activation, imaging, and detection research efforts. (right) If the sphere is removed, the irradiation provides a source of high energy neutrons. 135

Figure 5.32: Measured bare ^{252}Cf fast-neutron irradiation (Ω_F = 2.63 x 10^{-5}) pulse-height spectral features for the 1-cm^2 dual-integrated neutron detector. 136

Figure 5.33: Measured bare ^{252}Cf fast-neutron irradiation (Ω_F = 1.05 x 10^{-4}) pulse-height spectral features for the 4-cm^2 dual-integrated neutron detector. 138

Figure 5.34: Pulse-height spectra features for the dual-integrated 6x6-arrayed MSND with irradiation from the KSU unmoderated ^{252}Cf spontaneous fission neutron source (Ω_F = 1.07 x 10^{-3}). The pulse height spectra key is: (a) background with ^{252}Cf source in the shielded cask, (b) bare ^{252}Cf source with frontside irradiation, (c) bare ^{252}Cf source with backside irradiation, (d) ^{252}Cf source with backside irradiation and 1 cm of lead gamma-ray shielding. The large number of counts in channel 58 is attributed to amplifier clipping of large pulses. 139

Figure 5.35: Pulse-height spectra features for a ^{3}He gas-filled neutron detector from irradiation with the KSU unmoderated ^{252}Cf spontaneous fission neutron (Ω_F = 1.10 x 10^{-3}). The pulse height spectra key is: (a) background with ^{252}Cf source in the shielded cask and no moderator, (b) bare ^{252}Cf source, (c) ^{252}Cf source with 1 cm of lead gamma-ray shielding, and (d) bare ^{252}Cf source with 2.5 cm of HDPE on frontside (between detector and source). 141

Figure 5.36: Pulse-height spectra features for the dual-integrated 6x6-arrayed MSND with irradiation from the KSU unmoderated ^{252}Cf spontaneous fission neutron source (Ω_F = 1.07 x 10^{-3}). The pulse height spectra key is: (a) background with ^{252}Cf source in the shielded cask, (b) bare ^{252}Cf source with frontside irradiation, (c) bare ^{252}Cf source with backside irradiation, 2.5 cm of HDPE on backside, (d) bare ^{252}Cf source with frontside

irradiation, 2.5 cm of HDPE on backside, and (e) bare ^{252}Cf source with backside irradiation, 2.5 cm of HDPE on frontside. The large number of counts in channel 58 is attributed to amplifier clipping of large pulses. 143

Figure 6.1: Illustration of a cut-section assembly of the neutron energy-spectrum linear-unfolding detector system, utilizing dual-integrated 6x6-arrayed MSNDs, and measures the energy of a neutron based on the depth of interaction within neutron moderating material, e.g. HDPE. For simplicity and ease of view, only six MSNDs are shown, and the NELU detector scale is enlarged. 150

Figure 6.2: (left) Astronaut with Bonner ball neutron detector control unit and (right) detector module in Destiny laboratory. Source is from [127]. 151

Figure 6.3: Illustrations of advanced microstructure design with (left) interlaced microstructures and (right) opposing microstructures that are etched from both sides of the silicon diode. The interlaced design offers improved charge drifting electric field potential and the opposing design offers improved neutron absorption without the need of a second off-set detector. 154

Figure 6.4: SEM pictures of wet-etched advanced microstructure designs with interlaced microstructures (left) that are etched from both sides of the silicon diode to improve charge drifting electric field potential and opposing microstructures (right) to improve neutron detection efficiency. 154

Figure 6.5: Modeled electric potential solution within conformally-diffused 10 kΩ-cm Si, 500-µm deep, 25-µm pitch, front and backside interspersed-trench MSND. Each plot key describes the electric potential gradient within the Si fin for (a) -1 V, (b) -4 V, (c) -10 V, and (d) -50 V of applied bias... 155

Figure 6.6: Modeled transient solution of current versus time within conformally-diffused 10 kΩ-cm Si, 500-µm deep, 25-µm pitch, front and backside interspersed-trench MSND. The silicon fin is 25 µm in width and is the same modeled geometry and 10 V potential field as shown in Figure 6.5. 156

LIST OF TABLES

Table 2.1: A short list of neutron sources. 10
Table 3.1: Efficiencies (in percent recorded) for stacked straight trench dual-integrated top-device of width T and depth H filled with ^{6}LiF in a unit cell of width W_{cell} 39
Table 3.2: Efficiencies (in percent recorded) for stacked straight trench dual-integrated bottom-device of width T and depth H filled with ^{6}LiF in a unit cell of width W_{cell} . The bottom-device pattern dimensions for the simulated efficiencies are the same as the top-device pattern dimensions. The bottom device is off-set from the top device, where the bottom trench is centered with the top fin. 40
Table 3.3: Efficiencies (in percent recorded) for a stacked straight trench dual-integrated MSND with symmetric top and bottom devices of width T and depth H filled with ^{6}LiF in a unit cell of width W_{cell} . The bottom device is off-set from the top device, where the bottom trench is centered with the top fin. 41
Table 4.1: ICP-RIE Oxford PlasmaLab 100™ etch recipe to dry etch trench microstructures 312 microns deep with multistep processing. 47
Table 4.2: S.M.A.R.T. Lab metrology equipment information. 64
Table 5.1: Stacked MSND thermal-neutron (ϵ_{th}) and ^{137}Cs gamma-ray (ϵ_{γ}) detection efficiencies and neutron to gamma-ray rejection ratio (n/γ) for a specified LLD. 124
Table 5.2: Individual and stacked 4-cm^2 MSND thermal-neutron (ϵ_{th}) and ^{137}Cs gamma-ray (ϵ_{γ}) detection efficiencies and neutron to gamma-ray rejection ratio (n/γ) for a specified LLD. 130
Table 5.3: Intrinsic fast-neutron detection efficiencies (ϵ_{F}) for the stacked 6x6-arrayed MSND. The orientation of the detector, HDPE, and ^{252}Cf source are shown in sequential order according to arrangement, such that MSNDF and MSNDB stand for front and back irradiation, respectively. 144

LIST OF ACRONYMS

3D	-Three Dimensional
BOE	- Buffered Oxide Etch
Chn	- Channel
CV	- Capacitance versus Voltage
DC	- Direct Current
EDL	- Kansas State University Electronics Design Laboratory
EM	- Electro Magnetic
FWHM	- Full-Width Half Maximum
HARDE	- High Aspect Ratio Deep Etching
HDPE	- High Density Polyethylene
ICP-RIE	- Inductively Coupled Plasma Reactive Ion Etching
IV	- Current versus Voltage
LLD	- Lower Level Discriminator
MEMS	- Micro Electro Mechanical Systems
MSND	- Microstructured Semiconductor Neutron Detector
n/γ	- Neutron to Gamma-ray rejection ratio
SEM	- Scanning Electron Microscope
S.M.A.R.T. Lab	- Kansas State University Semiconductor Materials And Radiological Technologies Laboratory
TLD	- Thermoluminescent Dosimeter
VLSI	-Very Large Scale Integration

ACKNOWLEDGEMENTS

The research described in this dissertation was performed at the Semiconductor Materials and Radiological Technologies (S.M.A.R.T.) Laboratory, the Electronics Design Laboratory (EDL), and the Kansas State University (KSU) TRIGA Mark II nuclear reactor, Kansas State University, Manhattan, KS 66506, U.S.A. This research was supported in part by the Defense Threat Reduction Agency (DTRA) Contract DTRA-01-03-C-0051 and National Science Foundation Grant no. 0412208.

The author is greatly indebted to Prof. Douglas S. McGregor, your deep influence on my life through both knowledge and understanding will stay with me forever. The author would also like to thank the members of the S.M.A.R.T. Laboratory at Kansas State University, in no particular order, for their invaluable contributions to this work: Dr. Walter McNeil, Adam Streit, Ryan Fronk, Dr. Philip Ugorowski, Adam Brooks, Kyle Nelson, Ben Montag, Dr. Alireza Kargar, Martin Ohmes, Dr. Elsa Ariesanti, Troy Unruh, Reese Gehring, Bethany Holste, Brian Cooper, and Dr. Kara Ross. Additionally, much appreciation is given to the help and support from the EDL design team, Tim Sobering and Dave Huddleston, and the KSU nuclear reactor staff. The author wishes to extend his appreciation to his advising committee including Prof. J. Kenneth Shultis, Prof. Christopher M. Sorensen, and Prof. Zhijian (ZJ) Pei, for their guidance and support. Finally, the author would like to thank his family for their understanding and strong support.

DEDICATION

To the Bellinger Brotherhood.

Strength and Honor.

CHAPTER 1

INTRODUCTION

Equipped with his five senses, man explores the universe around him
and calls the adventure Science.
Edwin Powell Hubble

In this chapter, the motivation for the microstructured semiconductor neutron detector (MSND) is given. This includes commercially-available neutron detector weaknesses and how the MSND resolves those weaknesses. Thereafter, the organization of the thesis is discussed.

1.1 Motivation for the Thesis

Neutron detection has been important since early experimental studies of the atomic nucleus (circa 1932) [1]. Initial experiments used polonium-beryllium sources that relied on an, at the time unknown, (α,n) reaction and was referred to as beryllium radiation [1]. The detection of a neutron, in its earliest form, was measured through secondary interactions in matter by James Chadwick [1]; these early detectors were gas-filled radiation detectors, such as ionization chambers, proportional counters, and Geiger-Müller counters. Conversely, solid-state radiation detectors, originally referred to as conduction counters, had not been described in detail until 1945 by Van Heerden [2]. In addition, the combination of a neutron converter material layered on a solid-state radiation detector was not conceived until 1959 [3]. By this time, "atomic piles",

now known as nuclear reactors, were becoming widely available for scientific endeavors in the study of nuclear physics, and more specifically, neutron physics. Ushering in this age of the neutron, were the many practical uses for them, such as power generation, transmutation, neutron activation analysis, and weapons of mass destruction, to name a common few. Consequently, neutron sensing systems and technologies were, and are, needed to monitor neutron fields[1] and perform sophisticated scientific experiments and measurements.

Many neutron detection systems exist today; common systems include proportional gas counters (e.g., ^{3}He and $^{10}BF_3$), doped scintillators, thermoluminescent dosimeters (TLDs), and thin-film coated (e.g., ^{6}LiF and ^{10}B) semiconductor diodes. These detector systems all rely on ionizing reaction-products produced from transmutation, fission, or recoil nuclei reactions. Further detail of these reactions will be described in chapter 2. Transmutation and fission reactions are the most common thermal-neutron detection materials and rely on the high thermal absorption cross-section of some materials [4]. Common transmutation materials are ^{157}Gd, ^{3}He, ^{10}B, and ^{6}Li, given respectively in decreasing thermal-neutron absorption cross-section. Common fission reaction materials are ^{233}U, ^{235}U, and ^{239}Pu [4]. Note that the probability of neutron interaction decreases rapidly with increasing neutron energy for the previously mentioned thermal-neutron detection materials. Therefore, recoil nuclei reactions are the most common fast-neutron detection materials and rely on the elastic neutron scattering interaction with light nuclei for a detection method. In a specific interaction with a hydrogen nucleus, an incident neutron transfers a portion (or all) of its kinetic energy to the scattering nucleus, resulting in a recoil proton which is relatively easy to detect [4].

There are advantages and disadvantages to all current neutron detection systems. Many neutron detection systems are designed for specific experiments or applications, because of the lack of variety of neutron detection systems currently commercially available, new and versatile detection systems are needed to fill the application gaps of common commercially available neutron detection systems. General key advantages of an optimal neutron detector system for commercial applications include: *high neutron detection efficiency (>80%), high gamma-ray discrimination (>10^6n/γ), low power operation, ruggedness, active/remote readout, and*

[1] Note that although a large-enough field of neutrons are visible to the naked-eye through secondary Cerenkov radiation in the vitreous humour, many neutron radiation environments and applications are well below this deadly threshold of native human perception.

economic feasibility, with disadvantages being the lack-thereof. Until now, the work-horse of the neutron detection industry has been the ^{3}He gas-filled detection system, which has a high efficiency for thermal-neutron detection and good gamma-ray discrimination. The deficiencies of a ^{3}He detection system is that it requires high-voltage operation, is sensitive to microphonics [4], and has a high cost of production because of recent shortages of ^{3}He gas [5]. Doped and plastic scintillators are occasionally used for thermal- and fast-neutron detection, respectively, because of their moderate neutron detection efficiency and direct sensitivity to fast neutrons. However, doped and plastic scintillators have only moderate gamma-ray discrimination, (a property that can be mediated by pulse-shape discrimination), a high-cost and difficulty of production and implementation, and the need of fragile high-power photomultiplier tubes (PMTs) for radiation sensing. TLDs and thin-film coated semiconductor planar-diodes have also been used for thermal-neutron detection as low power, rugged, and economical neutron-detection systems. TLDs suffer from low efficiency, moderate gamma-ray discrimination, and no active readout capability [6]. Thin-film coated diodes have the added advantage of low cost very-large-scale integration (VLSI) mass production methodology, yet suffer from a low intrinsic-efficiency. These thin-film coated diodes have detection efficiency of no greater than 5% for common neutron-reactive material coatings [7]. Note that a neutron-reactive material coating thickness is optimized for maximum neutron-detection efficiency by considering the neutron absorption probability, energies and ranges of the reaction products, and the types of reaction product radiation (light/heavy ions, conversion electrons, or gamma rays) [7].

The attributes of the thin-film coated diode are markedly close to satisfying the criteria; however, it fails to satisfy one important criterion, namely it has a low neutron-detection intrinsic efficiency. The relatively low efficiency of these thin-film coated diodes, caused by reaction product self-absorption in the neutron sensitive coating, makes them ill suited for common applications such as real-time dosimetry and area monitors. The first original idea to increase the neutron detection efficiency of the solid-state thin-film coated diode was suggested by Muminov et al. in 1987 [8]. They proposed incorporating channels, i.e. microstructures, into the semiconductor diode and subsequently backfilling them with neutron-reactive material to increase the thermal-neutron detection efficiency over that of the coated-diode neutron detector. This increase in efficiency occurs because the surface area of the neutron reactive film in contact with the semiconductor is increased. This observation is only partly true. The efficiency also

increases because more than one reaction-product charge particle can contribute to the ionization in the bulk semiconductor [8]. However, no MSNDs were ever fabricated by Muminov. Efforts to study these microstructured semiconductor neutron detectors were later pursued by Schelten et al. [9, 10], Allier [11], and McGregor et al. [12]. Again, no MSNDs were fabricated. The first microstructured semiconductor diode was fabricated by Allier et al. in 1998 [13] and the first microstructured semiconductor-diode thermal-neutron detectors were simultaneously fabricated by Allier et al. [14] and McGregor et al. [15, 16] in 2001, each with only modest neutron detection efficiency improvement beyond a thin-film planar diode. The last decade has brought vigorous investigative work into the area of solid-state microstructured semiconductor neutron detectors [17-50]. The motivation for this dissertation is to investigate and fabricate advanced designs of the microstructured semiconductor neutron detector. The work described here includes large-area, deep-etched, single and stacked MSNDs with unprecedented thermal-neutron detection efficiency. Application of these MSNDs to produce large detector arrays is also discussed.

1.2 Contribution to MSND Science and Technology

A summary of the contribution of the work herein to MSND science and technology over previous work is listed below.

- Simulation of a ^{6}LiF backfilled stacked-MSND ion energy-deposition spectrum and calculation of expected intrinsic efficiency based on adjustable MSND microstructure parameters.
- Improvement of silicon micromachining plasma dry-etching methods through improved HARDE etching techniques reaching silicon microstructure depths beyond 300 microns with smooth and uniform sidewall features.
- Plasma dry-etching of advanced MSND microstructure patterns, including sinusoidal, chevron, and straight trench patterns.
- Initialization and advancement of silicon micromachining wet-etching methods for MSND mass production processing method exploiting (110) Si crystal plane high-selectivity difference between [111] and [110] planes via a KOH etchant.

- Improved MSND diode properties through selective diffusion and conformal diffusion, around and within silicon microstructures, respectively.
- Development of a nearly-solid ^{6}LiF backfill method into silicon microstructures for MSND mass production. In conjunction with this backfill method, a process was developed to produce ^{6}LiF nanoparticles.
- Increase size of the MSND from 0.28 cm^2 to 1 cm^2 and 4 cm^2, while retaining sub-μA leakage-currents and practical capacitances at the applied bias voltage.
- Development of a dual-integrated stacked-MSND system with the highest thermal-neutron detection efficiency ever reported for a solid-state semiconductor neutron detector.
- Development of a 6x6-element stacked-MSND array for increased neutron sensitivity and for using in neutron spectrometer applications.
- Measurements of MSNDs' thermal- and fast-neutron responses and intrinsic detection efficiencies, along with MSNDs' gamma-ray rejection ratios for a ^{137}Cs gamma-ray source, for different MSND designs.

1.3 Organization of Thesis

The microstructured silicon diode neutron detector offers substantial performance advantages over the conventional thin-film coated diode neutron detector. However, fabrication of the microstructured diode using familiar VLSI semiconductor processing technology is not trivial. VLSI processing technology was developed to create integrated circuits on a single chip of semiconductor material [51, 52]. Most of the processing technology was developed around planar semiconductor wafer processing. The need for 3D microstructuring of the semiconductor for these thermal-neutron detectors has presented difficult challenges in developing techniques to fabricate the microstructured semiconductor diode neutron detector. Discussion of the electronic characteristics of these newly developed microstructured diode processing techniques is presented. Once the microstructured diodes are fabricated, the microstructure void space must be filled with neutron reactive material. Discussion of suitable neutron reactive materials is presented, along with various successful and unsuccessful material backfilling technologies and techniques. Neutron and gamma-ray discrimination testing is also discussed and compared to

theoretical model predictions. The design, testing, and uses of the microstructured semiconductor neutron detector technology are then discussed.

In Chapter 2, a background discussion of the neutron is given, along with a review of common commercially available neutron detectors. In Chapter 3, discussion is presented of the MSND design theory and variables, along with MSND simulated neutron responses. In Chapter 4, semiconductor-device fabrication methods are presented that fully develop the necessary VLSI semiconductor-microstructuring process technology needed to fabricate advanced individual MSNDs and integrated MSND arrays. In Chapter 5, a discussion is given about the measured electronic properties for different MSND designs, along with the neutron and gamma-ray sensitivity for each design. In addition, neutron and gamma-ray sensitivity of arrayed MSNDs for large-area high neutron-sensitivity applications is reported. Finally in Chapter 6, a discussion about the conclusions that can be drawn from the various results is presented, along with recommendations for future work of microstructured semiconductor neutron detector technology.

CHAPTER 2

BACKGROUND

If I have seen further, it is by standing on the shoulders of giants.

Isaac Newton

In this chapter, background information about neutron physics, neutron sources, and common neutron reactive materials used for detection purposes is presented. Subsequently, a review of common neutron detectors is also presented.

2.1 The Neutron

Early studies investigating the inner workings of the atom (circa 1920) came with rather surprising results — the nucleus of an atom was filled with hydrogen atoms [53]. In 1920, Sir Ernest Rutherford had envisioned a tightly bound neutral hydrogen atoms (or in his words, a neutral doublet) existing within the nuclei of atoms. This original idea of Rutherford's was based on the atomic weight of atoms and the more recently known fact that the number of possible elements were fixed[2], which showed that the properties of an atom were defined by a number that varied by unity in successive atoms. With this information at hand, Rutherford deduced that the helium nucleus consisted of four hydrogen nuclei and two electrons [53]. A quoted script of the account is as follows: "*Under some conditions, however, it may be possible for an electron to*

[2] This concept was outlined earlier in-time by Moseley's improved Mendeleev periodic table.

combine much more closely with the H nucleus, forming a kind of neutral doublet. Such an atom would have very novel properties. Its external field would be practically zero, except very close to the nucleus, and in consequence it should be able to move freely through matter. Its presence would probably be difficult to detect by the spectroscope ..." [53]. The details on how a neutral hydrogen atom could exist within the confines of the nucleus were yet to be determined, but the presence of neutral mass within the atom was theoretically obvious according to Rutherford. Eventually, the notion of the neutron being a proton and electron bound together was abandoned, this being simply because of the fact that the spin of the neutron is **½** and not the composite of an electron and proton with a tangled spin of **1** [54]. It was not until much later (circa 1932) that Chadwick, once a student of Rutherford, experimentally verified the presents of Rutherford's theoretical neutral particle. He accomplished this neutron verification through his experimental observations of recoil energies of hydrogen and nitrogen atoms by neutron bombardment [1, 55]. The discovery of the neutron is one of the more captivating tales of discovery in nuclear physics, and is well narrated by Evans in *The Atomic Nucleus* [55].

2.1.1 Physical Properties of the Neutron

The physical properties of the neutron are characterized as a subatomic particle with no net electric charge and a mass slightly larger than a proton. The neutron is a nucleon and is classified as a baryon, and as such, not a fundamental particle (see Figure 2.1). It is composed of one up

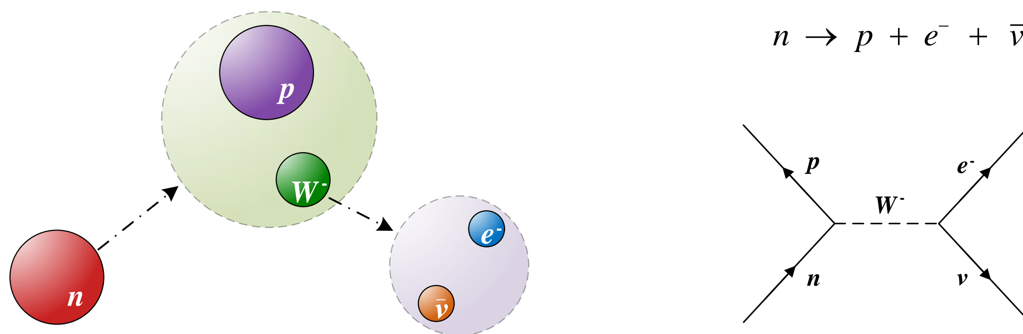

Figure 2.1: The fine-structure of the free neutron decay. (left) A free neutron will decay into three particles: a proton, an electron, and an antineutrino. (right) A Feynman diagram is depicted describing the free neutron beta decay via an intermediate heavy W⁻ boson.

quark and two down quarks [56]. Stable neutrons are usually only found in atomic nuclei (excluding neutron stars); such that, a free neutron decays via the weak interaction with a half-life of 10.25 minutes [57] according to the reaction shown in Figure 2.1 [56]. The number of neutrons in the nucleus of an atom determines the elemental isotope; it also correspondingly affects the neutron interaction cross-section, fission probability, and fusion probability of all atomic elements.

2.1.2 Neutron Sources

Because free neutrons are unstable, they can be obtained only from nuclear reactions (e.g., nuclear fission, nuclear fusion, photo-neutrons, (n, 2n) reaction, along with high-energy nuclear reactions (e.g. accelerator collisions or cosmic radiation particle showers). Because of the neutron's lack of electric charge, it is difficult to steer or contain them. Therefore, to utilize free neutrons for nuclear experiments, neutron activation analysis, neutron diffraction, power generation, radiological weapons of mass destruction, transmutation, along with many other applications [58, 59], readily available sources of neutrons are needed. A short list of such neutron sources is given in Table 2.1; a more exhaustive list of neutron sources with their physical details can be found in [4, 58, 60].

Table 2.1: A short list of neutron sources.

Neutron Source	Isotopes and Mechanics	Neutron Energy Range
Spontaneous Fission	^{252}Cf, ^{240}Pu	*e*V to M*e*V
Induced Fission	^{239}Pu, ^{235}U	*e*V to M*e*V
Fusion Generators	D + T → n + ^{4}He	14.2 M*e*V
	D + D → n + ^{3}He	2.5 M*e*V
Secondary Reactions	PoBe & AmBe (α,n)	*e*V to M*e*V
	$^{2}_{1}$H $(\gamma,$n$)$ $^{1}_{1}$H	
Nuclear Reactor	- Fission neutrons from the core	*e*V to M*e*V
	- Diffracted thermal collimated beam	0.0253 *e*V
Spallation	- High energy protons strike heavy target generating neutrons	*e*V to M*e*V
Exotic	- Plasma Pinch, Cosmic Rays, Sun	eV to GeV

Source: Knoll [4], Shultis [58], and ORNL [61].

2.1.3 Neutron Interactions for Detection

Neutron radiation is highly penetrating and ionizes mass indirectly. Because neutrons do not interact through Coulombic interactions with electrons, neutron detection must rely on measurement of secondary reaction-products resulting from a neutron capture or scatter. Neutron capture is the absorption of a neutron by an atom's nucleus, generally, causing the nucleus to become unstable and promptly decay or fission. These capture reactions are then used to indirectly measure a neutron's presence through charge sensing detector systems. A second type of reaction necessary for neutron detection is a scattering reaction, which can include both elastic (n,n) and inelastic (n,n') scattering [55]. Elastic scattering transfers some of the incident neutron's kinetic energy to the target nucleus (or compound nucleus). Inelastic scattering transfers some of the incident neutron's kinetic energy by momentary absorption of the neutron by the target nucleus and forming an excited compound nucleus, which may then de-excite through gamma-ray emission and an ejection of a lower kinetic-energy neutron [58]. Measuring neutron scatter reaction-products is a common method for fast-neutron detection; this neutron

measuring method is based on the recoil nucleus principle where neutrons are elastically scattered off light nuclei [4]. The recoil nuclei that result from neutron scattering on hydrogen atoms are called recoil protons, and detectors based on this interaction are commonly referred to as *proton recoil detectors* [4]. Fast-neutron detectors have many applications (e.g. neutron scattering experiments and neutron-source identification), but suffer the drawback of being dependent on the neutron having a large kinetic energy to cause a scatter within the detection medium. A common problem for a fast-neutron detector at some distance from a source is that a neutron that moves through the atmosphere is continuously being thermalized through scatters outside the detection medium. Hence, thermal-neutron detectors also have many applications, with a breadth well beyond those of fast-neutron detectors, because it is generally easier to purposefully thermalize a fast neutron with moderating materials, e.g., high-density polyethylene, to commonly increase absorption in neutron-capture materials, than to speed-up a thermalized neutron that is within the vicinity of a fast-neutron detector.

From all the stable nuclides, gadolinium has the highest thermal-neutron cross section. Of the many stable isotopes of gadolinium, the two most important isotopes with the largest absorption cross-sections for thermal neutrons are ^{157}Gd {$\sigma_a(E_{th})$ = 259,000 barns (b), natural abundance of 15.7%} and ^{155}Gd {$\sigma_a(E_{th})$ = 61,100 b, natural abundance of 14.8%} [62]. The reactions ^{157}Gd(n,γ)^{158}Gd and ^{155}Gd(n,γ)^{156}Gd lead to the emission of energetic conversion electrons ranging in energy from approximately 29 keV to 1.78 MeV and are produced with varying branching ratios [63-65]. Only 60% of neutron absorptions actually result in the emission of a conversion electron, and of those conversion electrons, 88.5% have energies below 100 keV [64, 65]. Enrichment of isotopic ^{157}Gd from natural gadolinium is economically infeasible for many neutron detection applications. The main advantage of gadolinium as a neutron reactive material is its large thermal-neutron absorption cross-section; hence, only a small amount of neutron converter material is needed to obtain a high neutron absorption probability. Yet, because the measurable reaction products are conversion electrons of varying low-energy, which are difficult to detect above the detection system's electronic noise, gadolinium's general use as a neutron detection material is not common [4].

The helium isotope ^{3}He {$\sigma_a(E_{th})$ = 5330 b, natural abundance of 1.4 ppm in air, mostly sourced from tritium decay} is the most widely used thermal-neutron detection material [4, 5, 66]. The thermal-neutron reaction ^{3}He(n,p)^{3}H releases a 0.573 MeV proton and a 0.191 MeV

triton particle ejected in opposite directions [4]. Because at room temperature ^{3}He is a gas, much of the reaction-product's total energy (Q-value: 0.764 MeV), can be captured and measured in simple gas-filled charged particle detection systems. The cross-section value falls rapidly with increasing neutron energy and is proportional to the inverse of the neutron velocity ($1/v_n$) in much of the thermal energy range and up to a neutron kinetic energy of 100 keV, above which reaction resonances occur [4]. Hence, because the Q-value of the ^{3}He neutron-reaction products is large enough to be easily detectable above the gas-filled detector's electronic noise, the neutron's kinetic energy imparted to the reaction products is not important for the gas-filled detector to have high neutron-detection efficiency.

The boron isotope ^{10}B {$\sigma_a(E_{th})$ = 3840 b, natural abundance of 19.8%} is commonly used for various types of neutron detectors because of its solid-state, high-absorption cross section, and its high-energy neutron-reaction products, which is an advantage over gadolinium. ^{10}B enriched to over 98% is readily available and can be acquired at reasonable costs from *Ceradyne, Inc*, for example. The thermal-neutron reaction ^{10}B(n,α)^{7}Li has two modes of decay: 94% of the thermal-neutron reactions result in the emission of a 1.47 MeV alpha particle and a 840 keV Li ion in the first excited state, which spontaneously emits a 480 keV gamma ray[3], and 6% of the thermal-neutron reactions result in the emission of a 1.77 MeV alpha particle and a 1.05 MeV Li ion in the ground state [4]. Similar to ^{3}He, boron also has a $1/v$ proportional cross-section in much of the thermal energy range and up to a neutron kinetic energy of 100 keV [4]. Boron is a chemically stable material and, in its purest form, behaves as a semiconductor with a resistivity of 10^{6} Ω cm [67]. The relatively large thermal-neutron absorption cross-section along with moderate crystalline density of ^{10}B (ρ = 2.18 g cm^{-3}), yields a macroscopic thermal-neutron cross section of 500 cm^{-1} (i.e., the 1st attenuation length being 20 microns).

Finally, the lithium isotope ^{6}Li {$\sigma_a(E_{th})$ = 941 b, natural abundance of 7.40%} is also commonly used for various types of thermal-neutron detectors because of its solid-state, high neutron-absorption cross section, and its high-energy neutron-reaction products, where this combination of attributes is an advantage over gadolinium and boron [4]. The thermal-neutron reaction ^{6}Li(n,t)^{4}He releases a 2.73 MeV triton and a 2.05 MeV alpha particle ejected in opposite directions. The reaction products from the ^{6}Li(n,t)^{4}He reaction are more energetic than those of

[3] It is commonly assumed and found that this photon nearly always escapes and does not contribute to the detector's response from the ^{10}B thermal neutron reaction.

the $^{10}B(n,\alpha)^7Li$ or $^{157}Gd(n,\gamma)^{158}Gd$ reactions, making detection and discrimination from background radiations more manageable. Similar to ^3He, lithium has a 1/*v* proportional cross-section in much of the thermal energy range and up to a neutron kinetic energy of 100 keV, with a large resonance-spike thereafter [4]. Pure lithium is a highly reactive alkali metal and is typically compounded, such as ^6LiF (ρ = 2.54 g cm^{-3}), to stabilize the element in atmospheric conditions. ^6Li isotopic enriched to 95% is readily available and can be acquired at substantial costs from *Oak Ridge National Laboratory Y12 group*. Compared to Gd and ^{10}B, the main advantage of ^6LiF as a neutron converter material is the emission of significantly higher-energy reaction products that increase the detector's output signal amplitude, thereby improving the detector's signal-to-noise ratio and gamma-ray discrimination.

2.2 Common Neutron Detectors in Review

There are a wide variety of neutron detectors available to the commercial consumer and the scientific researcher. The most common neutron detector designs that are readily available are discussed in the following Sections. These include gas-filled, thermoluminescent, scintillating, solid-form semiconductor, and thin-film coated semiconductor types of neutron detectors.

2.2.1 Gas-Filled Neutron Detectors

A gas-filled neutron detector is simply an ion chamber or proportional counter that is sensitive to neutrons. Such detectors may incorporate fill gases with large neutron absorption cross-sections (such as ^3He or $^{10}BF_3$)[4] making them highly efficient (> 80%) thermal-neutron detectors or by lining the walls of the gas chamber with a neutron sensitive coating (such as ^6Li, ^{10}B, or ^{235}U) and filling with detection gas (e.g., P10 quenched Ar gas). A more recent gas-filled neutron detector design incorporates the use of a matrix of coated fins to increase the surface area of neutron reactive materials or a solid fill of neutron reactive materials loaded in an aerogel or foam matrix [68]. The fill gas, whether neutron absorbing or not, is typically under pressure to increase reaction-product energy capture within the detection gas. Disadvantages to increased fill-gas pressure are a decrease in the detector's gamma-ray discrimination and that the gas may

[4] Note that a BF_3 gas-filled detector is both difficult to fabricate a detector from and to use in harsh environmental conditions, because it is a poisonous gas.

leak from the system during its operational lifetime, which changes the measured response of the detector over time by causing slower charge collection [4, 6, 69]. The general construction of a cylindrical gas-filled detector incorporates a pressurized gas-filled chamber with a very thin central stainless steel wire with a guard ring shielding the anode feedthrough [69] (see Figure 2.2). Both the neutron-absorber gas and lined gas-filled tubes suffer from the *wall effect*, in which the reaction products either strike the chamber wall or are born in the neutron absorber lining so they do not deposit the full energy of the reaction in the detection gas [4]. This effect smears the ion-energy deposition pulse-height spectrum towards lower energies, thereby, reducing the total detection efficiency and degrading the gamma-ray discrimination. As a result of gas loss, gas-filled neutron detectors can be difficult and expensive to manufacture. Additionally, they are also fragile, sensitive to microphotonic vibrations (i.e., mechanical shock), require high voltages (> 1000V), and are cumbersome to operate with the required counting electronics [4].

Figure 2.2: X-ray image of two ^{3}He gas-filled neutron detectors. The active regions of the detectors, when disregarding the field-tubes and insulators, are (left-detector) 5.5 cm by 4 cm diameter and (right-detector) 8 cm by 5.25 cm diameter. These detectors were used for the KSU diffracted thermal-neutron beam flux calibration [70].

2.2.2 Thermoluminescent Dosimeters (TLDs)

Neutron detectors that are compact, portable, and power-efficient are few in number, and the most popular detector of this type is the TLD. The neutron fluence is measured by observing an electronic structure change in a ^{6}LiF single crystal, where electrons, holes, and excitons (created from the ionization of the LiF crystal from the ^{6}Li neutron reaction products) may be caught in "traps" that are purposely incorporated into the single crystal structure [6]. These trap centers remain filled until the LiF crystal is heated to an appropriately high temperature, in which the trapped electrons and holes are freed and return to the ground state, thereby, emitting light. The amount of light emitted is proportional to the neutron dose or fluence [6]. TLDs are primarily used for gamma-ray measurements. Neutrons are recorded by LiF TLDs enriched with ^{6}Li (commonly referred to as TLD-600), and comparing the light output against an isotopically depleted ^{7}LiF TLD (commonly referred to as TLD-700). Hence, one can discern the corresponding doses in a mixed neutron and gamma-ray field [4]. Additionally, because of the TLD LiF human-flesh equivalence, they are commonly used as personnel dosimeters [4]. Disadvantages of TLDs include delayed dose determination and difficult gamma-ray discrimination because of the requirement of cross-referencing two TLDs, i.e., subtracting the gamma ray only sensitive TLD-700 response from a both neutron and gamma-ray sensitive TLD-600 response.

2.2.3 Scintillation Neutron Detectors

Scintillators used for the detection of neutrons include loaded-scintillating materials (e.g., organic, inorganic, and liquid types), scintillating plastics, which exploit the fast-neutron elastic-recoil interaction with hydrogen to produce an ionizing proton, and coated scintillators, which are coated with a thin-film of neutron-reactive material [4]. After the neutron interaction produces electron-ion pairs from the ionizing reaction-products in the scintillating material, the scintillation detection process is the same as detecting other types of ionizing radiation. Yet, because many of the reaction products are heavy charge particles, pulse shape discrimination can be used to distinguish neutron interactions from gamma-ray interactions [71]. Many scintillators are inherently rugged and others can be made rugged, but the photomultiplier counting electronics are fragile, bulky, require high voltage, are sensitive to changes in bias voltage and

magnetic fields, and require complex algorithms for discriminating a neutron interaction [72]. An alternative to using a photomultiplier tube to detect the light from the scintillator is to use a photodiode. However, use of a conventional or avalanche photodiode as the light-to-electronic conversion system is not ideal because of the small output signals, poor signal-to-noise ratio because of leakage current, size restriction caused by capacitance and shot-noise, and large pulse production from direct ionization of the diode from the source radiation [4, 73]. Additionally, an alternative to a photomultiplier tube to detect the light from a neutron interaction is to use photographic film or the dark-adjusted human eye.

2.2.4 Solid-Form Semiconductor Neutron Detectors

There are two types of common semiconductor neutron detectors, a thin-film coated planar diode and a solid-form semiconductor detector. The thin-film coated planar diode relies on an exterior coating of neutron converter material. By contrast, the solid-form semiconductor detector relies on internal interactions within the bulk of the semiconductor material. Common neutron converter materials used for thin-film coated planar-diodes are ^{6}Li and ^{10}B. Use of thin-film neutron converter materials suffer low neutron-detection efficiencies because of reaction product self-absorption energy loss in the thin-film converter material [12]. There have been some investigations to improve neutron detection efficiency by using a bulk semiconductor material as both the neutron converter material and as the semiconductor detector. However, only limited success has been shown for these solid-form neutron detectors, $^{199}HgI_2$ [74], $^{113}CdZnTe$ [75], and ^{10}BN [76, 77], with only failed attempts for $^{10}B_4C$ [78]. HgI_2 and CdZnTe both yield prompt gamma-ray emissions that are difficult to measure within the semiconductor material because of gamma-ray losses. Most compound ^{10}B solid-form semiconductor materials have shown significant charge-carrier trapping and poor energy-resolution of ion-energy deposition spectra [49, 76, 79], likely a result of imperfect methods used to produce the material. Additionally, results from growth processes performed on silicon substrates, where the capture layer is not distinct from the diode charge-collection region of the silicon substrate, makes it impossible to differentiate solid-form semiconductor device neutron-response characteristics, i.e., the neutron induced pulse-height spectrum, from a thin-film coated planar-diode neutron-response characteristics [80].

2.2.5 Basic Thin-Film Coated *pn* Junction Diode

Coated semiconductor diodes have been studied and used as neutron detectors for many decades [7, 12, 81]. The basic configuration consists of a common Schottky barrier or *pn* junction diode, upon which a neutron reactive coating, such as ^{10}B, ^{6}LiF, or Gd, has been applied (see Figure 2.3) [7]. Conventional VLSI processes, such as e-beam or sputter evaporative coatings, are used to apply most neutron reactive materials on diode surfaces as a batch process. As a result, wafer scale and batch fabrication of the thin-film coated planar diodes can be implemented for mass production with an overall economical production cost.

Again, since neutrons hold no electronic charge, methods used to recognize neutron interactions within a detector generally rely on second order effects. A thin-film coated diode detector relies on the creation of ionizing reaction-product radiation from a neutron interaction in the reactive film on the diode. The film material choice is optimized and based on neutron interaction probabilities and the type of secondary-emission ionizing radiation (charged particles or photons) [7, 11, 12, 78]. As illustrated in Figure 2.3, thermal neutrons that are absorbed in (n,α) neutron-reactive coatings spontaneously release ionizing reaction-products in opposite directions, such that only one product enters the semiconductor detector volume. Once in the detector volume, the ionizing radiation loses energy through Coulombic scattering, or in the case of a photon interaction, an ejected electron loses energy through Coulombic scattering, thereby creating a charge cloud of electron-hole pairs [7]. Because of the applied voltage and high-resistivity semiconductor material that is space-charge depleted, the electron-hole pairs separate and drift to their respective electrodes and consequently induce charge on the contact electrodes [82, 83]. This charge is then integrated by external amplifying and processing electronics and results in a measured neutron event (for additional detail see [7, 12]).

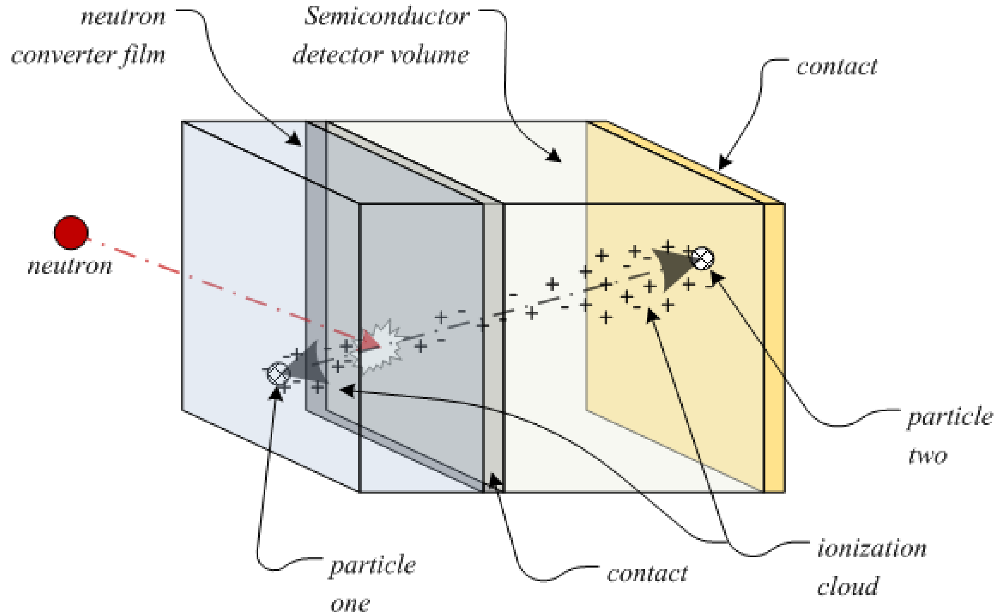

Figure 2.3: Basic illustration of thin-film coated semiconductor neutron detector design. It should be noted that some neutron-conversion films have more than one decay chain, therefore convoluting the ion energy-deposition optimization in the bulk semiconductor which is correlated to the film thickness. Additionally, notice that the film thickness is limited by the longest reaction-product range because of self-absorption.

Thin-film coated diodes are restricted to low thermal-neutron detection efficiencies, typically no greater than 5% intrinsic efficiency. The limited intrinsic efficiency is a result of reaction product energy self-absorption and discrete ranges as a function of "stopping power" in the neutron sensitive coating [12, 84]. To efficiently collect ionized charge carriers created from ionizing radiation interacting in semiconductor materials, a bias voltage must be applied across the active volume of the material. In many cases, this applied voltage is typically hundreds of volts [4]. Voltage enough to fully deplete a 1-cm^2 by 1-mm thick slab of high resistivity (50 kΩ-cm) silicon relies on blocking contacts to reduce thermionic leakage current. Limiting this leakage current is important so that a single high-energy radiation event within a semiconductor substrate alone can be measured, where the radiation event will generally only induce small currents (see Figure 2.4) [4]. Although it is not necessary to fully deplete a thin-film coated planar diode, because of the limited range of the reaction-product particles within the semiconductor (i.e., on the order of tens of microns), the active area of the detector is still limited to only a few square centimeters. Because of this limitation, many amplifying and pulse-

summing daughter circuits are needed to scale to a large (1 m^2) active area for increased neutron sensitivity, thereby, increasing the complexity and cost of a large arrayed system. Yet, this is not far beyond the complexity and cost of a comparable large-area ^{3}He gas-filled tube array, which is the current standard for large-area neutron detector systems.

Besides the aforementioned drawbacks, there are many advantages of coated diodes as neutron detectors. These include compact size, low power operation, low cost with VLSI production processes, and ruggedness. To date, the relatively low efficiency of these thin-film coated planar-diode detectors have made them unpopular for common applications such as real-time dosimetry, area and portal monitors, and neutron beam-line experiments.

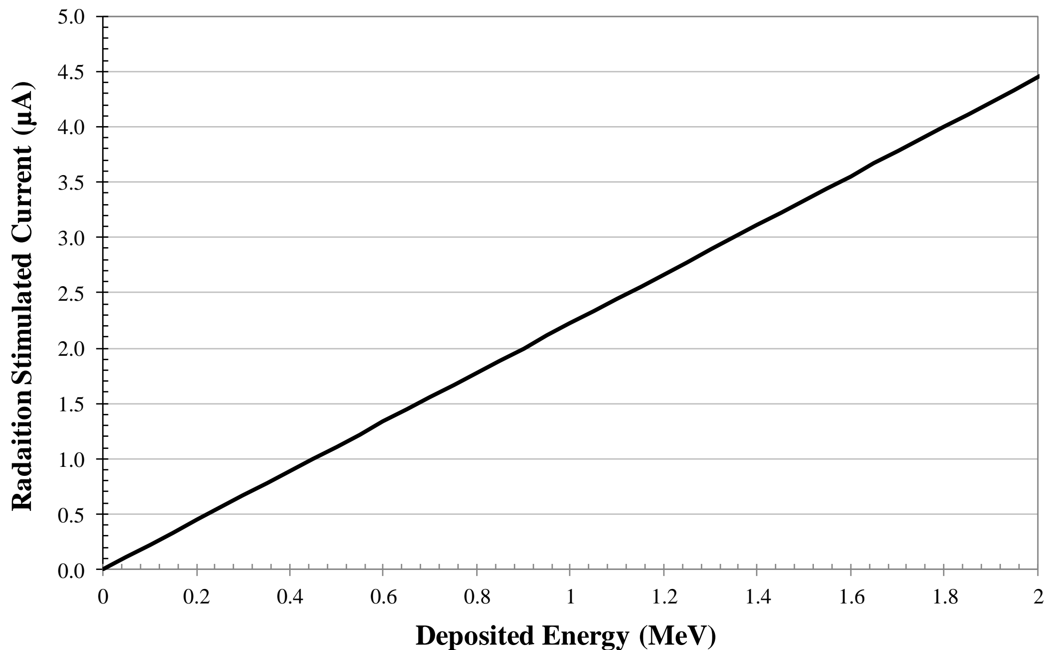

Figure 2.4: A graph of ideal approximate radiation-stimulated current in a 1 mm thick silicon diode. The calculated induced current assumes complete charge collection (no losses), radiation interaction charge-production at 3.6 eV per electron-hole pair, an approximate average charge mobility of 5×10^6 cm s^{-1} at 1000 V applied bias [85].

CHAPTER 3

MICROSTRUCTURED SEMICONDUCTOR NEUTRON DETECTOR: DEVICE DESIGN

I immediately thought of problems of neutron diffusion … described by certain differential equations into an equivalent form interpretable as a succession of random operations.

Stanisław Ulam

In this chapter, the theoretical device design of the MSND is discussed. The theoretical investigation of MSND designs includes discussion of how the design has improved upon the obsolete thin-film coated planar diode, including variable design features of the MSND's, and the impact of such variables on the MSND operation characteristics. Finally, an explanation of a MSND simulation model to predict expected ion-energy deposition spectra and MSND detection efficiencies from thermal-neutron interactions with different design features of the MSND is presented.

3.1 MSND Design Features

The most important drawback of the thin-film coated diode neutron detector is self-absorption of the reaction-product particles in the thin-film. The self-absorption of the reaction products in the thin-film restricts the coated diode to low neutron-counting efficiency. To limit this thin-film self-absorption drawback, the semiconductor diode can be microstructured and backfilled with neutron reactive material to maximize reaction-product energy capture within the

semiconductor detector volume (see Figure 3.1). Several groups have investigated various theoretical MSND designs [8, 9, 11, 29, 46, 78]. One of the key components to increasing the neutron detection efficiency of a semiconductor diode are the recent advances in high-aspect ratio deep etching (HARDE) techniques. HARDE techniques have allowed for unique compact microstructured neutron detectors with increased counting efficiency to be realized (see Figure 3.1) [22, 23, 39]. These MSNDs are fabricated by etching microstructured patterns into a semiconductor material and then backfilling the microstructure voids with an inert neutron converter material, such as ^{10}B or ^{6}LiF.

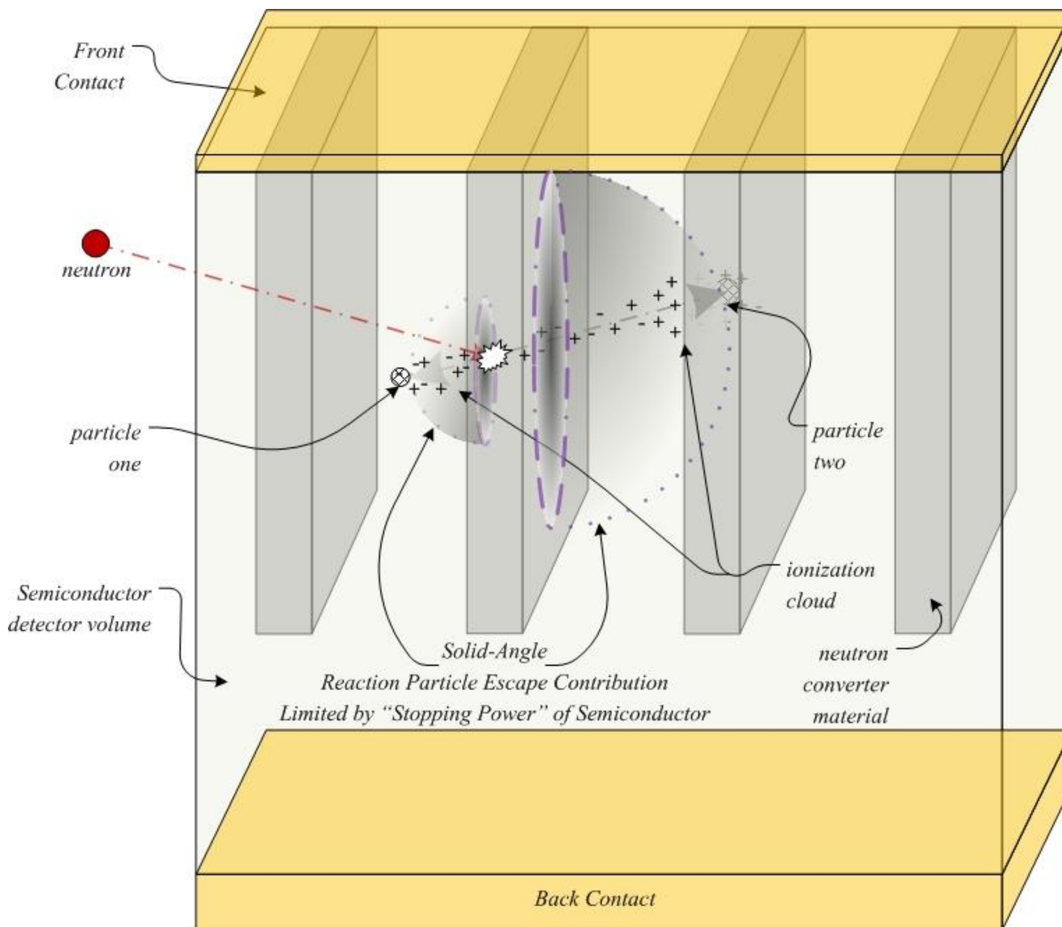

Figure 3.1: Shown is an illustration of the reaction-product charge particle variable energy deposition track through the microstructured semiconductor diode. It should be noted that some neutron-conversion materials have more than one decay chain, therefore convoluting the ion energy-deposition optimization which is correlated to the microstructure pattern size and shape specification in the semiconductor material.

This deep microstructure within the bulk semiconductor, backfilled with neutron reactive material, raises the neutron detection efficiency both by increasing the neutron absorption efficiency and by increasing the probability of registering an interaction above some lower level discriminator (LLD). This is evident by noticing that both energetic reaction products may contribute ionization to the semiconductor, therefore, increasing the amplitude of the pulsed signal from the detector. Thus, the self-absorption limited by the reactive-material thickness is largely reduced by the microstructured semiconductor backfilled volume. Hence, the MSND design dramatically increases the amount of neutron reactive material volume that can be used for neutron absorption. Overall, the neutron detection efficiency is significantly increased to more than an order of magnitude over that of a thin-film neutron detector. However, fabrication of the MSND has many challenges, necessitating an advancement of processing technology beyond that of commonly available VLSI technology.

Because of the wide availability of high-quality and high-purity silicon wafers, and because silicon has one of the lowest gamma-ray interaction cross-sections of the most common bulk semiconductors, silicon is a good choice for a semiconductor material to fabricate MSNDs. Furthermore, high-energy (> 100 keV) background photons do not contribute much to the measured ionization pulse-height signal in a silicon semiconductor device because of the low attenuation coefficient for high-energy photon interaction in silicon. If a photon interaction occurs, it would likely be a Compton scatter (see Figure 3.1), which would not transfer the full-energy of the original photon to the ionized electron. In addition, the ejected free electron would pass out of the silicon microstructure volume because of its long track-length in the low atomic number (Z) silicon, again, contributing even less of the full ionizable-energy within the detector.

Deep-etched silicon microstructures are easily fabricated with dry-etching, inductively-coupled plasma (ICP) reactive-ion etching (RIE) technology or with selective wet-etching by appropriate pattern alignment to specific crystal planes with (110) silicon [20, 86]. However, leakage current, capacitance, and electronic noise are important and serious issues to consider when cutting deep vertical microstructures into a *pn* junction diode that is to be used as a radiation detector. The leakage current contributes to electronic noise by reducing the ability to detect small signals and by saturating measuring electronics [27]. A great deal of work has been done to minimize the leakage current, while keeping the MSND operational performance and the utility of the fabrication process optimized.

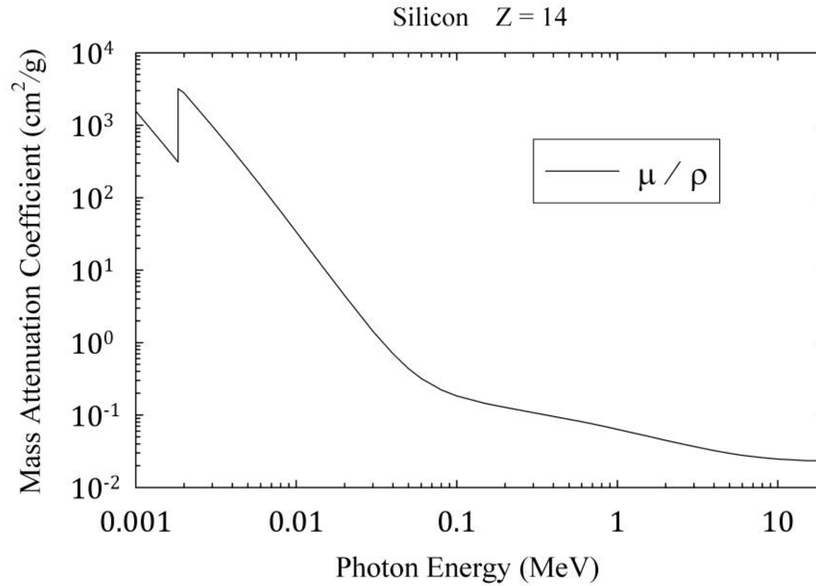

Figure 3.2: The mass attenuation coefficient, μ/ρ, as a function of photon energy for elemental silicon, data source [87]. Note that the total interaction cross-section, σ_T, is just the multiplication of μ/ρ by the atomic molar mass divided by Avogadro's number.

There are many isotopes that readily interact with neutrons to produce ionizing reaction products. Of particular interest are the (n,α) reactions with large thermal-neutron absorption cross-sections. These types of neutron reactive materials are well-matched converter materials because of their large-energy ionization potential and short ionization ranges in a bulk semiconductor. As mentioned in Chapter 2, ^{6}LiF is the neutron-reactive material of choice for the MSND technology because of its emission of significantly higher-energy reaction products than ^{10}B and Gd neutron-reactive materials, thereby, allowing improved neutron/gamma-ray (n/γ) discrimination ratios. Additionally, boron and gadolinium neutron reactive materials will be briefly reviewed. Processing a solid backfill of the ^{6}LiF neutron converter material into the silicon microstructures has been problematic. Although the first MSNDs were fabricated with ^{10}B as the converter [15, 88], MSND simulations have indicated that higher efficiencies and improved n/γ discrimination ratios are achieved with ^{6}LiF as the neutron converter backfill material [18, 45, 46]. Furthermore, because of the higher energies and longer reaction product ranges, the silicon microstructure feature dimensions can be on the order of 10-30 microns; whereas, ^{10}B backfilled MSNDs must have feature dimensions on the order of 2 microns or less to achieve similar efficiencies, where such technology has been pursued by other groups [32, 42].

Other semiconductor materials may also be considered, such as silicon carbide (SiC) and Diamond, both of which are much more difficult to obtain and both difficult to etch microstructures into because of material hardness. Although, interest in these hard materials still remain because SiC and Diamond have a much higher operating temperature range than Si [89]. Another common semiconductor material is gallium arsenide (GaAs), which has higher electron mobility than Si, but suffers increased recombination charge-loss because of its direct energy band-gap [52]. Additionally, GaAs suffers reduced gamma-ray discrimination because of its elemental composition of large atomic-number elements and higher mass density, which thereby increases the gamma-ray interaction cross-section of the bulk semiconductor material [90]. A detailed discussion of substrate materials and neutron reactive materials is presented elsewhere [46].

3.1.1 Microstructured Trench Design

The optimum design of the microstructured silicon etch pattern has many aspects. The first of which is the etch technique capability, where plasma dry-etching is functionally based on any photolithographic pattern, and wet etching is limited to crystalline plane alignment patterns [20, 86]. Secondly, the microstructured pattern of the neutron-conversion material will obviously demonstrate some unique angular-response characteristics, which are dependent on the pattern of the etched microstructure (see Figure 3.3). Some perforation patterns possess reduced counting response at certain azimuthal and polar angles of neutron incidence, a result of increased streaming through the MSND [48, 91]. Of all the designs considered [29, 43, 46, 91], the sinusoidal and chevron patterns have been shown to be the most angularly unresponsive designs [26]. But, for ease of fabrication and MSND stacking scenarios, the straight trench structure has been shown to be the most advantageous microstructure pattern design [22]. The microstructured semiconductor pattern that was specifically investigated was the straight trench parallel matrix shown in Figures 3.1 and 3.4. Once the neutron reactive material (^{6}LiF) and microstructure pattern shape (straight trench) were decided, the pattern dimensions were optimized. The microstructure dimensions may be dependent on whether the MSND will be a single device or an off-set stacked device detection-system for neutron detection efficiency gains from neutrons streaming through the silicon semiconductor material (see Figure 3.4).

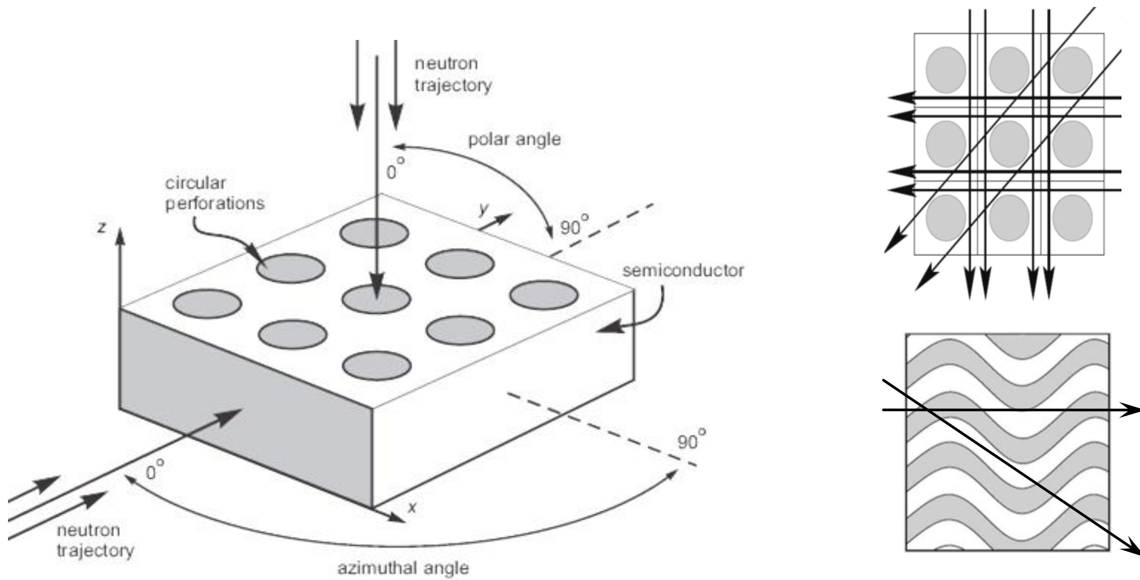

Figure 3.3: Illustration of angular response from neutron streaming paths through a cylindrical-hole and sinusoidal trench microstructured detector designs, source [48].

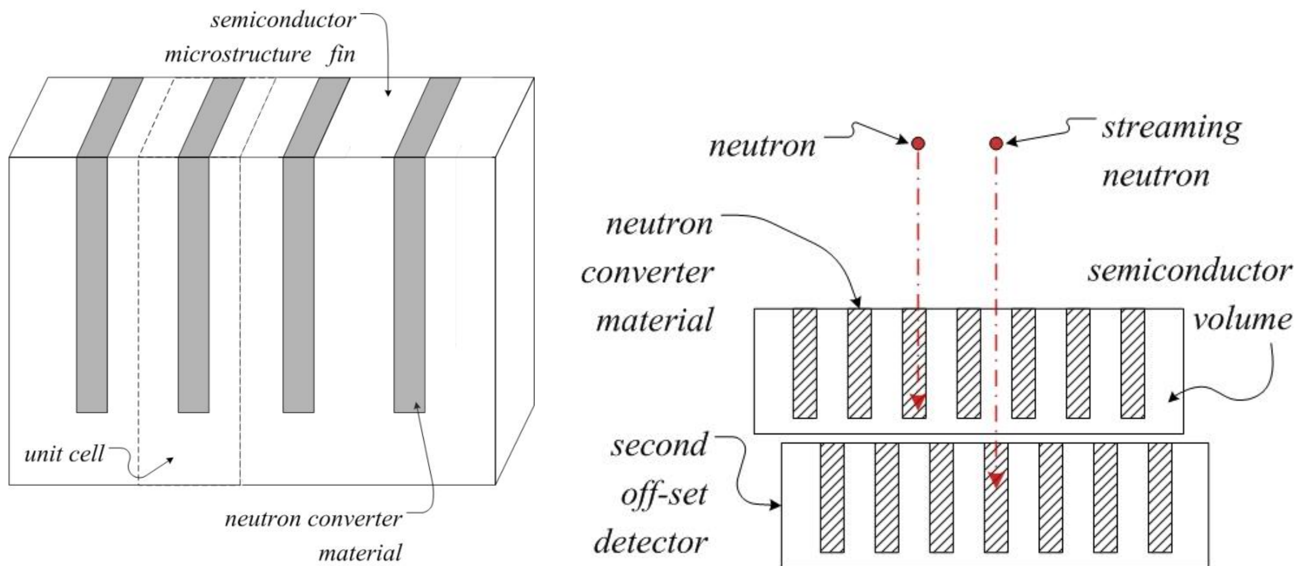

Figure 3.4: (left) The "trench design," composed of etched grooves backfilled with neutron reactive material, showing a unit cell as defined for calculations and modeling. (right) Neutron detection efficiency is increased, and streaming minimized, by stacking a 2nd detector off-set from the 1st. Note that the 2200 m/s neutron absorption cross-section of silicon is small, $\sigma_{Si,a}$ = 0.171 b [62].

The amount of ion energy deposited in the semiconductor detector medium is dependent on the dimensions of the ^{6}LiF backfill structure and the silicon semiconductor microstructure sizing as a result of different self-absorption and solid-angle escape probabilities of the reaction product ions. To optimize the MSND design, a compromise must be calculated between the amount of ^{6}LiF neutron converter material versus the amount of silicon detection material necessary to capture a sizeable portion of energy from the ionizing reaction products that is above some desirable LLD. As such, optimized dimension characteristics of both a single and dual-stacked straight trench MSND must be studied and simulated to determine the optimum sizing of the microstructure.

3.2 MSND Simulation Model Design

Herein a Monte Carlo simulation for the MSND is described. A model was developed to study the ion energy deposition and intrinsic thermal-neutron detection efficiency for a single and dual-stacked straight trench MSND design. With proper particle tracking and ion energy-deposition functions, the Monte Carlo simulation technique can be used to accurately estimate reaction-product ion energy-deposition spectra of a simulated MSND design specification. By tracking the reaction-products of a ^{6}Li and neutron reaction, the kinetic-energy deposited by the reaction products within MSND microstructure can be estimated. Reaction-product particle tracking is considered for both the ^{6}LiF backfill material and the microstructured semiconductor matrix. Once the spectrum has been estimated for specific MSND design parameters, the neutron detection efficiency is calculated. The efficiencies of different MSND design parameters were compared and an optimum configuration for the MSND was obtained.

3.2.1 Analytical Approach

To model the MSND response to thermal-neutrons, a Monte Carlo simulation method was developed (see 0), based upon the Shultis-McGregor methodology [17, 84], for estimating the ion energy-deposition spectra expected from a single straight trench MSND design for various dimensions of the etched features. Some assumptions were made to approximate the ion energy-deposition spectra and the corresponding predicted neutron detection efficiencies in the developed Monte Carlo simulation. It was assumed that:

1. The silicon semiconductor was transparent to neutrons and neutron scattering effects were ignored.
2. The detector was irradiated with a parallel beam of thermal-neutrons uniformly and normally illuminating the top surface of the detector.
3. The neutron absorption cross-section for ^{6}LiF converter material is the ion producing cross-section (i.e., neutron reactions with F and Si are ignored).
4. All energy deposited in the semiconductor material was assumed to contribute to the pulse-height signal of the detector, thereby, ignoring charge transport properties and imperfections in the semiconductor diode.
5. For a stacked detector design, the top and bottom detectors were identical in geometry.

The ion-energy deposition spectra physical model is described by the following mathematics. The neutron entry point (x_i, y_i) was uniformly and randomly sampled over the surface of the microstructured unit cell. Then, each neutron that entered the defined ^{6}LiF neutron-converter volume was given an interaction depth z_i that was randomly sampled over the normalized probability distribution function (*pdf*) defined by the neutron absorption probability $f(z_i)$, within the ^{6}LiF fill material, namely

$$f(z_i) = C\left[1 - \exp(-\Sigma z_i)\right], \tag{3.1}$$

where

$$C = \left[1 - \exp(-\Sigma D)\right]^{-1}, \tag{3.2}$$

Σ is the thermal average macroscopic cross-section for the ^{6}LiF converter material, D is the depth (or track length) of the neutron converter material and C is the proper normalizing constant. Now, by rearrangement, a random interaction depth can be found dependent on the neutron interaction *pdf*,

$$z_i = -\Sigma^{-1} \log\left[1 - \frac{R}{C}\right], \tag{3.3}$$

where R is a uniform random number generated on the domain [0,1]. Notice that if the neutron entry point is outside the defined neutron converter material space, the neutron passes through the MSND; this is important for the stacked-arrangement simulation model specifications.

Once a random interaction site (x_i , y_i , z_i) within the ^{6}LiF neutron converter material structure has been determined, a random isotropic direction must be given to the reaction products. A random direction $\Omega_i = (u_i , v_i , w_i)$ was chosen from an isotropic directional distribution, where (u_i , v_i , w_i) are the directional cosines for the random direction. The second reaction ion was given the opposite direction $(-u_i , -v_i , -w_i)$. Finally, the ions are tracked through the ^{6}LiF and silicon structures incrementally, and the energy deposition in each material is recorded and summed between the two interaction product types. Additional detail of the simulation methodology for the ion energy deposited in each material structure region is presented in 0. The ion energy-deposition spectra obtained from the simulation are ideal and do not include the effects from energy straggle, detector noise, other background ionization (gamma-rays), ion scattering, and other stochastic effects. Therefore, to help simulate an expected multi-channel analyzer recorded spectrum, the simulated spectra can be post-processed with a Gaussian averaging function as described in more detail in 0.

3.2.2 Modeled Neutron Beam and Source Considerations

The simulation neutron source was modeled to resemble a diffracted and collimated thermal-neutron beam, which is available as a standard research tool at numerous research reactor facilities. The thermal-neutron diffraction port at the Kansas State University (KSU) TRIGA Mark II nuclear reactor [50] has been used for experimental measurements for MSND verification [22]. The KSU TRIGA reactor diffracted and collimated thermal-neutron beam is well approximated by a parallel beam of uniformly distributed thermal neutrons (see Figure 3.5). Hence, a direct comparison can be made between the experimental performance of the MSNDs and that of the modeled thermal-neutron detection efficiencies and ion energy-deposition spectra.

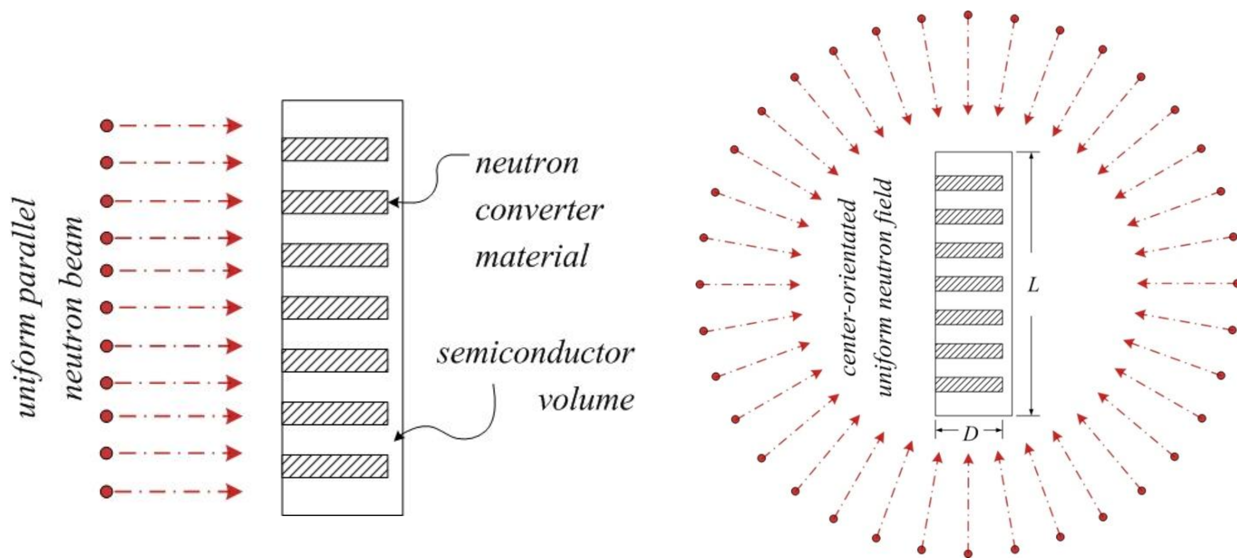

Figure 3.5: (left) Shown is the "trench design," composed of etched grooves backfilled with neutron reactive material, where a uniform parallel thermal-neutron beam is normally incident as defined for calculations and modeling. (right) An illustration of a center-orientated uniform neutron field configuration used by other groups [28]. In practical designs, the detector dimensions "L" are much larger than the microstructure depths "D".

It is pertinent to note that elsewhere [28] microstructured "pillar" MSNDs, where only a small unit cell is considered, were modeled using a center-orientated uniform neutron field with evenly distributed trajectories from 4π-directions (see Figure 3.5). This condition seems difficult to recreate[5] for verification purposes. In addition, this group [28] used the model to calibrate actual detectors instead of a blind verification with a calibrated detector, which can lead to an incorrect performance assessment. In the parallel beam case, which is perpendicular to the top face of the MSND, the modeled results give an intrinsic efficiency that can be extrapolated to larger MSNDs. If other neutron angular trajectories are to be considered, then the intrinsic efficiency of the MSND becomes severely dependent upon the intersection angle, as explained elsewhere [7, 47, 48, 91]. Otherwise, MSND efficiency calculations and experimental measurements can lead to a severe overestimation of the detector efficiency, explicitly explained elsewhere [92].

[5] Except maybe in the core of a nuclear reactor or a star (such as our Sun).

3.2.3 MSND Efficiency Estimation

The thermal-neutron detection efficiency of the straight trench microstructure pattern can be estimated through the previously mentioned Monte Carlo ion energy-deposition spectrum simulation. The detector efficiency is defined as the fraction of all thermal-neutrons incident on the detector (the unit cell in this case) that interact in the converter material and contribute a pulse-height signal (the total ion-energy deposition) above a specified LLD setting divided by the total incident neutron amount. The efficiency of the straight-trench microstructure design is easily calculated from the earlier derived spectra by summing all tallied counts in the spectra histograms above some desirable LLD energy cut-off. The post processing of the simulated efficiency, as opposed to tallying during the simulation, provides an organized way of measuring how the LLD setting affects the efficiency of the microstructure pattern.

In addition, as the size of the detector's microstructure geometry becomes relatively small[6], the detector efficiency is expected to converge on the total probability of neutron absorption in the converter volume from a geometric stand point. This limiting case is a verification check for the Monte Carlo simulations [84].

3.2.4 Stacked Detector Simulation Method

Stacking two microstructured detectors together can obviously improve detection efficiency as shown in Figure 3.6. Neutrons that stream through the silicon detection medium and are not captured in the neutron reactive material of the first detector can be caught by a second properly arranged off-set detector. Some microstructure patterns are better suited for this stacking arrangement than others. For instance, double stacking of the cylindrical-hole microstructure pattern may never be completely opaque to a normal uniform parallel beam of neutrons, without adding a third stacked detector to the arrangement. On the other hand, the straight trench microstructure pattern can be designed as such to be completely opaque to the prescribed neutron flux illustrated in Figure 3.6. Clearly, to increase the thermal-neutron detection efficiency of the stacked design, the amount of silicon microstructure detection material must be minimized to reduce neutron streaming effects. However, the thickness of the silicon microstructure must be

---

[6] Measured as the order of the shortest track length ion, the 2.05 MeV helium ion, in the ^{6}LiF converter material that still contributes energy above the LLD setting.

sufficiently thick in order to absorb enough ion energy above some LLD to register a count. In addition, consider that in the stacked arrangement, where the top detector's LiF backfill microstructure becomes decreasingly small, the bottom detector's response should approach that of the single detector system. This limiting case can therefore be used as a verification check of the Monte Carlo simulation of the stacking design.

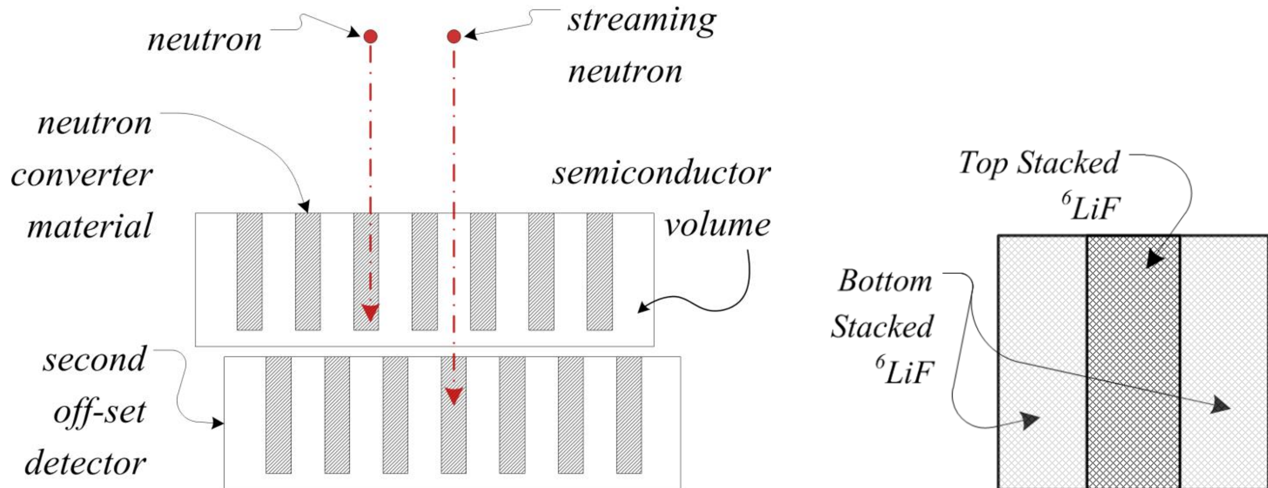

Figure 3.6: (left) Illustration of the stacked detector configuration for the straight trench microstructure design. (right) Notice in the top-side view that the straight trench pattern is completely opaque to normal incident streaming neutrons.

The stacked detector arrangement was modeled by calculating and summing the responses of two individual MSNDs. The straight unit cell, as shown in Figure 3.4, is a region identical in adjacent cells, and is repeated in the *x*-direction. The *y*-direction is considered infinite because the trench length in an actual MSND is much larger than the width; hence, reaction product energy losses from particles escaping at the ends have little effect on the final result [17, 18, 84]. Thus, only a single unit cell is needed to accurately model the expected thermal-neutron detection efficiency. The ^{6}Li(n,t)^{4}He charged particle reaction products exiting the cell at a lateral boundary would be measured in an adjacent unit cell; hence, a reflecting boundary condition for the MSND was used to include such events. Further detail is given in 0.

If the trench and semiconductor "fin" regions are identical in width, a simple exercise of doubling the efficiency would suffice to determine the stacked detector efficiency. However, if the trench is wider than the semiconductor fin, an accounting of absorbed neutrons must be

tracked and transferred to the second detector in the stack in order to correctly determine the total neutron interaction rate and thermal-neutron detection efficiency. The stacked detector model included neutron absorption losses from the first detector as they interacted or passed through to the second detector. The neutrons passing through a unit cell of the top detector were recorded, and shifted by half a unit cell to render the neutron interaction rate for a unit cell in the second detector. Afterwards, the reaction product interaction efficiency in the semiconductor was calculated. Figure 3.7 presents a neutron transmission image for the top detector, a shifted image of the incident neutron transmission as seen by the bottom detector, and the neutron interaction image for the bottom detector.

If the silicon fin width and ^{6}LiF backfill widths are equal, the MSND response for the top and bottom detectors are equal. As long as the trench width is greater than or equal to the semiconductor fin microstructure width, the stack configuration will be opaque to streaming neutrons. When the trench width is less than the semiconductor fin width, neutron streaming does occur and causes lower neutron detection efficiencies. Figure 3.8 illustrates the opposite case where the trench width and semiconductor fin width are not equal, with the ^{6}LiF-filled trench being wider that the semiconductor fin. Although thermal-neutron detection efficiency is increased for the top detector, the thinner semiconductor region absorbs less energy and causes the ion energy-deposition spectrum to shift towards lower energy channels.

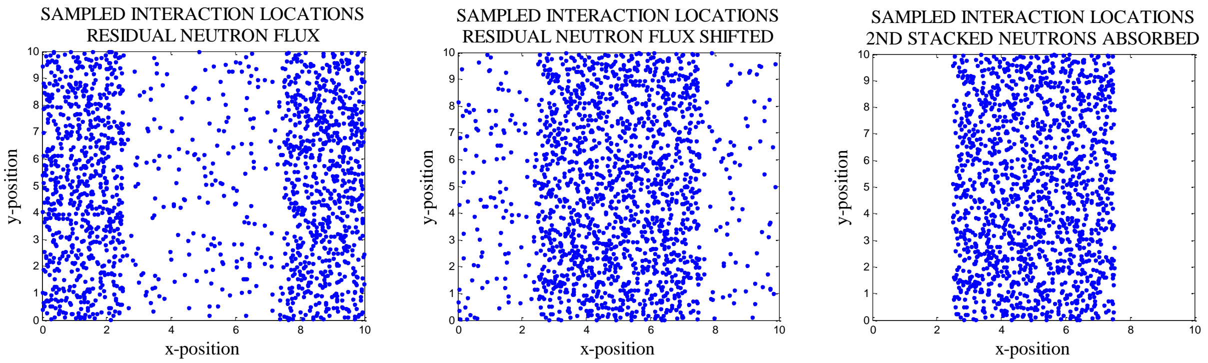

Figure 3.7: Shown are depictions of the neutron flux image transfer operations for the straight trench pattern with the trench width the same as the semiconductor fin width. Shown is the (left) neutron transmission image for the top detector where the center portion is the ^{6}LiF-filled trench region, (center) the shifted neutron flux image of neutrons that passed through the top detector so as to align with the bottom detector, and (right) the neutron absorption image for neutrons that interacted in the bottom detector. Note from the left and center images, some neutrons passed through the ^{6}LiF material.

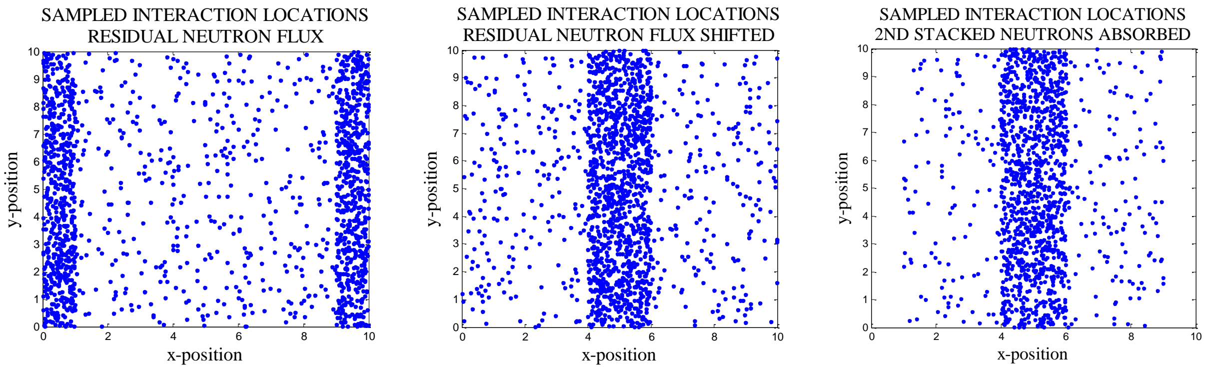

Figure 3.8: Shown are depictions of the neutron flux image transfer operations for the straight trench pattern with the trench width much larger than the semiconductor fin width. Shown is the (left) neutron transmission image for the top detector where the center portion is the ^{6}LiF-filled trench region, (center) the shifted neutron flux image of neutrons that passed through the top detector so as to align with the bottom detector, and (right) the neutron absorption image for neutrons that interacted in the bottom detector. Note from the left and center images, some neutrons passed through the ^{6}LiF material. Because the trench is much wider than the semiconductor fin, more neutrons are absorbed in the top detector than the bottom detector.

3.3 Simulated Reaction Product Ion-Energy Deposition Spectra

Simulated single-device MSND reaction-product ion energy-deposition spectra for varying microstructure parameters and patterns have been well developed previously [45, 46]. A single-device MSND ion energy-deposition spectrum can also be studied with the stacked MSND simulation by considering the top-detector ion energy-deposition spectrum alone. The stacked straight trench microstructure ion energy-deposition spectra for two varying parameters, depth and trench width, are represented in Figure 3.9. Figure 3.9 (A) and (C) show the calculated spectral results for the case in which the ^{6}LiF backfilled region is identical to the semiconductor fin region dimensions. Note that the spectral responses for the top and bottom detectors are practically identical, such that the stacked detector efficiency should basically double that of a single detector. There are a few notable spectral features, mainly the cut-off energies near 2.0 MeV and 2.7 MeV for the ^{6}Li(n,t)^{4}He reaction products, with the total Q value cutoff energy at 4.7 MeV, and a large dip in the energy spectra in the low-energy channel region of the spectra. The large dips in the low energy regions of Figure 3.9 (A) and (C) are fortuitous features characteristic of the microstructure design, caused by the increased probability that one or more reaction products will enter the semiconductor detector with significant energy deposition [46] (see Figure 3.1). As a result, the LLD can be set at high values without eliminating many of the neutron counts, thereby, increasing the n/γ discrimination ratio without significantly decreasing the detection efficiency.

Figure 3.9 (B) and (D) show the calculated spectral results for the case in which the ^{6}LiF region is much larger than the semiconductor fin region and clearly shows that the top detector has higher efficiency over the bottom detector. Note that the total spectral counts from the stacked MSND have shifted to lower channels and the gap widths of the dip in the spectra have decreased. The spectral shift of the bottom detector is a consequence of the reduced energy of the reaction products because of increased self-absorption energy-loss probability from the top-detector streaming-neutron interaction locations preference at the center of the ^{6}LiF region; see right-most depiction in Figure 3.8. In addition, the spectral-shape changes are a consequence of the thinner semiconductor fins, in which less energy is deposited, and results in more events appearing in the low energy channel regions of the pulse-height spectra. The stacked straight trench microstructure devices, where both detectors have the same microstructure, demonstrate

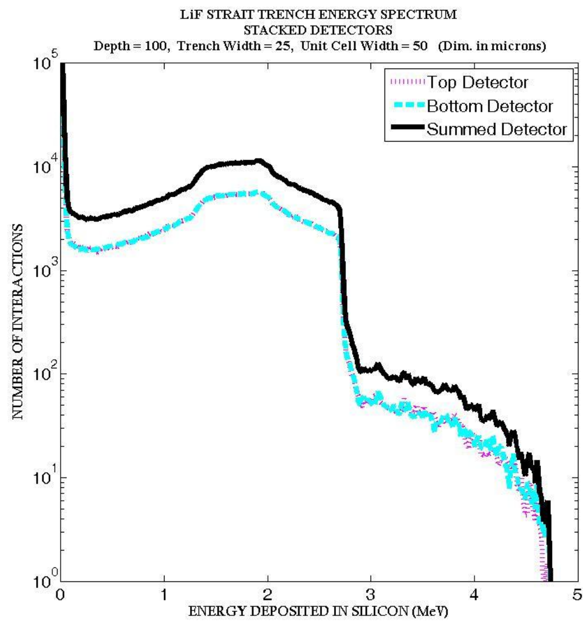

(A)

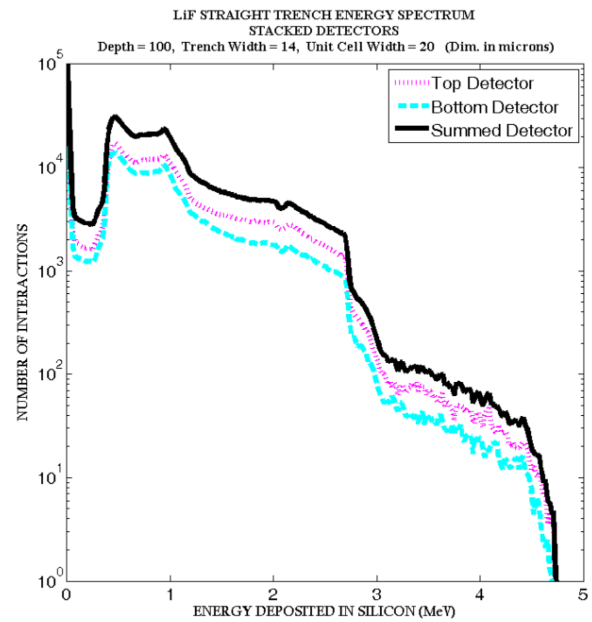

(B)

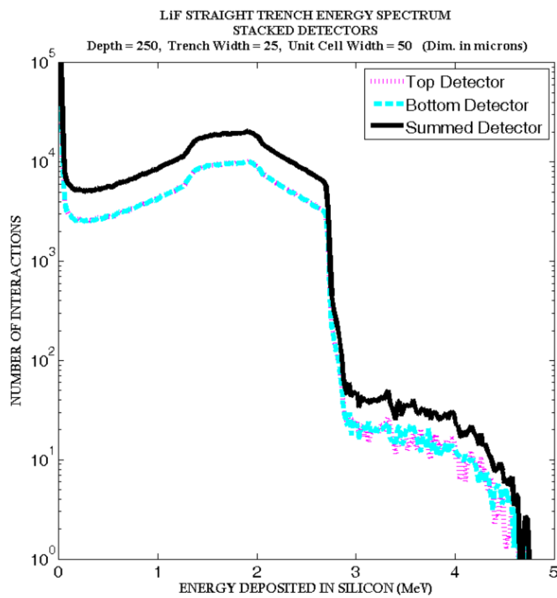

(C)

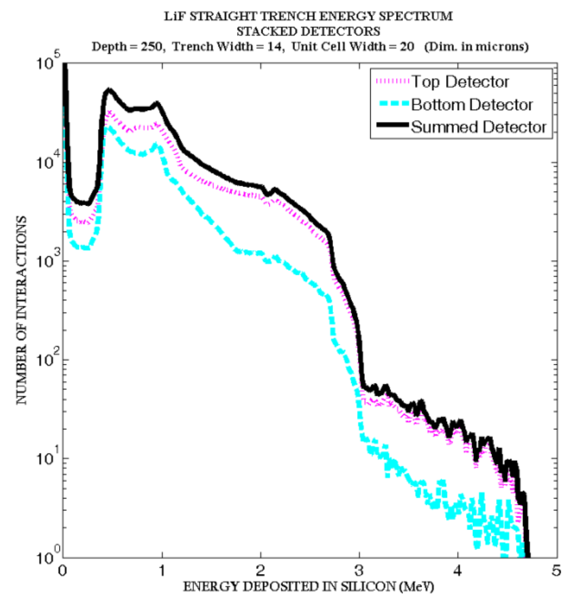

(D)

Figure 3.9: Straight trench ^{6}LiF-backfilled silicon microstructured stacked detector calculated ion spectra for four cases. Shown in (A) and (C) are cases in which the trenches and semiconductor fins are both 25 microns wide for depths of (A) 100 microns and (C) 250 microns. Shown in (B) and (D) are cases in which the trench and semiconductor fins are unequal, with the trenches being 14 microns wide and the semiconductor fins being 6 microns wide, for depths of (B) 100 microns and (D) 250 microns.

the best ion energy-deposition spectral response of the size parameters considered because of the higher energy response in the spectrum compared to the other microstructure width-parameter designs. Additionally, when the trench depth is 250 microns, few neutrons are actually transmitted through the ^{6}LiF neutron converter material of the top detector. Further discussion of the straight trench ion energy-deposition spectral shape, along with other variant microstructure parameters, is given in other studies [17, 45]. The developed simulation software code, which can be easily modified for varying stacked MSND parameters, can be found in 0.

3.4 Simulated Neutron Detection Efficiency

Simulated single-device MSND thermal-neutron detection efficiencies for varying microstructure parameters and patterns have been well developed elsewhere [17, 45, 93]. Additionally, individual MSND thermal-neutron detection efficiency can be studied by considering the top-detector ion energy-deposition spectrum alone in the stacked MSND simulation. The simulated thermal-neutron detection efficiency of each stacked MSND design is the fraction of all thermal-neutrons incident on the detector stack, to those that interacts in the converter material and contributes a pulse-height signal (i.e., ion energy deposition) above a specified LLD setting. Figure 3.10 depicts the expected intrinsic thermal-neutron detection efficiencies for stacked ^{6}LiF backfilled MSNDs with 250 micron deep features. For non-stacked (single) asymmetric trench structures in which the trench width is wider than the semiconductor fin width, produces higher efficiencies than symmetric designs provided that the LLD is set to low energy channels [17]. However, it is the symmetric design that offers higher efficiency for stacked microstructures.

In most cases, background radiations other than neutrons are present during a measurement. Gamma-ray radiation discrimination is the most important for viable commercial MSNDs, which is because of its prominent mass-penetration and ionizable energy potential. The n/γ ratio increases as the LLD is increased; however, valid neutron counts are also eliminated, which consequently lowers the detection efficiency. If the LLD is set in the low energy “dip” region of the spectrum, then only a small fraction of counts are lost, and the neutron detection efficiency remains high. If the LLD is increased above the “dip” region, then a significant fraction of

neutron counts are lost, which lowers efficiency but improves background radiation discrimination.

From Figure 3.9 (A) and (C), the dip region extends above 1 MeV; hence, the efficiency remains high as the LLD is increased up to 1 MeV, as shown in Figure 3.10 (A). At an LLD setting of 300 keV,[7] the efficiency for the stacked-MSND symmetric case with 25 micron wide and 250 micron deep trenches can deliver a total thermal-neutron detection efficiency of 47%. Note that the decline in efficiency is gradual as the LLD is increased to 1 MeV.

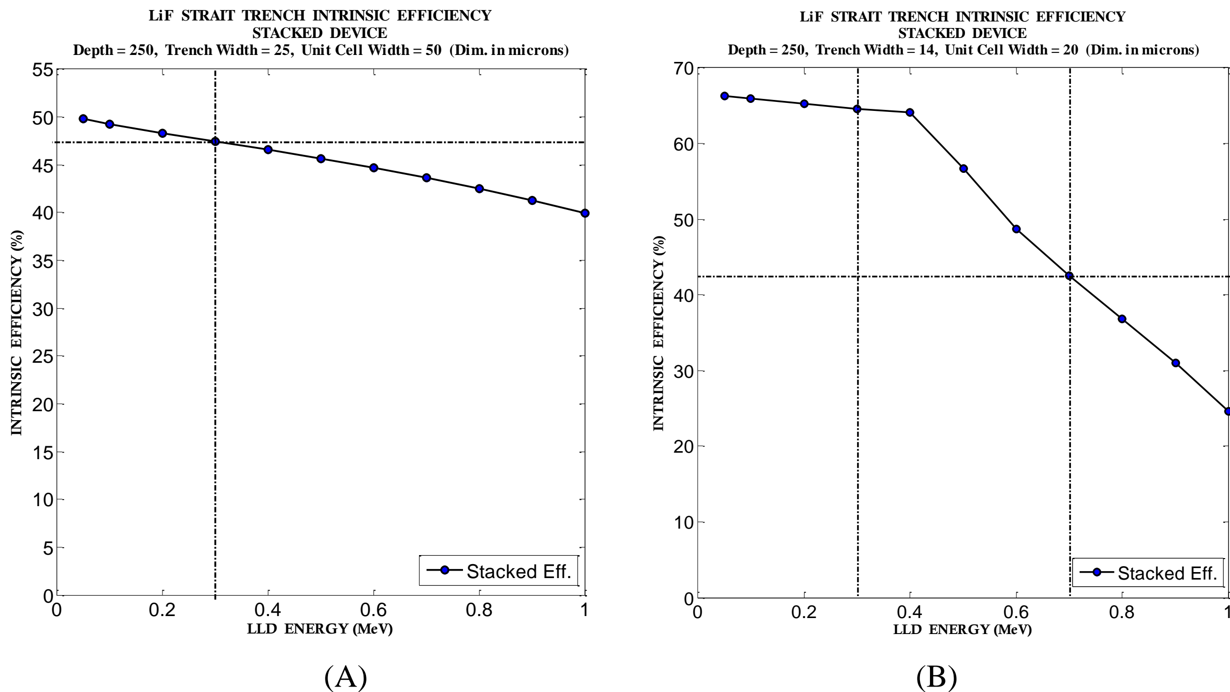

Figure 3.10: Predicted ^{6}LiF backfilled straight trench microstructured detector neutron detection efficiencies as a function of the LLD setting for cases in which the cell dimensions are (A) 50 microns with the trench feature size of 25 microns and (B) 20 microns with the trench feature size of 14 microns, with both microstructures 250 microns deep. The observed efficiency from the stacked MSNDs decreases as the LLD is increased.

The non-symmetric case of Figure 3.10 (B) with smaller microstructure features clearly has higher efficiencies if the LLD is set in the lower energy regions. However, from Figure 3.9 (B)

[7] 300 keV was chosen as five times 60 keV, which is the Compton crossover energy from photoelectric interaction prevalence to Compton scattering prevalence for silicon.

and (D), the dip in the spectra ends near 400 keV, and setting the LLD above that point will cause significant decrease in efficiency. Regardless, with the LLD set at 300 keV, the efficiency for the non-symmetric case (14 micron wide trenches, 6 micron wide semiconductor fins) with 250 micron deep trenches can deliver a total thermal-neutron detection efficiency of 64%. The increase in efficiency is directly related to the smaller feature sizes and not the asymmetry of the design. Previously reported [46], symmetric trench MSNDs with 10 micron wide trenches and semiconductor fins, can yield approximately 36% intrinsic thermal-neutron detection efficiency at an LLD setting of 300 keV. Obviously, stacking two of these detectors would exceed the 70% efficiency; yet, fabrication of such microstructures becomes difficult to micromachine and process into a MSND. To etch a microstructure pattern with 10 micron wide trenches and silicon fins into a silicon wafer that are at least 350 microns deep requires precise control of the etch process. Etching smooth and near vertical sidewalls into Si with an ICP-RIE dry etch is extremely difficult because of changing etch conditions as the microstructure is made deeper (for more detail see Section 4.1.1). To overcome these difficulties, a wet-etch technique has been developed in this work (see Section 4.1.2). Calculated efficiencies for straight trench dual-integrated MSNDs, along with separate top and bottom device efficiencies, are given in Tables 3.1, 3.2, and 3.3 for varying unit cell widths and MSND depths of 90 µm, 175 µm, 350 µm and 500 µm to be consistent with earlier reported MSND simulations [46]. For all cases the LLD was set at 300 keV.

From Table 3.1 it can be seen that there is general trend for the top-device (identical to a single device calculation) efficiency to increase as the ratio of the trench width to cell dimension (T/W_{cell}) increases. However, the detection efficiency decreases for especially small cell T/W_{cell} ratios (≥0.90), where the amount of semiconductor mass diminishes to such small values that the energy deposited in the thin semi-conductor fin-regions is too small to register a significant number of pulses above a 300 keV LLD.

Table 3.1: Efficiencies (in percent recorded) for stacked straight trench dual-integrated top-device of width T and depth H filled with ^{6}LiF in a unit cell of width W_{cell} .

T/W_{cell}	Cell width W_{cell} (μm)					Cell width W_{cell} (μm)				
	20	40	60	80	100	20	40	60	80	100
	Trench Depth H = 90 μm					Trench Depth H = 350 μm				
0.10	3.88	3.65	3.79	3.54	3.24	8.64	8.29	8.02	7.63	7.15
0.20	7.55	7.13	6.52	6.01	5.68	16.11	14.81	14.20	13.11	11.69
0.30	10.86	9.89	8.95	7.98	6.99	23.43	21.55	18.76	16.59	14.17
0.40	13.66	12.19	10.26	8.61	7.39	30.25	26.17	21.80	18.25	14.87
0.50	16.85	14.36	11.61	8.99	7.54	36.24	30.01	23.99	18.39	14.53
0.60	19.88	15.87	11.79	9.58	8.04	42.05	32.81	24.24	18.50	14.73
0.70	22.04	16.88	12.22	9.91	8.17	47.29	35.41	24.65	18.03	14.66
0.80	23.26	17.53	12.82	9.95	8.42	49.61	36.42	24.13	18.60	14.51
0.90	15.45	14.29	13.09	10.19	9.06	30.29	28.43	24.62	18.82	15.06
	Trench Depth H = 175 μm					Trench Depth H = 500 μm				
0.10	6.02	5.79	5.51	5.42	5.28	9.29	8.68	8.40	8.29	7.84
0.20	11.52	11.02	10.30	9.39	8.74	18.00	16.41	15.21	14.03	12.88
0.30	17.27	15.30	13.72	12.28	10.80	25.35	22.70	20.41	18.00	15.78
0.40	21.92	19.28	16.36	13.33	10.73	33.47	28.26	24.09	19.59	15.89
0.50	26.69	22.02	17.65	13.61	11.15	39.58	32.39	25.99	19.67	15.76
0.60	30.92	24.33	17.93	13.72	11.60	45.82	35.69	25.91	19.58	15.71
0.70	34.48	26.36	18.33	13.58	11.49	51.46	38.39	26.42	19.65	16.04
0.80	36.59	26.86	18.37	14.45	11.70	54.10	39.86	26.05	19.74	16.08
0.90	22.58	21.20	19.16	14.15	11.70	32.87	30.29	26.39	19.84	16.14

Neutrons are incident normally on the detector surface, and the LLD cutoff energy is 300 keV.

From Table 3.2 it can be seen that there is general trend for the bottom-device (identical in pattern dimensions to that of the top-device) efficiency to vary greatly as the ratio of the trench width to cell dimension (T/W_{cell}) increases, because of top-device neutron absorption (shadowing) effects (see Figure 3.9). The optimum case being a small cell width of equally-sized trench and semiconductor-fin dimensions (T/W_{cell} ratios = 0.50). Notice that for T/W_{cell} ratios greater than and less than 0.50, neutron shadowing reduces the detection efficiency decreases.

Table 3.2: Efficiencies (in percent recorded) for stacked straight trench dual-integrated bottom-device of width T and depth H filled with ^{6}LiF in a unit cell of width W_{cell} . The bottom-device pattern dimensions for the simulated efficiencies are the same as the top-device pattern dimensions. The bottom device is off-set from the top device, where the bottom trench is centered with the top fin.

T/W_{cell}	Cell width W_{cell} (μm)					Cell width W_{cell} (μm)				
	20	40	60	80	100	20	40	60	80	100
	Trench Depth H = 90 μm					Trench Depth H = 350 μm				
0.10	3.85	3.73	3.63	3.49	3.37	8.33	7.95	8.05	7.95	7.15
0.20	7.48	6.95	6.68	6.01	5.47	16.01	15.28	13.90	13.29	11.99
0.30	10.87	9.83	8.92	7.78	6.82	23.25	21.31	18.61	16.65	14.50
0.40	14.01	12.28	10.33	8.76	7.20	30.38	25.70	22.13	18.16	14.14
0.50	16.81	14.34	11.54	9.12	7.56	36.30	29.78	24.19	18.08	14.54
0.60	16.53	13.38	9.97	7.63	5.99	29.22	21.94	14.34	10.03	6.80
0.70	16.91	12.89	9.15	6.68	5.51	22.60	16.56	9.69	5.48	3.32
0.80	15.92	12.13	8.32	6.48	5.47	15.67	11.57	6.05	2.87	2.12
0.90	9.35	9.50	8.03	6.25	5.31	5.40	6.20	3.91	2.25	2.11
	Trench Depth H = 175 μm					Trench Depth H = 500 μm				
0.10	6.07	6.00	5.71	5.51	5.34	9.19	9.07	8.55	8.24	8.00
0.20	11.77	11.43	10.34	9.44	8.83	17.72	16.45	15.36	14.06	13.21
0.30	17.09	15.54	13.76	12.10	10.61	24.76	22.98	20.16	18.20	15.28
0.40	22.20	18.93	16.23	13.40	11.01	32.83	27.89	24.04	19.61	15.61
0.50	26.57	22.02	17.66	13.70	11.20	39.48	32.85	26.47	20.05	15.60
0.60	23.71	17.98	13.14	9.16	7.17	29.88	22.89	15.09	9.76	6.47
0.70	21.47	15.66	10.42	6.97	5.36	22.80	15.92	8.65	4.70	2.44
0.80	18.22	13.38	8.37	5.92	4.54	14.13	10.11	4.79	1.68	0.90
0.90	9.03	9.12	7.52	5.31	4.56	3.74	4.72	2.25	1.18	0.96

Neutrons are incident normally on the detector surface, and the LLD cutoff energy is 300 keV.

From Table 3.3 it can be seen that there is general trend for the complete dual-integrated MSND (identical pattern dimensions for top and bottom devices) efficiency to vary greatly as the ratio of the trench width to cell dimension (T/W_{cell}) increases, because of top-device neutron absorption (shadowing) effects (see Figure 3.9). Notice that for a trench depth of 90 microns the maximum detection efficiency with a cell width of 20 microns is with a T/W_{cell} ratio of 0.80. Yet, unlike the top-device (or single-device) maximum detection efficiency staying at a constant T/W_{cell} ratio of 0.80 for all depths, the stacked-MSND maximum detection efficiency shifts and converges to smaller T/W_{cell} ratios as the trench depth increase, with the optimum being a T/W_{cell} ratio of 0.50. Obviously this is because of shadowing effects becoming more prevalent as the trench depth increases.

Table 3.3: Efficiencies (in percent recorded) for a stacked straight trench dual-integrated MSND with symmetric top and bottom devices of width T and depth H filled with ^{6}LiF in a unit cell of width W_{cell} . The bottom device is off-set from the top device, where the bottom trench is centered with the top fin.

T/W_{cell}	Cell width W_{cell} (μm)					Cell width W_{cell} (μm)				
	20	40	60	80	100	20	40	60	80	100
	Trench Depth H = 90 μm					Trench Depth H = 350 μm				
0.10	7.73	7.37	7.42	7.03	6.61	16.97	16.23	16.07	15.58	14.30
0.20	15.03	14.08	13.20	12.02	11.15	32.13	30.09	28.10	26.40	23.68
0.30	21.73	19.72	17.87	15.76	13.81	46.67	42.87	37.37	33.24	28.67
0.40	27.67	24.46	20.58	17.38	14.59	60.63	51.87	43.94	36.41	29.02
0.50	33.65	28.70	23.15	18.11	15.10	72.54	59.79	48.18	36.47	29.07
0.60	36.41	29.25	21.76	17.21	14.02	71.27	54.76	38.58	28.53	21.53
0.70	38.95	29.77	21.38	16.60	13.68	69.89	51.97	34.34	23.51	17.98
0.80	39.18	29.65	21.14	16.43	13.89	65.28	47.99	30.18	21.47	16.62
0.90	24.80	23.79	21.12	16.44	14.37	35.70	34.63	28.53	21.08	17.17
	Trench Depth H = 175 μm					Trench Depth H = 500 μm				
0.10	12.08	11.79	11.22	10.93	10.62	18.47	17.75	16.95	16.53	15.84
0.20	23.29	22.44	20.64	18.83	17.57	35.72	32.87	30.58	28.09	26.09
0.30	34.36	30.84	27.48	24.38	21.41	50.11	45.68	40.57	36.20	31.06
0.40	44.12	38.21	32.60	26.74	21.74	66.30	56.15	48.13	39.21	31.50
0.50	53.26	44.04	35.31	27.31	22.35	79.06	65.23	52.45	39.72	31.36
0.60	54.63	42.31	31.07	22.89	18.78	75.70	58.58	41.00	29.34	22.18
0.70	55.95	42.02	28.76	20.55	16.85	74.26	54.31	35.07	24.35	18.48
0.80	54.81	40.24	26.74	20.37	16.23	68.22	49.97	30.84	21.42	16.98
0.90	31.61	30.31	26.69	19.46	16.26	36.61	35.01	28.63	21.02	17.10

Neutrons are incident normally on the detector surface, and the LLD cutoff energy is 300 keV.

3.5 Discussion

The thin-film coated planar-diode neutron detector is obsolete because of limited intrinsic efficiency from charge-particle self-absorption. Microstructuring a semiconductor diode to maximize reaction-product energy capture within the semiconductor detection material versus the amount of the neutron reactive material usable has proven to vastly improve the detection efficiency of a solid-state semiconductor neutron detector. In addition, the neutron detection efficiency of the compact MSNDs can be greatly improved by stacking two offset MSNDs and operating them as a single unit detector. Of all geometries presented here and elsewhere [29, 46], only the trench design and its variants can be stacked such that the top device converter does not shadow the second device converter, while still allowing for the sum of the converter areas to completely fill the total detector area. In other words, the efficiency can be doubled for a symmetric trench MSND in which the trench and semiconductor-fin widths are equal. However, if the detector is to be operated as a single device, an asymmetric design, where more neutron converter material is present, may yield higher detection efficiencies.

There are non-ideal conditions that will reduce the calculated efficiencies predicted in the present work. These conditions include incomplete charge collection, long carrier transport times in the semiconductor that cause ballistic deficits, and leakage currents that increase system noise. Inactive regions, from mechanical or chemical damage near the etched surface of the semiconductor, absorb reaction product energy before the ions reach the active semiconductor region. Collectively, these effects contribute to a spectral shift to lower absorbed energy, and ultimately, to a lower measured efficiency. Yet, the stacked MSND model can be used to understand expected performance trends and limitations for non-symmetric designs.

CHAPTER 4

MICROSTRUCTURED SEMICONDUCTOR NEUTRON DETECTOR: FABRICATION METHODOLOGY

For a successful technology, reality must take precedence
over public relations, for Nature cannot be fooled.
Richard Feynman

Details of the production of microstructured semiconductor neutron detectors are discussed in this chapter. The discussion focuses primarily on silicon as the radiation detection material. More in-depth treatment of semiconductor radiation detectors and their physics can be found in many textbooks such as Bertolini and Coche [94], Lutz [95], and Sze [85]. Discussion of silicon micromachining technology, along with neutron-reactive material backfilling methods, is presented. After discussion of wafer-level MSND fabrication, single, stacked, and arrayed MSND counting electronics integration is discussed. Finally, silicon foundry services used to mass-produce MSNDs, along with methods of initiating the transfer of the MSND technology to industry, is presented.

4.1 Micromachining of Silicon

Micromachining of silicon has been used for decades and is well established [96]. It is commonly used for specialized MEMS (micro-electro-mechanical systems) fabrication. Micromachining of silicon is the process of forming three-dimensional microstructures within bulk silicon. Two common techniques for etching microstructures into silicon wafers are dry and wet etching, where bulk refers to the mass removal of the silicon from a wafer, e.g., the creation of trenches in a silicon wafer. To fabricate the MSNDs, both techniques were studied and advantages and disadvantage for both micromachining processes were found.

4.1.1 Dry Etching

The fabrication of semiconductor sensors and micro-electro-mechanical systems (MEMS) requires precisely controlled etched profiles. The need for high aspect-ratio etching has been met by recent advances in plasma technology for deep reactive ion etching (DRIE) [97]. The dry anisotropic etching performed in this work was accomplished using inductively-coupled-plasma reactive-ion-etching (ICP-RIE) with high-aspect ratio deep etching (HARDE) techniques, which can provide a nearly vertical sidewall etch of any silicon wafer masked pattern. A representative schematic of the Oxford Plasma Lab™ 100 ICP-RIE system, along with process characterization and operation of the system, can be found in a study by Rice [20].

The physics of silicon-wafer masked etching utilizing the ICP-RIE process, consists of an radio frequency (RF)-induced, inductively coupled, high density, low pressure plasma that accelerates electrons with enough kinetic energy to break chemical bonds in the plasma gases, and, thereby, yielding ions and additional electrons for continued plasma creation [96]. Direct current (DC) bias across the plasma sheath accelerates the ions to bombard the target wafer positioned on the platen electrode; hence, both ion-milling (i.e., physical sputtering) and RIE are utilized for the HARDE DRIE silicon etching. Additionally, the high-density low pressure plasma increases the uniformity of the ion plasma-field, which improves microstructure etch-profile controllability and uniformity. With fluorinated chemistry, the key etch mechanism is the highly-selective chemical reaction between the silicon and the fluorine gas;[8] although, physical

[8] Commonly C_4F_8 and SF_6 plasma process gases are used as the fluorine source.

sputtering of the silicon substrate in the high-energy plasma does account for some silicon removal. The silicon etch rate, uniformity, anisotropy, and etch mask selectivity[9] are controlled by the ICP-RIE process parameters chosen for the silicon etch process [96]. Process parameters such as Platen DC power, silicon wafer temperature, ICP coil power, process pressure, gas flow, etch time, deposition time, wafer size, and exposed etch area[10] affect the silicon microstructure etch process and surface condition.

The process used to etch the MSND microstructures into silicon wafers is an iterative process, whereby, the etching (shallow etch in the silicon) and passivating[11] (fluorocarbon film is deposited on all surfaces) processes are alternated [98]. These steps are alternated repeatedly until the microstructure feature is completely etched, such that in this manner an anisotropic etch is performed, yielding vertical and somewhat smooth sidewalls (see Figure 4.1).

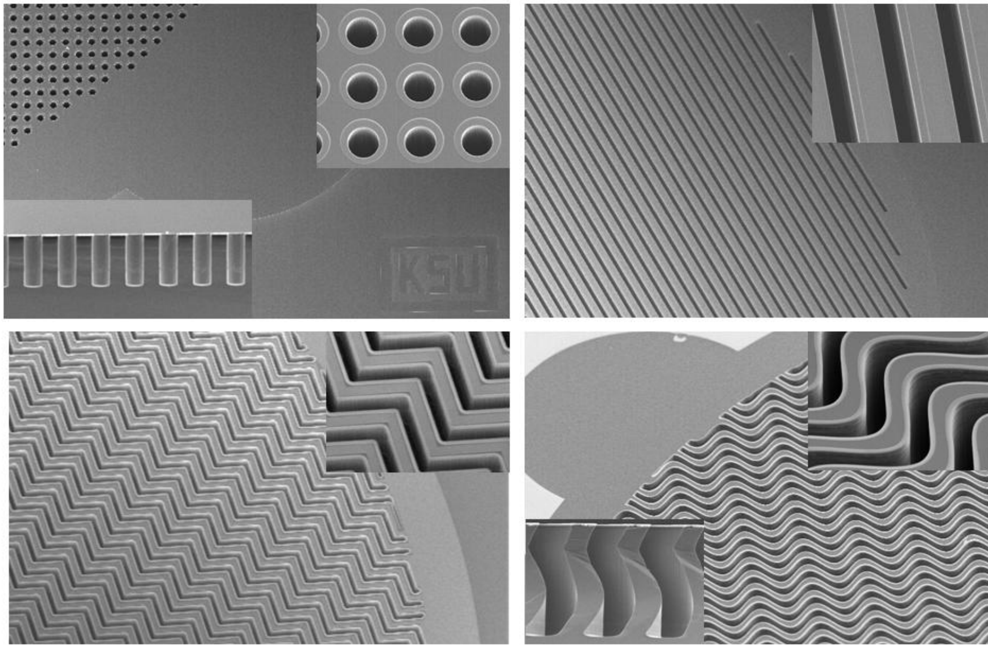

Figure 4.1: Shown are SEM pictures of microstructure patterns etched into a silicon substrate, showing detail of the circular hole, and straight, chevron, and sinusoidal trench, patterns. Sourced from [27], copyright © 2009, IEEE.

---

[9] In this case, selectivity refers to the difference in etch rate of one material over another. High selectivity refers to a slow etch (dissolving) rate over that of a simultaneously etching material and the converse being the opposite.

[10] Commonly referred to as the load effect [96], increased silicon surface-area, adjacent to the plasma, decreases the etch rate due to source fluorine ion concentration-dependent etching. Also noteworthy, larger volume trenches are easier to etch (improved uniformity and sidewall roughness) due to plasma etching gas transport improvement.

[11] In the HARDE etch process, a deposition step is used to passivate the etch sidewalls so as to preferentially anisotropically etch the silicon microstructures. A fluorocarbon film is deposited on the sidewalls and base of the etched feature, protecting it from further etch.

In most cases, a thick photoresist etch-mask (AZ® 2070 nLof) was used, but higher selectivity masks (SiO_2 and Si_3N_4) have also been studied. Further details of this ICP-RIE work are presented elsewhere [20]. Deeply etched (100-300 microns) microstructures are easily fabricated with inductively-coupled plasma etching technology (see Figure 4.2). An ICP-RIE Oxford PlasmaLab 100™ etch recipe to dry etch trench microstructures 312 microns deep is given in Table 4.1 and a SEM picture of the etched trench is in Figure 4.2. However, plasma-etched surfaces are a source of crystalline damage and contamination, which can reduce charge carrier lifetimes and increase recombination rates for charge carriers near the sides and the bottoms of the microstructures. To mediate this, the advantage of the ICP is apparent. By increasing the plasma density without increasing the kinetic energy of the ion bombardment, the voltage dropped across the plasma sheath is decouple from the power going into the plasma.

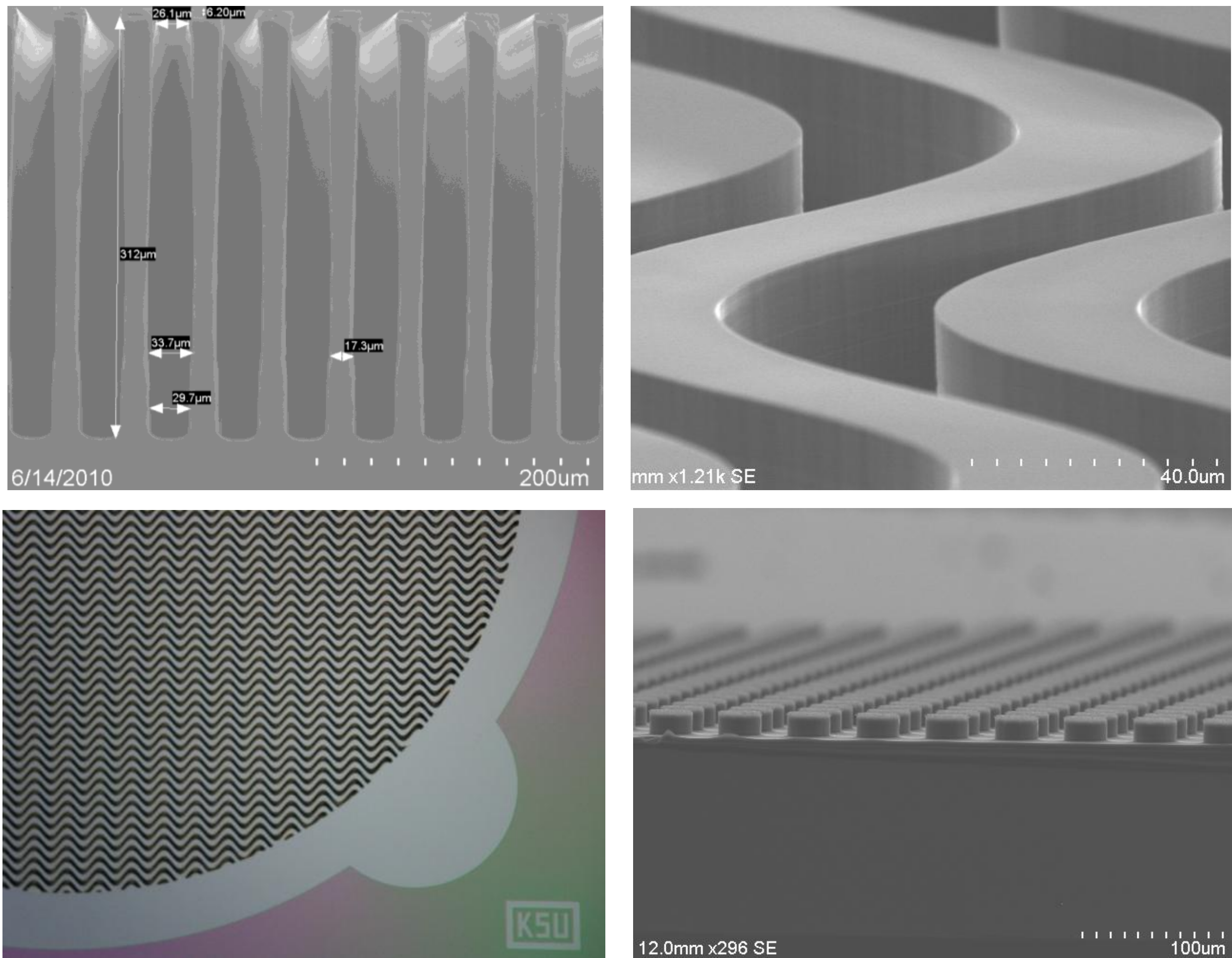

Figure 4.2: Shown are SEM pictures of microstructure patterns etched into a silicon substrate, showing detail of the straight trench, sinusoidal trench, and column (pillar) patterns.

Table 4.1: ICP-RIE Oxford PlasmaLab 100™ etch recipe to dry etch trench microstructures 312 microns deep with multistep processing.

Total Processing Time: 2 hr. : 29 min.

Step Number	1		2		3		4
Repeat Iteration	75		175		100		1
Parameter	Deposition Step	Etch Step	Deposition Step	Etch Step	Deposition Step	Etch Step	Etch Step
Gas Type	C_4F_8	SF_6	C_4F_8	SF_6	C_4F_8	SF_6	SF_6
Time (s)	8	15	8	17	10	18	30
Pressure (mTorr)	30	30	30	30	30	30	30
Wafer Temp. (C°)	10	10	10	10	10	10	10
He Backing (Torr)	5	5	5	5	5	5	5
Plate RF Power (W)	15	35	15	50	25	55	60
ICP Barrel Power (W)	800	1000	800	1000	1000	1000	1500
SF_6 Flow (sccm)	--	80	--	80	--	80	80
C_4F_8 Flow (sccm)	60	--	60	--	60	--	--

** standard cubic centimeters per minute (sccm)*

The leakage current and noise are serious problems when incorporating these DRIE vertical microstructures into a semiconductor device such as a *pn* junction diode. Leakage current contributes to electronic noise and reduces the ability to detect small signals. Microstructure surface roughness is also a major electronic-grade device issue when using RIE etching techniques. This roughness can have detrimental effects on the electronic stability of the electronic device. Because of the alternating passivating and etching steps used, horizontal scalloping (ribbing) of the sidewall will occur, at depths of 50 to 500 nm (see Figure 4.3). In addition, soft etch masks, such as photoresist, can be worn down more quickly at pattern feature edges than across the pattern feature as a whole; therefore, the etch rate is not consistent across the silicon substrate, and vertical striations, also known as sidewall-roughening, can occur. An example of these etched microstructure vertical striations can be seen in Figure 4.4. As a result, fabrication processes for deep microstructured devices have been developed to reduce surface damage and contamination from processing techniques [20]. One helpful approach includes adding an additional layer of SiO_2 masking material under the photoresist mask to help with vertical striations. An additional approach is to post process the DRIE microstructures with a silicon wet etch process (e.g., KOH[12], TMAH) to remove surface damage and contamination.

[12] In the case of potassium hydroxide (KOH), the residual potassium is removed by a 1HCl : $4H_2O$: $1H_2O_2$ cleaning bath for 10 minutes at 70°C.

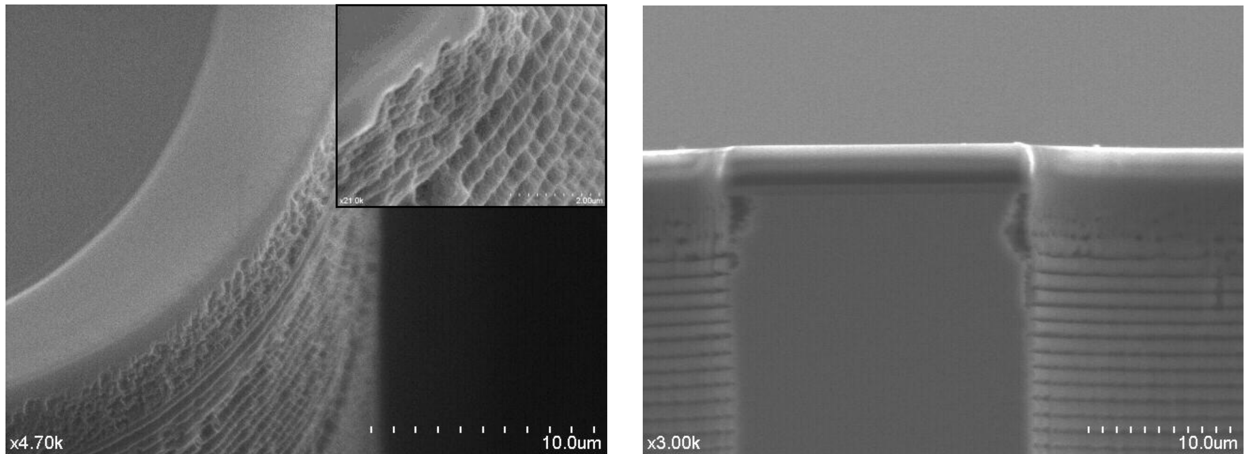

Figure 4.3: Microstructure patterns etched into a silicon substrate, showing detail of the horizontal scalloping (lateral etching) of the silicon microstructure sidewall because of *the alternating etch-deposit process.*

Some disadvantages of DRIE plasma etching exist. The DRIE process creates microstructure sidewall roughness and surface contamination from the plasma etching process, where these conditions are difficult to control during a single wafer etching process (see Figure 4.4). It is also difficult to attain repeatability from wafer to wafer processing. Aspect ratios of 10:1 for the trenches are possible, but more advanced designs of up to 35:1 are especially difficult to maintain good sidewall surface condition and reduced contamination from etching gases. The plasma etching process is time consuming and a bottleneck in the batch processing of multiple wafers, with many systems limited to processing one wafer at a time and some more advanced systems up to 12 small (4" dia.) wafers at a time [99]. In order to increase etch rates, high power is required, leading to significant substrate damage.

The advantages of DRIE plasma etching include the following. The etching of any shape and size of a microstructure masked pattern is achievable. It is an industry proven technology [85, 96], with capabilities of etching into a wide range of materials including compound semiconductors, metals, dielectrics, ferroelectrics, polymers, and magnetic materials, some of which may be superficial or integrated material layers.

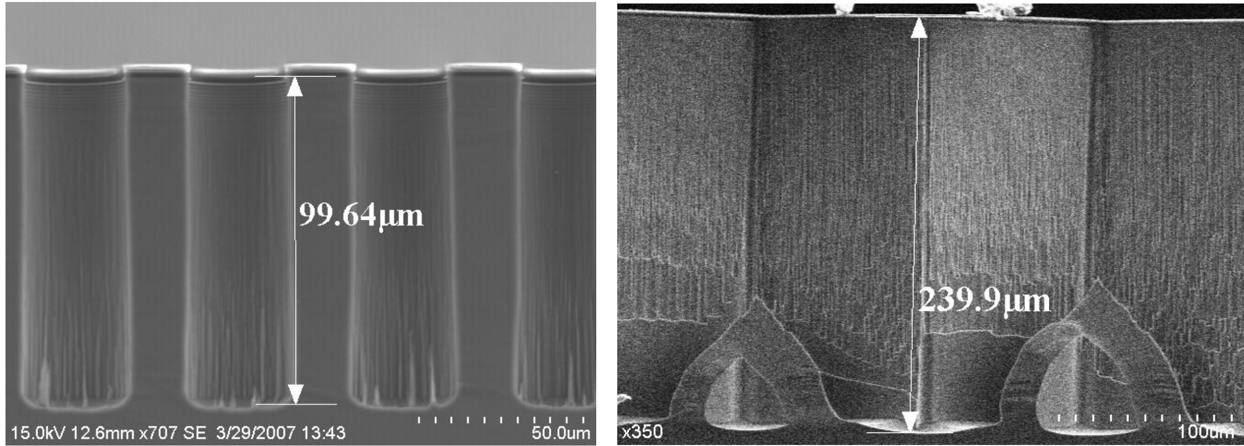

Figure 4.4: Microstructure patterns etched into a silicon substrate, showing detail of the etched microstructure vertical striations from mask edge failure.

4.1.2 Wet Etching

Silicon wet etching can be isotropic, anisotropic, or specific. Isotropic wet etching progresses equally in all directions. Conversely, anisotropic wet etching is directionally dependent, producing near vertical sidewalls, with specific selectivities to particular crystal planes of the silicon substrate or through some other limiting factor, such as surfactants and transport-enhancing additives to improve etch-rate selectivity to particular silicon crystal planes. In more specialized applications, specific wet etching can create definite shapes that are etched according to the selectivity of silicon crystal planes, e.g., pyramid structures [100]. Obviously, the orientation and shape of a mask pattern influences the 3D shape of a wet-etched microstructure. For example, to produce an etched straight trench, it is necessary to align the long edges of the mask rectangle pattern in parallel to the (111) crystal planes (see Figure 4.5). Only four high aspect ratio microstructure designs are available for the (110) orientated silicon wafer: straight trench, chevron trench[13], rhombus hole, and a rhombus pillar. If the pattern is not properly aligned to these higher selectivity planes, the wet etch will remove material according to selectivity of the crystalline planes, and consequently, severe undercutting of the masking layer will be observed (see Figure 4.5).

[13] The chevron is inherently difficult to produce because of difficulties in pattern alignment. In addition, etch selectivity of the chevron pattern is reduced because of dangling bonds in the Si lattice at the corner edge of the converging (111) planes. This problem is also apparent when etching the rhombus pillar.

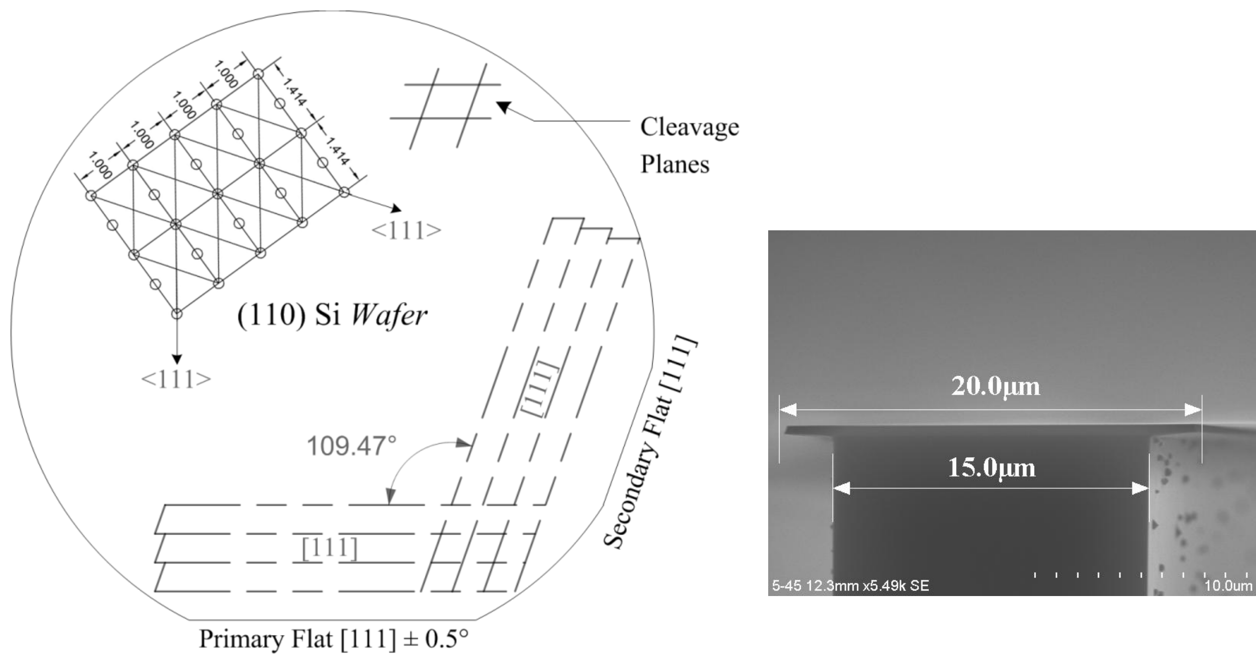

Figure 4.5: (left) Standard (110) crystal plane-orientation projection for silicon; showing the rhombic pattern alignment of (111) planes normal to the surface (110) plane. The normal (111) traces do not meet each other at 90°, but instead at 70.53° and 109.47° [86, 100]. Also, the wafer will easily cleave along the (111) planes. (right) Severe undercut of SiO_2 mask because of *improper pattern alignment with (111) planes.*

Three, four, and five inch diameter silicon wafers were used in this work, where the microstructured patterns were aligned according to the primary flat (see Figure 4.5). The wet-etch anisotropic etchant used in this work had varying concentration grades of potassium hydroxide[14] in de-ionized water. The crystal plane selectivity is dependent on concentration and temperature of the aqueous KOH etchant solution. The etching reaction of KOH and silicon can be characterized as the chemical reaction between the surface silicon and the hydroxyl ions, forming silicate products and hydrogen [101]. Aqueous KOH has one of the largest selectivity ratios of (110)/(111), typically around 300:1 [100, 102], but can be up to 500:1 [103].

An aqueous solution of 50% KOH *by volume* at 70°C was used for most wet etching in this work and yielded an approximate 50 micron per hour etch rate; additional silicon (110) KOH etch rates can be found elsewhere [102, 103]. Pattern masking materials often used for wet etching silicon are silicon dioxide (SiO_2) and silicon nitride (Si_3N_4), with selectivities in the

[14] KOH source, 50% (w/v) aqueous solution, Ricca Chemical, from Fisher Scientific.

aforementioned KOH solution of 0.15 μm/hr and <1 nm/hr, respectively [101]. Although aqueous KOH etches the SiO_2 masking layer quicker than another well known silicon etchant, tetramethyl ammonium hydroxide (TMAH), TMAH suffers from severe undercutting of the etch mask with deep trenching because of a small selectivity ratio of (110)/(111), typically around 30:1 [104]. Therefore, aqueous KOH was chosen as the silicon anisotropic wet-etching agent for this work. Assortments of etched microstructures are shown in Figures 4.6 and 4.7.

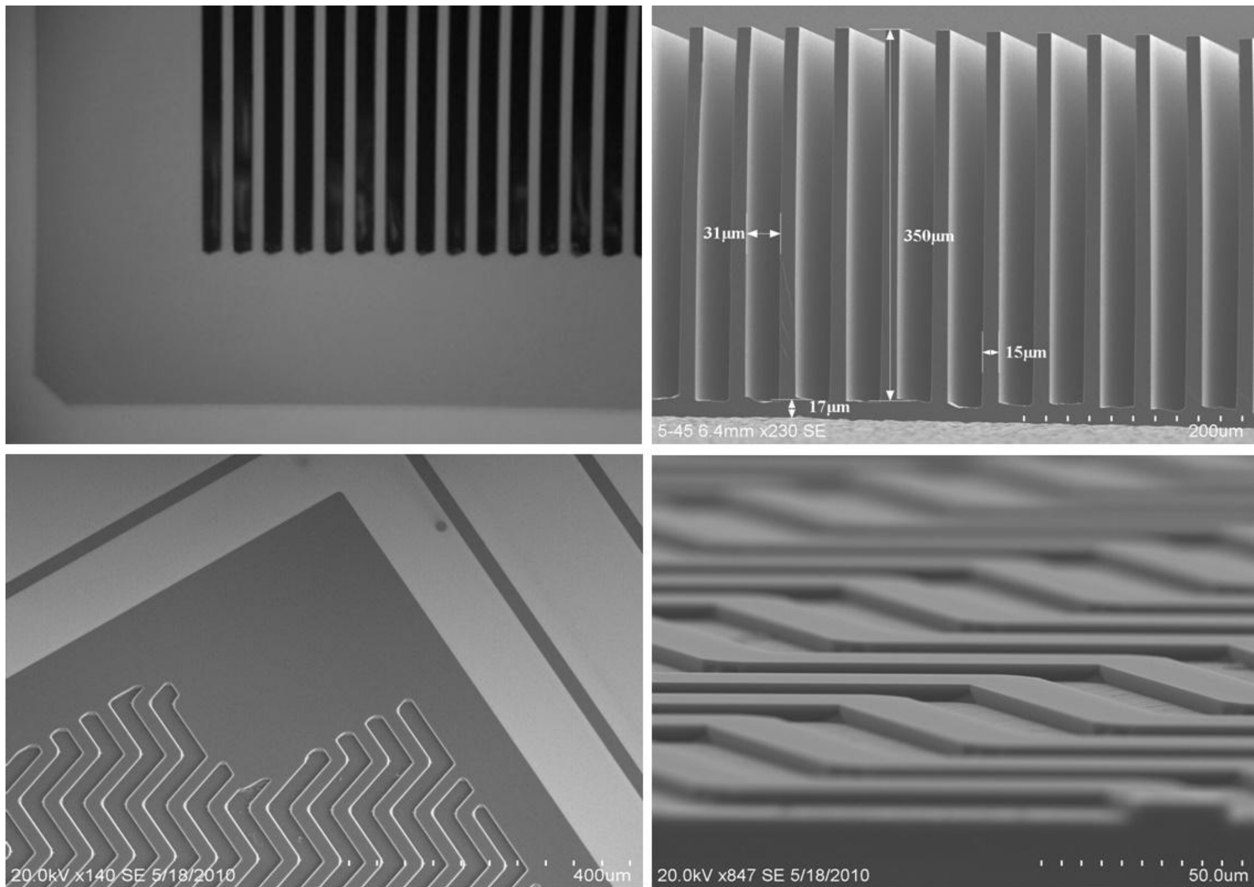

Figure 4.6: Images of wet-etched straight and chevron trench microstructures. The upper left shows above-view of straight trench microstructure, the upper right shows a cleaved side-view of high-selectivity deep-etched trenches, and the two bottom pictures show an above-view and side-view of chevron trench microstructures, moving left to right.

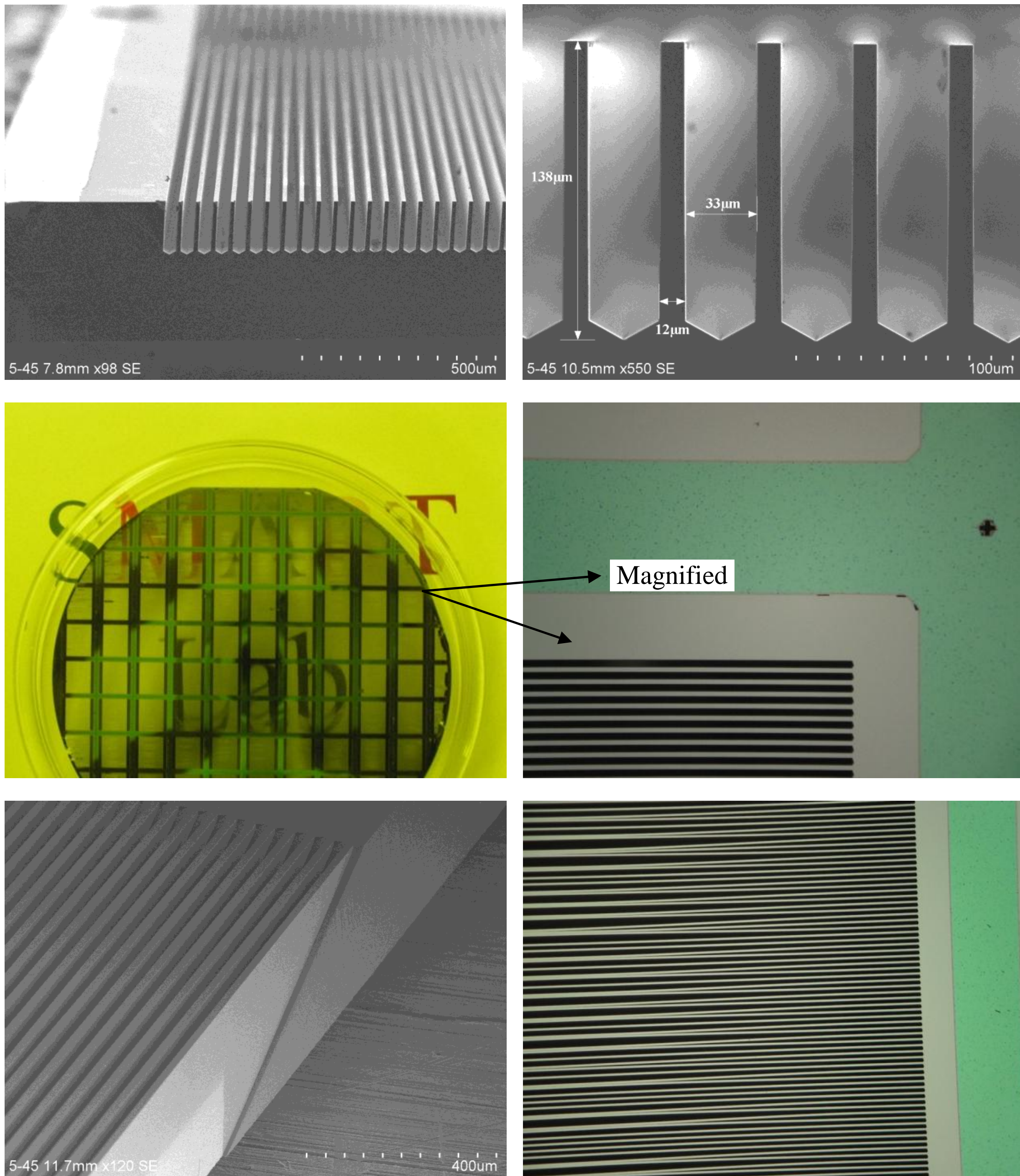

Figure 4.7: Images of wet-etched straight trench microstructures. The upper left shows an above-view of trench microstructure, and the upper right shows a cleaved side view of etched trenches. The middle left picture displays visible words behind a through-etched wafer, and the middle right picture shows a magnified view of the fully-perforated wafer. The bottom left picture is a SEM image of the through trenches, and the bottom right picture displays an above-view of the silicon fins warping because of the lack of a lateral support structure.

There are some disadvantages of wet-etching that exist. Because of the limitation of using higher selectivity silicon crystal-lattice planes, only four microstructure designs are available. Attaining high resistivity (>5 kΩ-cm) silicon (110) wafers is difficult because of its rare use in industry. The advantages of wet etching are the following. Wet-etching produces negligible mechanical damage to the silicon wafer during etching as compared to DRIE dry etching, which causes subsurface damage through ion bombardment [105]. High aspect ratio etching has proven achievable at selectivities of 500:1 [96]. Batch processing is easily accomplished and dramatically reduces the required time to etch compared to that of a single wafer dry-etching process. Moreover, the process requires relatively inexpensive wet chemicals and the necessary processing equipment is simply a temperature controlled heated bath of etchant solution.

4.1.3 Fabrication of the Microstructured *pn* Junction Diode

The most common type of *noninjecting* or *blocking* contact for silicon is a *pn* junction. In the absence of an applied voltage, the majority carriers in the *n*-type region, *electrons*, migrate to the region of smaller concentration, the *p*-type, or acceptor-rich region [94]. The converse is true for the majority carriers in the *p*-type region, *holes*, which migrate to the *n*-type, or donor-rich region. Because it is necessary for the two different regions to be in thermodynamic contact, *pn* junctions are commonly created on single-crystal wafer of silicon, where the impurity content in one region of the silicon material is changed (see Figure 4.8).

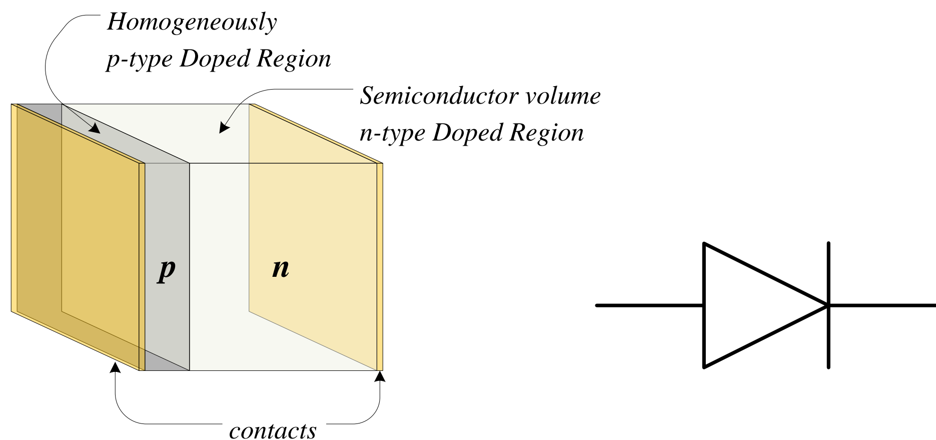

Figure 4.8: An illustration of a pn junction diode (left) in a fabricated solid-state structure and (right) electronic device schematic representation.

This thermodynamic equilibrium diffusion leaves fixed ionized sites (donors and acceptors) within the junction, thereby forming a space-charge region (a depletion layer) within the vicinity of the interface creating a charge-deficient region [94]. Because of the removal of the charge carriers normally present, this depleted region has very high resistivity [106]. Once equilibrium is reached when the Fermi level is constant[15] throughout the silicon material, the space-charge region creates an electric field directed from the *n*-type region to the *p*-type region, which is commonly referred to as the built-in voltage [94].

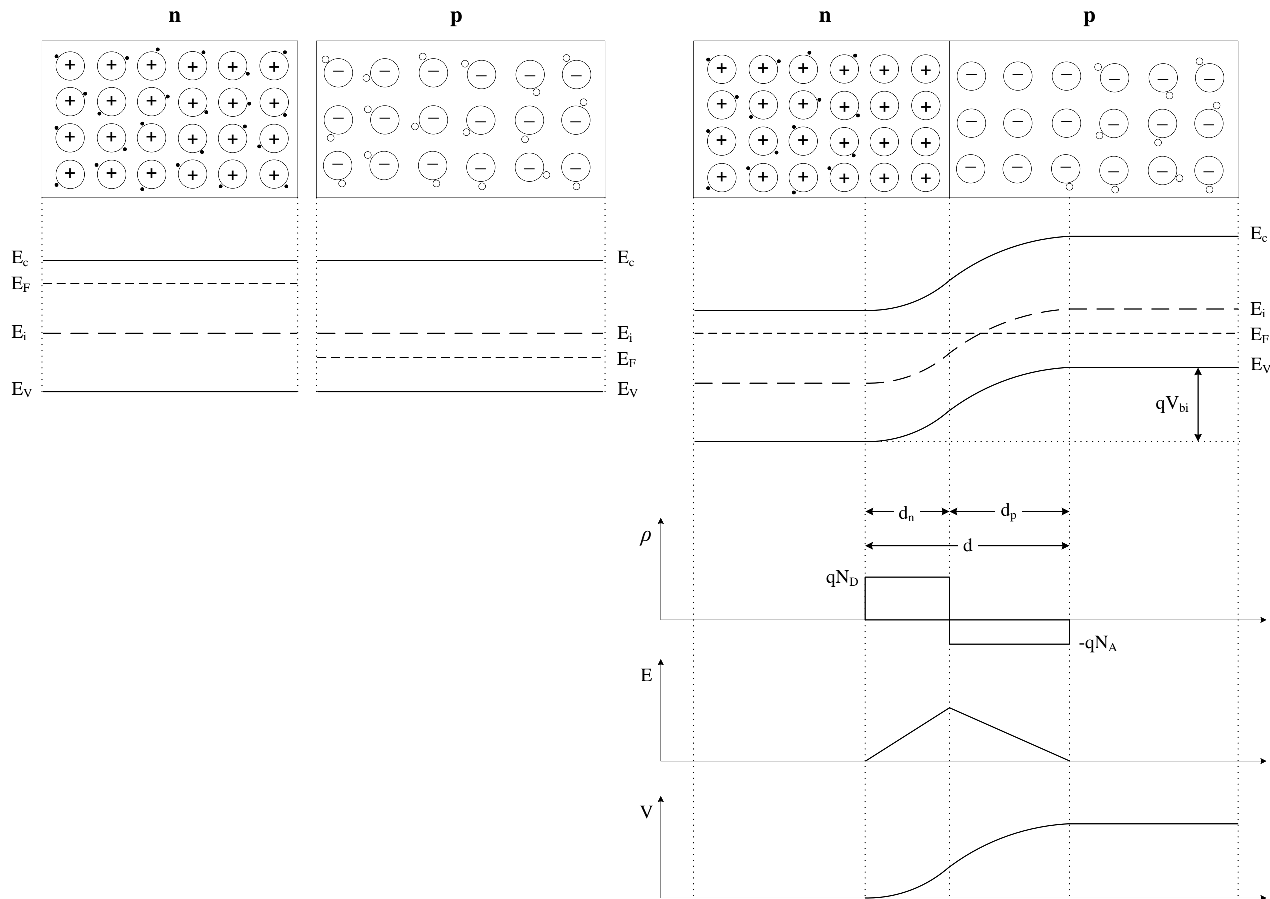

Figure 4.9: An illustration of a pn junction diode in thermodynamic equilibrium with (left) two dopant type regions in separation and (right) when the two different regions are brought together in thermodynamic contact (after Lutz [95]).

---

[15] This is because of minority carrier current compensating the diffusion current, where electrons from the *p*-type move to the *n*-type region, and the holes move from the *n*-type to the *p*-type region [92].

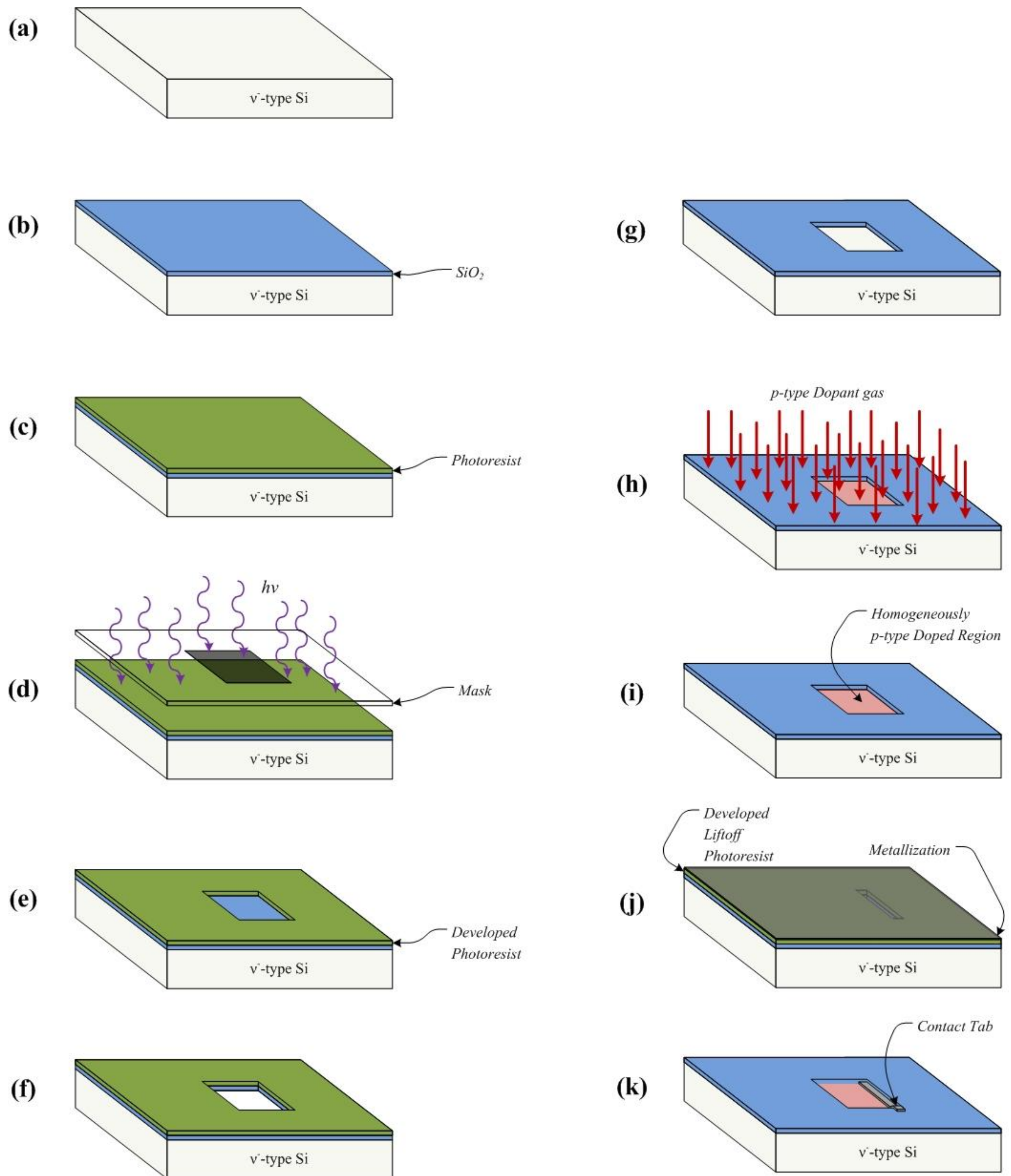

Figure 4.10: Diagrams of (a) a bare n-type silicon wafer, (b) thermal oxide layer, (c) application photoresist masking layer, (d) lithography imaging of the selective diode area, (e) wafer after development, (f) SiO_2 removal, (g) photoresist removal, (h) cleaned and p-type dopant diffusion, (i) pn junction formed from degenerate doping of silicon, (j) wafer after developed liftoff lithography and evaporated metallization, and (k) the completed pn junction diode with a metal contact.

The reverse bias diode used in this work was formed from slightly doped n^- substrate silicon material, commonly referred to as ν^- material. The diode consists of a highly doped shallow p^+ layer on the ν^- wafer substrate material, with a highly doped shallow n^+ layer on the back of the MSND. The purpose of this n^+ layer is twofold; it provides a good ohmic contact between the metal contact and the substrate, and simultaneously, it allows the operation of the MSND in overdepleted mode [95]. A Schottky junction or MOS (metal-oxide-semiconductor) could be used in place of the *pn* junction. The present work focuses primarily on the *pn* junction diode because of its ease of use in fabricating complex MSND designs. Figure 4.10 shows the major steps of a planar *pn* junction diode fabrication process. These steps include cleaning, oxidation, lithography, dopant gas diffusion, and metallization. Additional detail of MSND fabrication are given in [39] and 0.

4.1.4 Silicon Cleaning

To process the silicon wafers into MSNDs with VLSI technologies, it is necessary to clean the silicon surface and remove shallow-depth contamination. In this study the silicon wafers are chemically cleaned with a Piranha[16] bath at 130°C for 15 minutes to remove organic contaminants, followed by a Baker Clean®[17] bath at 70°C for 15 minutes[18] to remove metallic and particle contaminants. The residual oxide is then removed from the wafers with a 30 second dip in a buffered hydrofluoric acid (HF) solution, commonly referred to as a buffered oxide etch[19] (BOE) solution. The wafer is immediately thereafter spin-rinsed and placed in a processing furnace, e.g., diffusion or oxidation furnace. All MSND wafers were cleaned with this process before any high temperature processing was completed, e.g., oxidation and diffusion processing.

4.1.5 Silicon Oxidation

Silicon dioxide, SiO_2, has been the most important processing technology for VLSI silicon device fabrication. A thermal SiO_2 layer can be used as a diffusion mask, so that the impurity

[16] 1 H_20 : 1 H_2SO_4 : 1 H_2O_2
[17] 25 H_20 : 5 BakerClean® : 1 H_2O_2
[18] This method is superior to the original RCA cleaning process for removing surface contaminates on Si [107].
[19] JT Baker® Buffered Oxide Etch 6:1, an aqueous NH_4:HF etchant solution.

diffusion[20] of many dopants through SiO_2 is very small compared to that of silicon [52]. The SiO_2 layer is an ideal masking material for junction diffusion isolation. In addition, the SiO_2 layer can act as a charge-barrier field oxide (i.e., a passivation layer) around a device. SiO_2 growth on a silicon wafer involves heating the wafer in a flowing pure-atmosphere of either wet[21] or dry oxygen at temperatures between 800°C to 1,200°C for several hours to a desired layer thickness. The silicon wafer oxidation rate depends on many parameters, such as crystallographic orientation of surface silicon, the oxidation temperature in the process furnace, the oxidation process time, and the thickness of native oxide on the silicon wafer [96]. The mechanism of the thermal oxidation of silicon and the prediction of the thickness in terms of processing time and temperature are given in great detail elsewhere [51, 52, 96]. An advantage of wet oxidation is that its growth rate and achievable thickness is greater than that of a dry oxidation process layer; however, the quality of a grown SiO_2 layer through dry oxidation is better both mechanically and electronically than that of a grown wet oxide layer. The selectivity of SiO_2 to silicon, in both dry and wet etching, is superior to photoresist masking. Furthermore, a SiO_2 masking layer can easily be patterned using ICP-RIE, utilizing a C_4F_8 and O_2 dry-etch plasma (for details see [20]), or can be removed using a BOE wet etch.

4.1.6 Silicon Nitride Masking

Silicon nitride, Si_3N_4, in comparison to SiO_2, is a superior masking material in regards to a higher selectivity of the mask pattern to that of the bulk underlying silicon for KOH wet etching [102]. Also, Si_3N_4 has a similar resistance to impurity diffusion [96]. Si_3N_4, can be grown on a silicon wafer surface through a chemical vapor deposition (CVD) method, either by a high-temperature and low-pressure chemical vapor deposition (LPCVD) method or a low-temperature plasma sputtering process, which was the choice method in this work [96]. A Si_3N_4 layer can be patterned using ICP-RIE or can be removed using a wet etch, such as hot-phosphoric acid [108]. In addition, using a plasma sputtering process, Si_3N_4 can be patterned using a photoresist liftoff. The main disadvantages are higher production costs and difficulties in removal using a hot-phosphoric acid wet etch.

---

[20] According to Fick's first law, in response to a concentration gradient, there is a net redistribution of material.

[21] Steam is added to the oxygen gas supply from either a boiling deionized water bubbler or a pure-hydrogen gas quartz torch; the latter being the preferred choice for improved oxide purity.

4.1.7 Photolithographic Masking

Photolithography is a vital part of VLSI fabrication technology and is reviewed in many texts [51, 52, 96]. In the present work, photolithography is used to define the geometry of the *pn* junction for the MSND. Specifically, photolithography is the transfer of a masking pattern to a substrate by coating the substrate with a photosensitive material or polymer, commonly referred to as photoresist, or simply “resist”, and the subsequent exposure of the material to masked radiation to change the properties of the masked regions of the photoresist material, thereby, making it selectively removable. The general photoresist coating process is simple. A small amount of photoresist is deposited on the center of a substrate, a silicon wafer in this work, and spun on a vacuum chuck in a photoresist spinner at high speeds (500-5,000 rpm). This method uniformly distributes the resist and removes excess resist from the surface of the substrate. This spinning process leaves a very thin layer of some uniform thickness ranging from submicron to hundreds of microns on the substrate surface. The resist is then exposed to ionizing radiation, commonly ultraviolet (UV) light, through a mask with a specific pattern. Through a series of thermal and chemical treatments, the photoresist is developed, or regionally removed, and hardened. This completes the transfer of the masking pattern to the substrate. The photoresist mask may act as a protective mask during dry or wet etching processes or may be used to lift off evaporated or sputtered films deposited on the substrate (see Figure 4.11).

Photoresists are typically hydrocarbon-based polymers, usually dissolved in a solvent for application, whose properties are chemically altered when exposed to ionizing radiation [96]. When the radiation is absorbed, the chemical bonds within the polymer are broken and restructured. Through this action, the resist polymer becomes more or less soluble in a pH-basic developing solution that depends on the tone of photoresist, e.g., negative or positive tone. By definition, negative photoresist becomes less soluble in a developer solution in response to radiation, while the positive photoresist responds in the opposite manner [96]. The photoresists come in many different viscosities, and through the adjustment of the spin speed and time, the final thickness of the photoresist layer can be predicted. After application of the photoresist on a substrate, the substrate is baked to remove any remaining solvents, thereby hardening the photoresist and promoting adhesion. The photoresist is then exposed to ionizing radiation and if required, baked again to aid in pattern transfer and to further harden the photoresist. Finally, the

photoresist is developed by immersing the patterned substrate in the photoresist manufacturer's recommended developing solution.

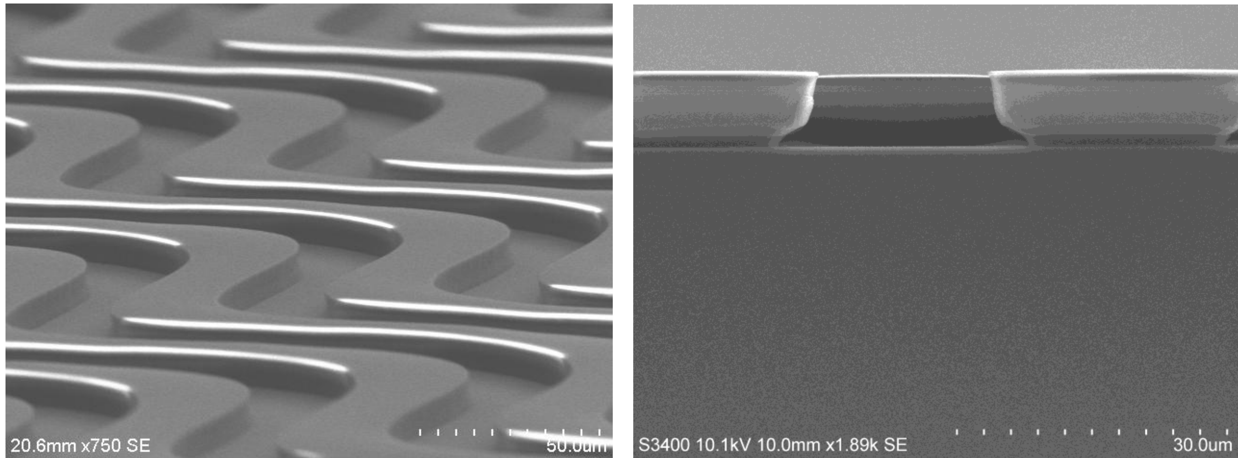

Figure 4.11: (left) Applied dry-etching photoresist mask on bare silicon. (right) Side-view of applied liftoff photoresist patterning, commonly used for selective material layering through photoresist removal by lifting the topologically deposited material layers (i.e., metal contacts). It is essential to have an undercut of the photoresist for a liftoff, where the deposited film will not encase the masking photoresist, and the solvent can thereby remove the underlying photoresist.

The photoresists used in this work were AZ P4620 (positive) and AZ nLof 2070 (negative) by *AZ Electronic Materials*. Before applying the photoresist, it is essential that the substrates are thoroughly cleaned and the surfaces dehydrated, which is commonly done through substrate baking. In addition to dehydrating the silicon surface to promote photoresist adhesion, an "adhesion promoter" [22] can be used such as hexamethyl disilazane (HMDS). This is especially important for resist adhesion to silicon dioxide, which is a difficult material for photoresist to bond to because of surface moisture forming latent OH^- surface bonds. Resist strongly adheres to a clean and unprocessed SiO_2 layer, but when the surface is chemically contaminated or modified, as in the case of partial BOE etching leaving hydrophilic dangling surface bonds in the SiO_2 layer, the resist only weakly adheres. Through studies of BOE partial-etching of a SiO_2 surface layer on silicon wafers, it was observed that the etched surface is highly hydrophilic.

[22] It is worth mentioning that the label of "adhesion promoter" is a misnomer. The interface layer of the silicon dioxide and HMDS form methylated silicon-hydroxide, a water repellent layer, which prevents the aqueous developer from penetrating between the photoresist layer and the wafer's surface, thereby preventing lifting of the photoresist structure during developing.

Because photoresist adhesion is poor on silicon wafers with absorbed surface water from humidity, methods to improve adhesion to a partial-etched SiO_2 layer were investigated. During the investigation, it was noticed that the partial-etched SiO_2 layer becomes hydrophobic in water after coating with isopropyl alcohol (IPA). The surface becomes hydrophilic once effort has been made to remove the surface contaminate in a DI water bath for several minutes. Therefore, IPA was spin-coat applied to silicon wafers with partially removed SiO_2 layers, before HMDS application, to further promote adhesion. Application of this IPA primer method proved absolutely necessary to ensure strong resist adhesion during long (e.g., 30 min.) BOE pattern transferring. A likely reason for this adhesion promotion is because of IPA being a non-ionic tensioactive compound with a hydrophilic and a hydrophobic part of the molecular carbon chain [109]. Hence, the hydrophilic end bonds to the SiO_2 surface leaving a hydrophobic surface state to which the photoresist will strongly bond.

Removing the photoresist is accomplished by either immersing the substrate in a chemical stripper (e.g., Kwik Strip®, Acetone) or exposing the resist to an oxygen plasma, which is commonly referred to as ashing. Another important photoresist application process is photoresist bridging over microstructures. This is specifically important for the MSND technology because of post-microstructure metallization necessary for the diode contact. Photoresist bridging is accomplished by spinning high viscosity photoresist slowly (<500 rpm) over the microstructures and then letting the photoresist dry at room temperature for one hour before baking the photoresist for hardening. Photoresist spin recipes are given in 0.

4.1.8 Impurity diffusion

Fabrication of a *pn* junction is accomplished by selectively altering the electrical properties of specific regional silicon sites on a wafer through the introduction of impurities. Such impurities are commonly referred to as dopants. To incorporate these dopants into the bulk silicon crystal, solid-state diffusion is utilized. Solid-state diffusion is defined as the redistribution of an initially localized high concentration material throughout a background medium from random thermal motion [85]. This localized material is developed by patterning a SiO_2 layer that serves as a barrier to impurity diffusion and then uniformly depositing a dopant material on the silicon wafer. This can be accomplished either through solid-source (e.g., BN and

SiP_2O_7)[23] or liquid-source (e.g., BBr_3 and $POCl_3$)[24] high-temperature (800 - 1100°C) deposition within a controlled environment furnace tube. Dopants can also be incorporated into the semiconductor material through ion implantation, which is used for shallow depth implantation; however this method was not considered in this work. Deep semiconductor junctions, ranging from 0.1 - 2 μm, require doping processes that are followed by a "drive-in" step to diffuse the dopants to some desired depth and concentration, that is limited by the solid solubility of the semiconductor material.

4.1.9 Contact metallization

A metallization process is used to make a clean ohmic connection with the diffused *pn* junction. Metal films are commonly deposited through physical vapor deposition (e.g., thermal or e-beam evaporation and sputtering). A liftoff lithography process can be used to define small specific contact areas, and for larger areas of specificity, machined shadow masks can be used. In this work, a thin layer of titanium (Ti) was used as a metallic binding agent to adhere gold (Au) and aluminum (Al) to the silicon junction surface. In addition, titanium makes an ohmic contact with a *p*-type junction. MSND contacts consisted of 500 Å of Ti and either 5000 Å of Au or 5000 Å of Al, depending on the intended application of the MSND. Gold was used for non-encapsulated applications because of gold's resistance to oxidation. To make connection with the amplification electronics, a 25-μm diameter wire was bonded from the *p*-type top contact to the input of the preamplifier.

4.1.10 Metrology: MSND IV and CV Characteristics

Junction rectification characteristics are important when judging the quality of a fabricated *pn* junction. Commonly, current versus voltage (IV) and capacitance versus voltage (CV) plots are created to study the rectification characteristics. Leakage or dark current is severely detrimental to signal production from a *pn* junction device. Leakage current limits the applied bias to the device so that the depletion depth is limited in the silicon. In addition, leakage current

[23] Boron and phosphorus solid source wafers are from PDS® Products, purchased from Saint-Gobain Advanced Ceramics.

[24] Boron and phosphorus liquid sources are generally transported by a carrier gas and deposited by decomposition.

increases the detection amplification system noise and decreases the signal-to-noise ratio of the MSND. Therefore, it is important to know the leakage current of a junction device so as to determine the operating range and quality of the fabricated MSND. For high resistivity silicon, the generation current[25] is the largest factor for diode leakage current. It is given by [110],

$$I_{gen} = \frac{1}{2} q \frac{n_i}{\tau_e} WA \quad , \tag{4.1}$$

where q is the electronic charge, n_i is the intrinsic carrier concentration, W is the depletion width (or depth), A is the junction area, and τ_e is the effective carrier lifetime. Notice that all parameters are constant for a given diode geometry except τ_e; also, generation current is proportional to the area of the diode, therefore there is a limit to the size of the diode that can be fabricated for low leakage current applications.

CV characteristics of a rectifying junction are used to determine the semiconductor depletion depth (space-charge region[26]) at varying applied voltages. In addition, the change in voltage signal is related to the produced charge and capacitance of the diode,

$$\Delta \mathrm{V} = \frac{\Delta Q}{\mathrm{C}} \quad , \tag{4.2}$$

where ΔV the change in voltage signal, varies by the change in charge (ΔQ) and reduces in magnitude by inverse capacitance (C). Therefore, the higher the capacitance of the detection device, the smaller is the output-voltage signal produced by radiation induced charges within the device. Also, knowledge of diode capacitance can provide insight to help with the design of MSND amplifying electronics.

In this study the MSND rectifying-junction **IV characteristics** were measured using an IV-curve-tracing system and an electro-magnetic (EM) radiation-shielded dark box. The reverse bias leakage currents for varying MSNDs were compared to simple planar *pn* junction diodes of

---

[25] Leakage current of a silicon diode originates from three sources: (1) surface leakage current, (2) generation current in the depletion region, (3) diffusion current from undepleted bulk neutral regions, more detail on leakage current sources can be found here [109].

[26] The space-charge region is restricted and fully contained in the low-doped substrate because of the fabrication of extremely asymmetric junctions, which for this work are thin very high *p*-doping on a low-doped *n*-substrate.

similar design, but without the microstructures. The MSND rectifying-junction **CV characteristics** were measured using a 1MHz CV plotter system[27] and an EM shielded dark box. The reverse-bias capacitance characteristics for varying MSNDs were again compared to simple planar diodes of similar design. Junction rectification characteristics were measured with equipment in the S.M.A.R.T. Lab metrology station (see Figure 4.12 and Table 4.2).

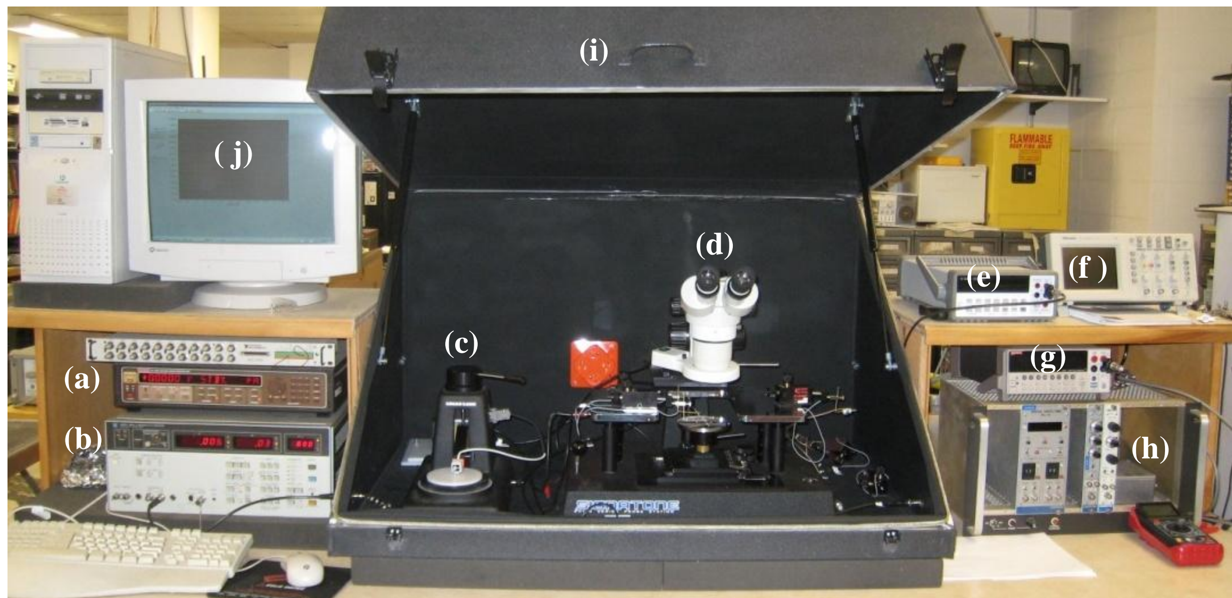

Figure 4.12: Pictured is the S.M.A.R.T. Lab metrology station. Included equipment are (a) a high voltage source measure unit system, (b) a 1MHz C-V plotter system, (c) a 4-point resistivity measuring system, (d) a single point probing station, (e) a digital multimeter, (f) an oscilloscope, (g) a 1100 Source Meter, (h) a NIM Bin, (i) an EM-shielded dark box, and (j) a computer with LabVIEW interface card and VI communication software.

[27] The Hewlett-Packard CV-curve-tracing system cannot apply negative voltage; therefore, the devices were connected to the system with reversed polarity, such that a positive bias was applied to the backside contact and the ground was connected to the topside contact.

Table 4.2: S.M.A.R.T. Lab metrology equipment information.

Equipment	Manufacturer	Model Number
High Voltage Source Measure Unit	Keithley Instruments	237
1MHz C Meter/C-V Plotter System	Hewlett Packard	4280A
4-Point Resistivity Measuring System	Lucas Labs	308
Single Point Probing Station	Signatone	H100
Digital Multi-Meter	Agilent	34401A
Oscilloscope	Tektronix	2002
1100V Source Meter	Keithley Instruments	2410
NIM Bin (Modular Counting System)	EG&G Inc.	M100
EM-Shielded Dark Box	S.M.A.R.T. Lab	--
Computer with LabVIEW Interface Card	National Instruments	--

4.2 Backfilling of Neutron Reactive Material into Si Microstructures

Many methods exist to backfill material into microscopic void structures in semiconductor crystals. The foremost problem is deciding which method is appropriate for preserving the chemical, electrical, and structural integrity of the semiconductor bulk crystal while completely backfilling material into the microstructures. Commercially applied microstructure backfilling techniques commonly include chemical vapor deposition (CVD) and plasma enhanced CVD (PECVD). Both techniques use gas-phase chemical reactions at the silicon microstructure surface with reactant precursors. This is not a viable approach for LiF backfilling because of the lack of available reactant precursors. Many LiF backfilling methods for MSND microstructures have been investigated in the present work. Such microstructure patterns include cylindrical holes, straight trenches, chevron trenches, and sinusoidal trenches. The microstructure void widths range from 15 to 30 microns and vary in depth from a few tens of microns to hundreds of microns. The optimal MSND microstructure depth is determined by the thermal-neutron attenuation distance in the neutron reactive backfill material, solely ^{6}LiF in this work. The optimized microstructure depths range from 300 microns (i.e., approximately two mean free path (mfp) lengths in solid LiF backfill material) to 500 microns ≈ 3 mfp. To backfill ^{6}LiF material

into microstructured silicon, five backfilling methods have been considered: powder filling, electron-beam evaporation, liquid melt, low pressure condensation (LPC), and centrifugal nano-powder filling.

4.2.1 LiF Backfilling via Unprocessed LiF Powder Inclusion

LiF powder is produced by reacting ^{6}Li (95%) metal with deionized (DI) water to make ^{6}LiOH. Hydrofluoric acid (HF) is titrated into the ^{6}LiOH solution, thereby, precipitating out the salt ^{6}LiF. The LiF powder that is created in this manor tends to form large, micro-sized cubic crystals, and varies greatly in cubic particle sizes, ranging from submicron to tens of microns in dimension (see Figure 4.13). These relatively large crystals tend to cause problems when backfilling the Si microstructures. For example, the large sized cubic-crystals reduce the overall packing density that can be obtained within the silicon microstructure trenches. Therefore, the neutron absorption and, correspondingly, the neutron detection efficiency, is reduced because of the incomplete packing of the LiF powder within the trenches. The method of physically pushing the LiF powder material into the void microstructures by hand is pictured in Figure 4.14. Although physically pushing LiF material into the silicon microstructures has proven successful, it is not a commercially viable process for mass production because of high production rate limitations and low LiF packing-fraction density within the void microstructures.

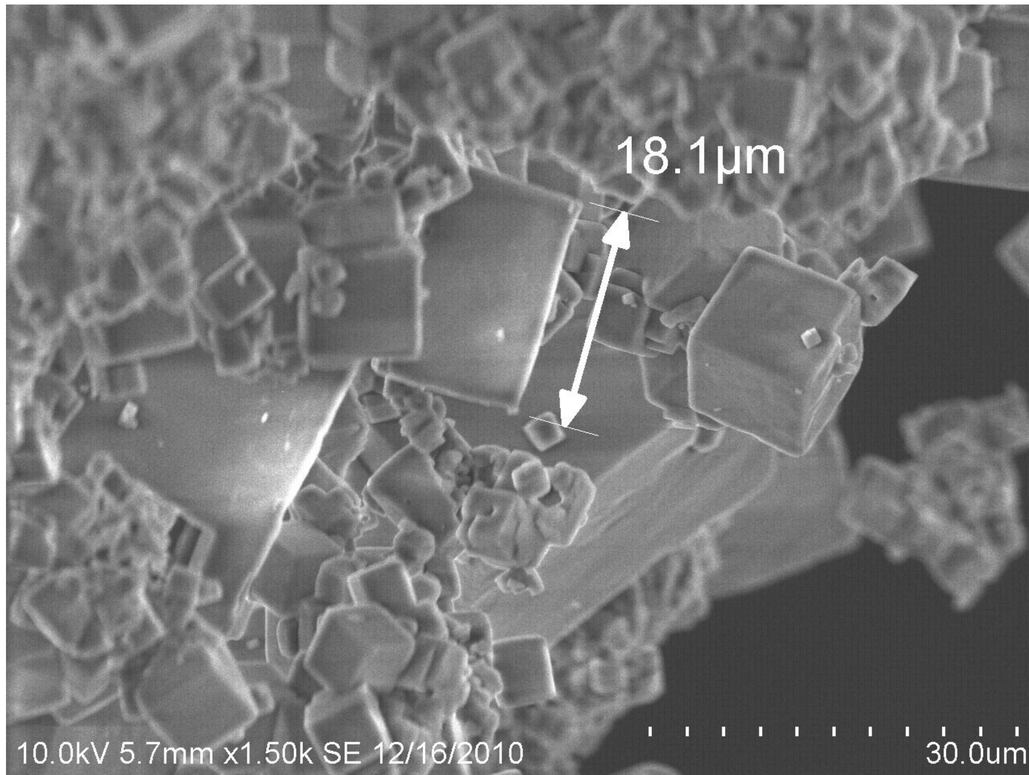

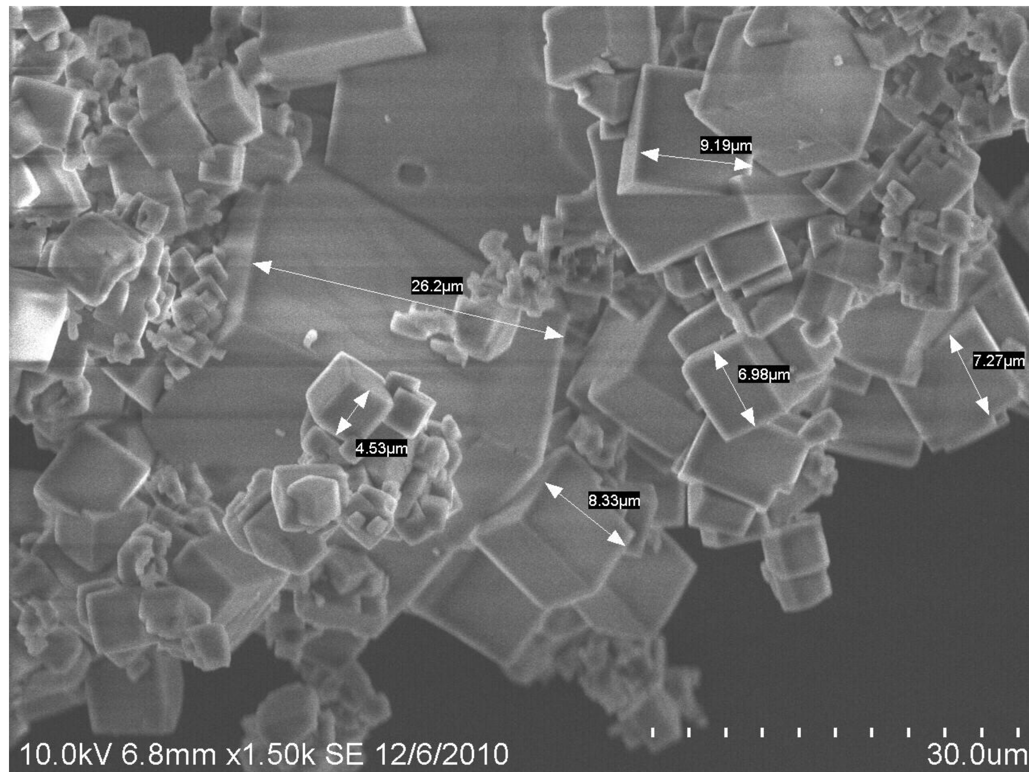

Figure 4.13: Pictures of micron-sized LiF is typical of commercially available or solution made material. Note the varying particle sizes of the cubic crystals, ranging from sub-micron to tens of microns.

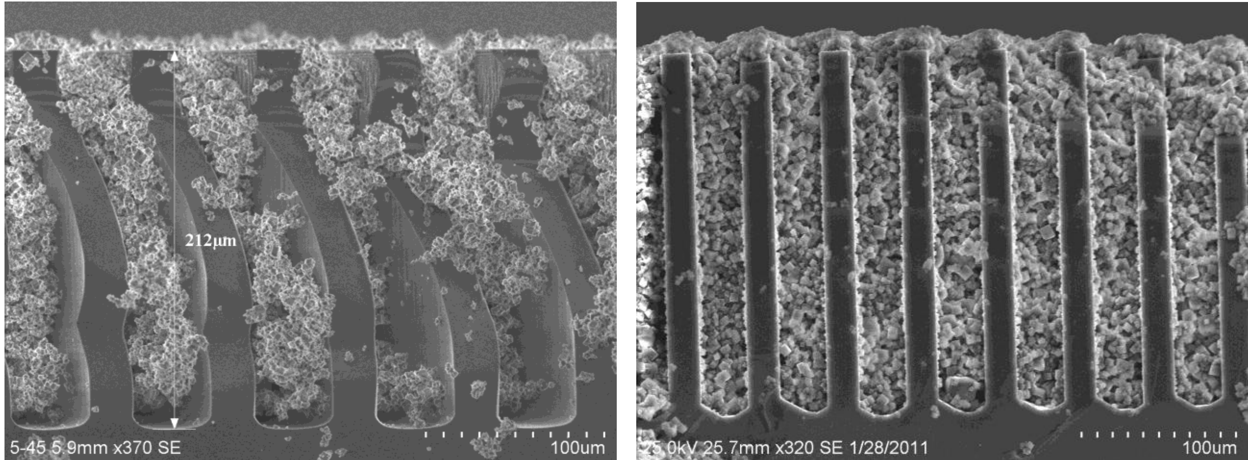

Figure 4.14: Solution-precipitated LiF powder backfilled into straight trench microstructures that are (left) 212 microns deep and (right) 250 microns deep. Notice that the coarse material loosely packs into the microstructures, leaving large packing fraction voids.

4.2.2 LiF Backfilling via Electron Beam Evaporation

The electron beam evaporation method of depositing LiF material into microstructured silicon fails because of the microstructure opening sealing-closed as LiF material builds-up at the entrance of the microstructure. Cleaved samples of nearly closed cylindrical microstructure holes are shown in Figure 4.15.

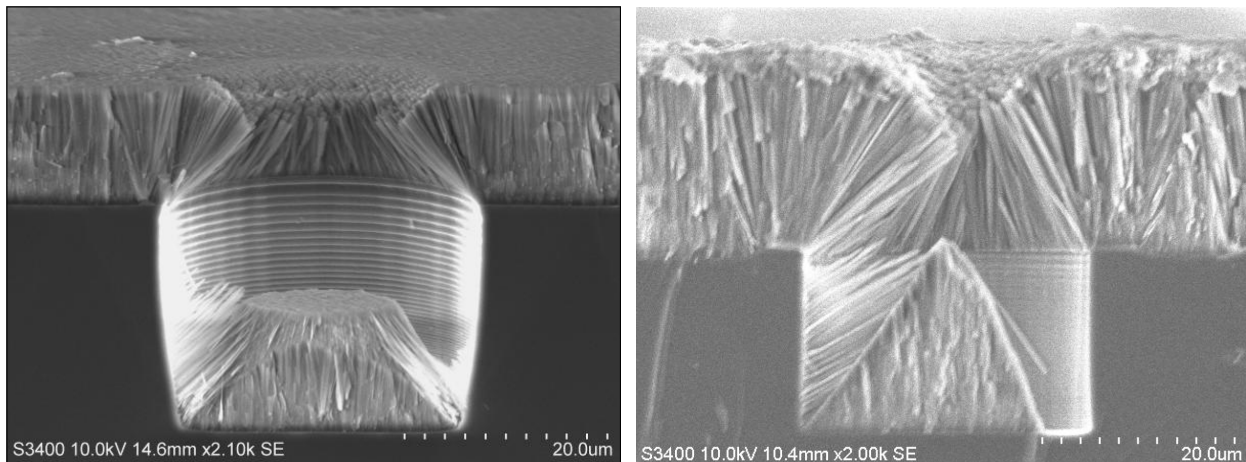

Figure 4.15: Electron beam evaporation of LiF material onto silicon microstructures with 30 μm diameter by 20 μm deep cylindrical holes. Notice that the holes close as the LiF builds-up at the top perimeter of the hole opening, therefore limiting its use as a backfilling method.

Notice in Figure 4.15 that the polycrystalline morphology of the evaporated LiF film. The columnar fibrous LiF structure of the crystalline film prematurely seals the microstructure leaves behind a void in the lower portion of the microstructure hole. Therefore, high aspect-ratio deep microstructures cannot be solidly backfilled with the e-beam evaporation method. This problem limits the use of the electron beam evaporation method as a deep-microstructure backfilling method for LiF or other materials.

4.2.3 LiF Backfilling via Solid Melting

Melting LiF powder into the silicon microstructures can be accomplished by heating under a nitrogen atmosphere the source LiF powder placed within the microstructures, along with the silicon wafer, to the melting temperature of LiF (867°C). Such melting is shown in Figure 4.16. However, the electrical properties of the silicon diode after the melting process are severely degraded. The resulting diode has leakage currents on the order of milliamps when a reverse bias was applied to the silicon diode. This leakage current is many orders of magnitude above the minimum allowable leakage current for a MSND. One noticeable cause is the reaction of the liquid LiF with the microstructure surface oxide SiO_2, which was either natively grown or grown to passivate the microstructured silicon diode. Another cause for the diode degradation is that the necessary heat to melt the LiF material is within the range of silicon dopant drive-in temperatures (~800°C); hence, the introduction of containments, such as lithium, a fast *n*-type diffuser in silicon, destroys the rectifying properties of the previously formed silicon *pn* junction.

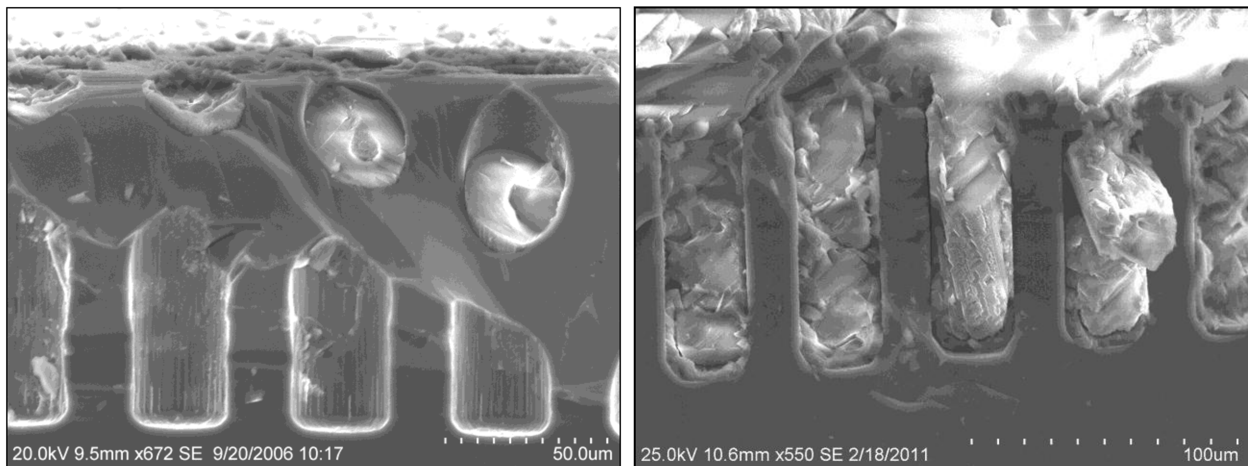

Figure 4.16: Melting of LiF material into microstructured silicon. The samples have been cleaved to investigate the fill composition of (left) cylindrical holes and (right) straight trenches.

4.2.4 LiF Backfilling via Low Pressure Condensation (LPC)

A low pressure condensation (LPC) method, to backfill LiF into high aspect ratio microstructured silicon diodes, was developed to address the problems encountered in the previous methods for backfilling. These problems include preserving the chemical, electrical, and structural integrity of the semiconductor *pn* junction while solidly backfilling LiF into the semiconductor microstructures.

The LPC prototype system, illustrated in Figure 4.17, was designed to process one 3-inch Si microstructured wafer. The microstructured silicon wafer is centered along the axis of a silicon carbide tube[28] and positioned perpendicularly to an inert argon carrier-gas that flows over a ^{6}LiF filled carbon crucible placed in the center of the furnace tube. The tube is evacuated to 100 mTorr with a 10-cfm rotary-vane vacuum pump. The surface of the silicon wafer is held at a constant temperature by a cold chuck, which is liquid nitrogen conductively cooled, such that a thermal gradient from the front to the back of the wafer develops because of radiant and convective energy transport from the furnace (see Figure 4.18). The silicon wafer temperature is measured with a thermocouple feedthrough that is positioned on-top of the wafer surface. Much like the molecular sieve of a sorption pump, the LiF vapor condenses within the holes and fills them with a preference from the bottom up. Consequently, this backfill method prevents blockage and premature plugging of the microstructure openings. The preferential deposition of LiF material within micron-scale microstructures depends on particle diffusion across the surface and within the depths of the silicon microstructures. In addition, the movement and sticking location of LiF particles is a function of the LiF particle sticking coefficient[29] and angular trajectory. Hence, the sticking coefficient varies across the entire microstructure substrate because of surface temperature variations within the microstructures and varying particle kinetic energies. As determined by experimentation, the total required time for the LiF LPC deposition ranges from 8 to 24 hours, depending on LPC operating parameters and the depth of microstructure voids to be backfilled.

[28] A carbon sleeved alumina (Al_2O_3) tube can also be used.

[29] The sticking coefficient is described as the ratio of absorbed particles to some defined surface to that of the total number of particles impinged upon the same surface during the same period of time.

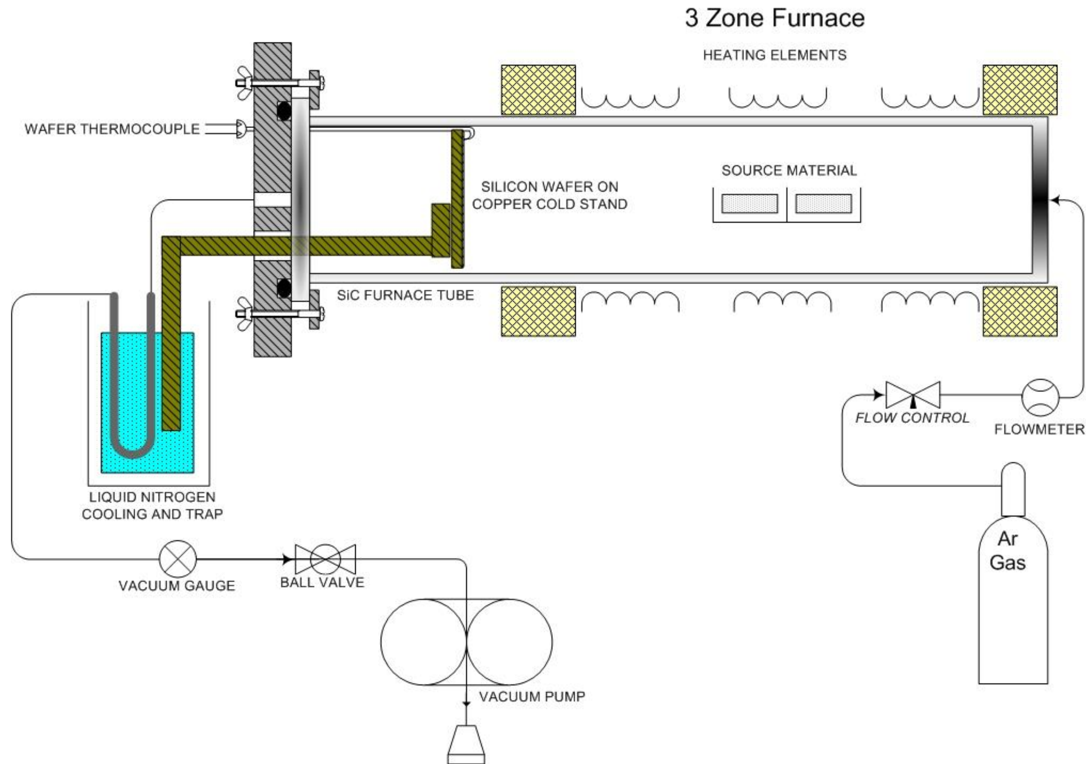

Figure 4.17: A schematic view of the LPC system, partially broken away, which can provide dynamic, low-temperature, 200 - 500°C, LiF condensation filling of Si microstructures.

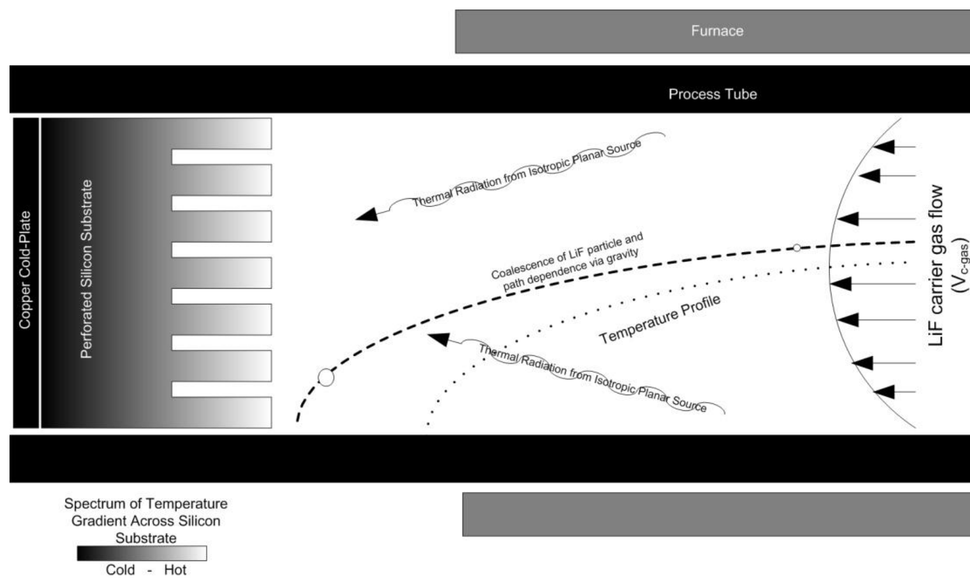

Figure 4.18: A more detailed schematic of the transport physics of the LPC system. The surface of the silicon wafer is held at a constant temperature from a cold chuck, such that a thermal gradient from the front to the back of the wafer is developed because of the radiant and convective energy transport from the furnace.

After backfilling of LiF within the microstructures, a thick LiF film is deposited on the entire surface of the silicon wafer test sample (see Figure 4.19). To inspect the LPC microstructure filling characteristics, the encapsulating film was physically lifted from the test sample. During initial experimentation with the LPC system, carrier gas flow-rates were varied (1 to 3 sccm) at a constant furnace temperature 880°C, which induced a frontside-surface temperature of 200°C on the Si wafer. As shown in Figure 4.19, the trenches were sealed closed, a result similar to the e-beam evaporated LiF backfilling results shown in Figure 4.15.

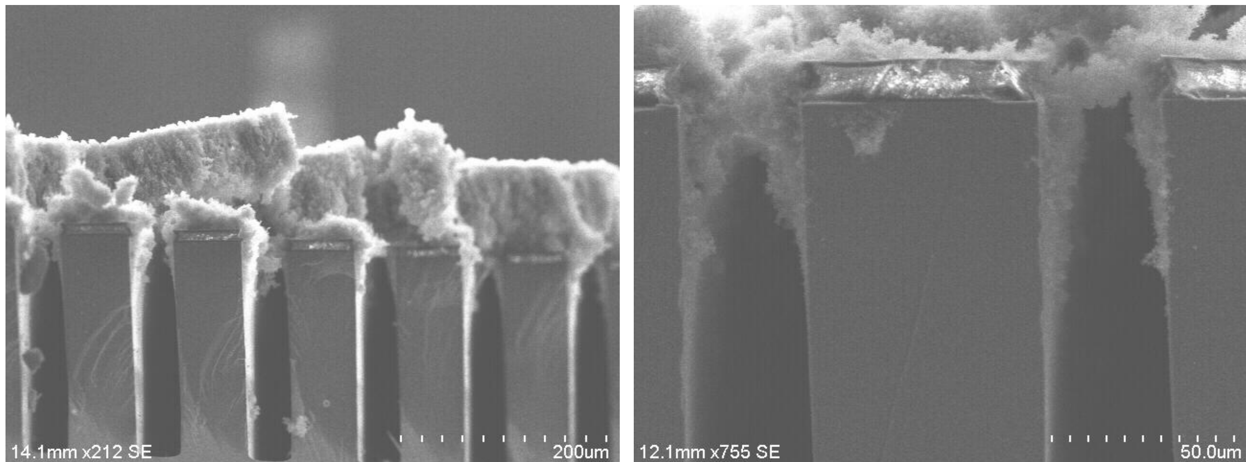

Figure 4.19: Representative pictures of initial experimentations of LPC depositing LiF material in 30 μm wide by 200 μm deep trench silicon microstructures with a low argon carrier-gas flow rate (1 - 3 sccm) and 880°C furnace temperature. The complete LPC process time was eight hours and the surface temperature of the silicon was ~200°C. Notice that the openings of the trench microstructures have sealed closed and the bulk of the LiF material has been deposited on the surface of the silicon wafer.

To improve LPC deposition within the microstructures, the LiF evaporation rate and wafer surface temperature were increased; hence, the surface sticking coefficient was reduced by raising the process furnace temperature higher to 1100°C. The carrier gas flow-rate was constant at 3 sccm. Because of the reduction of the silicon surface sticking coefficient, complete LiF backfilling of the microstructures was accomplished (see Figure 4.20). Notice in Figure 4.20, the LiF material deposited in the silicon microstructure holes extends out as a column from the cleaved section of the silicon test sample; additionally, the holes have been backfilled with slightly porous LiF material. Although improved backfilling results were found, the measured temperature of the silicon wafer during the deposition process was discouragingly found to be

approximately 575°C. At this temperature and at the length of the process time of 10 hours, with process parameters of 2 hrs ramp-up, 4 hrs process flow, 4 hrs ramp-down, a diode does not survive because of junction spreading from diffusion and LiF[30], along with other contaminants, diffusing into the silicon, thereby, destroying the diode junction.

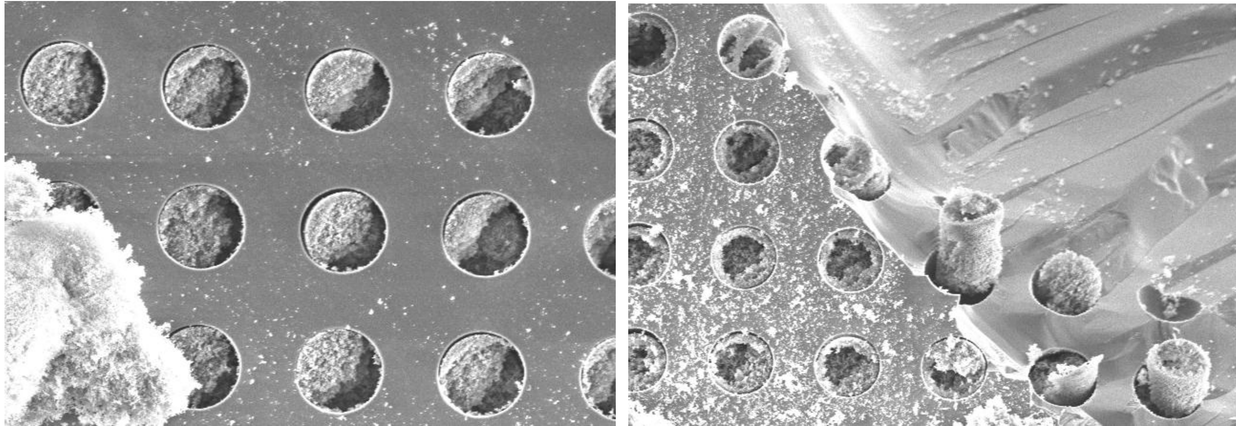

Figure 4.20: Representative pictures of experimentations of improved LPC depositing LiF material in 30 μm diameter by 100 μm deep cylindrical silicon microstructures with a low argon carrier-gas flow rate of 3 sccm and 1100°C furnace temperature. The complete LPC process time was ten hours and the surface temperature of the silicon was 575°C. (right) Notice that the sample has been cleaved to investigate the fill composition of the holes and showing columns of slightly porous material.

To improve further the LPC system, the wafer temperature was reduced by setting up a temperature gradient in the process tube of 950°C, 1100°C, and 1000°C, for the nearest-to-wafer heating zone to the farthest heating zone, respectively,[31] and by doing so, the wafer temperature was reduced to 380°C. Because of the gas-flow increase and zonal temperature gradient adjustments, the LPC coalesced particle size was reduced and the LiF condensation was much less porous material, appearing almost solid (see Figure 4.21).

Although the temperature of the silicon surface was reduced, it was still high enough for surface contaminate to diffuse into the silicon and destroy the diode. In addition, only one wafer may be processed at a time with a shallow-microstructure process time of >14 hrs; this is an

[30] Lithium is a fast *n*-type diffuser in silicon.

[31] Note that it was also possible to reduce the surface temperature of the wafer by moving the wafer-cold finger assembly farther away from the nearest heating zone. But, by doing so, much of LiF material condensed on the outer-furnace inner-tube surface. Therefore, a loss of carrier-gas transported LiF material was inconveniently evident. Such that, being closer to the furnace heating zone levied a higher deposition rate.

obvious bottleneck for mass producing the MSND. Therefore, this method of backfilling was abandoned for the MSND neutron reactive material backfill fabrication.

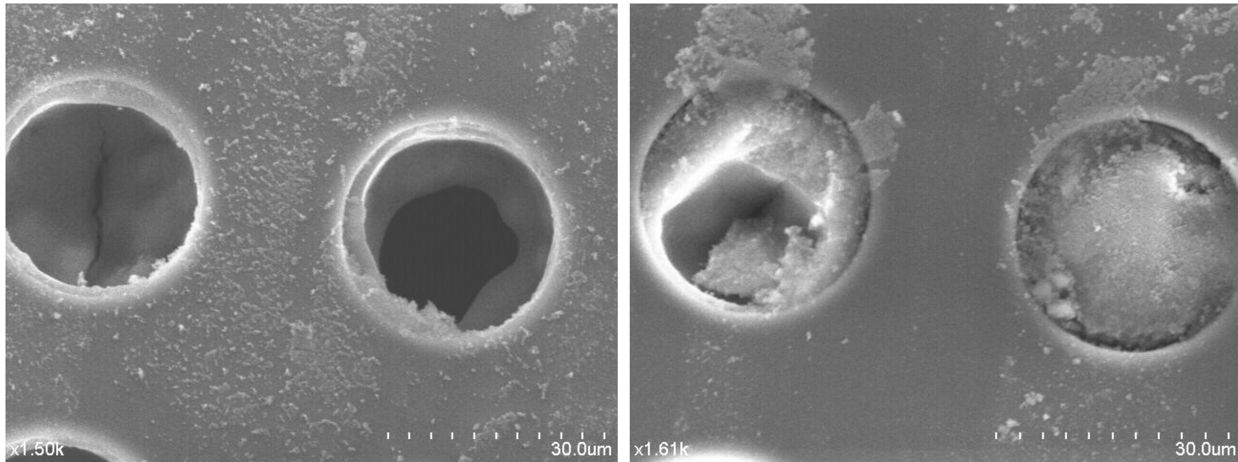

Figure 4.21: Representative pictures of experimentations of improved LPC depositing LiF material in 30 μm dia. by 50 μm deep cylindrical silicon microstructures with a higher argon carrier-gas flow rate of 10 sccm and furnace temperatures of 950°C/1100°C/1000°C, for the nearest-to-wafer heating zone to the farthest heating zone, respectively, with the surface temperature of the silicon at 380°C. Because of *the gas-flow rate increase and zonal temperature gradient adjustments, the LPC coalesced particle size was reduced. (left) Shown is the condensation of solid material at the bottom of the holes to be more prevalent at a process time of 8 hrs. (right) Shown is the same LPC recipe as (left), but for a longer process duration time of 14 hrs.*

4.2.5 LiF Backfilling via Nanoparticle LiF

Laboratory precipitated and commercially available ^{6}LiF powder is composed of large, micro-sized, cubic crystals as shown in Figure 4.22. The coarse ^{6}LiF powder material tends to cause problems when backfilling MSNDs, such that the large sized cubic-crystals reduce the overall packing density that can be obtained within the trenches (see Figure 4.14). This inefficient packing of the LiF powder within the trenches reduces the neutron absorption efficiency and, correspondingly, the detection efficiency. Therefore, to accommodate low-temperature deposition processes and to increase the packing density of the LiF material within the Si microstructures, it is important to reduce the crystalline size of the LiF powder. Although some nanoparticle LiF material is produced during the standard reactive precipitation process, it

is not in large quantities and is mixed with the larger crystalline material. It has proven difficult and inefficient to harvest the smaller material from the whole batch. In the commercial industry, some nano-materials are produced through what is known as “top down” technology, where the raw material is pulverized into nanomaterial, e.g., high energy ball milling, jet milling, or other size reducing mechanisms [111]. The more popular way of forming nanomaterials in industry is through “bottom up” technology, where instability in phase formation nucleates the nanomaterial [111].

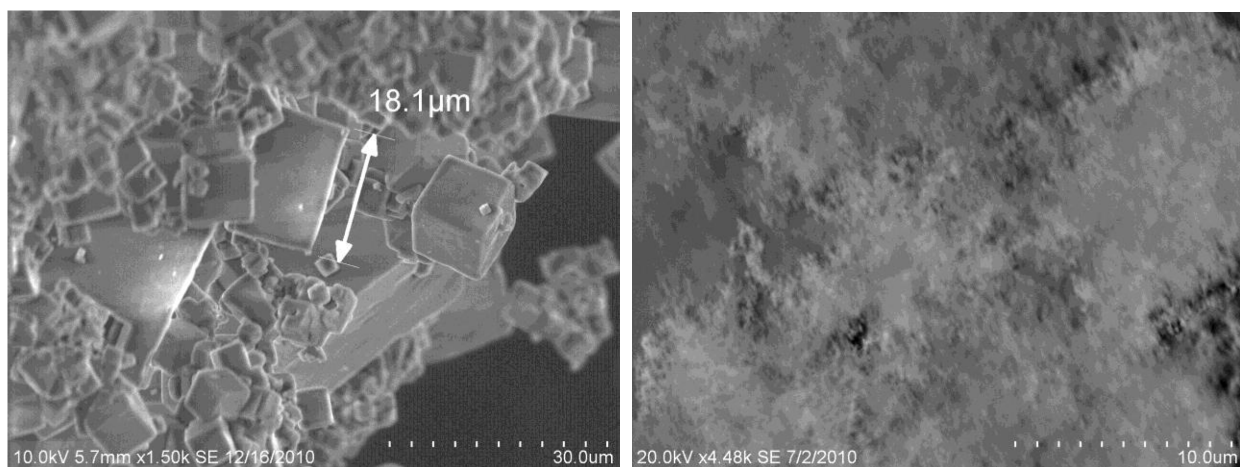

Figure 4.22: (left) Micron-sized ^{6}LiF is typical of commercially available or solution made material. Note the varying particle sizes of the cubic crystals, ranging from sub-micron to several microns. (right) Nanoparticle ^{6}LiF material that was produced via the vapor-condensation method.

From the LPC experimental work previously mentioned, it was discovered that coarse LiF powder may be reduced to nanoparticle powder through a vapor transport condensation method, which would correspond to the “bottom up” technology approach of nanomaterial production (see Figures 4.21 and 4.22). By slightly adjusting the LPC system, nanoparticle powder LiF material can be produced in gram quantities. A schematic of the LiF nano-sizing system is shown in Figure 4.23. In this schematic, LiF powder is placed in a carbon crucible inside a SiC furnace tube, is heated to just under the boiling point, and then transported via an inert carrier gas (e.g., argon or helium) to a thermophoretic or electrostatic precipitator (ESP).[32] In addition, the LiF

[32] Although ESP is a common name for this type of system, a more appropriate name would be electrophoretic condenser.

vapor diffuses throughout the chamber, leaving the heated zone with a bias in the direction of the inert carrier-gas flow and thermophoretically condenses back onto the surface of the furnace tube directly outside the furnace hot zone.

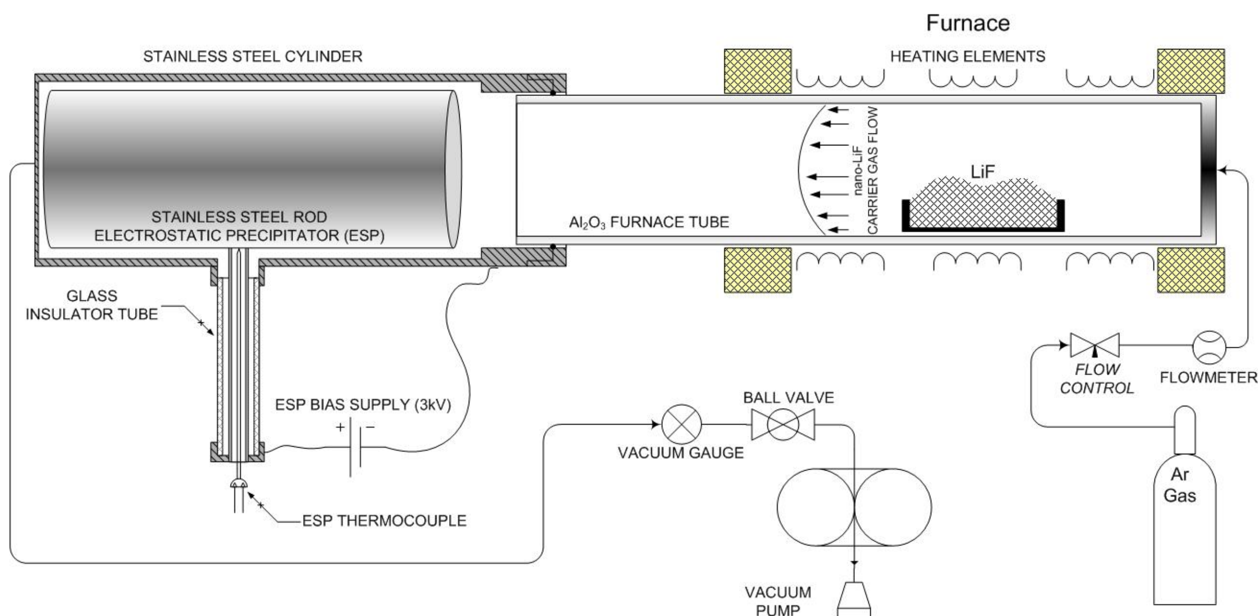

Figure 4.23: A schematic of the LiF nano-sizing system. LiF is loaded into a carbon crucible under an argon atmosphere and is heated to just below the boiling point to control the evaporation rate of the LiF vapor. The nanoparticle vapor electrostatically condenses on the stainless steel rod and cylinder preferentially because of *the applied electric field between the two anodes. The deposited nanoparticle powder LiF material is then physically removed from the electrodes.*

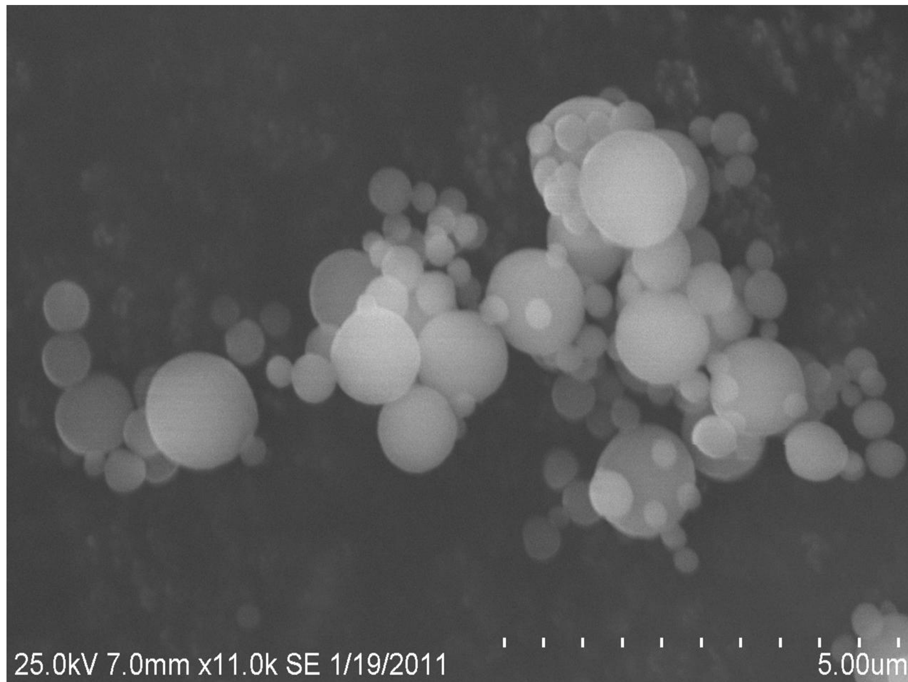

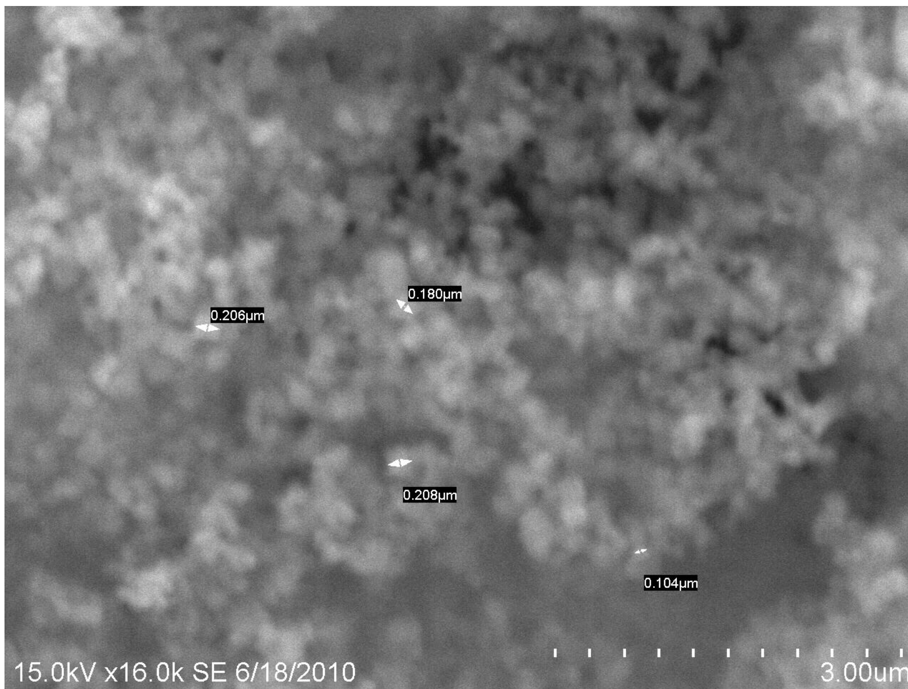

Figure 4.24: Fractals of LiF-agglomerated nanoparticles produced via LiF vapor condensation. (top) The nanoparticle material has collected into a series of small spheres through electrostatic forces and then agglomerated spheres form into fractal agglomerates of varying dimension. (bottom) With increased carrier-gas flow, the LiF nanoparticle material is given less time to coalesce into spheres and, therefore, the size of the LiF-agglomerated nanoparticles are coherently reduced. Sourced from [112], copyright © 2011, IEEE.

As the LiF vapor material moves through the SiC tube, spheres of bound nanoparticle LiF material form and agglomerate into fractals of varying orders as indicated in Figure 4.24. In this state, the agglomerated material, carried by the argon gas flow, is governed by aerosol dynamics of fractal agglomerates [113]. The process of LiF nanoparticle powder condensation is driven largely by thermophoresis and electrophoresis. Because of the motion of the coalesced LiF nanoparticles through the non-conductive SiC tube, a buildup of charge on the particles themselves makes it possible for electrophoretic condensation at the ESP.

The velocity of a LiF nanoparticle, because of the thermophoretic forces, is described by the kinetic theory of gasses [113],

$$c_t = \frac{-3\nu\nabla T}{4\left(1+\pi\alpha/8\right)T} \ , \qquad d_p << l_p \ , \tag{4.3}$$

where c_t the thermophoretic velocity, varies based on the temperature of the carrier gas T, the kinematic viscosity of the gas v, and the accommodation coefficient α, and holds true for all agglomerates whose diameter d_p is much smaller than the mean free path of the gas l_p. As the LiF vapor exits the heating zone, thermophoresis forces the agglomerated particle to the surface of the tube where it cools rapidly. Therefore, the size of the agglomerated spheres can be controlled by reducing the vaporization rate or increasing the carrier gas flow rate and temperature to increase the particles velocity through the furnace and, consequently, reducing the amount of coalesced material on an individual spherical particle.

Van der Waals forces keep the particles on the surface of the SiC tube. Yet, the majority of the nanomaterial can be collected at the ESP because of buildup of charge on the particles themselves. The layer of LiF nanoparticle powder, deposited throughout the tube and on the ESP, is harvested easily by knocking or scraping the material from the tube and the ESP. The entire process takes 2 to 5 hours, allowing for the potential of LiF nanoparticle powder mass production. Additionally, the ESP can be removed while the furnace is at the LiF vaporization temperature by including a sealing valve before the ESP; hence, nanoparticle material can be continually produced without the loss of time because of furnace temperature ramp-up and ramp-down.

Energy-dispersive X-ray spectral analysis (EDS) with a *Hitachi* S-3400N scanning electron microscope was conducted on the LiF nanoparticles to probe for the presence of LiF and

contaminates within the material. A representative EDS spectrum and fluorine atomic percentage of LiF particles is provided in Figure 4.25. Elemental lithium X-ray response is not possible with the EDS system because of the characteristic low-energy fluorescent X-rays being absorbed in the EDS detector window. The data confirms the lack of substantial contamination of the nano-LiF material during the thermal vapor and subsequent reconstituting size-reduction processing.

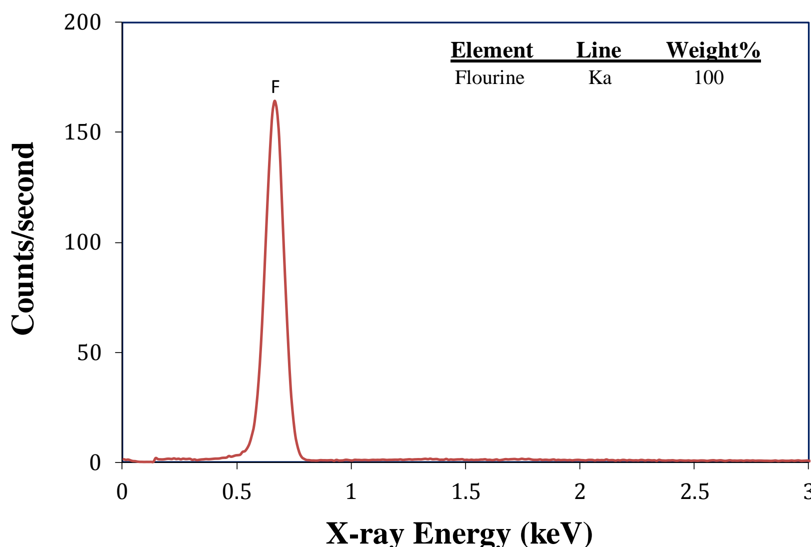

Figure 4.25: EDS spectrum of the LiF nanoparticles showing the dominate presences of the element fluorine. Lithium X-ray response is not present because of *X-ray absorption in the EDS detector window. Sourced from [112], copyright © 2011, IEEE.*

The usefulness of being able to create nanoparticle LiF is not limited to MSND thermal-neutron detectors. There is potential for its application in scintillators, particularly liquid scintillators, as a dispersed neutron converting material. Similar work has shown the particle size can be tuned, such that under UV illumination the photon is wavelength downshifted to a characteristically longer wavelength photon [114]. Based on this idea, a scintillation photon in a solid or liquid scintillator can be wavelength shifted to better match a photocathode for a photomultiplier tube or better couple to a solid-state diode detector. Other conjectured advantages of using nanoparticle quantum dots (QDs) as a scintillation or a wavelength shifting mechanism [114] over, or in conjunction with, fluorescent dyes is to improve light collection efficiency by reducing self-absorption, to reduce nonradiative exciton recombination, and to decrease the decay-time of the induced luminescence by removing the slower multi-state luminescent dye with nanoparticle direct band-gap QD fluorescent emission [115].

4.2.6 LiF Backfilling via Centrifugal Deposition

The simplest method found to backfill silicon microstructures with LiF nanoparticle powder is to press the powder into the silicon microstructures mechanically. Although this process is simple and inexpensive, it is inefficient and often ineffective at completely filling high aspect-ratio deep microstructures. The powder can be pressed into each MSND with approximately 100 kPa (~15 psi) by hand, but commonly leaves voids in the LiF filler material. Unfortunately, because of the unevenness of the by-hand-force application, it is not uncommon for silicon microstructures to be broken during this process or for packing densities to vary across both a single detector element and the entire silicon wafer. Additionally, each MSND must be attended to separately when pressed by hand, making large production runs difficult. An improved means for applying a much larger and more uniform force on the LiF backfill material, which also allows batch processing to backfill the microstructures, is to use a centrifuge to deposit nanoparticle LiF powder. In preparation, a colloid of LiF nanoparticle powder is suspended[33] in an isopropyl alcohol solution and a microstructured silicon wafer is placed at the bottom of a container, after which the container is filled with the LiF colloid. The silicon microstructures are then backfilled with nanoparticle powder LiF by spinning the container and colloid in a centrifuge[34] at 5000 rpm for 30 minutes.

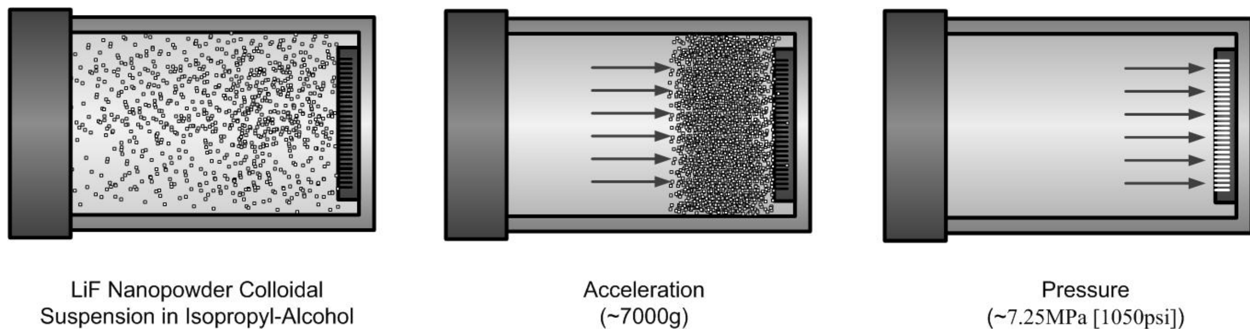

Figure 4.26: A progressive illustration of centrifugal LiF deposition in semiconductor microstructures via LiF nanoparticle powder colloidal-suspension in isopropyl alcohol. This method offers a vast improvement for mass production over physically pressing the LiF nanoparticle powder into the microstructures. The size of the diode inside the bottle has been exaggerated for effect.

---

[33] To disperse the LiF nanoparticle powder, the nanoparticle powder is mixed with isopropyl alcohol in a 1-liter centrifuge bottle and submerged into an ultrasonic water bath for 10 minutes to disperse the colloid solution.

[34] The centrifuge is a *Sorvall* RC-3C Plus™ with a H-6000A rotor.

Through this method, the suspended LiF nanoparticle powder settles into the microstructures of the silicon wafer and is compressed under the centrifugal pressure felt at the surface of the microstructured silicon, depicted in Figure 4.26, which is described by Bernoulli's equation with a varying centripetal force field, a_c(r), with no angular acceleration,

$$
\begin{aligned}
P &= \rho a_c(r) \Delta x \ , \\
&= \int_{r_{Top}}^{r_{Device}} \rho a_c(r) dr = \rho \int_{r_{Top}}^{r_{Device}} w^2 r \ dr = \rho w^2 \int_{r_{Top}}^{r_{Device}} r dr \ , \\
&= \rho w^2 \left[\tfrac{1}{2} r^2 \right]_{r_{Top}}^{r_{Device}} = \tfrac{1}{2} \rho w^2 \left[r_{Device}{}^2 - r_{Top}{}^2 \right] ,
\end{aligned}
\qquad (4.4)
$$

where the hydrostatic pressure P at the MSND, varies with the rotational velocity w of the sample, the density ρ of the colloid suspending solution, the radial distance r_{top} from the center of the rotor to the top of the fluid, and distance r_{Device} from the center of the rotor to the MSND. Specifically, a microstructured silicon wafer is loaded in a 1 L bottle and rotated in a *Sorvall* H-6000A rotor at 5000 rpm. The pressure at the MSND surface is approximately 7.25 MPa (~1050 psi), which is 70 times greater than the by-hand pressed method. Additionally, the pressure is perfectly uniform across the silicon wafer. The centrifugal method for deposition allows many of individual MSNDs[35] to be processed simultaneously. Because of the low-temperature deposition afforded by the centrifugal LiF backfilling method, no chemical, electrical, and structural integrity damage of the silicon material occurs. Thus, the centrifugal deposition method has been found to be the superior method for backfilling LiF into MSNDs compared to all the previous methods.

Shown in Figure 4.27 are pictures of centrifugally backfilled MSNDs with LiF nanoparticle powder in high aspect-ratio, wet-etched, straight-trench microstructures. The fine LiF nanoparticle powder backfills the deep microstructures with densely packed LiF material. Additionally, the packed LiF material within the trenches has been compacted together into large clumps; this is the result of the compactness of the centrifugally deposited nanoparticle powder.

---

[35] Six silicon wafers can be processed at a single time in the *Sorvall* H-6000A rotor.

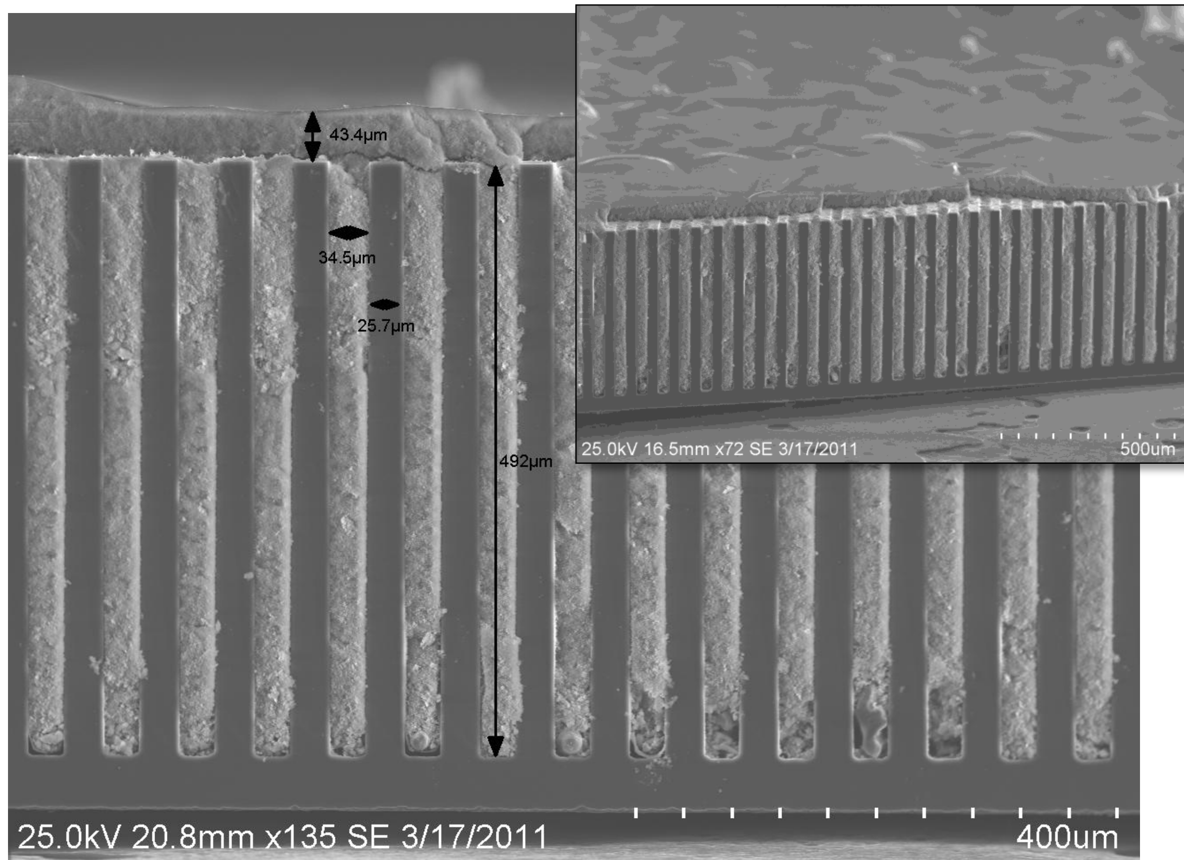

Figure 4.27: SEM pictures of centrifugally backfilled MSNDs with LiF nanoparticle powder in high aspect-ratio wet-etched straight trench microstructures. (top-left and bottom-left) Shown are 225 µm and 100 µm deep trenches filled with nanoparticle LiF material, respectively. (top-right) Pictured is a top-slant view of the MSND represented in the top-left picture; notice fine nanoparticle powder coating layer, characteristic of centrifugal deposition, where the smallest particles fall last because of *particle drag forces. (bottom-right) Shown is a top-view of the filled 100 µm deep trenches. Sourced from [21], copyright © 2010, IEEE.*

4.3 MSND Fabrication

Based on the MSND simulation results and the development of practical silicon processing techniques, various microstructure patterns and optimized dimensional parameters can easily be fabricated. For the initial MSND design, conservative parameters were chosen. These MSNDs were fabricated with straight trench pattern with ^{6}LiF backfilled trench-regions identical in size to the semiconductor fin-regions and various pitches between 25 to 35 microns. These fabrication parameters were chosen on the basis of ease of fabrication and a large low-energy spectral "dip" in the pulse-height distribution frequency for the MSND, so as to produce a superior gamma-ray discrimination ratio without much loss in neutron detection efficiency.

These MSNDs were manufactured on a single high-resistivity silicon wafer. Initially, an oxide was grown on a 5-15 kΩ-cm *n*-type silicon wafer in which a diffusion window was patterned. Microstructured perforations were then etched into the silicon diffusion windows with an ICP-RIE process or a KOH wet-etch process where the trench pattern was aligned to the <111> planes in a (110) orientated silicon wafer. Individual and arrayed MSNDs were batch processed on three inch and four inch diameter wafers (depending on array size), each with an active square-area of 1-cm^2. The individual MSNDs have straight trenches etched 250 microns to 450 microns deep by 25 microns to 35 microns wide, where the trenches are periodically spaced 50 microns to 60 microns apart. The straight trench design maintains high neutron detection efficiency while creating an opportunity to off-set stack the detector chips to maximize neutron absorption as indicated in Figure 3.6. After the etch process, the wafer was chemically cleaned (as described in Section 4.1.4) and *p*-type regions were conformally-diffused uniformly into individual MSND microstructures across the wafer, thus forming *pn* junctions within the trenches. A Ti-Au or Ti-Al metal contact[36] was fabricated on the backside of the wafer to make an electrical ground contact, thereby, completing the diode structure and enabling depletion through the bulk of the individual MSNDs. More detail of actual fabricated MSND features are given with their respective neutron sensitivity results discussed in the Chapter 5 and in 0. In the case of the large MSND arrays fabricated on 4-inch silicon wafers, which were fabricated by a

[36] Titanium was used as a bonding metal and diffusion barrier against the diffusion of gold (which is a fast diffuser in Si) and to prevent *spiking* [95] of the aluminum contact. A barrier metal Ti/W alloy was also used in some cases to improve the adhesion of the Au or Al to the Si surface.

silicon foundry, details of MSND fabrication are given in 0. Finally, ^{6}LiF powder was either hand-packed or centrifugally packed into the microstructures to function as the neutron absorbing converter material.

A series of silicon *pn* junction fabrication techniques for the MSND are reported elsewhere [24, 39, 70]. The progression of this work has reduced the leakage current by orders of magnitude over the original microstructured pierced planar-junction design. After the pierced junction design, the diodes were selectively-diffused around the microstructure patterns, with a separation distance between the diode and the etched sidewalls of the trenches. Another improvement came with the addition of an oxide passivation in the trenches, which substantially reduced rectifying leakage-currents at reverse bias voltages between 1 and 10 volts. Even greater improvement of the MSND design, both reduction of leakage current and improved pulse-height spectral characteristics, was accomplished through the fabrication of the diode within the microstructures, which is presented here and elsewhere [24]. Hence, the diode conforms within and around the sidewalls and bottom of the deep trench silicon microstructures. A cross-section illustration of a fabricated conformally-diffused MSND is shown in Figure 4.28.

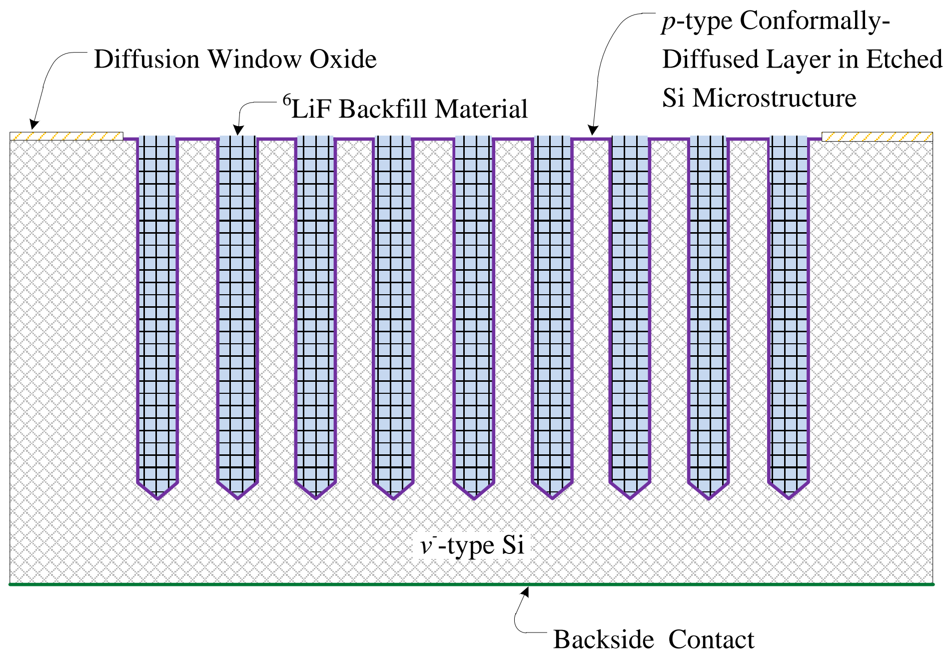

Figure 4.28: Cross-section illustration of a fabricated MSND with conformally-diffused diode structure.

4.4 Prototypical Individual MSND Counting Electronics

The MSNDs produce very little free charge[37] when neutrons are absorbed and ionize the semiconductor *pn* junction. Therefore, charge-amplification equipment is needed to produce a significant pulse-readout signal. To better couple with the electronic characteristics of the MSND, a preamplifier is used in conjunction with a standard amplifier. Basic neutron-measurement testing of the MSNDs consisted of mounting an individual detector chip in a 4-pin readout metal-enclosure header, shown in Figure 4.29, which was connected to an *Ortec* 142A preamplifier, followed by connection to a high-voltage power supply[38] and a *Canberra* 2022 amplifier. The distribution of the MSND pulse-height output signal was measured with an *Ortec* trump MCA card and *Maestro*™ software. Knowledge of the MSND signal pulse-height distribution is used to set the operating LLD and compare the actual MSND operation to that of theory discussed in Chapter 3.

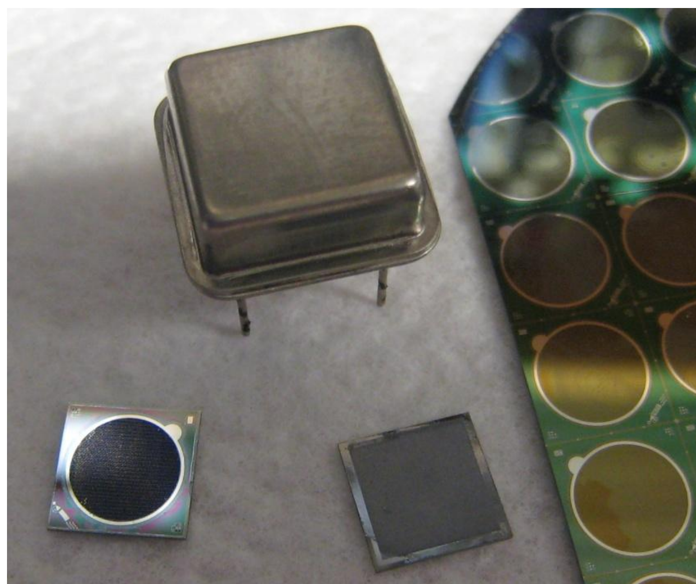

Figure 4.29: Shown are 6-mm diameter and square MSNDs with an assembled 4-pin readout metal-enclosure header used for single MSND neutron testing.

[37] For an average energy deposited of 1 MeV in the bulk Si of the MSND and a conservative estimated-energy to generate electron-hole pairs of 3 times the Si band gap (~3.6 eV), the average amount of charge produced in the MSND bulk Si from the neutron reaction products is 80 fC.

[38] Because of the specific load resistor used in the preamplifier, the MSND applied-bias voltage was divided by a factor of 10. As a result, a low noise high-voltage power supply was used to apply a low-voltage bias to the MSND devices.

Compact and sophisticated MSND readout electronics for advanced MSNDs, such as the 1-cm^2 dual-integrated MSND and the multiple-MSND arrays, were designed and constructed by Tim Sobering and his staff at the KSU Electronics Design Laboratory (EDL). The counting-electronics fabricated by EDL include readout assemblies, interconnecting cables, and MSND testing fixtures.

4.5 Dual-Integrated Stacked MSND Fabrication

To fabricate large-area (1-cm^2 elements) individual and stacked detectors, individual MSNDs were manufactured on a silicon wafer according to process specifications outlined in Section 4.3. Individual MSND chips were cut from a processed silicon wafer and then mounted as a dual-integrated detector system.

4.5.1 Dual-Integrated Stacked MSND Counting Electronics

Amplifying and readout electronics for large-area individual and dual-integrated stacked MSND were specifically designed in-house by the EDL. These electronics consisted of a sandwiched detector board and a separate motherboard (see Figure 4.30). The separate motherboard configuration was used for research purposes as it simplifies testing multiple detector types through the use of common electronics including (1) an adjustable 0 V to 30 V detector bias, (2) bias current compensation, (3) pulse shaping and gain, (4) an analog output for pulse-height analysis, and (5) a "digital" output from a discriminator. Figure 4.31 presents a schematic of the dual-integrated MSND's basic readout circuit. On the preamplifier board, a copper foil is sandwiched between two printed circuit boards that have an exposed backside plane. This foil provides the connection for the positive bias voltage to the detector cathodes. Two neutron detectors are mounted to the copper foil using conductive silver epoxy. On the front of the prototype circuit (PC) boards the detector anodes are wire-bonded to gold pads that are electrically connected by a post through the sandwiched boards. In this configuration, the anodes of each detector are common and applied to the input of a charge sensitive preamplifier. Because high counting rates are expected for some applications, a relatively short signal integration time constant of 2-10 μs is used. The preamplifier board can also be reconfigured such that the feedback from a downstream integrator can be applied to compensate for large

leakage currents resulting from varying types of MSND designs, in which some designs exhibit higher leakage-currents than others. All connections to and from the preamplifier board are on a single row 10-pin edge connector. The stacked detector and motherboard are placed in an aluminum box because the detectors are photosensitive and need to be electrostatically shielded to reduce ambient background noise. Further detail of the stacked MSND electronic readout system can be found elsewhere [23].

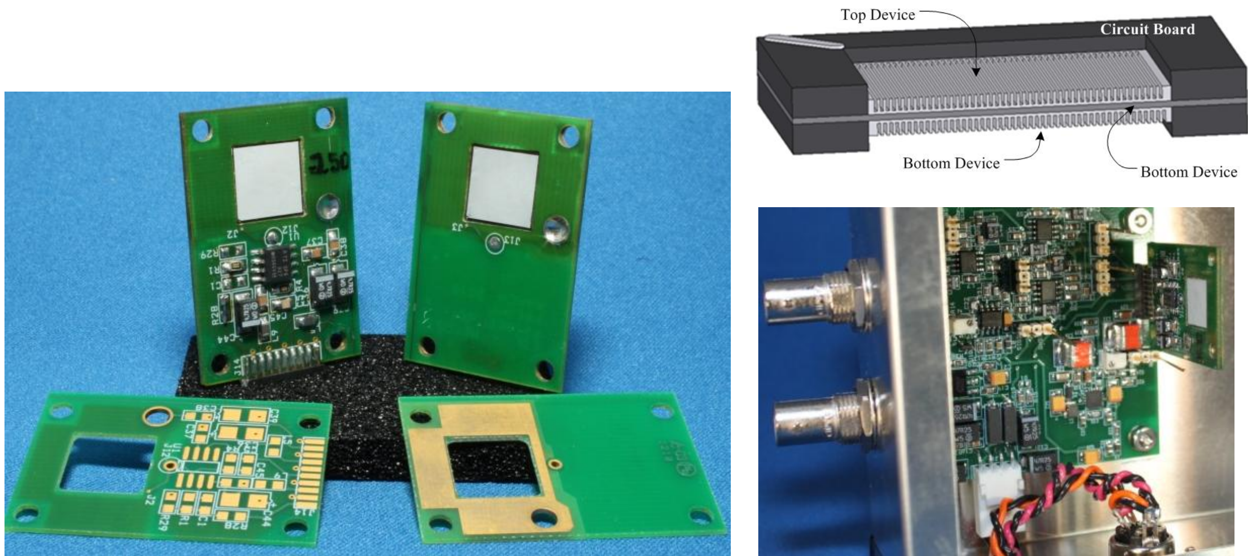

Figure 4.30: Shown (left) are dual-integrated packaged MSNDs with preamplifying circuitry, (top-right) a cut-section illustration of the stacked MSND arrangement of the dual-integrated MSND, and (bottom-right) a picture of the detector package and motherboard. The motherboard provides an adjustable detector bias, bias-current compensation, pulse shaping and gain, an analog output for pulse-height analysis, and a "digital" output from a discriminator. Sourced from [21], copyright © 2010, IEEE.

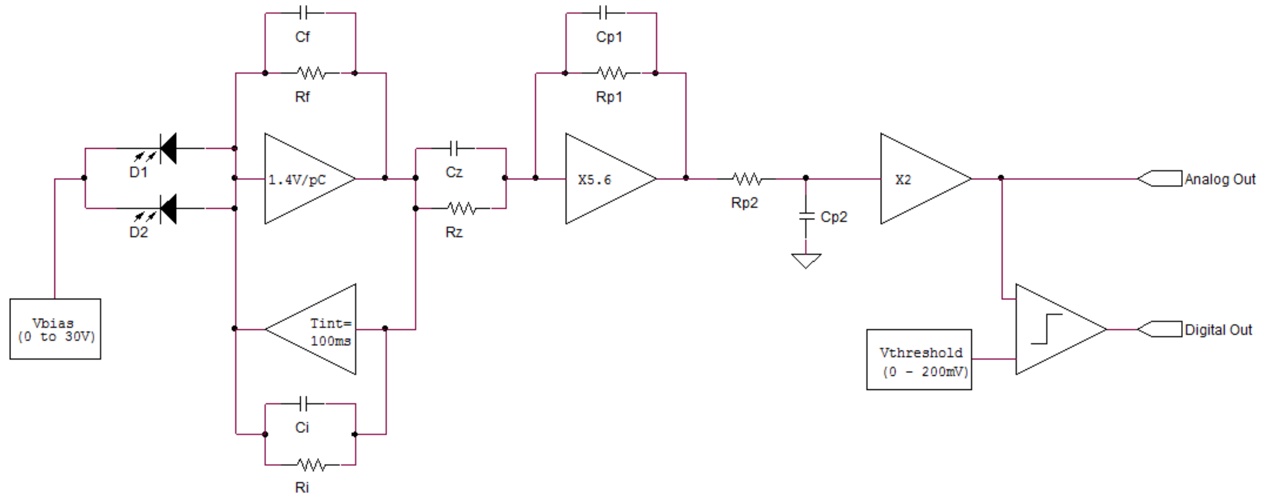

Figure 4.31: Diagram of the dual-integrated stacked MSND's basic readout circuit for pulse amplification, adjustable detector bias, bias current compensation, pulse shaping and gain, analog output for pulse-height analysis, and digital output from a discriminator.

4.6 Large-Area Individual and Stacked MSND Designs

To fabricate a more aggressively-sized MSND area, e.g., 4-cm^2 elements, individual MSNDs are manufactured on a silicon wafer according to process specifications outlined in Section 4.3. A 4-cm^2 MSND chip is then cut from a processed silicon wafer and mounted as an individual MSND. Additionally, two 4-cm^2 MSND chips are mounted back-to-back as a 4-cm^2 dual-integrated stacked MSND.

4.6.1 4-cm^2 Large-Area Individual and Stacked MSND Counting Electronics

The 4-cm^2 large-area individual and dual-integrated stacked MSND amplifying and readout electronics were specifically designed in-house by the EDL and used the same electronics and components as the 1-cm^2 stacked MSND described in Section 4.5.1. The individual 4-cm^2 MSND is fabricated by mounting one 4-cm^2 MSND chip on the dual integrating preamp board and leaving the backside device vacant. The dual-integrated stacked MSND is fabricated by mounting two 4-cm^2 MSND chips back-to-back to operate as a single device (see Figure 4.32).

Figure 4.32: Shown are (left) the 4-cm², large-area, dual-integrated, stacked, MSND package with preamplifying circuitry and (right) a picture of the detector package and motherboard. The motherboard provides an adjustable detector bias, bias-current compensation, pulse shaping and gain, an analog output for pulse-height analysis, and a digital output from a discriminator.

4.7 Dual-Integrated 6x6-Arrayed MSND Design

To fabricate dual-integrated stacked-detector arrays for assembled large-area panel arrays, a whole 6x6-element MSND array, with 1-cm^2 individual elements, is manufactured on a four inch diameter silicon wafer according to process specifications outlined in Section 4.3. The 6x6-element MSND chip is cut from a processed silicon wafer and two chips are mounted as a dual-integrated detector system.

4.7.1 Counting Electronics for the Stacked 6x6-Arrayed MSND

Two 6x6-element MSND array chips are mounted with highly specialized counting electronics designed by EDL, which are compact and designed to be fitted together like *Legos*™ into a large panel array for improved neutron detection sensitivity (see Figure 4.33).

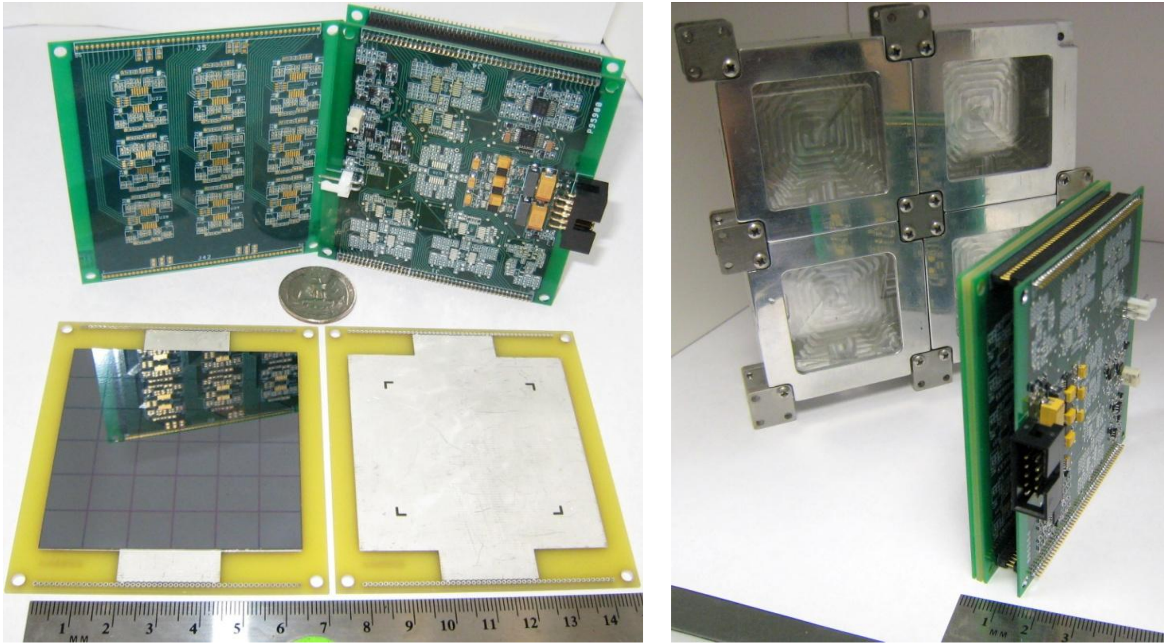

Figure 4.33: Shown (left) is a disassembled dual-integrated 6x6-element MSND array (1-cm^2 elements) with amplifying circuitry, adjustable detector bias, bias current compensation, pulse shaping and gain, an analog output for pulse-height analysis, and a digital output from a discriminator. Two 6x6-element MSND arrays are mounted back to back, where both sides of the mounting board are shown in the lower half of the picture. Pictured (right) is the assembled dual-integrated 6x6-arrayed MSND, with a characteristic aluminum housing for assembling many 6x6-element MSND arrays into a large detector panel array.

The counting electronics are similar to those used with the dual-integrated MSND. MSNDs described in Section 4.5.1, except they are packaged compactly together on 4-stacked boards consisting of one MSND mounting board, two preamplifier boards, and one amplifier/signal-shaping board (see Figure 4.34). The two 6x6-element MSND array chips are mounted back-to-back on an aluminum plated mounting board, with the preamplifier board mounted on top of each array. The mounting board provides the connection for the positive bias voltage to the common cathode on the backside of the silicon. The contact connection wires for the 36 individual MSNDs are wire-bonded to the top of the MSND chip through holes in the preamplifier board. In this configuration, the anodes of each detector are applied to the input of a charge sensitive preamp with a ~10.2 μs time constant and a nominal gain of 1.4 mV/fC. A relatively short time constant is used because high counting rates are expected for some applications. The preamp board can be reconfigured such that feedback from a downstream

integrator can be applied to compensate for the DC offset caused by the large leakage currents resulting from the trenching of the detectors. All connections to and from the preamp board are on two single-row 50-pin edge connectors. The preamplifier signals are routed to a motherboard which provides power, an adjustable +0 V to +2.5 V detector bias, pulse shaping and gain, an analog output for pulse-height analysis, and a “digital” output from a discriminator. In addition, to reduce the amount of circuitry required, four preamplifiers are connected to one shaping amplifier. The input signal is processed by a pole-zero cancellation stage with a gain of -56 and time constants of 12.1 µs (zero) and 10 µs (pole). The discriminator output is a 3.3 V logic level that is “high” as long as the analog output is above threshold. The output impedance was set to drive a counter with 1 kΩ input impedance. The analog output is a Gaussian-like pulse with a FWHM width of 18.5 µs and a gain of ~130.2 mV/fC. The input noise is 1.06 fC(rms). All values were measured using a 100 pF detector capacitance. The simulated detector capacitance was chosen based on measured MSND capacitance values at a detector reverse bias of 2.5 V. Overall each channel requires less than 250 µA.

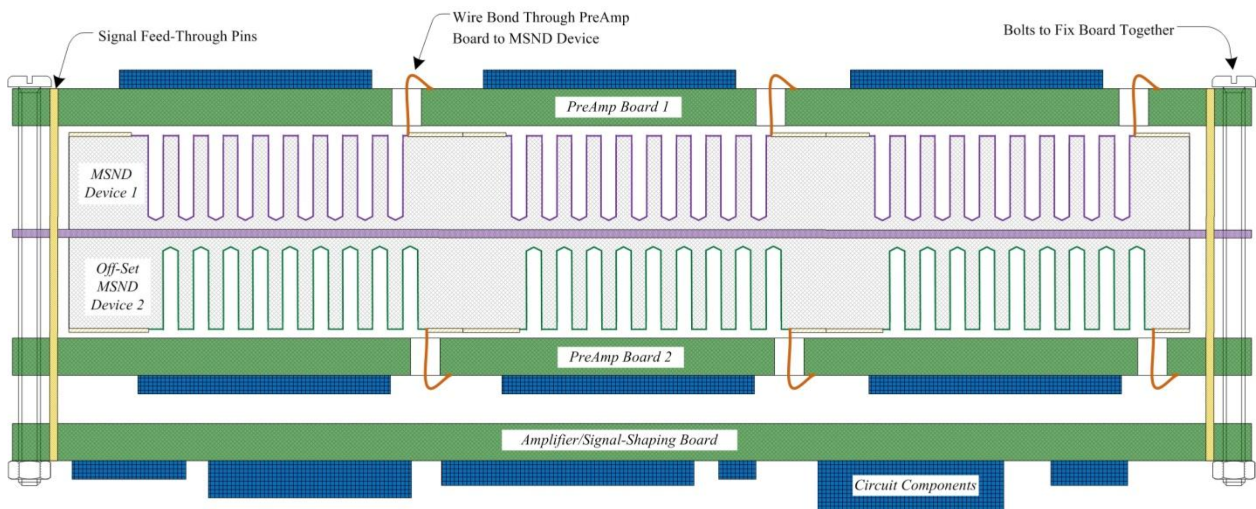

Figure 4.34: Illustration of a cut-section assembly of the dual-integrated 6x6-element MSND array with preamplifier board, stacked MSND array mounting board, and summed-amplifying/digitizing circuitry board. For simplicity and ease of view, only 3 MSNDs are shown, and the MSND scale is enlarged.

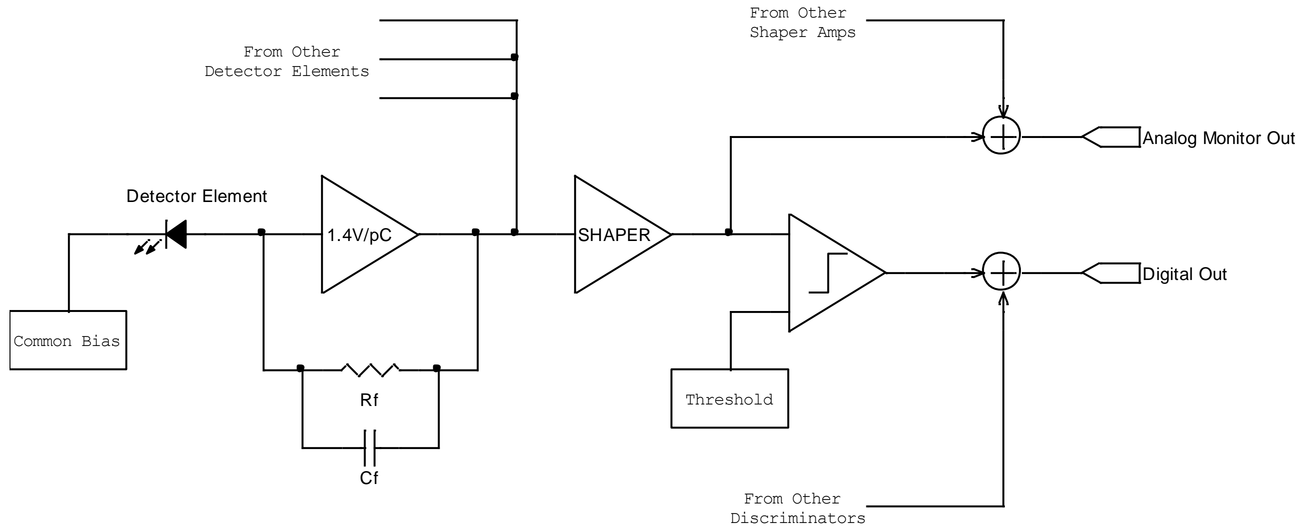

Figure 4.35: A diagram representing the 6x6-element MSND array basic readout circuit schematic for pulse amplification, adjustable detector bias, pulse shaping and gain, analog output for pulse-height analysis, and digital output from a discriminator.

4.8 Foundry Services

Semiconductor foundries usually manufacture integrated circuits (ICs) and transistors on the behalf of other *fab-less* companies and design laboratories that cannot afford the high labor and capital costs required for VLSI mass-production. As a result, there is a niche market for batch-production semiconductor foundry companies to supply these *fab-less* chip-design semiconductor companies and research and design (R&D) universities with a manufacturing resource. Because of the MSND VLSI-production processing methodology, wafer-level mass production of MSNDs is accomplished through a simple technology-processing methodology transfer to a compatible semiconductor foundry. The cost for a production run,[39] which may vary from foundry to foundry depending on the foundry's expertise and equipment sophistication, is an important consideration. The MSND production cost is also related to the complexity of the MSND design. The single-sided MSND is simple to manufacture, based on single-sided semiconductor processing techniques, but fabrication of the dual-sided interspersed trenched MSND design requires increased processing steps and sophisticated lithography masking

[39] Usually a production run will be quoted the same price for one to a *Lot* of wafers, where a *Lot* is usually 25 wafers. This occurs because semiconductor wafers can be batch processed and as a result, many semiconductor equipment manufacturers have developed equipment that can process 25 wafers at one time.

equipment for backside-alignment. As a result, the production costs associated with the dual-side MSND design are significantly higher than those for a single-sided MSND.

Although MEMS production technology is not uncommon, many ICs are produced based on single-sided planar processing techniques, and as a consequence, many semiconductor foundries are unfamiliar with MEMS production techniques. Therefore, MSND processing technology transfer can be difficult. To duplicate a silicon foundry facility is very difficult, if not nearly impossible because of the numerous variables that effect semiconductor wafer processing results, although Intel does endeavor to do just this. Thus, to reproduce the MSND technology at another production facility requires a transfer of processing techniques. In order to easily facilitate the transfer of MSND fabrication technology, a process *"Run Card"* was developed between the semiconductor processing foundry (e.g., Bi-CMOS [116]) and KSU S.M.A.R.T. Laboratory semiconductor processing facility [117]. A process *Run Card* is a detailed semiconductor device manufacturing process outline shared between the *fab-less* chip-design Company or University Laboratory and the Foundry. This outline is intended to convey the necessary device processing-techniques to correctly manufacture the MSND chip design. A process outline for both the single-sided and the interspersed dual-sided MSND designs was developed and transferred to a semiconductor foundry. The process outlines or Run Cards are presented in 0.

CHAPTER 5

MICROSTRUCTURED SEMICONDUCTOR NEUTRON DETECTOR: NEUTRON SENSITIVITY TESTING

A fact is a simple statement that everyone believes. It is innocent, unless found guilty.
A hypothesis is a novel suggestion that no one wants to believe. It is guilty, until found effective.
Edward Teller

The electronic characteristics of MSNDs and their performance when irradiated with various types and energies of ionizing radiation are described in this chapter. Both thermal- and fast-neutron detection efficiencies for single, stacked, and arrayed MSNDs are reported. MSND gamma-ray discrimination for varying LLD thresholds is presented. Implications of specific design features for the various types of MSNDs are discussed with respect to neutron detection efficiency versus gamma-ray discrimination.

5.1 MSND Electronic Characteristics

In rectifying-diode devices, the signal forming volume is mostly[40] limited to the space-charge depleted region where a significant electric field is well established [95]. Thus, the depth of the depletion volume is important for capturing the ionizing energy of the charged-particle reaction products. If the range of a charged-particle reaction product in the sensor material is significantly greater than the depletion region depth, some ionization will occur outside the active volume and a smaller and longer signal pulse results. Therefore, it is important to apply adequate reverse-bias

[40] For a partially depleted detector volume, charge is not only collected from the space-charge region but also from the bulk neutral (undepleted) region [93]. A small (and slow) signal is expected because part of the generated charge carriers recombine; though electrostatic repulsion does play a part in pushing the carriers apart, the time for the diffusion of the charge carriers in the neutral zone is much longer because of low field effects.

to extend the depletion volume and ensure that most of the charge carriers produced are swept out of the device, thereby improving the speed and magnitude of the signal. Consequently, reverse-bias leakage current and capacitance are important parameters to determine the correct bias-voltage setting and the design of amplifying-electronics for the rectifying-diode devices. Reverse-bias leakage current and capacitance are reported for various MSNDs in the following Sections.

5.1.1 Electronic Performance of 1-cm^2 Individual MSNDs

Leakage currents and capacitances as a function of the reverse bias voltage applied for 1-cm^2 straight-trench MSNDs are shown in Figures 5.1 and 5.2, respectively. Leakage currents and capacitances of early MSNDs with smaller sizes and patterned with circular holes and sinusoidal trenches can be found in the literature [39]. Notice in Figure 5.1 that the deep conformally-diffused MSNDs (>150 µm) with leakage currents at a reverse bias of less than 3 volts are on the same order of magnitude as the traditional simple planar diode.[41] At this voltage the conformally-diffused MSND has low enough leakage current and large enough space-charge depleted volume that measurable signal is produced from the neutron reaction products. Yet, the pulse-height signal generation is reduced because of incomplete charge collection from the weak electric field within the silicon fins of the microstructured conformally-diffused diode and the large capacitance. Notice also that at a reverse bias of 4 volts and above for the deep conformally-diffused MSNDs, the leakage current increases dramatically, much like reverse-bias diode break down seen in planar diodes with high electric-fields. This leakage current increase is likely because of incomplete diode formation within the trenched microstructures, because of the difficulty of depositing boron oxide sourcing-material, during the diffusion process, deep within the high aspect-ratio microstructured trenches.[42] Because of this incomplete junction formation, the conformally-diffused diode may only be partially formed within the trenches; as the applied reverse bias increases, the small spreading-resistance of the diffused *p*-type region spreads the

---

[41] As mentioned earlier, the bulk of the leakage current of an ideal diode would be because of generation current. Yet, it is expected that as Si material is removed within the microstructures, the generation leakage-current would decrease because of the depletion of silicon volume, thereby removing defects that act as generation-recombination centers for the minority charge-carriers responsible for the diode leakage-current.

[42] At the liquid source BBr_3 diffusion temperature (e.g., 1000 C), B_2O_3 is nearly in liquid phase with its boiling point higher than 1600 °C [114]. Therefore, incorporating B_2O_3 homogeneously into the conformal layer of simultaneously-grown SiO_2 within the microstructures is more difficult.

voltage potential across the diode surface. Yet with a few volts, the diode shorts to the undepleted region of the silicon (the unformed low-density *p*-type layer deep at the bottom of the high aspect-ratio trenches) and surface leakage current increases and dominates the MSND's IV characteristics.

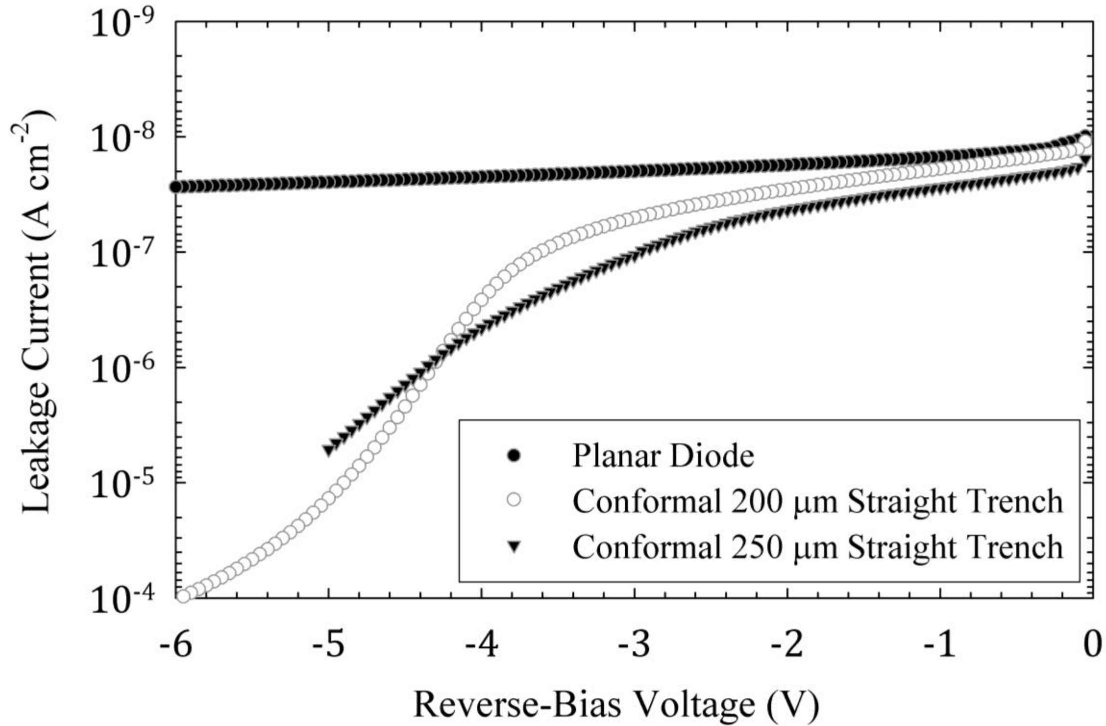

Figure 5.1: Leakage-current comparison of a planar-diffused detector and conformally-diffused MSNDs with 200 µm and 250 µm deep straight-trenches. All square MSNDs were 1-cm^2.

In the conformally-diffused diode capacitance plots in Figure 5.2, for the various depths of 1-cm^2 straight-trench MSNDs, notice that the conformally-diffused MSND capacitances are lower than the traditional simple planar diode. This is an unexpected result because of the increased surface-area of the microstructured conformally-diffused diode, but may be because of the reduced silicon detector volume from the microstructures. Also notice that starting at a reverse bias of 3 volts for the 250 µm deep MSND, the capacitance begins to drop rapidly, where the planar diode does not show this type function; this decrease in capacitance is also true for the 200 µm deep MSND starting at a reverse bias of 5.5 volts. Presently, it is unknown why these capacitance "shelves" appear, but they are likely related to the depletion of the silicon fin-volume and the spreading resistance of the conformally-diffused *p*-type layer. When modeled as

a parallel-plate capacitor, as the reverse bias increases, the voltage potential spreads across the conformally-diffused diode, increasing the area of the MSND and proportionally increasing the capacitance. However, as the depletion depth increases, i.e., the dielectric distance between the electrodes is increased, the capacitance proportionally decreases.[43] Therefore, this interplay between increasing and decreasing capacitive forces controls the value of capacitance until the voltage potential has spread across the conformally-diffused diode, i.e., completing the *p*-type layer electrode, and the depletion volume has moved past the bottom of the trench, entering the non-microstructured bulk silicon.

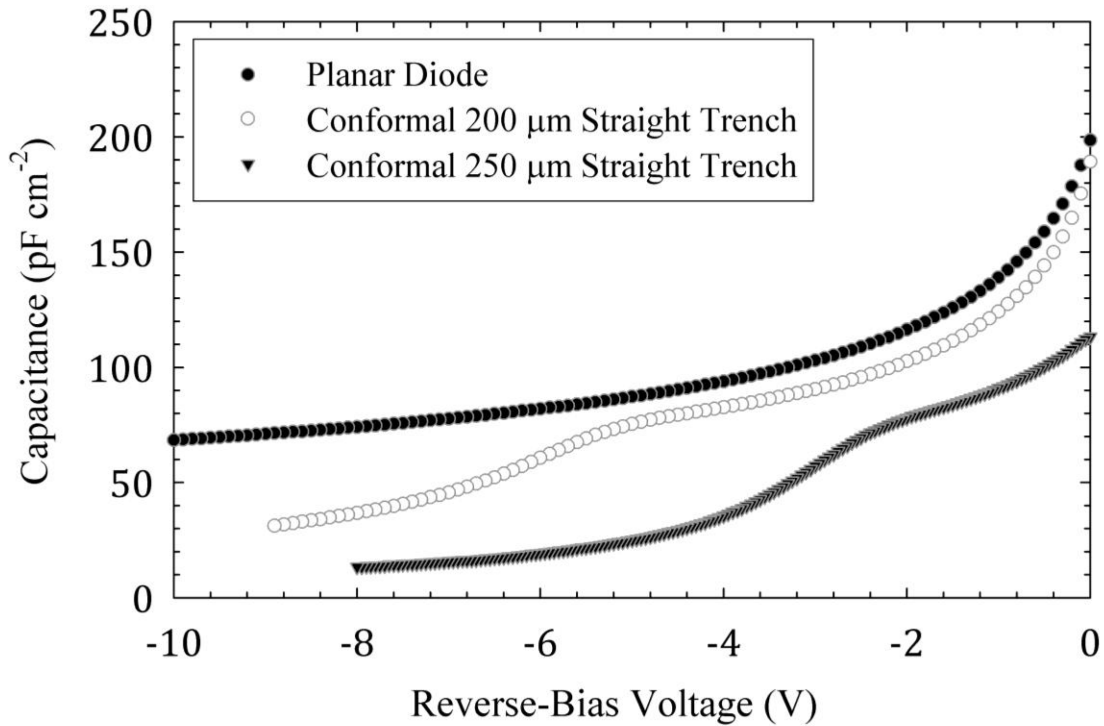

Figure 5.2: Capacitance comparison of a planar-diffused detector and conformally-diffused MSNDs with 200 μm and 250 μm deep straight-trenches. All square MSNDs were 1-cm².

In both cases of the IV and CV characteristics of the conformally-diffused MSND, the spreading resistance of the *p*-type layer electrode is a controlling factor in the operation of the MSND. To improve IV characteristics of the conformally-diffused diode, a longer *p*-type diffusion time was used to ensure complete conformally-diffused diode formation within the

[43] The capacitance C of the parallel-plate capacitor is defined as, $C = \varepsilon_{Si}\varepsilon_0 A/W$ [115] where ε_{Si} is the dielectric constant for silicon, ε_0 is the permittivity constant, A is the electrode area, and W is the depletion width.

microstructures, thereby preventing junction shorting to undepleted regions. It is worth mentioning that the microstructured-diode electronic characteristics may be improved by either increasing the diffusion time, thereby decreasing the sheet resistance of the p-type layer electrode or by conformally depositing a thin metal contact layer within the microstructured trenches. However, the second approach has the inherent problem of finding methods to deposit the metal layer within the microstructure trenches, which might be accomplished through electroplating methods. Although decreasing the spreading resistance of the diode is an improvement by decreasing the necessary reverse-bias voltage for low-capacitance MSND operation, higher spreading-resistance can be beneficial. By restricting the electric field disproportionately across the conformally-diffused diode, the electric field is predominately drawn parallel with the silicon fins as opposed to being perpendicular within the depths of the microstructure trenches. This benefit allows for stronger electric fields within the silicon fins (much like the selectively-diffused planar diode structure discussed elsewhere [24, 39]). Considering the weak electric-field problems of the conformally-diffused diode mentioned elsewhere [22, 23], developing microstructured diodes with strong electric fields would improve signal formation and charge-collection speed by sweeping ionized charge quickly and efficiency to their respective electrodes.

5.1.2 Electronic Performance of 4-cm^2 Individual MSNDs

Leakage currents and capacitances for various depths of 4-cm^2 square-area straight-trench MSNDs are shown in Figures 5.3 and 5.4, respectively. Notice in Figure 5.3 that the 200 μm deep conformally-diffused MSNDs with leakage currents at a reverse bias of less than 3 volts are on the same order of magnitude as the simpler planar diode. At this voltage the conformally-diffused MSND has sufficiently low leakage current and sufficiently large volume in which the space-charge is depleted, that the device can be used for neutron counting.

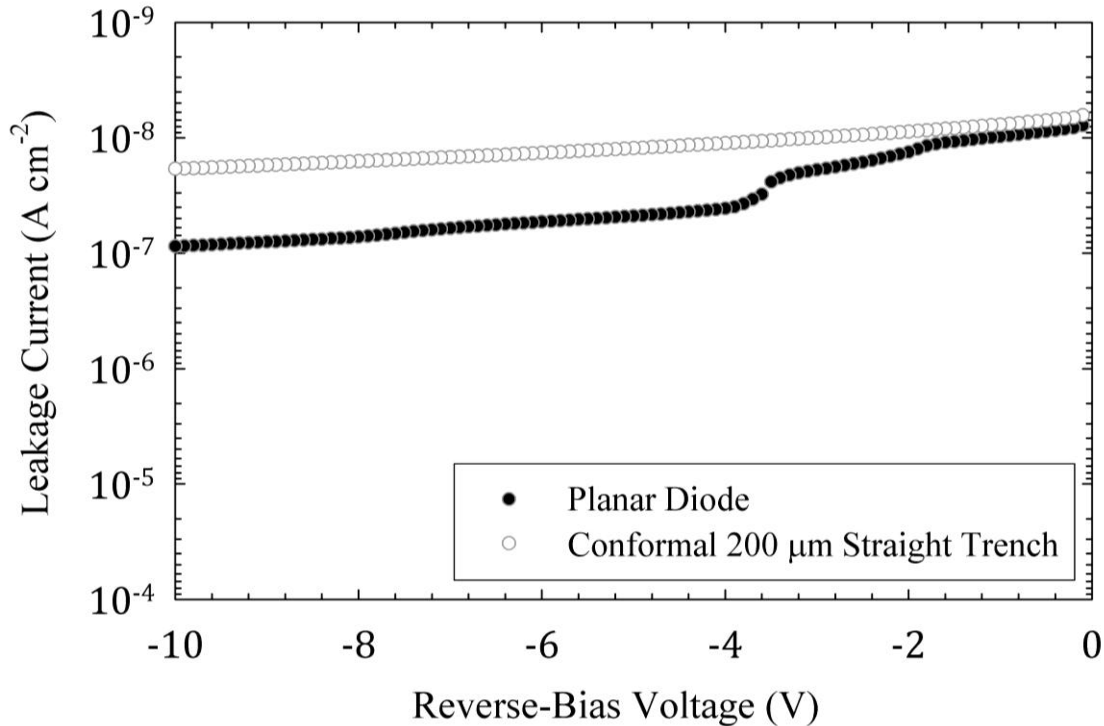

Figure 5.3: Leakage-current comparison of a planar-diffused detector and conformally-diffused MSND with 200 μm deep straight-trenches. All square MSND areas were 4-cm^2.

In the conformally-diffused diode capacitance plots in Figure 5.4, for a 200 µm deep and 4-cm^2 straight-trench MSND, notice that the MSND capacitance is lower than the traditional simple 4-cm^2 planar diode. Similar to the 1-cm^2 MSND in Section 5.1.1, the capacitance is unexpectedly less than the 4-cm^2 planar diode. Also notice that starting at a reverse bias of 1 volt for the 200 µm deep MSND, the capacitance begins to drop rapidly until about 3.5 volts. By contrast, the planar diode does not show this behavior. Additionally, at a reverse bias of 5 volts the capacitance of the 4-cm^2 MSND is 130 pF. This capacitance is relatively high compared to smaller MSNDs, but not high enough to cause problems in signal formation with charge-sensitive preamplification electronics from either designs offered by EDL or those that are commercially available, e.g., ORTEC® 142B preamplifier (100 pF - 1000 pF).

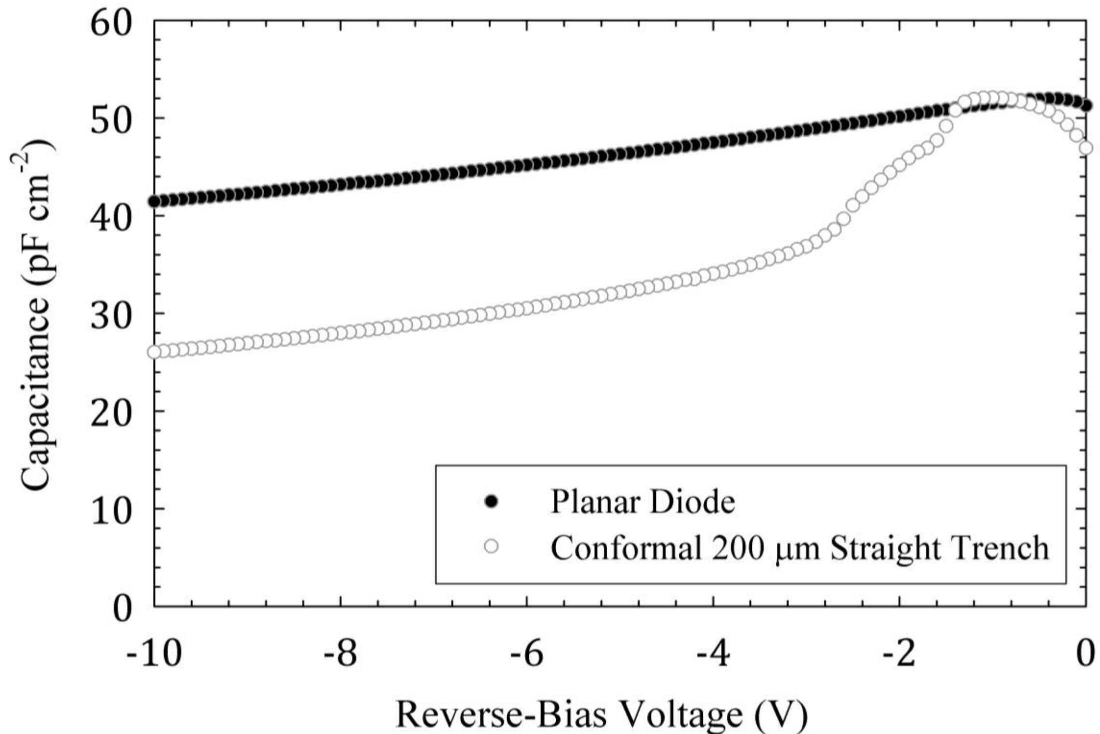

Figure 5.4: Capacitance comparison of a planar-diffused detector and conformally-diffused MSND with 200 µm deep straight-trenches. All square MSND areas were 4-cm^2.

5.1.3 Alpha-Particle Simulated Neutron-Response Testing

To simulate a neutron response, an americium-241 alpha-particle source was used as a source of ionizing radiation. ^{241}Am emits two alpha particles of energies 5.49 MeV and 5.55 MeV [120]. These energies are comparable to the full-energy capture of both the 2.73 MeV triton and the 2.05 MeV alpha particles released by the thermal-neutron capture in ^{6}Li. A microstructured diode was mounted on a probe station in a light-tight box and was connected to an ORTEC 142A preamplifier and Canberra 2022 amplifier. The alpha source was placed directly on top of the microstructured diode. Signal pulse-height frequencies were observed and recorded with an ORTEC *Trump PCI Card*™ multichannel analyzer (MCA).

The pulse-height spectrum collected from the ^{241}Am alpha particle source provided information about the performance of the microstructured diode sensor. A pulse-height spectrum was collected from a 4-cm^2 conformally-diffused microstructured diode. The energy resolution of the microstructured diode cannot discern the two different alpha particle energies and,

therefore, only a single full-energy peak is measured (see Figure 5.5). Alpha-particle simulated neutron-response pulse-height spectra from earlier MSND diodes can be found elsewhere [39].

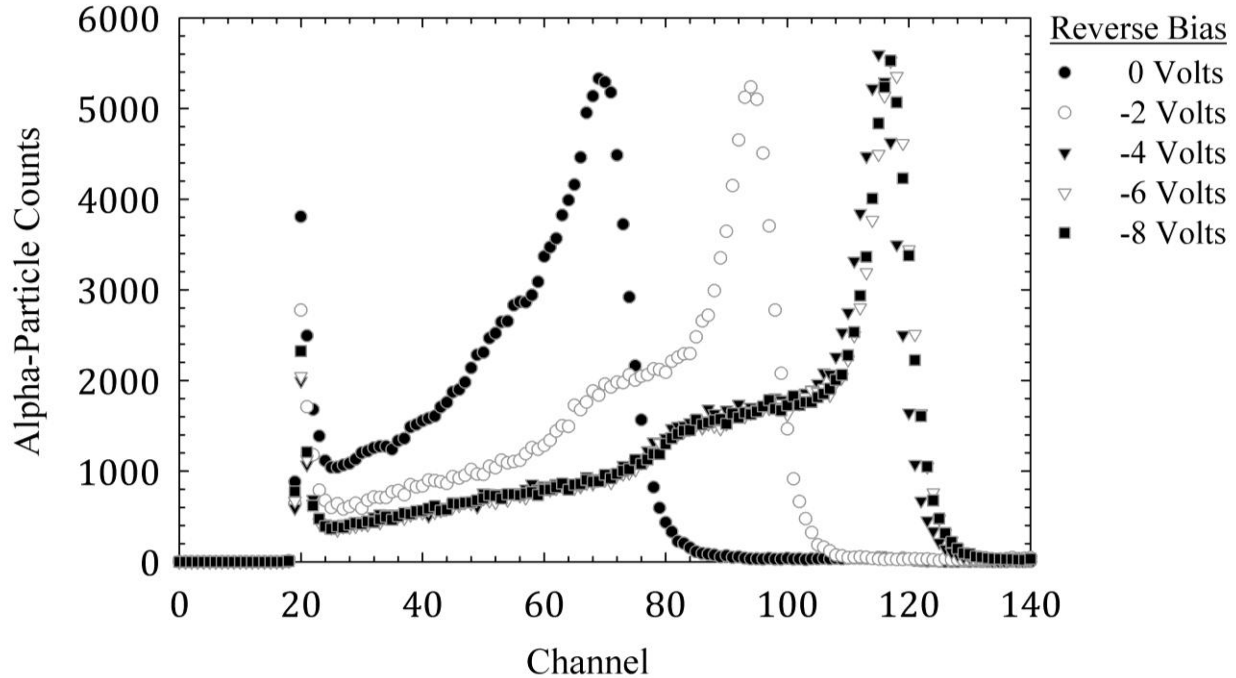

Figure 5.5: ^{241}Am alpha particle response of a conformally-diffused MSND with 200 μm deep straight trenches. The alpha source was placed at the diagonally-opposite corner of the MSND probing point placement on the diode. The square MSND area was 4-cm^2.

The lower-level discriminator was set at a level that prevented counts from the electronic noise being recorded. The peaks in the superimposed pulse-height spectra of Figure 5.5 indicate that the sensitive volume (or depletion region) is large enough to capture most of the energy of the ionizing alpha particles at 0 volts applied bias. Also notice that as the voltage on the microstructured diode is increased, the amplitude of the pulse-height distribution increases until approximately 4 volts applied bias, at which point, the amplitude remains constant for increased applied bias. This saturation of the pulse height distribution is because of three phenomena.

1. Increasing the bias voltage increases the electric field within the silicon fins of the microstructured diode, thereby reducing trapping and, hence, more of the free charge generated by the ionizing reaction ions is collected.
2. Because no metallization was applied to the top of the diode, the spreading resistance of the conformally diffused layer causes the potential to vary across the diode surface at

small voltages, thereby producing a nonuniform electric-field within the silicon fins. This effect is reduced by an increased reverse-bias voltage.

3. The amplitude effect might also be due partially to incomplete depletion within the silicon fins, an effect that also is reduced by increased reverse-bias voltage.

Notice that the second phenomenon is consistent with the spectral characteristics of the IV and CV results shown in Figures 5.3 and 5.4. In addition, directly related to the first and third phenomena, the full-width half maximum (FWHM) of the full-energy peak decreases with increasing voltage and becomes invariant at voltages above 4 volts applied bias. This constant FWHM and pulse-height shows that there is complete charge collection within the depth of the silicon microstructure fin.

5.2 MSND Thermal-Neutron Efficiency Measurements

Intrinsic efficiencies and neutron sensitivities of individual, stacked, and arrayed MSNDs were measured with thermal neutrons, fast neutrons, and a combination of both via ^{252}Cf. The experimental setup and neutron source calibration are reported here.

5.2.1 Diffracted Thermal-Neutron Beam Calibration and MSND Testing

The thermal-neutron intrinsic efficiency of a MSND was found with a 0.0253 eV diffracted neutron beam from the Kansas State University TRIGA Mark II nuclear reactor [50] (see Figure 5.6). The neutron flux was calibrated with a Reuter-Stokes ^{3}He gas-filled proportional detector.[44] Details of the ^{3}He gas-detector calibration method can be found elsewhere [70]. The size of the diffracted thermal-neutron beam was controlled by varying-sized cadmium apertures in a revolving-index assembly. The beam sizes are 1.0 mm, 2.5 mm, and 5.0 mm, 1.0 cm, and 1.27 cm. To align a neutron detector easily in the diffracted neutron beam, a LASER beam was axially centered in the beam by an out-of-beam source placement and reflection off a silicon wafer (see Figure 5.6).[45]

---

[44] Model No. P4-1603-207, Serial No. 97D05759, Pressure: 60 PSIA, High Voltage: 1300 V, see Figure 2.2.

[45] The 2200 m/s neutron absorption and scattering cross sections of silicon are small, $\sigma_{Si,abs}$ = 0.171b and $\sigma_{Si,scatt}$ = 2.167b, respectively [62].

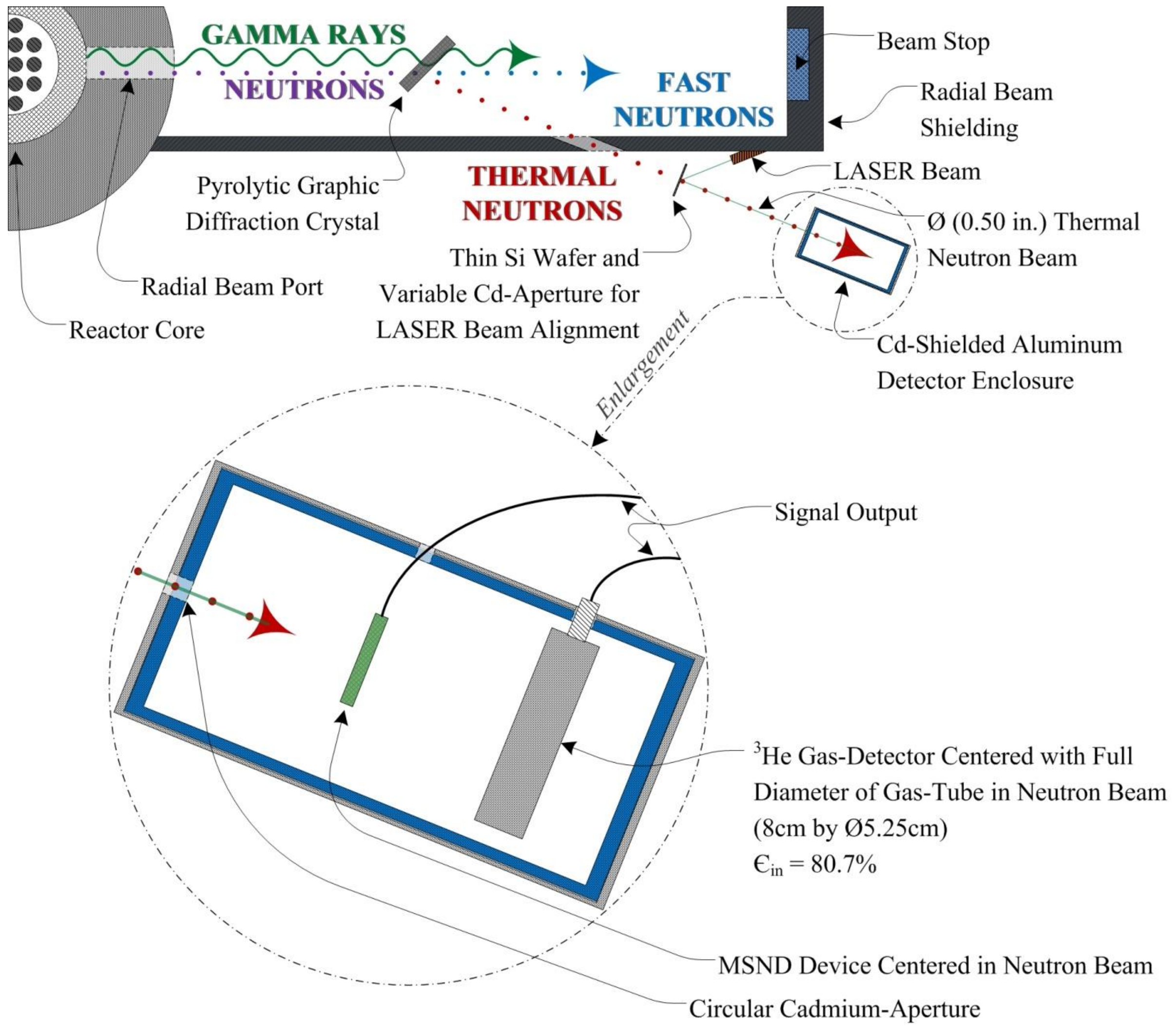

Figure 5.6: Illustration of KSU TRIGA Mark II Reactor radial-beam-port diffractometer setup for the MSND and the ^{3}He detector in the diffracted thermal-neutron beam line.

For the neutron-detection efficiency measurements of the MSND, a pulse-height spectrum was collected for a specific MSND in the diffracted neutron beam with and without a Cd shutter, so as to allow the collection of responses with and without thermal neutrons. The neutron detection efficiency $\varepsilon_{\mathrm{MSND}}$ was calculated by dividing the summed neutron counts collected from an MSND with an LLD set above the system noise level, by the thermal-neutron flux determined with a calibrated ^{3}He detector [70],

$$\varepsilon_{MSND} = \frac{\sum_{LLD} P}{\Phi\, A\, t}\ , \tag{5.1}$$

where ε_{MSND} varies by the summation of P the MSND pulses above some LLD, Φ the diffracted thermal-neutron beam flux, A the MSND active area, and t the measured count time. The neutron detection efficiency uncertainty was derived through Gaussian statistics and propagation of error. Note that if the diffracted thermal-neutron beam diameter is smaller than the active area of the MSND, then the MSND efficiency calculation is no longer dependent on the active area A, and A in Eq. (5.1) is replaced by area A_b of the beam.

5.2.2 Performance of an Individual MSND

Neutron detection performance of earlier MSND designs, e.g., circular hole and sinusoidal trench patterned designs and planar selectively-diffused diodes with in-hole-oxidation for passivation, can be found elsewhere [25-27], and, with more detail in a dissertation about these earlier MSNDs by McNeil [39]. These pervious MSNDs suffered poor signal-to-noise ratios and high leakage currents. To improve signal generation and reduce leakage current of the MSND, a microstructure conformally-diffused MSND processing technique was applied as detailed in [24]. The conformal concept was first published elsewhere by McGregor [121]. The improved signal-to-noise ratio of the pulse-height spectra for 50 µm, 100 µm, and 150 µm deep sinusoidal trench MSNDs are shown in Figures 5.7, 5.8, and 5.9, respectively, with a comparison of the conformally-diffused and selectively-diffused MSND neutron response presented in Figure 5.10. MSND ^{137}Cs and ^{60}Co gamma-ray responses for these older MSNDs can be found here [27, 39]. These MSND were ICP-RIE plasma etched with trench widths and Si fin widths ranging from 22 µm to 35 µm and backfilled with coarse ^{6}LiF powder.

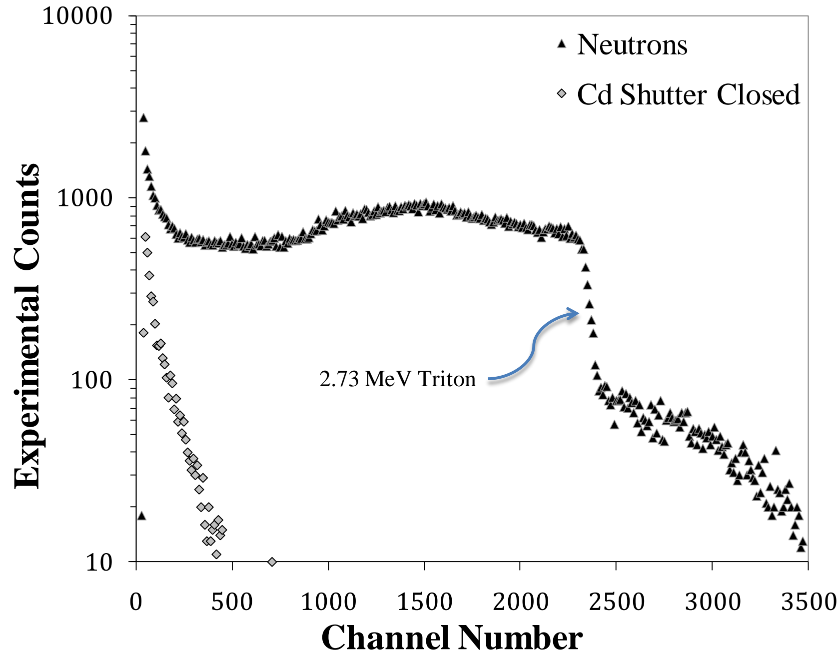

Figure 5.7: Pulse-height spectra for 50 μm deep sinusoidal etched pattern backfilled with ^{6}LiF coarse powder. At an LLD = 300 keV (channel 260), the measured thermal-neutron detection efficiency was 7.00 ± 0.02%. Sourced from [38], copyright © 2008, IEEE.

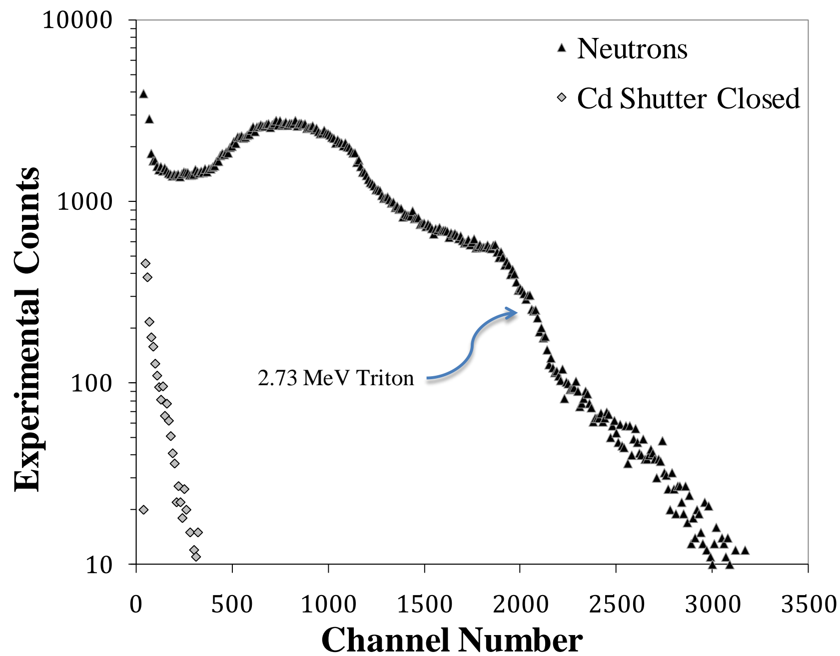

Figure 5.8: Pulse-height spectra for 100 μm deep sinusoidal etched pattern backfilled with ^{6}LiF coarse powder. At an LLD = 300 keV (channel 230), the measured thermal-neutron detection efficiency was 11.94 ± 0.03%. Sourced from [38], copyright © 2008, IEEE.

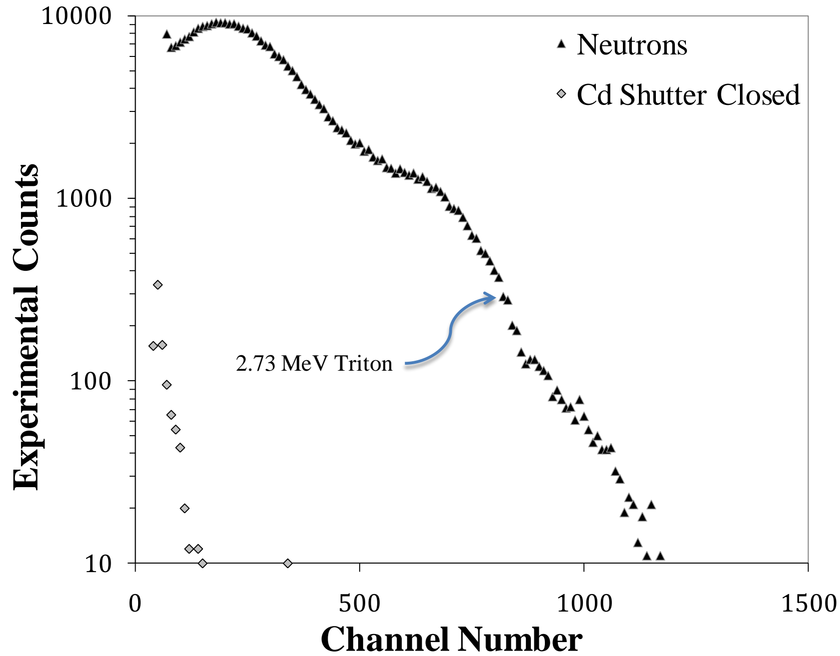

Figure 5.9: Pulse-height spectra for 150 μm deep sinusoidal etched pattern backfilled with ^{6}LiF coarse powder. At an LLD = 300 keV (channel 90), the measured thermal-neutron detection efficiency was 13.11 ± 0.03%.

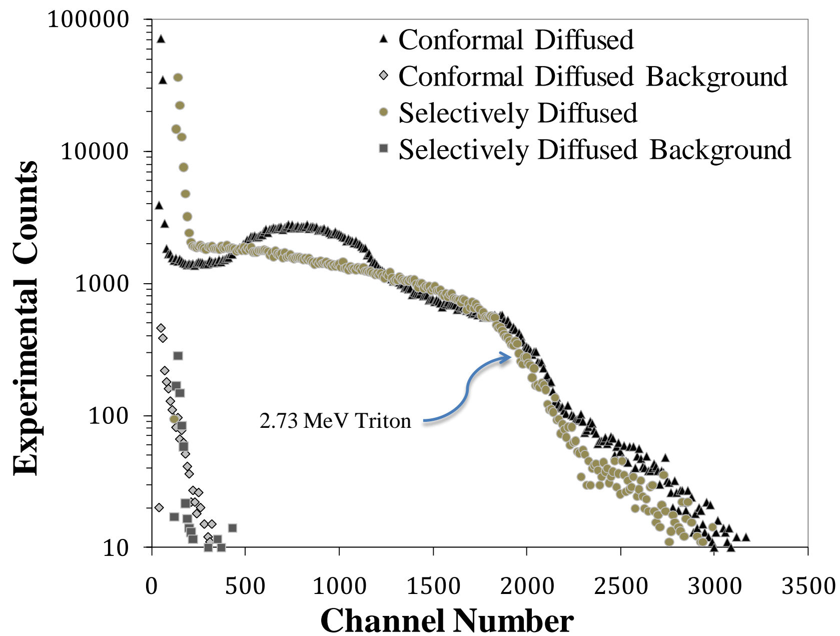

Figure 5.10: Pulse-height spectra comparison of a selectively diffused and a conformally-diffused 100 μm deep sinusoidal etched pattern backfilled with ^{6}LiF coarse powder. At an LLD = 300 keV (channel 230), the selectively and conformally-diffused MSND measured thermal-neutron detection efficiencies were 8.96 ± 0.06% and 11.94 ± 0.03%, respectively.

The intrinsic efficiencies for the thermal-neutron sensitivity of a selectively-diffused diode design and a conformally-diffused diode design resulted in measured efficiencies of 8.96 ± 0.06% and 11.94 ± 0.08%, respectively, for identical MSNDs of 28-mm^2 active-area and etched depths of 100 μm [24]. The conformally-diffused MSND collected more neutron counts than a geometrically-identical selectively-diffused MSND. The improvement provides more evidence for an increased depletion depth and larger active region in the conformally-diffused MSND over that of the selectively-diffused MSND. In addition, the pulse-height spectrum of the conformally-diffused MSND better matches the predicted pulse-height spectrum of a trench MSND shown in Figure 3.9. Continuing with the conformally-diffused diode design and increasing the depth of the silicon microstructure to 245 μm, the MSND intrinsic efficiency was increased to 20.40 ± 0.05% (see Figure 5.11) [25].

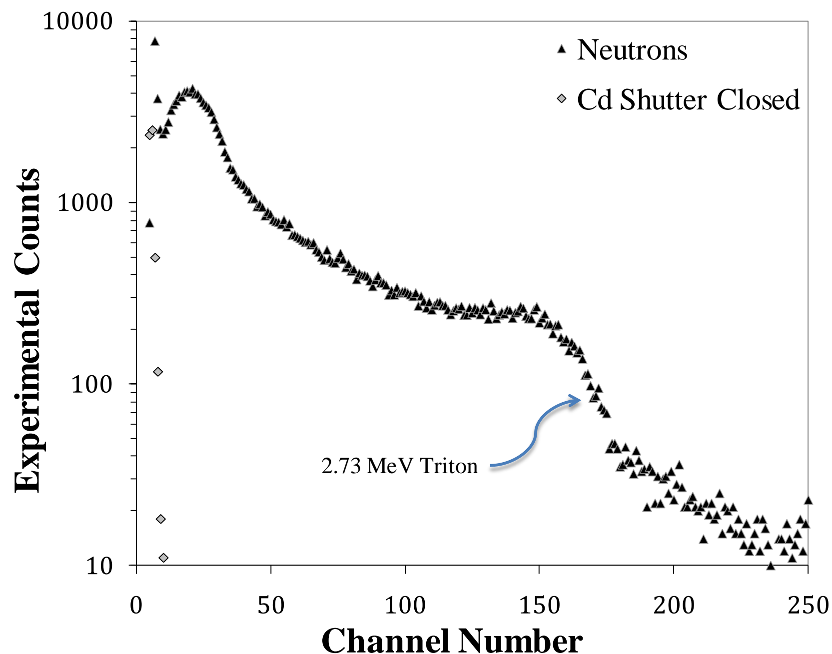

Figure 5.11: Pulse-height spectra for 245 μm deep sinusoidal etched pattern backfilled with ^{6}LiF coarse powder. At an LLD = 160 keV (channel 10), the measured thermal-neutron detection efficiency was 20.40 ± 0.05%. Sourced from [25], copyright © 2009, IEEE.

Notice that the signal-to-noise ratio has decreased for the 245-μm sinusoidal MSND, shifting the pulse-height spectrum toward the low-energy gamma-ray and electronic-noise sensitive region. Although the background noise has also shifted towards the noise floor, with numerous counts at a channel number of 10 and below, to set the LLD at 300keV (channel 19) for

improved background radiation discrimination, the detection efficiency falls to 16.16 ± 0.05%. Analysis and discussion of this spectral shift towards lower energy channels for continuously deeper MSNDs is further explored in Section 5.2.4.

Evidence for the validity of the MSND technology is demonstrated in Figure 5.12, which compares the pulse-height spectra for a thin-film coated planar diode and the conformally-diffused 100 μm deep sinusoidal-etched MSND backfilled with ^{6}LiF coarse powder. Clearly, the 100 μm MSND significantly outperforms the planar diode. The MSND has a large number of additional counts between channels 10 to 100 and five times as many counts between channels 60 to 75. Finally, the conformally-diffused MSND yielded a three times increase in the thermal-neutron detection efficiency above the common thin-film planar diode, a result that shows a clear advantage of MSND technology for neutron detection.

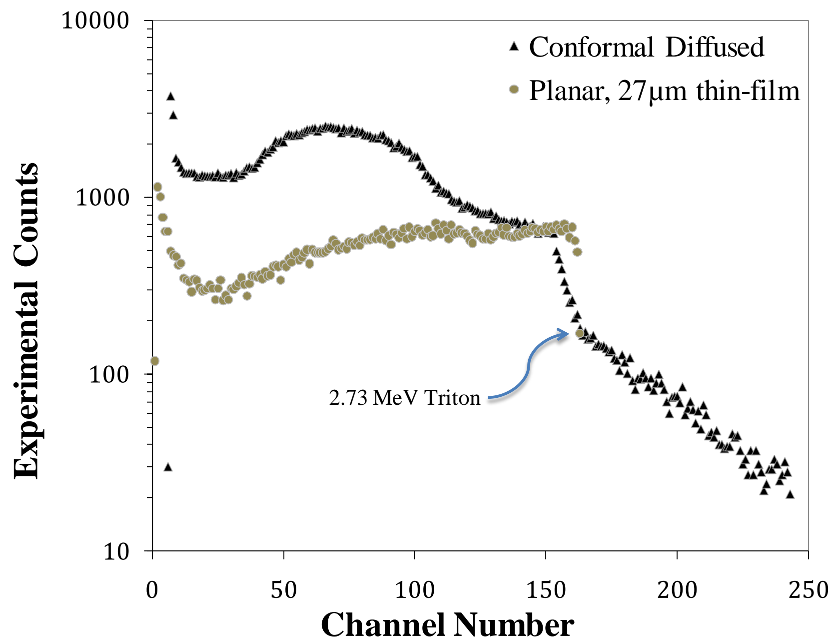

Figure 5.12: Pulse-height spectra comparison of a selectively diffused and a conformally-diffused 100 μm deep sinusoidal etched pattern backfilled with ^{6}LiF coarse powder. At an LLD = 300 keV (channel 18), the selectively and conformally-diffused MSND measured thermal-neutron detection efficiencies were 4.03 ± 0.06% and 11.94 ± 0.08%, respectively. Both MSNDs were measured in the thermal-neutron beam for 300 seconds and both have an active area of 28 mm².

The conformally-diffused 100-μm deep sinusoidal ICP-RIE etched pattern MSND was independently tested with a ^{60}Co source[46] to determine the high energy gamma-ray detection efficiency. The gamma-ray source was place exactly 1 cm away from the detector and a counting spectrum was taken. A background count was also taken to subtract any background counts and noise contributions. The gamma-ray detection efficiency was determined by dividing the source fluence into the integrated counts in the spectrum. These results were then compared to the thermal-neutron detection efficiency measured for the conformally-diffused MSND. With the LLD set at 200 keV, the gamma-ray rejection ratio was determined to be greater than 3×10^6 neutrons per gamma ray, and with the LLD set to 500 keV the gamma-ray rejection ratio is greater than 1.6×10^7 neutrons per gamma ray [70].

5.2.3 MSND Angular Response Performance

The angular responses of circular hole and sinusoidal patterned MSNDs were measured in the KSU diffracted thermal-neutron beam. Each MSND face was positioned parallel to the neutron beam, such that the MSND was at a 90 degree polar angle (see Figure 3.3). A thin-film planar-diode detector was rotated about the azimuthal axis from 0° through 180° in 10° increments. The thin-film planar-diode detector was considered a benchmark for a non-varying response in the diffracted neutron beam. Microstructured circular hole and sinusoidal trench designs were then tested for angular response using the same method and experimental arrangement as the planar-diode detector. The normalized angular responses of all three detectors are shown in Figure 5.13.

The angular response of the circular hole MSND is seen to be non-uniform with respect to the angular response of the thin-film planar-diode detector. This result was anticipated by neutrons streaming paths through the specific types of microstructured pattern designs; detailed MSND angular response simulations have been investigated in [47]. By comparison, notice that the angular response of the sinusoidal MSND approximately matches the angular response of the thin-film planar-diode detector, confirming the uniform angular response of the sinusoidal MSND design. The circular hole MSND suffered dramatic changes in neutron response over

[46] Cobalt-60 decays by releasing two high-energy gamma rays, 1.17 MeV and 1.33 MeV. The activity at the time of the experiment was 4.62 μCi.

azimuthal angular rotation because of neutron streaming. The square lattice hole pattern[47] suffers neutron streaming along the major lattice directions, 0° and 90°, and minor lattice direction, 45° (see Figure 3.3). In addition, streaming can also be expected for other geometric lattices, such as a hexagonal lattice pattern of holes at increments of 60°. The straight trench MSND is expected to follow the same trend as the circular hole MSND and lose response (detection efficiency) at an azimuthal direction of 0°, because of neutron streaming through the silicon fins.

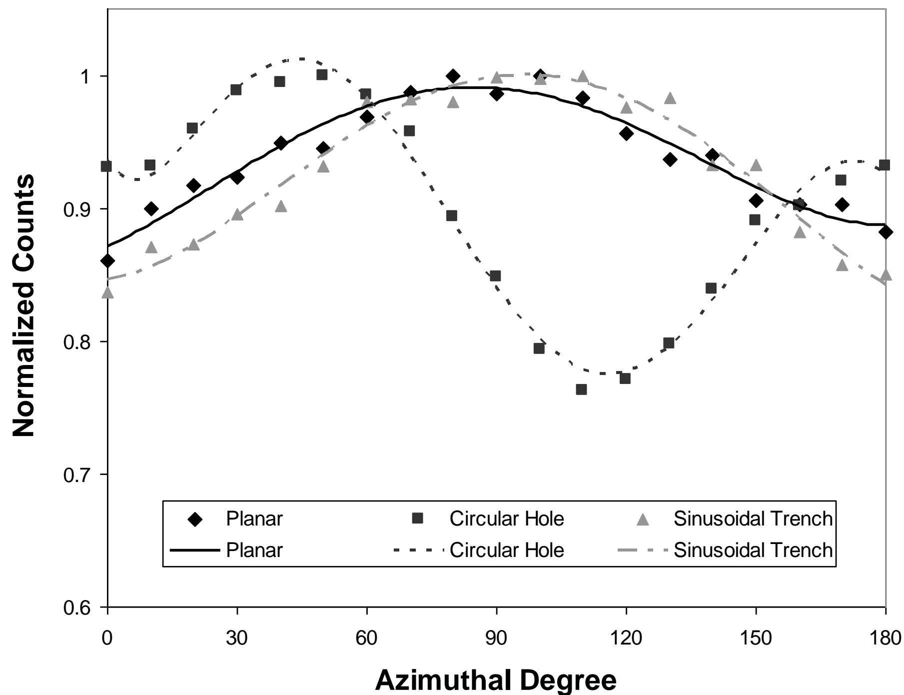

Figure 5.13: Normalized angular response of circular hole and sinusoidal trench MSNDs compared against the angular response of a thin-film planar detector. The data is fit with spline-interpolated lines. Sourced from [26], copyright © 2007, IEEE.

5.2.4 Performance of Stacked Dual-Integrated MSNDs

An important clear advantage for the MSND is the high efficiency achieved with a single MSND. Furthermore, these MSNDs can be stacked and dual-integrated into a single MSND to dramatically increase the counting efficiency of the neutron detector. An MSND with 113 μm

---

[47] Here the shape of the hole is undefined, for any shape (e.g., square hole, hexagonal hole, rhombus hole) of the hole type pattern will suffer neutron streaming at different lattice directions.

deep sinusoidal trenches achieved 12.7 ± 0.03% and dual-integrating two of these 113 μm deep MSNDs, with identical active-areas of 28 mm^2, achieved 21.0 ± 0.04% (see Figure 5.14) [25]. The sinusoidal trenches were ICP-RIE plasma etched with trench widths and Si fin widths ranging from 22 μm to 35 μm[48] and backfilled with coarse ^{6}LiF powder. The improved fabrication design with *pn* junctions diffused within the microstructures has lowered the leakage current and improved the pulse-height signal from the stacked MSNDs. The dual-integrated MSND operates on 1 volt of reverse bias. Notice that the pulse height spectrum is slightly different from a single 100 μm MSND and appears more like the 245 μm MSND. The spectrum shows a downward shift of the pulse height signal from the detector. This shift is likely because of an overall increase in capacitance of the dual-integrated MSNDs, hence reducing the pulse height signal from the stacked detector.

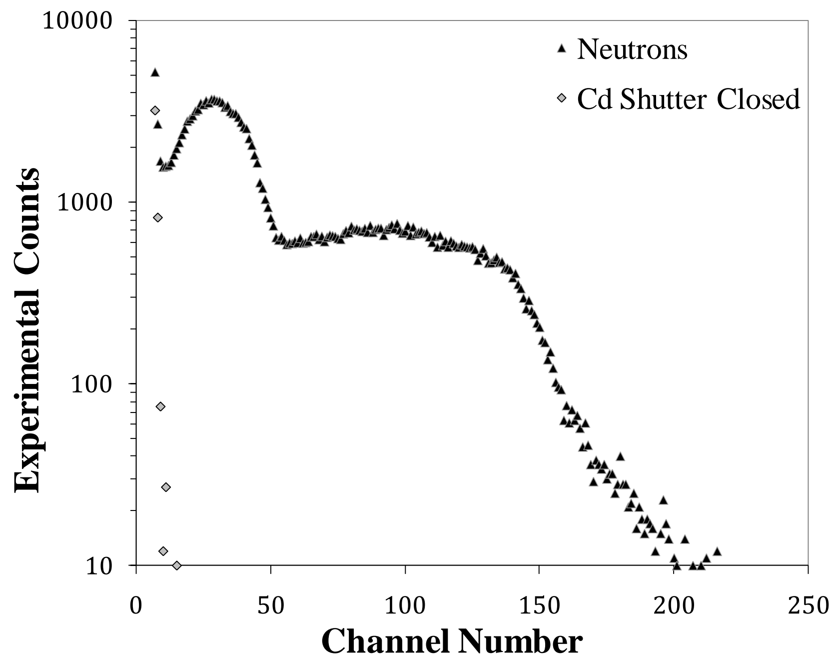

Figure 5.14: Pulse-height spectra for dual-integrated 113 μm deep sinusoidal etched pattern backfilled with ^{6}LiF coarse powder. At an LLD = 15 Chn, the measured thermal-neutron detection efficiency was 21.0 ± 0.04%. Sourced from [25], copyright © 2009, IEEE.

[48] The varying trench and Si fin widths are because the sinusoidal shapes do not fit uniformly together because of the sine shape of the microstructures. See Figure 4.2 for visual representation.

To improve further the neutron detection efficiency, individual MSND chips were increased in size to 1 cm^2 and ICP-RIE plasma etched with a straight trench pattern with trench width and Si fin widths of 25 μm to a depth of 250 μm and backfilled with coarse ^6LiF powder. The dual-integrated neutron counting efficiency was measured for a stacked MSND configuration of two 250-μm deep MSND chips. The dual-integrated MSND operated with 4 volts of reverse bias. The combined leakage current for the 1-cm^2 dual-integrated MSND was 800 nA/cm^2 (see Figure 5.1). In Figure 5.15, the pulse-height spectrum of the dual-integrated MSND shows many more counts than for any previously reported single or dual-integrated MSNDs (see Figure 5.14) [25]. Notice that the pulse-height spectrum shows a downward shift of the pulse-height signal from the stacked and deep-etched MSND. Some of this shift may be because of an overall increase in capacitance of the stacked MSND, thereby reducing the pulse-height signal from the detector. However, a similar pulse-height shift towards the low-energy region was observed with continuously deeper etch microstructures (see Section 5.2.2). With the Cd shutter closed the gamma-ray component was negligible at a LLD setting above channel 11. With the LLD set to channel 11 (375 keV) the intrinsic efficiency was measured to be $34.01 \pm 0.05\%$. Ultimately, deeper microstructured trenches and dual-integrated MSNDs show a reduction in pulse-height, which can decrease the n/γ rejection ratio. Note that the gamma-ray interactions within the MSND also diminish with deeper microstructures (as a result of a smaller interaction volume), thereby, permitting lower LLD settings, and a superior gamma-ray discrimination, which has been previously shown to be 3×10^{-6} n/γ at an LLD of 500 keV [70].

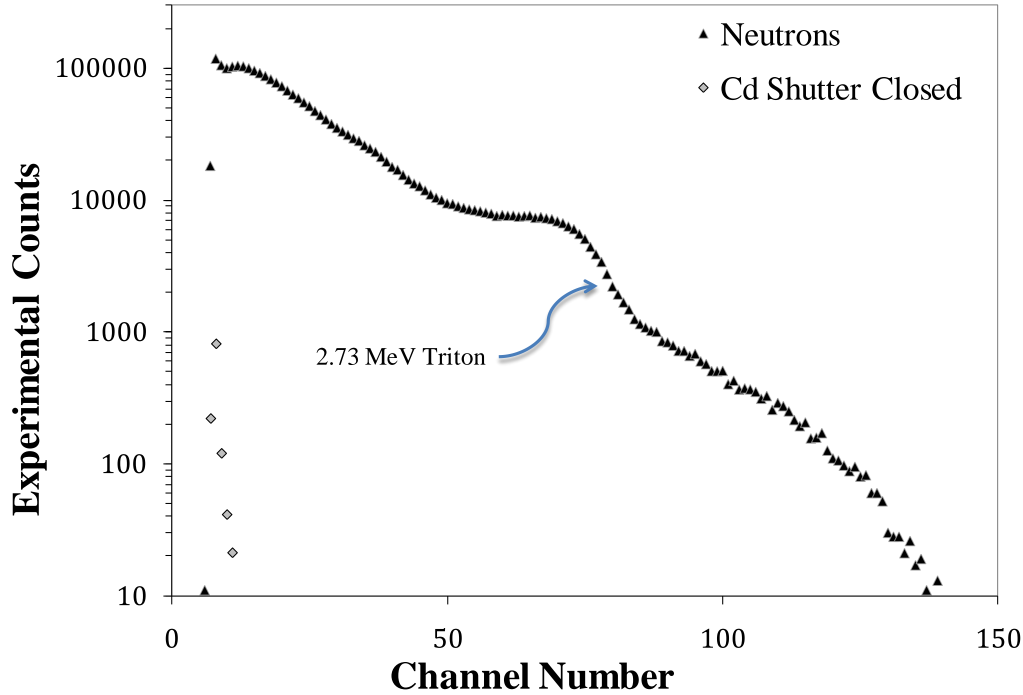

Figure 5.15: Pulse-height spectrum from conformal-diffused diode dual-integrated detector with 250 μm deep straight trench microstructures, showing response with and without (Cd shutter closed) neutrons. The preamplifier electronic signal integration time was set at 2 μs. At an LLD = 11 Chn (375 keV), the measured thermal-neutron detection ε_{tn} was 34%.

To better understand why the pulse-height spectrum of deep microstructured MSNDs shift to lower energies, a simulation was created using the *Silvaco* TCAD software package [122] to study the electric fields generated by the conformal diffusion process, how these electric fields move charge through the Si microstructure fins, and the time-response of a signal pulse. An earlier version of the simulation model is presented in [39], whereas this work expands on the earlier model by investigating the variable trench depths and 25 μm Si fin widths. *Silvaco* TCAD is a set of software packages commonly used in industry for semiconductor device modeling. The TCAD software calls on the ATLAS and ATHENA tools bundled in the TCAD package as Poisson solvers for semiconductor device physics and time-transient device simulations. The model geometry specifications were defined to mimic a shallow (1-μm) boron diffusion within the MSND microstructure, thereby, creating a conformal *pn* junction diode within the microstructures. The bulk silicon resistivity was 10 kΩ-cm with *n*-type phosphorus background dopant. A 3-dimensional portion of a microstructured Si diode was constructed with trench

depths of 100 μm and 250 μm and a potential solution was obtained for 1 V, 4 V, 10 V, and 50 V reverse bias. The electric potential solutions within 100 μm, 250 μm, and 350 μm deep trench MSNDs are shown in Figures 5.16, 5.17, and 5.18, respectively. In the case of small voltages of 1 V and 4 V, the electric field is distributed within the silicon fin. Now notice that there is a greater potential gradient below the trench microstructure rather than in the Si fin for applied reverse biases of 10 V and 50 V. Additionally, the 350-μm MSND shows very little electric field potential gradient development in the Si fin beyond 1 V.

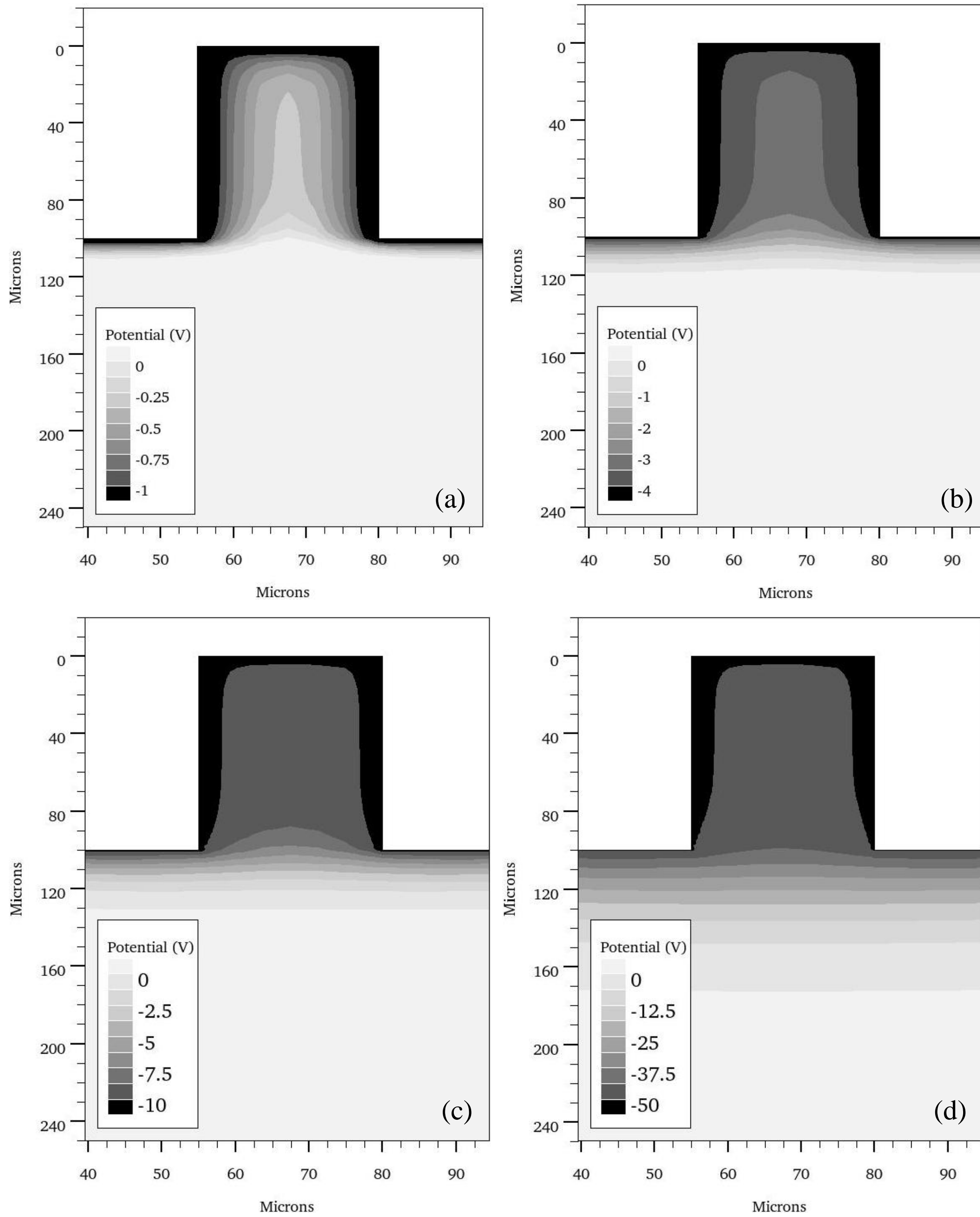

Figure 5.16: Modeled electric potential solution within conformally-diffused 100 μm deep trench MSND. Each plot key describes the electric potential gradient within the Si fin for (a) -1 V, (b) -4 V, (c) -10 V, and (d) -50 V of applied bias.

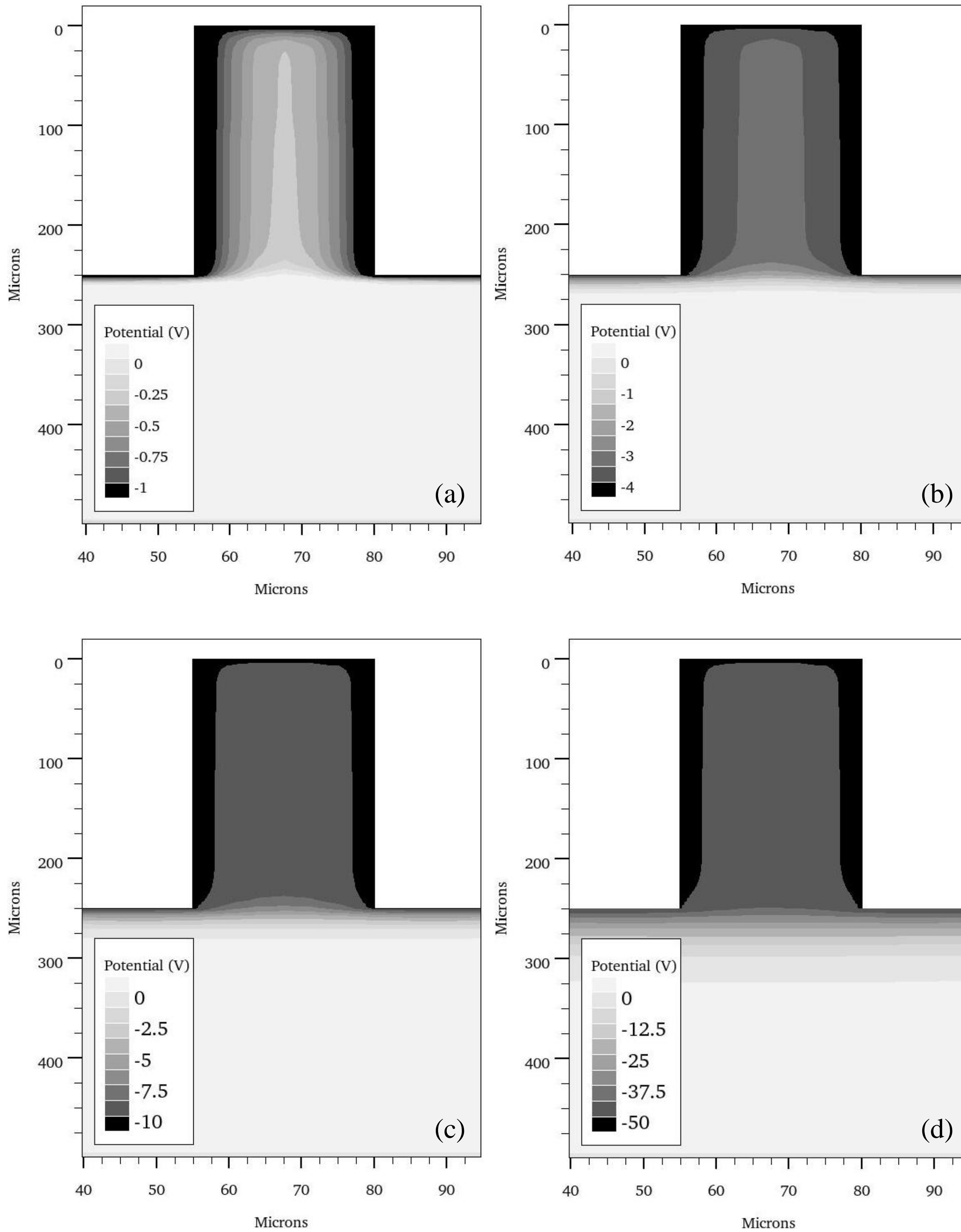

Figure 5.17: Modeled electric potential solution within conformally-diffused 250 µm deep trench MSND. Each plot key describes the electric potential gradient within the Si fin for (a) -1 V, (b) -4 V, (c) -10 V, and (d) -50 V of applied bias.

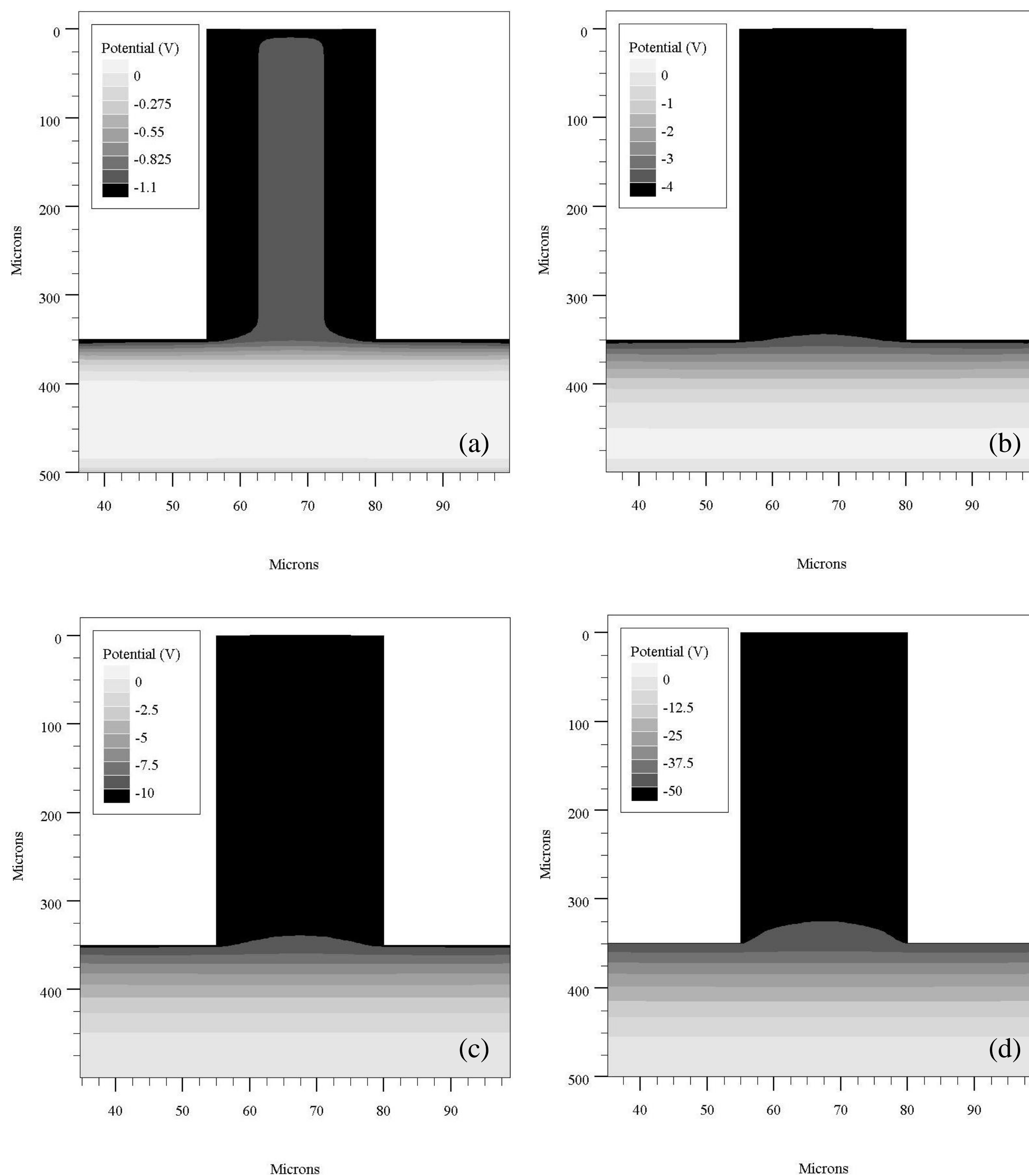

Figure 5.18: Modeled electric potential solution within conformally-diffused 350 μm deep trench MSND. Each plot key describes the electric potential gradient within the Si fin for (a) -1 V, (b) -4 V, (c) -10 V, and (d) -50 V of applied bias.

To better understand how the weak electric field affects MSND signal induction, a transient solution of current versus time was modeled. Within the diode structure, a single-event-upset was defined as a cloud,[49] 30-μm by 10-μm diameter cylinder, of electron-hole pairs centered midway between the Si fin and at a starting depth of 5 μm from the top surface of the MSND in all three model variations. The amount of charge defined in the simulation was representative of the number of electron-hole pairs generated from the kinetic energy capture from the triton in a 25 μm Si fin (1.23 MeV).[50] A time-transient solution was obtained, which revealed the current appearing at the top electrode of the MSND as a function of time.

This simulation of charge transport is not intended to determine an absolute response for the MSND. There are many variables that affect the total signal that is induced and observed, e.g., charge trapping, charge recombination, and a varying electric potential of the diode because of spreading resistance of the conformal diffusion. The simulation was developed to investigate the relative differences in MSND signal behavior between shallow and deep trench depth geometries. Even though the silicon material is depleted of charge carriers in the Si fins, the electric field gradient is only established at the bottom of the fin microstructure, as depicted in Figures 5.16 and 5.17. As a result, the ionization charge cloud developed in the Si fin stagnates and slowly moves along the weak electric potential. With the *p*-type junction layer surrounding the developed charge cloud on three sides, the holes are quickly drawn to the *p*-type conformal conductive-layer, inducing a charge on the biasing electrode. Conversely, the electrons slowly diffuse toward the ground electrode until the high electric field region is reached, at which point they are quickly drawn out, inducing the rest of the charge signal. Additionally, an earlier investigation of single-event-upset charge collection with thicker Si fin and shallower trench microstructures was performed by McNeil, [39] in which he simulated a time-lapsed report of the ionized charge as it moves through the weak electric field within the Si fins.

As the microstructure trenches are etched deeper from 100 μm to 250 μm, the charge current flow within the Si fins is prolonged. In the case of 250 μm deep trench microstructures, it takes

---

[49] The outward diffusion of the charge cloud, from a reaction-product particle ionization track, becomes broad very rapidly. As such, the timescale of the drifting charge to produce a signal pulse, the transition from a track-like shape to a diffuse cloud, appears nearly instantaneous. As a result, there is no need to define the shape of the ion track specifically; therefore, the charge cloud was defined generically as a cylinder with entry and exit points and a radius in the Si fin.

[50] As calculated by TRIM [119]. The average energy to generate an electron-hole pair in Si is 3.6 eV, therefore, 3.42×10^5 charge pairs were generated. This amount of charge pairs was used for the single-event-upset simulation.

10 microseconds to collect most of the signal pulse from the MSND (see Figure 5.19). Furthermore, for the 350 μm deep trench microstructures, it takes well beyond 10 microseconds to collect an entire signal pulse from the MSND. Therefore, the electronic signal integration time for the dual-integrated 250 μm MSND of 2 microseconds was insufficient to integrate the charge signal. The single-event-upset transient solutions of the MSNDs, i.e., current versus time, demonstrates that microstructured trenches etched deeper than 100 μm have slow charge migration times. *Silvaco* TCAD input code for these models is given in 0.

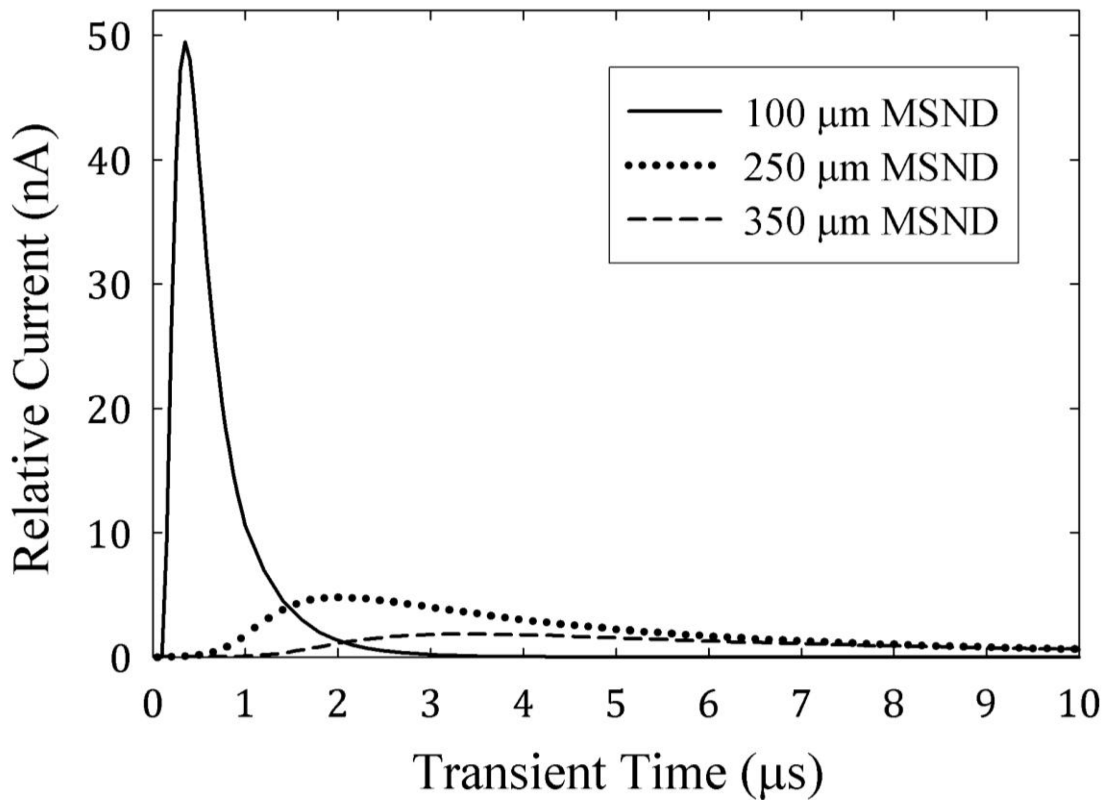

Figure 5.19: Modeled transient solution of current versus time within 100-μm, 250-μm, and 350-μm deep straight trench MSNDs. The silicon fin is 25 μm in width and is the same modeled geometry and potential field as shown in Figures 5.16, 5.17, and 5.18.

5.2.5 Improved Performance of Stacked Dual-Integrated MSND

After it was understood that the downward shift of the pulse-height spectrum of the 1-cm^2 area and 250 μm deep straight-trench dual-integrated MSND was because of slow charge

migration within the Si fins, the preamplification charge integration time was increased from 2 μs to 10 μs. A pulse-height spectrum was collected from the stacked dual-integrated MSND with longer charge integration time in the diffracted neutron beam with and without a beam blocking Cd shutter so as to allow the collection of responses with and without thermal-neutrons (see Figure 5.20). Prompt gamma-rays emitted from the thin Cd shutter appear in the spectrum as numerous pulses at low energy near the noise floor of the detector system. Additionally, because the neutron beam is not purely thermal neutrons [50], some epi-thermal and fast neutrons are not absorbed in the Cd shutter and are measured by the MSND.

The dual-integrated MSND again operated on 4 volts of reverse bias. Notice in Figure 5.20 that the old preamplifier design pulse-height spectrum was shifted to lower channels, but by increasing the preamplifier charge integration time to 10 μs for the same MSND, the pulse-height spectrum has shifted to higher channels, away from the noise/gamma-ray floor. In addition, the MSND exhibits the expected spectral shape predicted in Section 3.3 and elsewhere [46]. Similar to the other tested MSNDs with the Cd shutter closed [25], the gamma-ray component was negligible at an LLD setting above channel 11 for the 2 μs signal integration time design and channel 15 for the 10 μs signal integration time design. As detailed earlier in Section 5.2.4, the intrinsic efficiency for the 2 μs signal integration time design was measured to be 34.01 ± 0.05%, with the LLD set to channel 11 (375 keV). For the 10 μs signal integration time design, with the LLD set to channel 15 (300 keV), the intrinsic efficiency was measured to be 42.22 ± 0.06%. For the 10-μs signal integration time design, with the LLD set to channel 22 (450 keV), the intrinsic efficiency was measured to be 36.02 ± 0.05%. With the increase in charge collection time to 10 μs, the dual-integrated MSND has increased in intrinsic neutron detection efficiency by five percentage points; a substantial gain for the conformally-diffused stacked MSND.

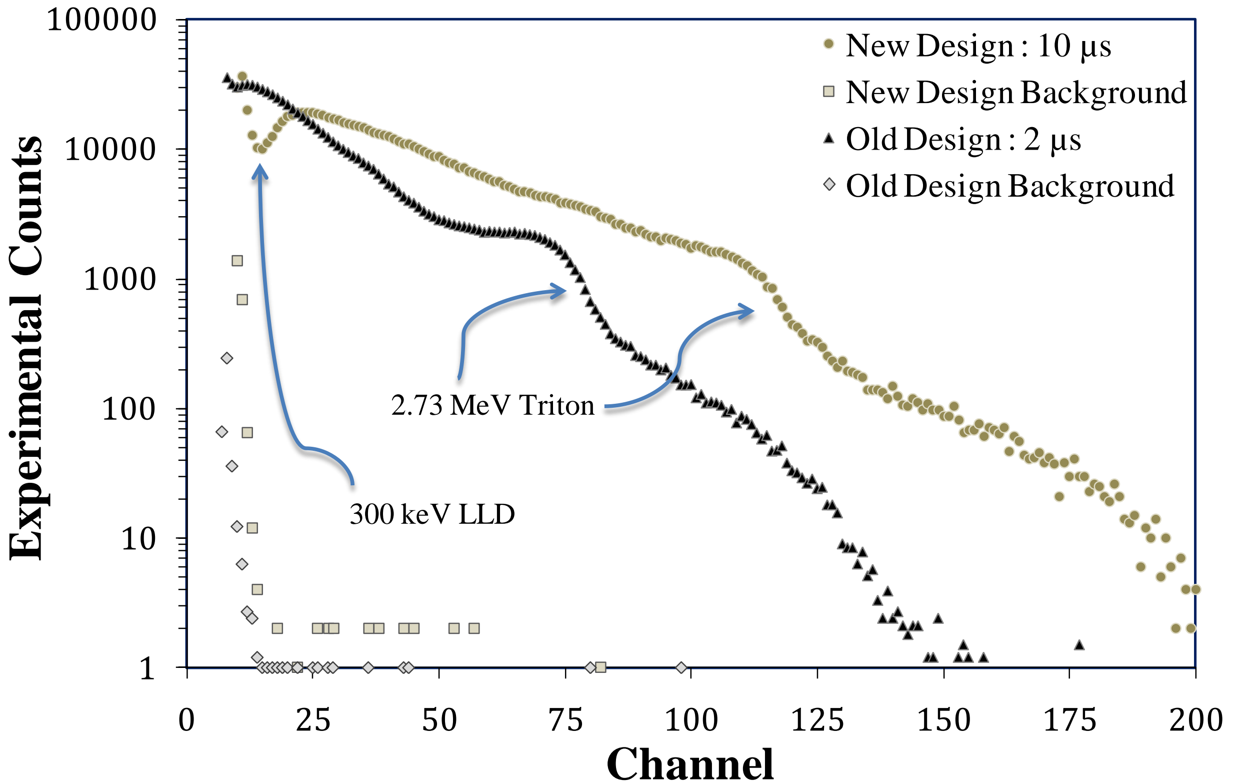

Figure 5.20: Pulse-height spectra comparison of the previous 2-μs charge integration-time preamplifier old design versus the improved 10-μs charge integration-time preamplifier new design for the dual-integrated 250 μm deep straight trench microstructure backfilled with ^{6}LiF. At an LLD = 15 Chn (300 keV), the measured thermal-neutron detection ε_{tn} was 42% for the 10 μs charge integration-time preamplifier design. Sourced from [21], copyright © 2010, IEEE.

5.2.6 Gamma-Ray Discrimination Performance for the Dual-Integrated MSND

The actual gamma-ray flux with the Cd shutter in place was not measured; however, the stacked MSND described in Section 5.2.5 was independently tested with a ^{137}Cs source with an activity of 73.1 mCi, to determine the gamma-ray detection efficiency, i.e., rejection ratio. The gamma-ray source was place 50 cm away from the detector and a counting spectrum was taken. A background count was also measured to subtract any background counts and noise contributions. The gamma-ray detection efficiency ε_{γ} was calculated by Eq. (5.2),

$$\varepsilon_\gamma = \frac{\sum_{LLD} P_\gamma}{\Phi_\gamma\, A\, t} \,, \tag{5.2}$$

where ε_γ varies by the summation of P_γ the MSND pulses above some LLD, Φ_γ the gamma-ray source flux through the detector which was 86,021 γ cm^{-2} s^{-1}, A the MSND active area, and t the measured count time. The gamma-ray source fluence through the detector was calculated by Eqs. (5.3) and (5.4) [6],

$$\Omega_{MSND} = 4\arctan\left(\frac{\varepsilon}{\eta\sqrt{\varepsilon^2+\eta^2+1}}\right),\ \varepsilon = \frac{Width}{Length},\ \eta = \frac{2(Dist.From\,Source)}{Length} \,, \tag{5.3}$$

where the fractional solid angle, Ω_F, is used to determine the probability of a neutron or gamma-ray intersecting the detector,

$$\Omega_F = \frac{\Omega_{MSND}}{4\pi\ str.} \,. \tag{5.4}$$

The neutron to gamma-ray rejection ratio n/γ was determined by Eq. (5.5),

$$\frac{n}{\gamma} = \frac{\varepsilon_{MSND}}{\varepsilon_\gamma} \,, \tag{5.5}$$

where n/γ rejection ratio varies by ε_{MSND} the MSND neutron detection efficiency and ε_γ the MSND gamma-ray detection efficiency.

The gamma-ray pulse-height spectrum of the stacked 1-cm^2 MSND is shown in Figure 5.21. Notice that the response of the dual-integrated detector is relatively equivalent to that of the Cd-shutter detector response. From Figure 5.22, with the LLD set at 300 keV (channel 15), the gamma-ray detection efficiency was determined to be greater than 1.87 x 10^{-5} measured-event per gamma ray, with a n/γ rejection ratio of 2.20 x 10^4 neutrons per gamma ray, and with the LLD set to 450 keV (channel 22) the gamma-ray detection efficiency is greater than

3.49×10^{-7} measured-event per gamma ray, with a *n/γ* rejection ratio of 1.00×10^{6} neutrons per gamma ray. These data are summarized in Table 5.1. Also notice in Figure 5.22, that the n/γ rejection ratio is almost constant past LLD channel 35, because only a few counts were recorded above this channel. In addition, because the *n/γ* rejection ratio is inversely proportional to the gamma-ray detection efficiency, which goes to zero at channel 98 at which the *n/γ* rejection ratio becomes infinite.

Deeper microstructured trench MSNDs show a slight reduction in pulse-height, which can decrease the gamma-ray rejection ratio. Yet, the gamma-ray interactions within the MSND also diminish with deeper perforations (because of a smaller interaction volume), thereby, allowing smaller LLD settings and superior gamma-ray discrimination. The stacked MSND demonstrates a smaller gamma-ray rejection ratio than the ^{60}Co results presented in Section 5.2.2. This change is likely because of the smaller photon interaction cross-section for Si with the higher energy ^{60}Co gamma rays (see Figure 3.2), hence fewer ionization events occur in the bulk silicon per gamma ray passing through the MSND. Also, the stacked MSND has more bulk silicon because there are two detector chips, in which a high-energy photon can interact. The stacked MSND gamma-ray response measurement was performed in the KSU reactor bay, which has a higher background of neutrons than natural background (0.0134 n cm^{-2} s^{-1} [124]). Thus, some higher-energy measured events may be because of background neutron radiation. Note that this reactor background also applies to the case for the background spectrum of the ^{3}He gas detector shown in Figure 5.35, which indicates background neutron interactions at a rate of 0.060 n cm^{-3} s^{-1}, for the 8-cm by 5.25-cm diameter active-volume ^{3}He tube.

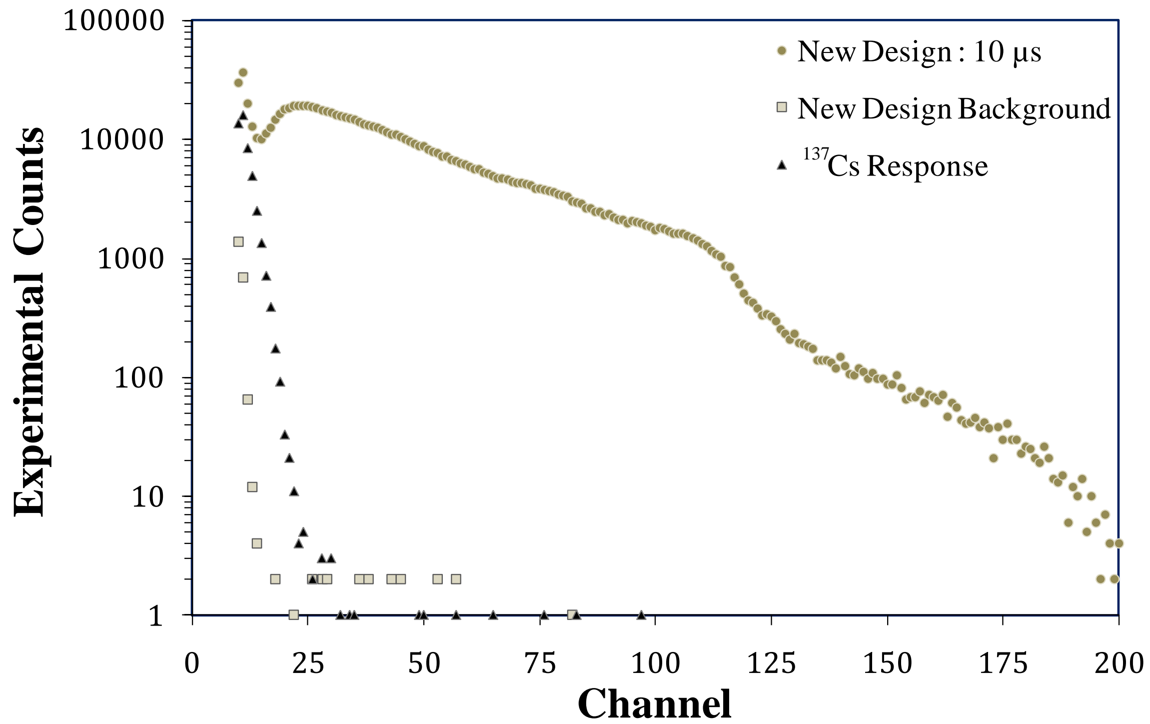

Figure 5.21: Measured ^{137}Cs gamma-ray irradiation (Ω_F = 3.18 x 10^{-5}) and neutron irradiation pulse-height spectral features for the dual-integrated neutron detector with the 10-µs signal integration time design.

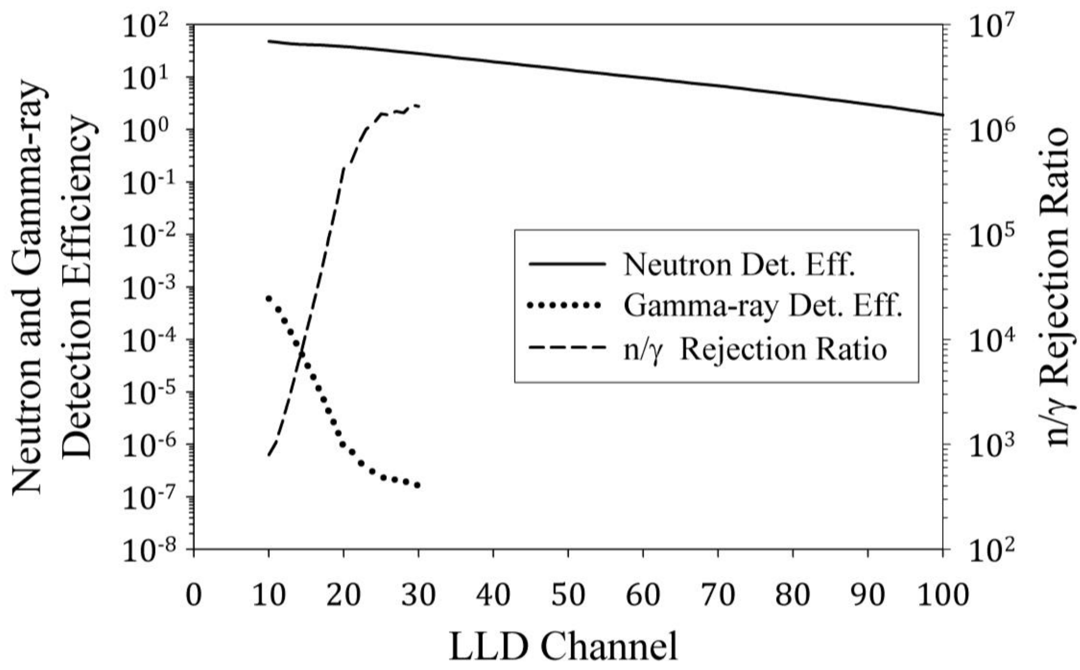

Figure 5.22: Comparison of the measured neutron detection efficiency, the measured ^{137}Cs gamma-ray detection efficiency, and the n/γ rejection ratio of the stacked 1-cm^2 MSND.

Table 5.1: Stacked MSND thermal-neutron (ϵ_{th}) and ^{137}Cs gamma-ray (ϵ_{γ}) detection efficiencies and neutron to gamma-ray rejection ratio (n/γ) for a specified LLD.

LLD (Chn)	ϵ_{th}	ϵ_{γ}	**n/γ**
15	42.2%	1.87×10^{-3} %	2.20×10^{4}
22	35.8%	3.49×10^{-5} %	1.00×10^{6}

5.2.7 Performance of 4-cm^2 Large-Area Individual and Stacked MSNDs

A pulse-height spectrum was collected from an individual 4-cm^2 MSND with a 10-μs charge integration time in the diffracted neutron beam with and without a beam blocking Cd shutter so as to allow the collection of responses with and without thermal-neutrons (see Figure 5.23). Additionally, because the neutron beam is not purely thermal neutrons [50], some epi-thermal and fast neutrons are not absorbed in the Cd shutter and are measured by the MSND. The 4-cm^2 MSND operated on 1 volt of reverse bias. The straight trench microstructure pattern was ICP-RIE plasma etched with trench widths and Si fin widths of 30 μm to a depth of 200 μm, conformally-diffused, and backfilled with nano-sized ^{6}LiF powder. Notice in Figure 5.23 that the pulse-height spectrum is significantly separated from the noise/gamma-ray floor. Even though the MSND is 2 times larger than the stacked 1-cm^2 MSNDs, the charge collection is still complete and, thus, forms large distinguishable neutron interaction pulses. In addition, the MSND exhibits the expected spectral shape predicted in Section 3.3 and elsewhere [46], with a pulse-height frequency dip at low energy.

For the 4-cm^2 large-area MSND design, with the LLD set to channel 25, just above the majority of the background signal, the intrinsic efficiency was measured to be 16.33 ± 0.09%. For the MSND design, with the LLD set to channel 32, the intrinsic efficiency was measured to be 15.94 ± 0.09%. Notice that by increasing the LLD from channel 25 to 32, the thermal-neutron detection efficiency only decreased by 0.39% in efficiency. This dip in the pulse height distribution in the low energy region is vitally important for retaining neutron detection efficiency while discriminating background radiation.

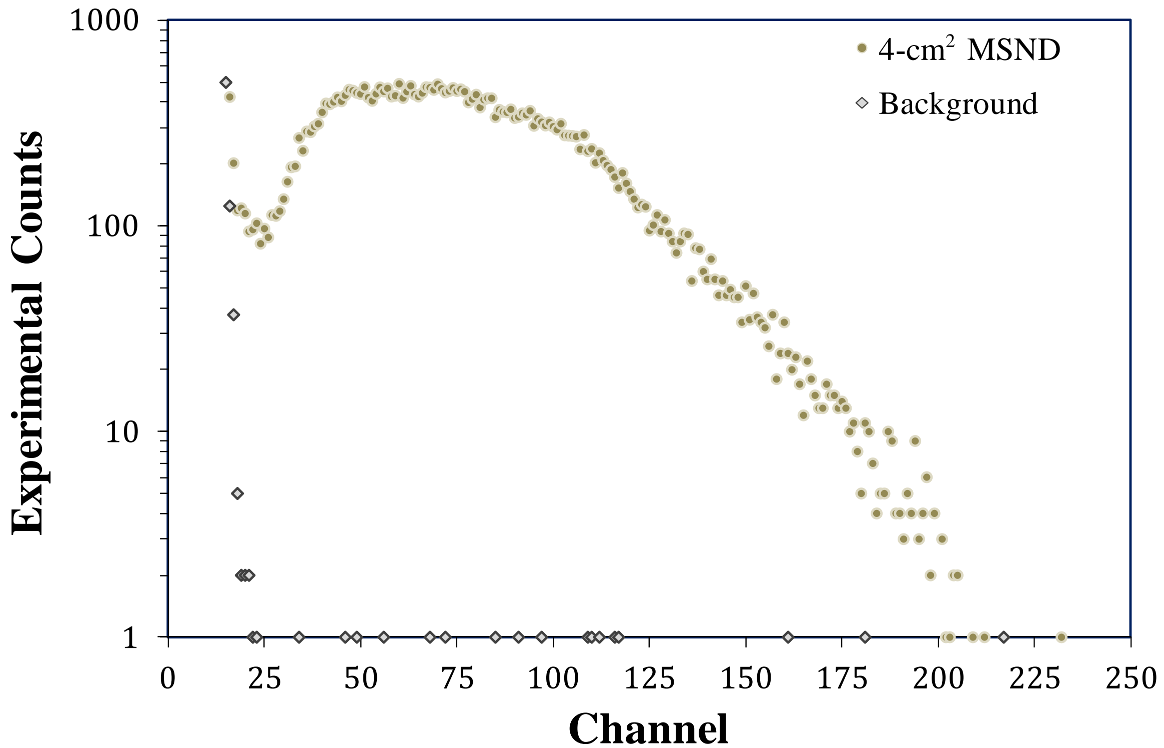

Figure 5.23: Pulse-height spectra for the individual 4-cm^2 MSND with 200 μm deep, straight trench microstructures backfilled with ^{6}LiF. At an LLD = 25 Chn, the measured thermal-neutron detection was 16.3% and at an LLD = 32 Chn, the measured thermal-neutron detection was 15.9%.

To further improve neutron detection efficiency, individual 4-cm^2 large-area MSND chips were stacked back-to-back, as was done with early generation 1-cm^2 MSNDs (see Figures 4.30 and 4.31). Dual-integrated neutron counting efficiency was measured for a stacked MSND configuration of two 200 μm deep, 4-cm^2 area, MSND chips. The dual-integrated MSND operated with 1 volt of reverse bias. The combined leakage current for the 4-cm^2 dual-integrated MSND was 78 nA (see Figure 5.3). In Figure 5.15, the pulse-height spectrum of the dual-integrated MSND shows many more counts than previously reported single and dual-integrated MSNDs [28] (see Figure 5.14). Notice that the pulse-height spectrum shows a downward shift of the pulse-height signal from the individual 4-cm^2. Some of this shift may be because of an overall increase in capacitance of the stacked MSND, thereby reducing the pulse-height signal from the detector. For the stacked configured 4-cm^2 large-area MSND design, with the LLD set to channel 18, just above the majority of the background signal, the intrinsic efficiency was measured to be 32.39 ± 0.16%. In addition, with the LLD set to channel 28, the intrinsic efficiency was measured to be 28.99 ± 0.14%.

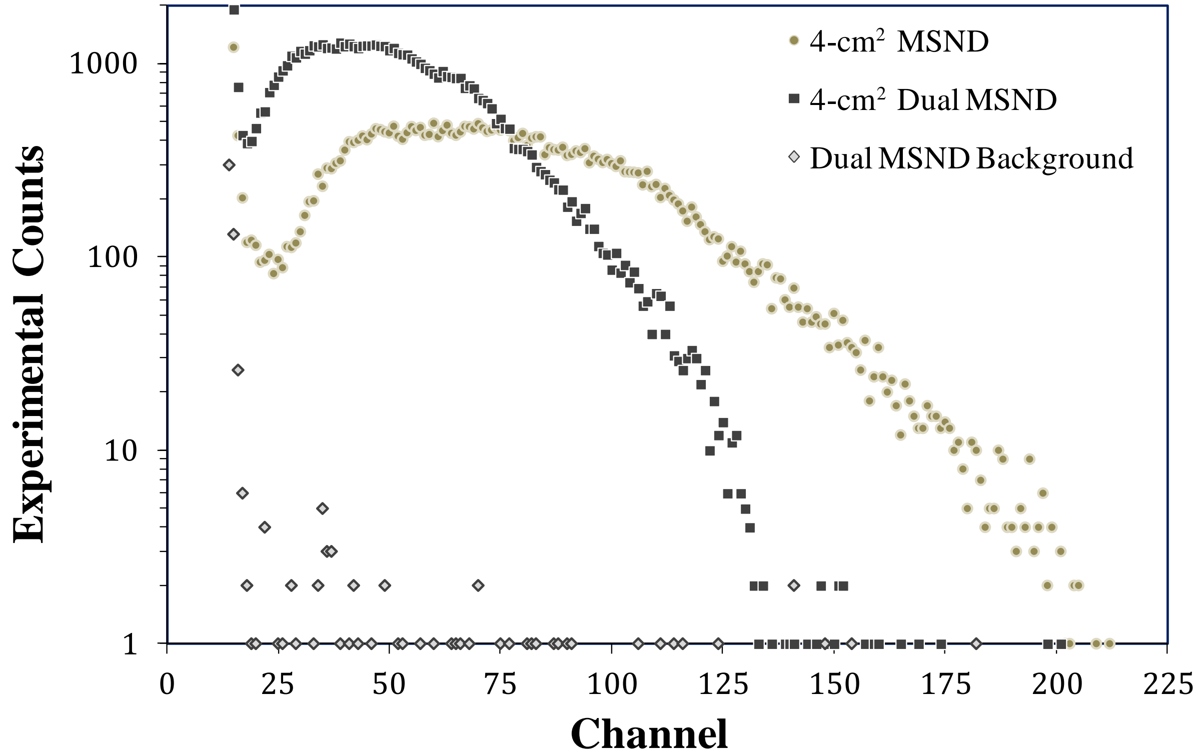

Figure 5.24: Pulse-height spectra comparison for the individual and stacked 4-cm² MSND with 200 μm deep, straight trench microstructures backfilled with ⁶LiF. At an LLD = 18 Chn, the measured thermal-neutron detection efficiency was 32.4%, and at an LLD = 28 Chn the measured thermal-neutron detection efficiency was 29.0%.

5.2.8 Gamma-Ray Discrimination for the 4-cm² Large-Area MSNDs

The individual and stacked 4-cm² large-area MSNDs were independently tested with a ^{137}Cs source with an activity of 71.69 mCi, to determine the gamma-ray detection efficiency, i.e., rejection ratio. The gamma-ray source was placed 50 cm away from the detector and a counting spectrum was taken. A background count was also taken to subtract any background counts and noise contributions. The gamma-ray rejection ratio was determined by dividing the integrated gamma-ray counts in the measured spectrum by the source fluence through the 4-cm² detector, which was calculated with Eqs. (5.3) and (5.4). The gamma-ray pulse-height spectrum response is shown in Figure 5.25.

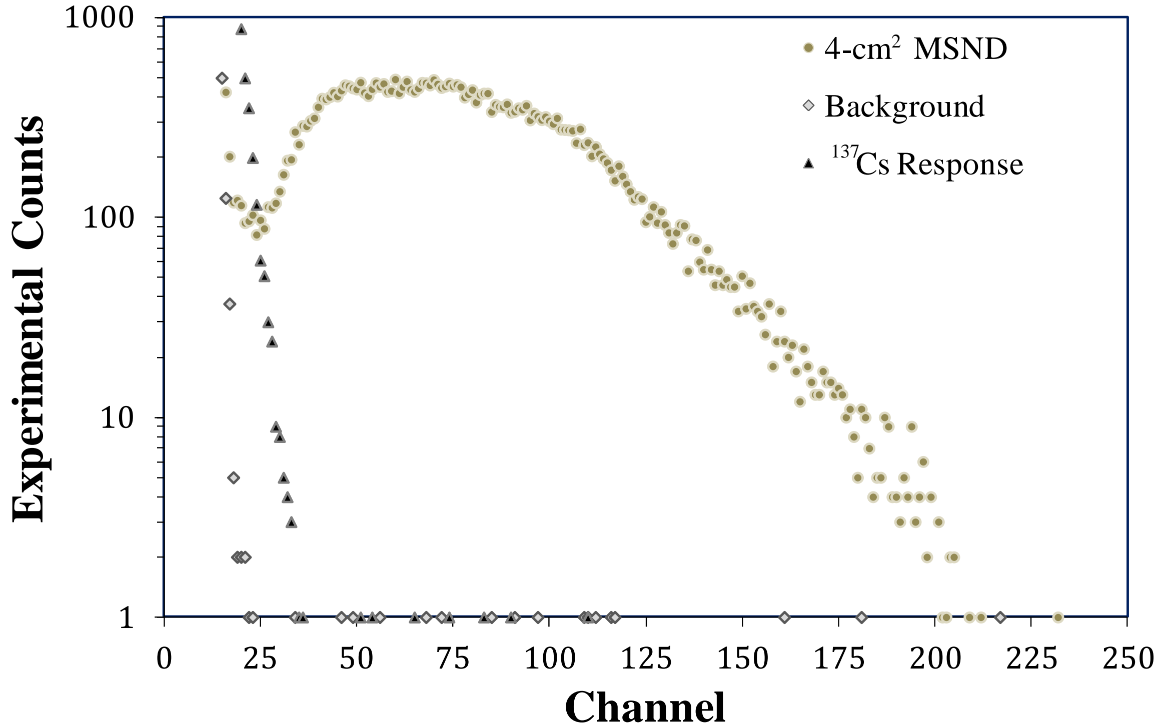

Figure 5.25: Measured ^{137}Cs gamma-ray irradiation (Ω_F = 1.27 x 10^{-4}) and neutron irradiation pulse-height spectral features for the dual-integrated neutron detector with the 10-µs signal integration time design.

With the LLD set at channel 25, the gamma-ray detection efficiency was determined to be greater than 1.85 x 10^{-6} measured-event per gamma ray, and with the LLD set to channel 32 the gamma-ray detection efficiency is greater than 3.95 x 10^{-8} measured-event per gamma ray. The neutron to gamma-ray rejection ratio (n/γ) for 662 keV photons is then easily calculated by dividing the MSND detection efficiency by the gamma-ray detection efficiency. The n/γ for the stacked MSND with an LLD set at channel 25 is 8.83 x 10^4 and with an LLD set at channel 32 is 4.04 x 10^6. These data are summarized in Table 5.2. Similar to the stacked 1-cm^2 MSND discussed earlier, the deeper microstructured trench shows that the gamma-ray interaction pulse heights from the MSND are small, resulting in superior gamma-ray discrimination. Also, the individual 4-cm^2 MSND has more bulk silicon than the 1 cm^2, to interact with a high energy photon, yet the n/γ is better because of higher frequency of larger pulse heights from neutron interactions. Again, the MSND gamma-ray response measurement was performed in the KSU reactor bay, which has a higher background of neutrons than natural background as discussed in Section 5.2.6.

The gamma-ray pulse-height spectrum response for the stacked 4-cm^2 large-area MSND is shown in Figure 5.26. With the LLD set at channel 18, the gamma-ray detection efficiency was determined to be approximately 5.44 x 10^{-5} measured-event per gamma ray and with the LLD set to channel 28, the gamma-ray detection efficiency is approximately 7.90 x 10^{-8} measured-event per gamma ray.

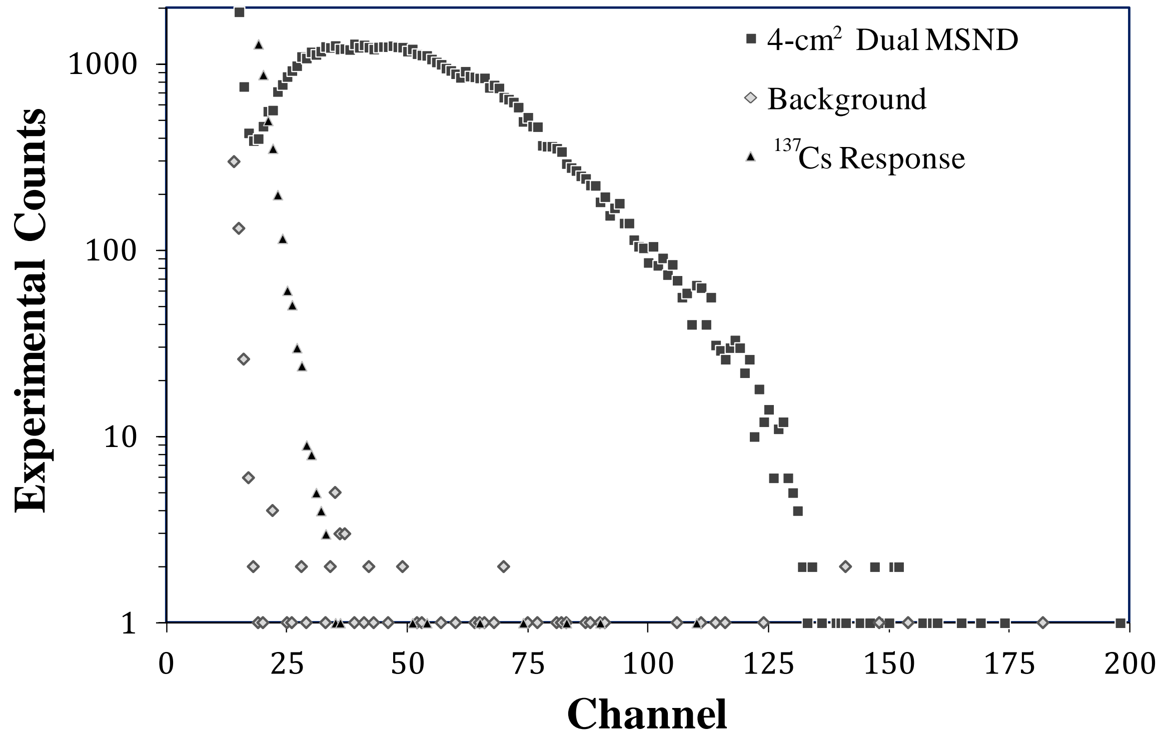

Figure 5.26: Measured ^{137}Cs gamma-ray irradiation (Ω_F = 1.27 x 10^{-4}) and neutron irradiation pulse-height spectral features for the dual-integrated 4-cm^2 MSND with the 10-μs signal integration time design.

The n/γ response for 662 keV photons is then easily calculated by dividing the MSND detection efficiency by the gamma-ray detection efficiency, see Eq. (5.5). From Figure 5.27, the n/γ ratio for the stacked MSND with an LLD set at channel 18 is 5.95 x 10^3 and with an LLD set at channel 28 is 3.67 x 10^6. These data are summarized in Table 5.2. The stacked straight-trench MSND show a downward energy shift in the pulse-height distribution to that of an individual MSND, which can decrease the n/γ rejection ratio. In addition, the stacked MSND has more bulk silicon, because there are two detector chips that can interact with a high-energy photon, thereby, decreasing the n/γ rejection ratio. Again, the MSND gamma-ray response measurement was

performed in the KSU nuclear reactor bay, which has a higher background of neutrons than natural background, as discussed in Section 5.2.6. Notice in Table 5.2 that for the stacked 4-cm^2 MSND with the LLD set in the pulse-height distribution dip, the neutron detection efficiency is high and nearly double that of the individual MSND, but n/γ rejection ratio is very poor. However, when the LLD is raised to 28, with a neutron detection efficiency loss of three percentage points, the n/γ rejection ratio is very high. Again this demonstrates the advantage of the ^{6}Li high-energy neutron reaction products over ^{10}B (see [44, 46]) and ^{157}Gd for gamma-ray discrimination without detriment to the neutron detection efficiency.

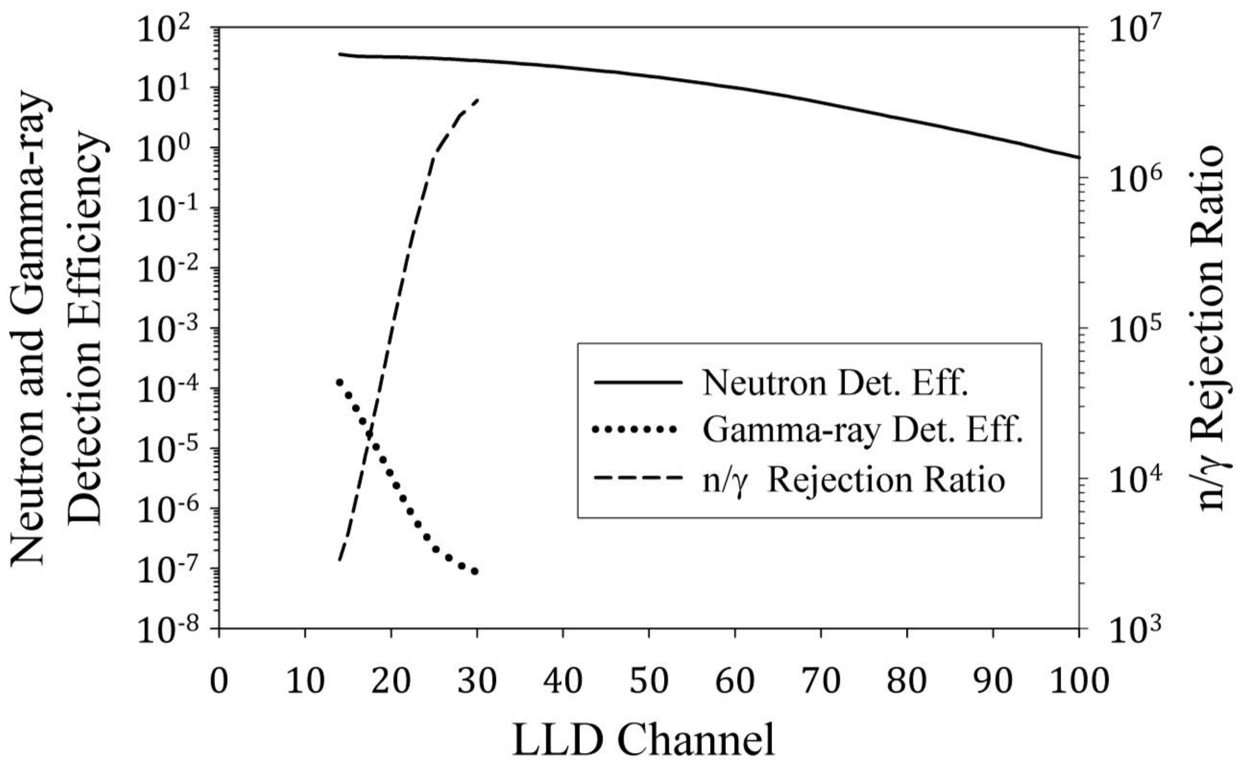

Figure 5.27: Comparison of the measured neutron detection efficiency, the measured ^{137}Cs gamma-ray detection efficiency, and the n/γ rejection ratio of the stacked 4-cm^2 MSND.

Table 5.2: Individual and stacked 4-cm^2 MSND thermal-neutron (ϵ_{th}) and ^{137}Cs gamma-ray (ϵ_γ) detection efficiencies and neutron to gamma-ray rejection ratio (n/γ) for a specified LLD.

LLD (Chn)	ϵ_{th}	ϵ_γ	n/γ
Individual MSND			
25	16.3%	1.85×10^{-4} %	8.83×10^{4}
32	15.9%	3.95×10^{-6} %	4.04×10^{6}
Stacked MSND			
18	32.4%	5.44×10^{-3} %	5.95×10^{3}
28	29.0%	7.90×10^{-6} %	3.67×10^{6}

5.2.9 Performance of Stacked Dual-Integrated 6x6-Arrayed MSNDs

A dual-integrated stacked-detector for assembled large-area panel arrays, was manufactured from two 6x6-arrayed (1-cm^2 individual elements) MSNDs that were fabricated on 4-inch diameter, 7-14 kΩ-cm *n*-type, Si wafers. The straight trench microstructures were etched with a KOH wet-etch process and were 60 µm deep by 25 µm wide, with a trench pitch of 50 µm. The MSND had a conformal *pn* junction within the trenches and a Ti-Al metal contact was fabricated on the backside of the wafer to make an electrical ground contact. ^{6}LiF nanopowder was packed into the microstructures. The leakage current for an individual-element 1-cm^2 MSND was 45 nA cm^{-2} at a reverse bias of 2.5 volts.

The stacked 6x6-arrayed MSND neutron-counting efficiency was measured in the 0.0253 eV diffracted neutron beam (1.25-cm diameter) described in Section 5.2.1. The stacked arrayed MSND intrinsic efficiency was measured with the MSND centered in the diffracted neutron beam. A pulse-height frequency spectrum was collected for the 6x6-arrayed MSND and is shown in Figure 5.28. Notice that the 6x6-arrayed MSND exhibits the expected spectral shape predicted in Section 3.3, with a pulse-height frequency dip at low energy. The dip is not nearly as significant as individual and single-element stacked MSNDs discussed earlier and is likely because of some of the 72 MSNDs not performing as well as the rest, thereby, resulting in smaller pulse heights. Note that the 6x6-arrayed MSND is limited in pulse-height spectral response for LLD placement to that of the response of the worst MSND in the 72-element

MSND array. The large number of counts in channel 58 is attributed to amplifier clipping of large pulses. For the stacked 6x6-arrayed MSND, with the LLD set to channel 20, just above the majority of the background signal, the intrinsic efficiency for frontside irradiation[51] was measured to be $7.03 \pm 0.04\%$.

The measured thermal-neutron detection intrinsic efficiency was found to be much less than the expected calculated intrinsic efficiency of 18.9% found elsewhere [46]. A fraction of the difference may be accounted for by the large neutron-streaming unmicrostructured regions (0.65 mm wide) between the individual elements of the MSND array, and that were not factored into the calculated intrinsic efficiency. Because the 1.25-cm diameter neutron-beam is centered on a single stacked-element of the array, 13.8% of the beam area does not intersect an active region of the arrayed neutron detector. In addition, thermal neutrons are lost through absorption and scattering in the top-mounted motherboard, preamplification board, and the MSND mounting board and their respective electronic components (see Figure 4.34). To verify this hypothesis, a motherboard[52] and mounting board[53] attenuation experiment was performed. Each board was separately placed in the diffracted thermal-neutron beam at 1 kW of power and a summed count was taken with the calibrated ^{3}He detector with and without the board. In this way the thermal-neutron attenuation for each board was measured. The motherboard attenuated 16.8% of the beam and the mounting board attenuated 28.7% of the beam. Obviously the boards were absorbing a large number of the neutrons and should be reduced in thickness or, at least, another board type should be used that has lower neutron attenuation.

[51] For frontside irradiation the motherboard was between the detector and neutron source.

[52] The motherboard and preamplification board were made from FR-4 epoxy-glass material from *Advanced Circuits* and was 762 µm thick.

[53] The mounting board was made from FR-4 epoxy-glass material from *Advanced Circuits* and was 1,575 µm thick.

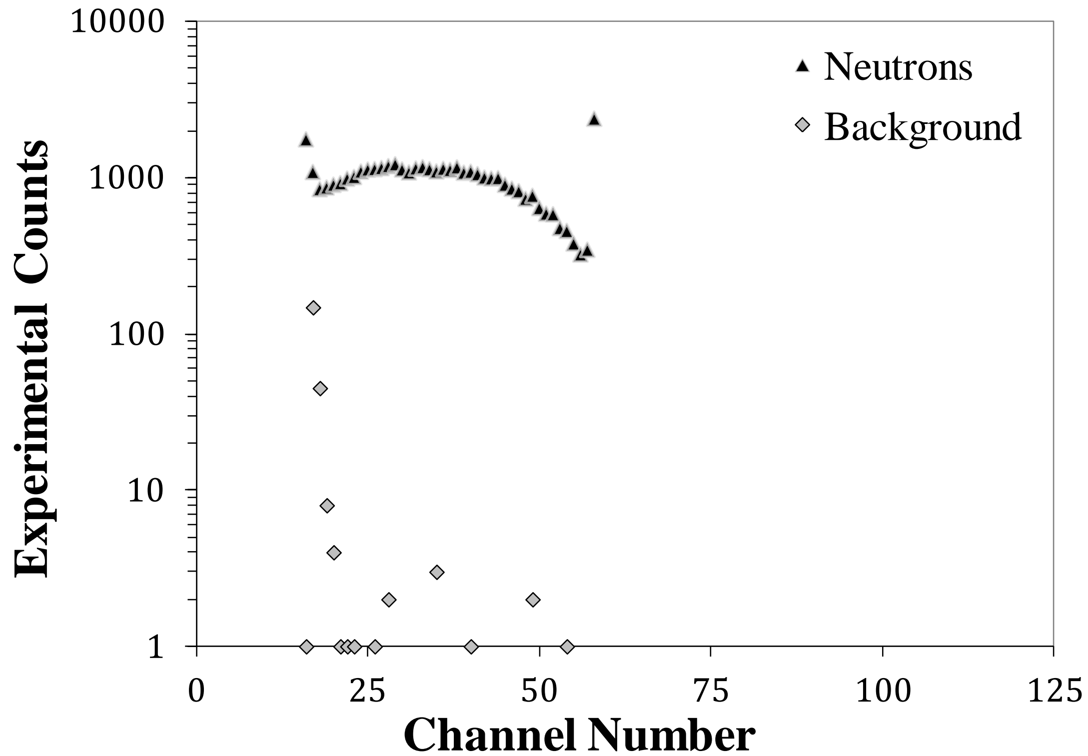

Figure 5.28: Pulse-height spectra for the 6x6-arrayed MSND with 60 μm deep, straight trench microstructures backfilled with ^{6}LiF. At an LLD = 20 Chn, the measured thermal-neutron detection was 7.03%. The large number of counts in channel 58 is attributed to amplifier clipping of large pulses.

5.2.10 Gamma-Ray Discrimination of the Stacked 6x6-Arrayed MSND

The stacked 6x6-arrayed MSND was independently tested with a ^{137}Cs source with an activity of 71.74 mCi, to determine the gamma-ray detection efficiency, i.e., the rejection ratio. The gamma-ray source was place 55 cm away from the detector and a counting spectrum was taken for frontside and backside.[54] A background count was also taken to subtract any background counts and noise contributions. The gamma-ray rejection ratio was determined by dividing the integrated gamma-ray counts in the measured spectrum by the source fluence through the 6x6-arrayed MSND, which was calculated by Eqs. (5.3) and (5.4). The gamma-ray pulse-height spectra response is shown in Figure 5.25.

[54] For "frontside" the motherboard was between the detector and source and for "backside" the orientation was flipped.

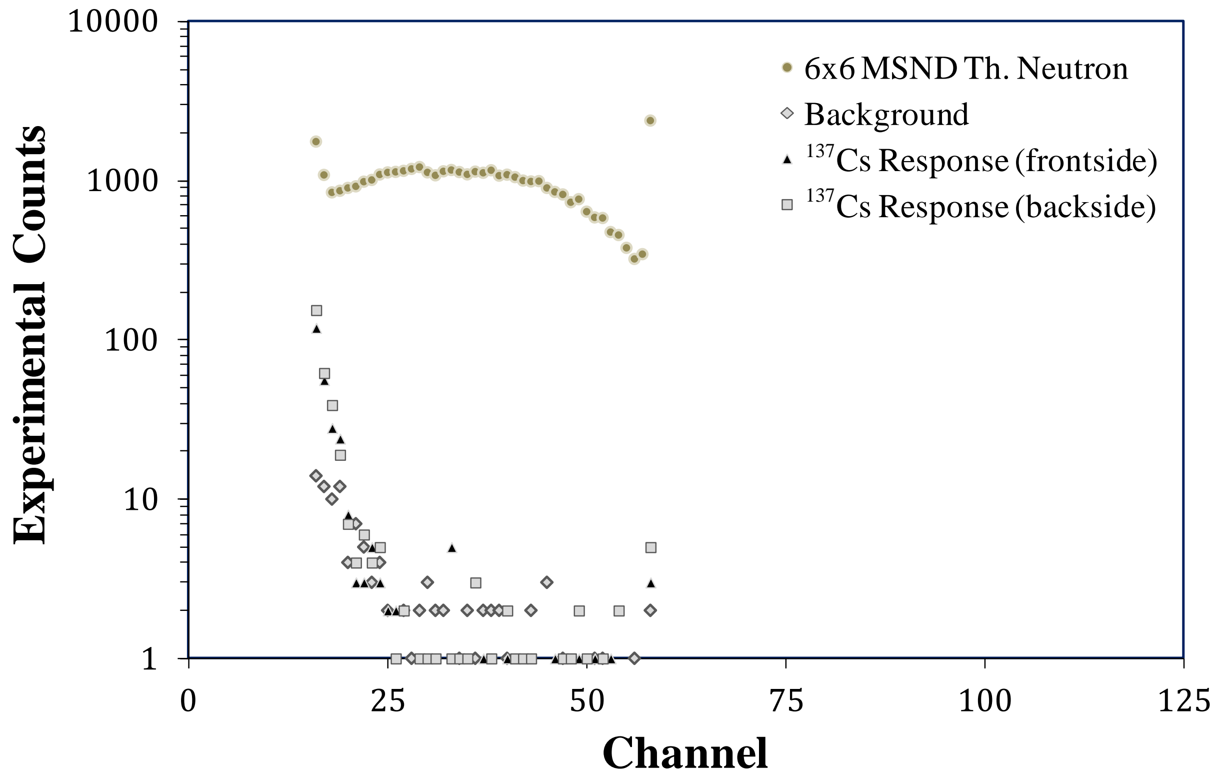

Figure 5.29: Measured ^{137}Cs gamma-ray irradiation (Ω_F = 1.07 x 10^{-3}) and thermal-neutron irradiation pulse-height spectral features for the dual-integrated 6x6-arrayed MSND. The large number of counts in channel 58 is attributed to amplifier clipping of large pulses.

With the LLD set at channel 20, the gamma-ray detection efficiency was determined to be greater than 7.42 x 10^{-9} measured-event per gamma ray. The neutron to gamma-ray rejection ratio (n/γ) for 662 keV photons is then easily calculated by dividing the MSND detection efficiency by the gamma-ray detection efficiency. The n/γ ratio for the stacked MSND with an LLD set at channel 18 is 9.47 x 10^{8}. Similar to the stacked 1-cm^2 MSND discussed earlier, the gamma-ray interaction pulse heights from the MSND are small, resulting in superior gamma-ray discrimination. Also, the 6x6-arrayed MSND has more bulk silicon than the 1 cm^2, to interact with a high energy photon, yet the n/γ ratio is better because of higher frequency of larger pulse heights from neutron interactions because of better signal formation from the shallow 60-µm trenches. Again, the MSND gamma-ray response measurement was performed in the KSU reactor bay, which has a higher background of neutrons than natural background as discussed in Section 5.2.6.

5.3 Moderated and Unmoderated ^{252}Cf Response

The MSNDs are designed specifically for thermal-neutron detection, because of the high thermal-neutron absorption cross-section of common neutron reactive materials. To detect fast neutrons, the primary emission from many fission sources, the neutrons must be thermalized to lower energies (see Figure 5.30). Many neutron detectors are based on the moderation concept because neutron absorption is highest at low energies. Therefore, it is common to incorporate HDPE surrounding the detector to thermalize fast neutrons.

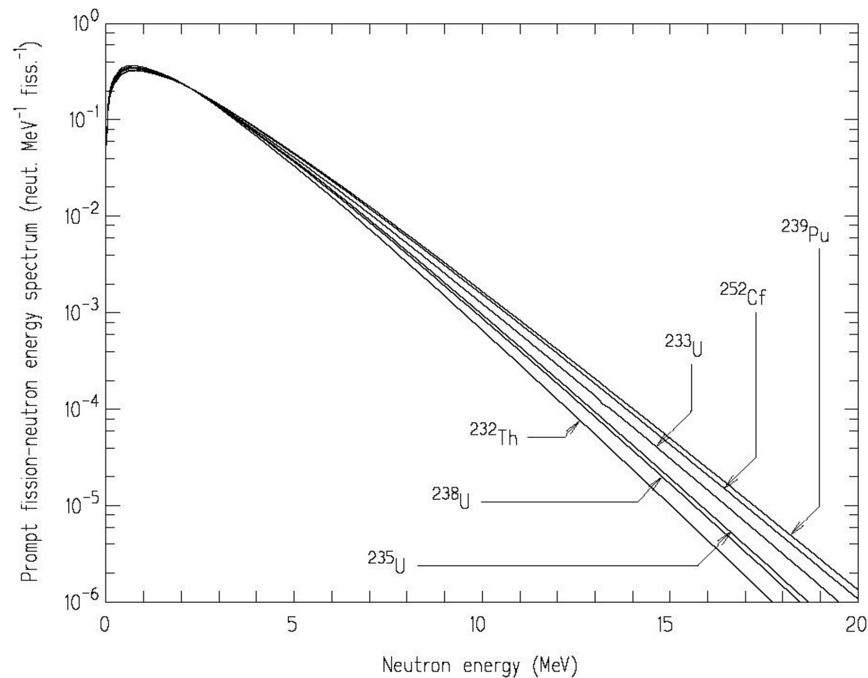

Figure 5.30: Energy spectrum of prompt neutrons produced from the fission of fissionable nuclei as calculated by Walsh [125]. Results for ^{233}U, ^{235}U, and ^{239}Pu are for thermal-neutron-induced fission, results for ^{232}Th and ^{238}U are for fast-neutron (2 MeV)-induced fission, and results for ^{252}Cf are for spontaneous fission. Figure from [90] with permission.

To measure a fast-neutron response from the MSND technology, a ^{252}Cf spontaneous fission source was used. The KSU ^{252}Cf source can be configured two different ways. First, the source can be bare, offering a Maxwellian spectrum of mostly fast neutrons which are very difficult to detect without first thermalizing the neutrons. Secondly, the source can be capped with a large moderator ball filled with D_2O and encased in a thin sheet of cadmium (see Figure 5.31). With this moderator ball, the ^{252}Cf fission neutron-energy spectrum is shifted to

characteristics of a typical nuclear power reactor environment for NIST certified dosimeter calibration [126]. Details of the KSU Californium source are given in 0.

Figure 5.31: Pictures of the KSU Californium source. ^{252}Cf spontaneously fissions, providing a source of high-energy neutrons. (left) The Cd encased D_2O sphere at the top of the irradiator is in place to provide a neutron energy spectrum similar to the neutron energy in a nuclear reactor. The spectrum permits calibrating neutron dose rate-meters for use in a nuclear reactor environment, as well as various activation, imaging, and detection research efforts. (right) If the sphere is removed, the irradiation provides a source of high energy neutrons.

5.3.1 Dual-Integrated 1-cm^2 MSND Response to a Bare ^{252}Cf Neutron Source

The dual-integrated 1-cm^2 MSND, discussed in Section 5.2.5, was placed 55 cm from the KSU bare ^{252}Cf source to measure the fast-neutron response of the MSND. The MSND was orientated with the planar face directed to the ^{252}Cf point source, such that the neutron field intersected perpendicular to the planar-side of the detector face, which is the same as the diffracted neutron beam measurements. To calculate the fast-neutron detection efficiency, the solid angle of the MSND, $\mathbf{\Omega_F}$, was found using Eqs. (5.3) and (5.4). The intrinsic fast-neutron detection efficiency, $\epsilon_{^{252}Cf}$, for the dual-integrated 1-cm^2 MSND when irradiated with the KSU bare ^{252}Cf source was found with Eq. (5.6),

$$\epsilon_{^{252}Cf} = \frac{MSND\,Neutron\;Cts}{Neutron\,Generation\;Activity \times\; time\; \times\; \Omega_F}. \tag{5.6}$$

The MSND neutron counts were found by summing all pulses above an LLD channel of 11 in the ^{252}Cf MSND response pulse-height spectrum minus the summed background counts (see Figure 5.32). Notice that the spectrum shows more pulses at low energy than the thermal-neutron response spectrum shown in Figure 5.20, yet the characteristic low energy dip is still present. This characteristic dip can be attributed to fast-neutron scattering interactions in and around the MSND imparting low-energy ionizing radiation within the detector. The intrinsic fast-neutron detection efficiency[55] for the dual-integrated 1-cm^2 MSND, using the bare ^{252}Cf source with a neutron-generation activity of 1.12 x 10^7 *n*/s, was found to be 0.608 ± 0.011%. Additionally, increasing the LLD channel to 16 for improved gamma-ray discrimination, the intrinsic fast-neutron detection efficiency was found to be 0.525 ± 0.010%.

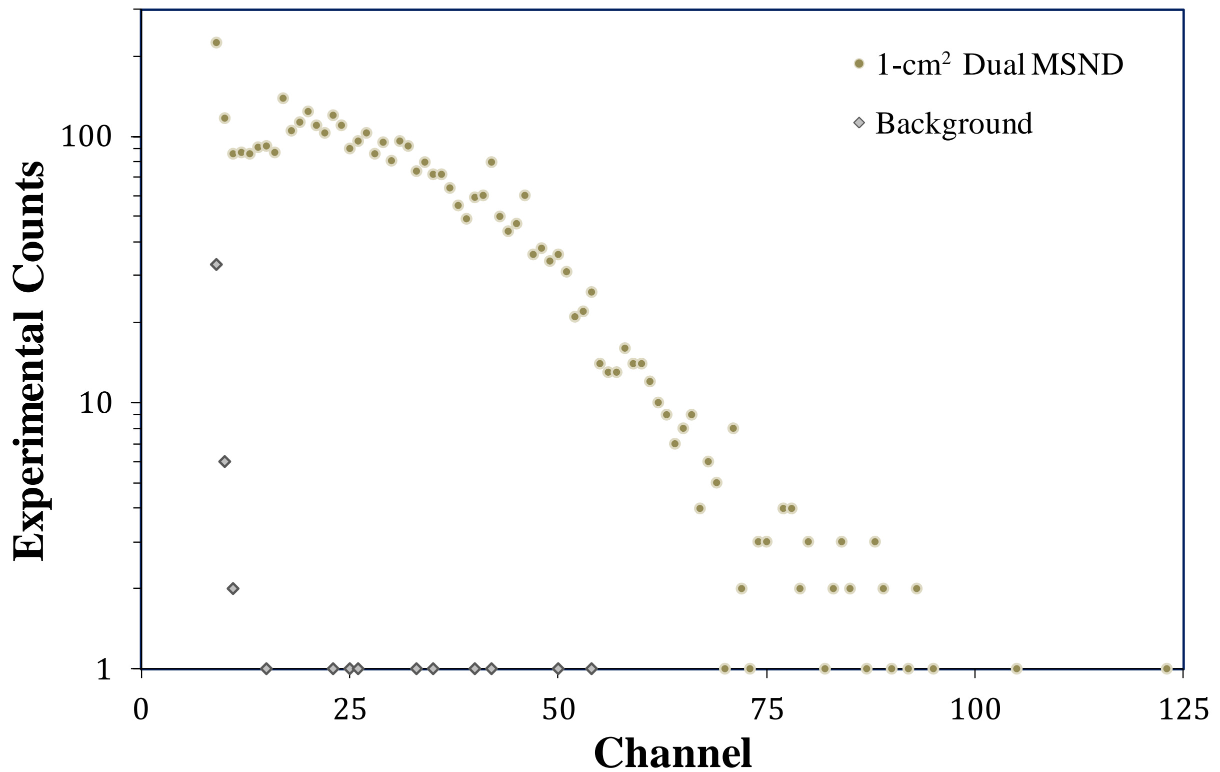

Figure 5.32: Measured bare ^{252}Cf fast-neutron irradiation (Ω_F = 2.63 x 10^{-5}) pulse-height spectral features for the 1-cm^2 dual-integrated neutron detector.

[55] Note that this is the neutron detection efficiency with no moderator material present.

5.3.2 Dual-Integrated 4-cm^2 MSND Response to a Bare ^{252}Cf Neutron Source

The dual-integrated 4-cm^2 MSND, discussed in Section 5.2.7, was placed 55 cm from the KSU bare ^{252}Cf source to measure the fast-neutron response of the MSND. The MSND was orientated with the planar face directed to the ^{252}Cf point source, such that the neutron field intersected perpendicular to the planar-side of the detector face, which is the same as the diffracted neutron beam measurements. To calculate the fast-neutron detection efficiency, the solid angle of the MSND was found using Eqs. (5.3) and (5.4). The intrinsic fast-neutron detection efficiency for the dual-integrated 4-cm^2 MSND when irradiated with the KSU bare ^{252}Cf source was found with Eq. (5.6). The MSND recorded counts were found by summing all pulses above an LLD channel of 18 in the ^{252}Cf MSND response pulse-height spectrum minus the summed background counts (see Figure 5.33). Notice that the spectrum shows more pulses at low energy than the thermal-neutron response spectrum shown in Figure 5.24, resembling the 1-cm^2 MSND fast-neutron response. Again, this spectral performance can be attributed to fast-neutron scattering interactions. The intrinsic fast-neutron detection efficiency for the dual-integrated 4-cm^2 MSND, using the bare ^{252}Cf source with an activity of 1.12×10^7 *n*/s, was found to be $0.302 \pm 0.006\%$. Additionally, increasing the LLD channel to 24 for improved gamma-ray discrimination, the intrinsic fast-neutron detection efficiency was found to be $0.255 \pm 0.005\%$. The 4-cm^2 dual MSND intrinsic fast-neutron detection efficiency is nearly half that of the 1-cm^2 dual MSND. The 4-cm^2 MSND intrinsic thermal-neutron detection efficiency is almost three-quarters that of the 1-cm^2 MSND.[56] It is not yet fully understood why the scaling difference between the fast and thermal-neutron detection efficiencies are not the same when comparing the 4-cm^2 dual MSND with the 1-cm^2 dual MSND. One hypothesis is that the thermalized fast-neutrons are lost through absorption and scattering in the preamplification board that is sandwiched between the two 4-cm^2 MSND chips (see Figure 4.32), which was shown to be a problem earlier with the 6x6-arrayed MSND (see Section 5.2.9).

[56] Note that the 4-cm^2 dual MSND device was a shallower-trenched microstructure, therefore, it was expected that the intrinsic neutron detection efficiency would be lower than the 1-cm^2 dual MSND device.

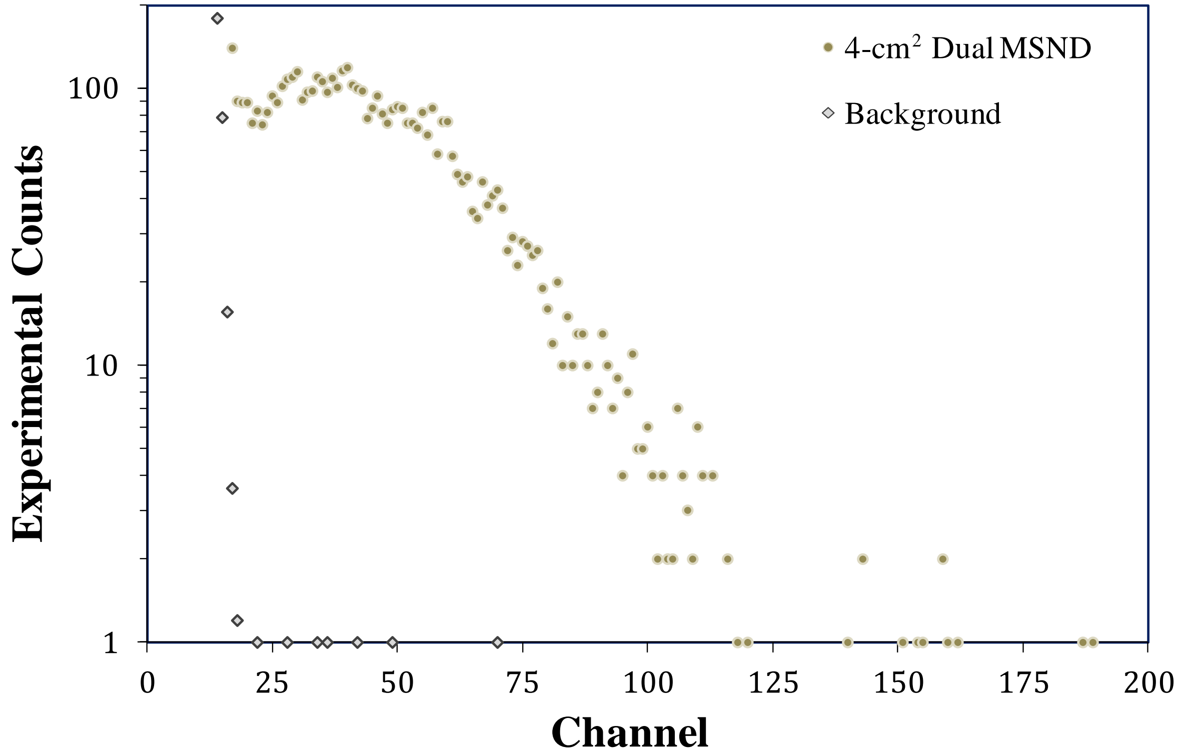

Figure 5.33: Measured bare ^{252}Cf fast-neutron irradiation (Ω_F = 1.05 x 10^{-4}) pulse-height spectral features for the 4-cm^2 dual-integrated neutron detector.

5.3.3 6x6-Arrayed MSND Response to a Bare ^{252}Cf Neutron Source

The dual-integrated 6x6-arrayed MSND, discussed in Section 5.2.9, was placed 55 cm from the KSU bare ^{252}Cf source to measure the fast-neutron response of the MSND. The arrayed MSND was orientated with the planar face directed to the ^{252}Cf point source, such that the neutron field intersected perpendicular to the planar-side of the detector face, which is the same as the diffracted neutron beam measurements. To calculate the fast-neutron detection efficiency, the solid angle of the MSND was found using Eqs. (5.3) and (5.4). The intrinsic fast-neutron detection efficiency for both front and backside neutron irradiation[57] of the dual-integrated 6x6-arrayed MSND, when irradiated with the KSU bare ^{252}Cf source, was found with Eq. (5.6). The MSND recorded counts were found by summing all pulses above an LLD channel of 20 in the ^{252}Cf MSND response pulse-height spectra minus the summed background counts (see

[57] For 'frontside' the motherboard was between the detector and source and for 'backside' the orientation was flipped.

Figure 5.34). Notice that the spectra show more pulses at low energy, resembling the 1-cm^2 and 4-cm^2 MSND fast-neutron response. Again, this likely can be attributed to fast-neutron scattering interactions. Additionally, note that the change in low-energy pulses with the 1-cm thick lead gamma-ray shield was not significant. The intrinsic fast-neutron detection efficiency for the frontside irradiated, dual-integrated 6x6-arrayed MSND, using the bare ^{252}Cf source with an activity of 1.14 x 10^7 *n*/s, was found to be 0.079 ± 0.001%. With the same setup as the frontside irradiation except the array assembly was flipped, the intrinsic fast-neutron detection efficiency for the backside irradiated dual-integrated 6x6-arrayed MSND was found to be 0.074 ± 0.001%. Notice that there was a slight reduction in fast-neutron detection efficiency with backside irradiation, where the motherboard is likely thermalizing some of the neutron field. The fast-neutron detection efficiency for the 6x6-arrayed MSND is very low, which was expected, and further justifies the importance of moderator material for efficient fast-neutron detection.

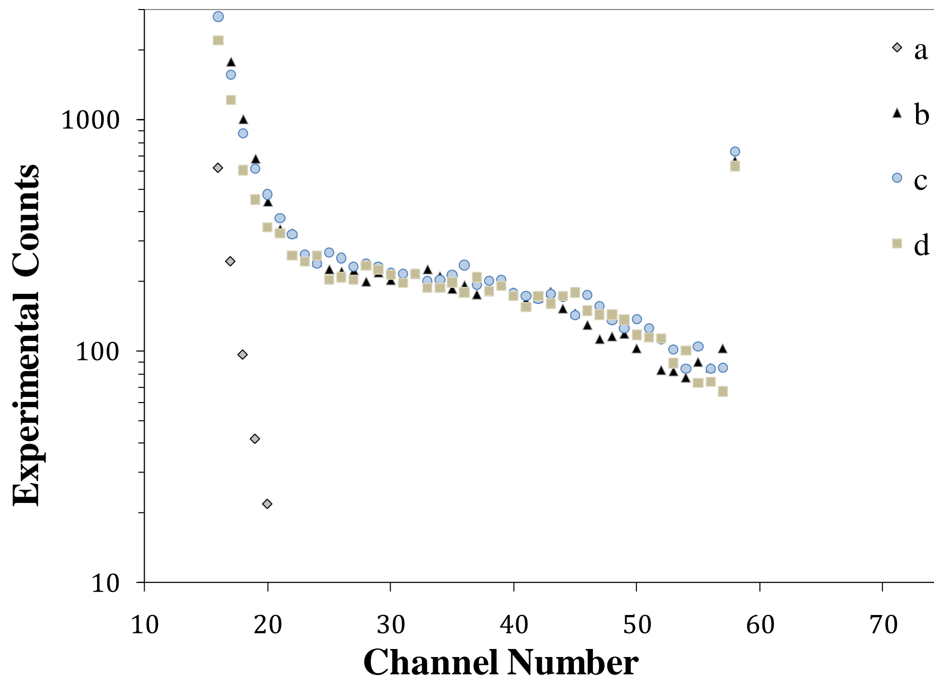

Figure 5.34: Pulse-height spectra features for the dual-integrated 6x6-arrayed MSND with irradiation from the KSU unmoderated ^{252}Cf spontaneous fission neutron source (Ω_F = 1.07 x 10^{-3}). The pulse height spectra key is: (a) background with ^{252}Cf source in the shielded cask, (b) bare ^{252}Cf source with frontside irradiation, (c) bare ^{252}Cf source with backside irradiation, (d) ^{252}Cf source with backside irradiation and 1 cm of lead gamma-ray shielding. The large number of counts in channel 58 is attributed to amplifier clipping of large pulses.

5.3.4 ^{3}He Gas-Filled Neutron Detector Response to a Bare ^{252}Cf Neutron Source

A high efficiency ^{3}He gas-filled neutron detector[58] was tested in a spontaneous fission neutron field from a bare ^{252}Cf source as a direct comparison to the MSND in the same neutron field discussed in Section 5.3.1. The unmoderated ^{3}He gas-filled proportional detector was placed at the same distance of 55 cm from the ^{252}Cf source as the dual-integrated MSND for a direct comparison of fast-neutron detection. In addition, the ^{3}He gas-filled proportional detector was placed at the same distance of 55 cm from the ^{252}Cf source with a 2.5-cm by 7.5-cm square HDPE block directly in front of the detector tube as a comparison to the 6x6-arrayed MSND in the same neutron field discussed in Section 5.3.5. The ^{3}He detector was orientated sideways to the ^{252}Cf point source, such that the neutron field intersected perpendicular to the axis of the detector (not along the long axis). To calculate the fast-neutron detection efficiency, the solid angle of the 8-cm by 5.25-cm diameter ^{3}He tube (see Figure 2.2) was found using Eqs. (5.3) and (5.4). The intrinsic fast-neutron detection efficiency for the ^{3}He tube, when irradiated with the KSU bare ^{252}Cf source, was found with Eq. (5.6). The ^{3}He detector recorded counts were found by summing all pulses above an LLD channel of 25 in the ^{252}Cf neutron source ^{3}He-detector response pulse-height spectra minus the summed background counts (see Figure 5.35). Notice that the spectra show pulse heights with a broad and uniform distribution up to channel 175 and thereafter the counts drop-off severely. Again, this characteristic is likely because of fast-neutron scattering interactions. Small ionization-energy events because of neutron absorption near the inactive field-tube ends and at the detector walls may also contribute to the broad pulse-height distribution. Note that the change in low-energy pulses with the 1-cm thick lead gamma-ray shield was not significant. Additionally, notice that the HDPE moderated spectrum has more counts at the upper-energy part of the neutron-response pulse-height spectrum. This is because of the increased amount of moderated neutrons entering the ^{3}He detector and being absorbed in the active region of the detector volume (away from the insensitive field-tubes ends), thereby, increasing the reaction-product energy-deposition amount per event recorded. The fast-neutron intrinsic detection efficiency for the ^{3}He gas-filled detector, using the bare ^{252}Cf source with an activity of 1.14×10^{7} *n*/s, was found to be $0.728 \pm 0.003\%$ at an LLD channel of 25. The moderated fast-neutron intrinsic detection efficiency for the ^{3}He gas-filled detector, using the

[58] Model No. P4-1603-207, Serial No. 97D05759, Pressure: 60 PSIA, High Voltage: 1300 V, see Figure 2.2.

bare ^{252}Cf source with an activity of 1.14 x 10^7 *n*/s, was found to be 1.396 ± 0.002% at an LLD channel of 25. Notice that the fast-neutron intrinsic detection efficiency for the unmoderated ^{3}He detector is 9 times that of the unmoderated 6x6-arrayed MSND with 7% thermal-neutron detection efficiency and is 1.2 times that of the 1-cm^2 stacked MSND detection efficiency. Therefore, a deeper trenched, i.e. higher thermal detection efficiency, 6x6-arrayed MSND should be *nearly equivalent to the ^{3}He gas-filled detector*.

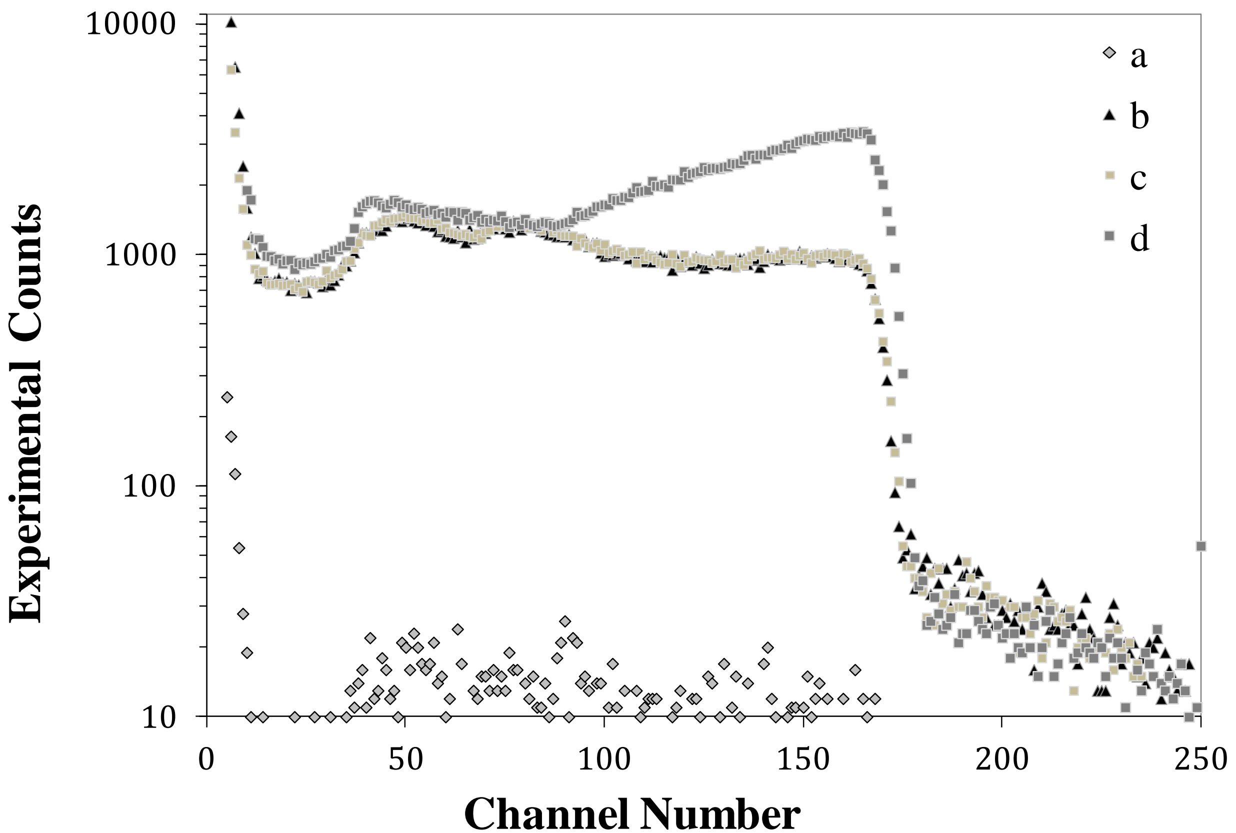

Figure 5.35: Pulse-height spectra features for a ^{3}He gas-filled neutron detector from irradiation with the KSU unmoderated ^{252}Cf spontaneous fission neutron (Ω_F = 1.10 x 10^{-3}). The pulse height spectra key is: (a) background with ^{252}Cf source in the shielded cask and no moderator, (b) bare ^{252}Cf source, (c) ^{252}Cf source with 1 cm of lead gamma-ray shielding, and (d) bare ^{252}Cf source with 2.5 cm of HDPE on frontside (between detector and source).

5.3.5 6x6-Arrayed MSND Response to HDPE-Moderated ^{252}Cf Neutron Source

The importance of utilizing materials with neutron moderator content, i.e., hydrogen and carbon, to increase fast-neutron sensitivity of the 6x6-arrayed MSND was studied. The same detector setup and fast-neutron detection efficiency calculation was used as described in Section 5.3.3. The intrinsic fast-neutron detection efficiency for both frontside and backside neutron irradiation[59] of the dual-integrated 6x6-arrayed MSND with a 2.5-cm by 7.5-cm square HDPE block in front and behind[60] the MSND was found. The MSND recorded counts were found by summing all pulses above an LLD channel of 20 in the ^{252}Cf MSND response pulse-height spectra minus the summed background counts (see Figure 5.36). The MSND counting time was the same as the experiment performed in Section 5.3.3 with only the bare ^{252}Cf source. Notice the increase in neutron counts and the shift in the pulse height frequency to higher channel numbers, as expected for the thermal-neutron response as shown in Figure 5.28.

The intrinsic fast-neutron detection efficiency for backside irradiation with the 2.5-cm HDPE block behind of the dual-integrated 6x6-arrayed MSND, using the bare ^{252}Cf source with an activity of 1.14×10^7 *n*/s, was found to be $0.115 \pm 0.001\%$. The intrinsic fast-neutron detection efficiency for frontside irradiation with the 2.5-cm HDPE block in front of the dual-integrated 6x6-arrayed MSND, was found to be $0.176 \pm 0.001\%$. The intrinsic fast-neutron detection efficiency for backside irradiation with the 2.5-cm HDPE block in front of the dual-integrated 6x6-arrayed MSND, was found to be $0.227 \pm 0.001\%$. A comparison of the different neutron efficiencies is given in Table 5.3.

[59] For ‘frontside’ the motherboard was between the detector and source and for ‘backside’ the orientation was flipped.

[60] For ‘in front’ the HDPE was between the detector and source and for ‘behind’ the orientation was flipped.

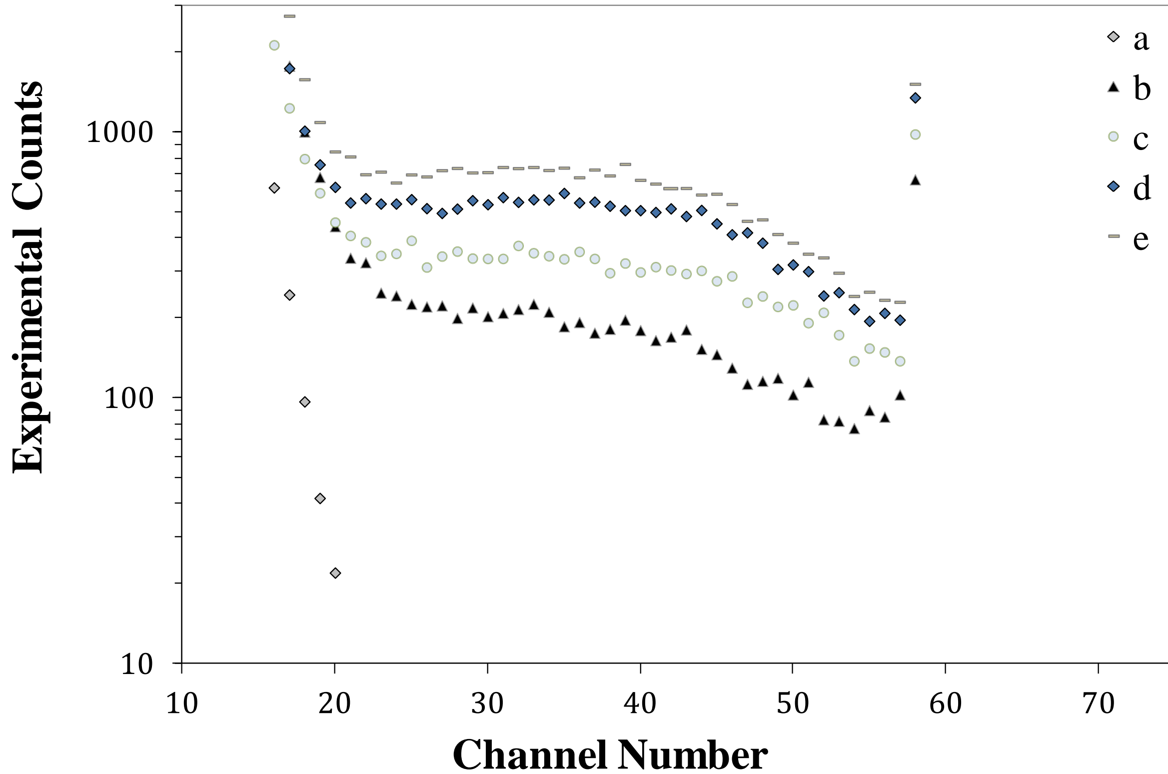

Figure 5.36: Pulse-height spectra features for the dual-integrated 6x6-arrayed MSND with irradiation from the KSU unmoderated ^{252}Cf spontaneous fission neutron source (Ω_F = 1.07 x 10^{-3}). The pulse height spectra key is: (a) background with ^{252}Cf source in the shielded cask, (b) bare ^{252}Cf source with frontside irradiation, (c) bare ^{252}Cf source with backside irradiation, 2.5 cm of HDPE on backside, (d) bare ^{252}Cf source with frontside irradiation, 2.5 cm of HDPE on backside, and (e) bare ^{252}Cf source with backside irradiation, 2.5 cm of HDPE on frontside. The large number of counts in channel 58 is attributed to amplifier clipping of large pulses.

The difference between the 0.115% detection efficiency arrangement and the 0.176% arrangement is likely because of the absorption of thermal neutrons in the motherboard, which was known to occur for thermal neutrons as discussed in Section 5.2.9. Notice that with the highest efficiency case, the fast-neutron detection efficiency improved by almost 3 times the unmoderated case. In the case of fast-neutron detection, moderating material may be more important than having a large number of detectors. The 0.227% intrinsic efficiency means that the 6x6-arrayed MSND records approximately 1 of every 400 neutrons intersecting the MSND. By comparison, a 10 inch diameter Bonner sphere or REM ball neutron detector (detector projected area ≈ 500 cm^2), the standard hand-held detector used for fast-neutron dosimetry, has

approximately 0.03% intrinsic efficiency for 1.5 MeV neutrons [4]. Also notice that the ^{3}He gas-filled detector moderated fast-neutron intrinsic detection efficiency is only 6 times more than the moderated efficiency of the 6x6-arrayed MSND. This efficiency gain further narrows the gap between the ^{3}He gas-filled detector and the MSND array technology.

Table 5.3: Intrinsic fast-neutron detection efficiencies (ϵ_F) for the stacked 6x6-arrayed MSND. The orientation of the detector, HDPE, and ^{252}Cf source are shown in sequential order according to arrangement, such that MSNDF and MSNDB stand for front and back irradiation, respectively.

Detector (LLD)	ϵ_{th}	ϵ_F			
		No HDPE	**MSND*B*/HDPE/^{252}Cf**	**MSND*F*/HDPE/^{252}Cf**	**HDPE/MSND*B*/^{252}Cf**
Stacked 6x6 MSND					
20	7.03%	0.079%	0.227%	0.176%	0.115%
^{3}He Detector					
25	80.7%	0.728%	1.396%	--	--

CHAPTER 6

CONCLUSIONS AND FUTURE WORK

The important thing in science is not so much to obtain new facts
as to discover new ways of thinking about them.
William Lawrence Bragg

Conclusions and the contribution to the science of solid-state neutron detection are described in this chapter. Potential use of the MSND for current and future applications are presented and discussed. Finally, future work is considered for improved MSND design features such as increased neutron detection efficiency, MSND operational-environment testing, and augmented signal formation and integration within the MSND.

6.1 Contribution to the Science of Solid-State Neutron Detection

Until recently, neutron detectors were either fragile, large in size for high efficiency, expensive, commercially available in limited supply, angular dependent, operated at high voltages, had to rely on large bulky electronic equipment, or were some combination of these tradeoffs. Traditional gas and scintillator neutron detectors must be handled delicately, and therefore are not designed for rough and rugged applications. For personal dosimetry, TLDs are commonly used because they are solid-state and economical, yet they do not support active readout. Thin-film coated semiconductor neutron detectors have been around for many decades,

and have the advantage of being compact, rugged, low power, economical to produce in mass quantity, and with active readout capabilities, but have suffered from small neutron detection efficiencies. The limiting aspect of these thin-film coated planar-diode detectors are the restriction on the layer thickness of the neutron converter material because of self absorption. Recently, new techniques have been developed to create microstructures in a semiconductor diode that are backfilled with neutron absorbing materials to create a high efficiency solid-state neutron detector. In the present work, these techniques have been refined and improved to fabricate 3D microstructured semiconductor neutron detectors with reduced leakage current, reduced capacitance, highly anisotropic deep etched trenches, and increased signal-to-noise ratios. By diffusing a *pn* junction into the deep microstructures, the carrier transport characteristics improved and are reflected in the MSND pulse-height spectra, which compare well to simulated spectra. In addition, the generated pulses have larger magnitudes with these design improvements, shifting the spectrum towards higher channels and away from the noise floor. As a result of these fabrication improvements, the new MSND detection systems function with better gamma-ray discrimination and the MSNDs are easier to fabricate than previous designs. In addition to the microstructured diode fabrication improvement, a superior ^{6}LiF neutron reactive material nearly-solid backfill and batch processing method was developed. This process incorporates a LiF nano-sizing process and a centrifugal batch process for backfilling the nano-LiF material.

The highest thermal-neutron detection efficiency ever reported for a solid-state semiconductor neutron detector was presented in this work. The MSND was 1 cm^2 and measured a thermal-neutron detection efficiency of 42%. This MSND also offered an intrinsic fast-neutron detection efficiency of 0.608%, which is almost equal that of an 8-cm by 5.25-cm diameter cylindrical ^{3}He proportional gas detector, which was 0.728%. In addition, a 4-cm^2 MSND was fabricated and measured a thermal-neutron detection efficiency of 32%. By increasing the size of the individual MSND element, less signal processing electronics are need, thereby reducing the cost and volume of a packaged system. Both MSNDs show excellent neutron to gamma-ray rejection ratios, which are on the order of 10^6, without much loss in thermal-neutron detection efficiency. Individually, the MSND is intrinsically highly sensitive to thermal neutrons, but not extrinsically sensitive because of their small size. To improve upon this, individual MSNDs were tiled together into a 6x6-element array on a single silicon chip. Individual elements of the array

were tested for thermal-neutron detection efficiency and found to be 7%. The array also showed an excellent n/γ reject ratio of 10^8. Overall, because of the inadequacies and costs of other neutron detection systems, the MSND is the premier technology for many neutron detection applications.

6.2 Applications for the MSND Technology

Because the MSND technology is low-cost, mass producible, rugged, low-power, and compact, with active readout capabilities, it can easily be applied to many current and future neutron detection applications. The solid-state neutron detector can be used as a basic element (building block) for assembling many types of practical and robust neutron-detection systems required for many applications. Discrete MSNDs can be used for small and compact detectors, such as personal dosimeters, industrial monitors (neutron topography), while arrays of the MSNDs can be used in large area imaging systems. MSND systems are easy to use, requiring no maintenance, and provide the capability to monitor neutron radioactive materials and neutron beam lines in real time with little investment cost in comparison to competitor technologies. A few of these hypothetical applications, along with some applications that have already been built, are mentioned in this Section.

6.2.1 Real-Time Dosimeters

Neutron dosimetry is typically achieved in one of two ways. The first and most common is in conjunction with a thermoluminescent (TLD) badge that is not real time and requires separate equipment to determine the neutron dose. The second utilizes neutron sensitive gas detectors that can provide real-time readout, however, they are not as rugged as the TLD chips and are much more expensive to manufacture and operate. The best features of the TLD and neutron-sensitive gas detector are currently available as the MSND. MSNDs can provide real-time readout, are cheap to manufacture, require a very small foot print on a circuit board, which can easily be implemented into small personal neutron dosimetry packages.

6.2.2 Radioactive Waste Monitoring

Once radioactive material is stored, the containers must continually be monitored for structural failure of the container. A preferred monitoring system would be a passive system, in which many small detectors are dispersed in the storage chamber and wirelessly report to a central hub. To accurately monitor the entire chamber, a vast number of low-power neutron detectors are needed. Current MSND battery life for signal processing electronics can last for months and are constructed from economical electronics that are a fraction of the cost of a comparable commercially available ^{3}He gas detector.

In addition, shipping radioactive hazardous waste, such as spent fuel assemblies to repositories, requires real-time monitoring to actively watch for containment loss issues. But, shipping the waste requires limited interrogation volume, with a necessity of many detectors to cover all possible leak volume. Current gas detectors would be very expensive to mount around the shipping container and may not be robust enough to survive the transportation. The microstructured semiconductor neutron detectors would be ideal for monitoring the waste during transit, because of their compactness, cheapness, low-power operation, and active readout.

6.2.3 Material Scattering Experiments with the Spallation Neutron Source

Neutron science research at Oak Ridge National Laboratory (ORNL) is currently making vast and innovative developments in materials science through neutron scattering experiments. These techniques provide unparallel mechanisms for studying the structure and dynamics of materials, (some inspections are in-situ during material fabrication) at the molecular level. ORNL has the world's highest flux reactor-based neutron source (the High Flux Isotope Reactor) and the world's most intense pulsed accelerator-based neutron source (the Spallation Neutron Source), and as such, ORNL can provide neutron scattering capabilities unavailable anywhere else in the world.

A one-dimensional (1D) pixel array has been designed specifically for small angle neutron scattering (SANS) experiments to be performed at the spallation neutron source (SNS) of Oak Ridge National Laboratory. To meet the experiment requirements, an array has been designed and fabricated on silicon with microstructured pixels 100 μm wide and 4 cm long. A 1024 pixel array prototype system that includes 16 chips of 64 pixels each, with a pitch of 120 μm, and

readout electronics composed of PATERA amplifiers. The PATERA was designed specifically for the large flux of the SNS and the high efficiency neutron detector array (HENDA). The performance of the 1D silicon pixel array is discussed elsewhere [39, 40].

6.2.4 MSND Neutron Spectrometer Design

A neutron energy-spectrum linear-unfolding (NELU) detector system can be designed and fabricated from individually packaged dual-integrated arrayed MSNDs. Multiple detectors can be layered between neutron-moderating materials, such as high density polyethylene. Neutrons of greater energy penetrate farther into the moderating material, producing more counts on detectors at the back of the stacked assembly of MSNDs. On the contrary, neutrons of lower energy only stimulate detectors at the front of the stack (see Figure 6.1).

The NELU spectrometer's HDPE moderator material can be shaped in the form of a rectangular block, with cavities removed for placing stacked element MSNDs inside. The neutron source energy is determined by directing the length of the spectrometer system toward a neutron source or orientating the NELU long-axis in a neutron beam. By utilizing the same 6x6 MSND arrays mentioned in Section 4.7.1, and stacking them as large-area individual detectors in the segmented moderator, the neutron energy spectrum can be measured by the MSND count frequency response according to interaction depth in the HDPE neutron moderating material. Additionally, to abate neutron energy-spectrum cross-talk between pre and post MSND detector systems, a cadmium absorber plate is placed after each detector array. Therefore, thermalized neutrons that backscatter or pass through a detector without interaction are absorbed in the cadmium and removed from the neutron energy frequency response produced by the linear-unfolding array of stacked detectors. Output from the multiple detector MSND arrays can be serially addressed with respect to stacked depth location; as such, the detector count frequency and depth location is referenced and outputted to graphical interface software that displays count frequency versus detector location (see output illustration in Figure 6.1).

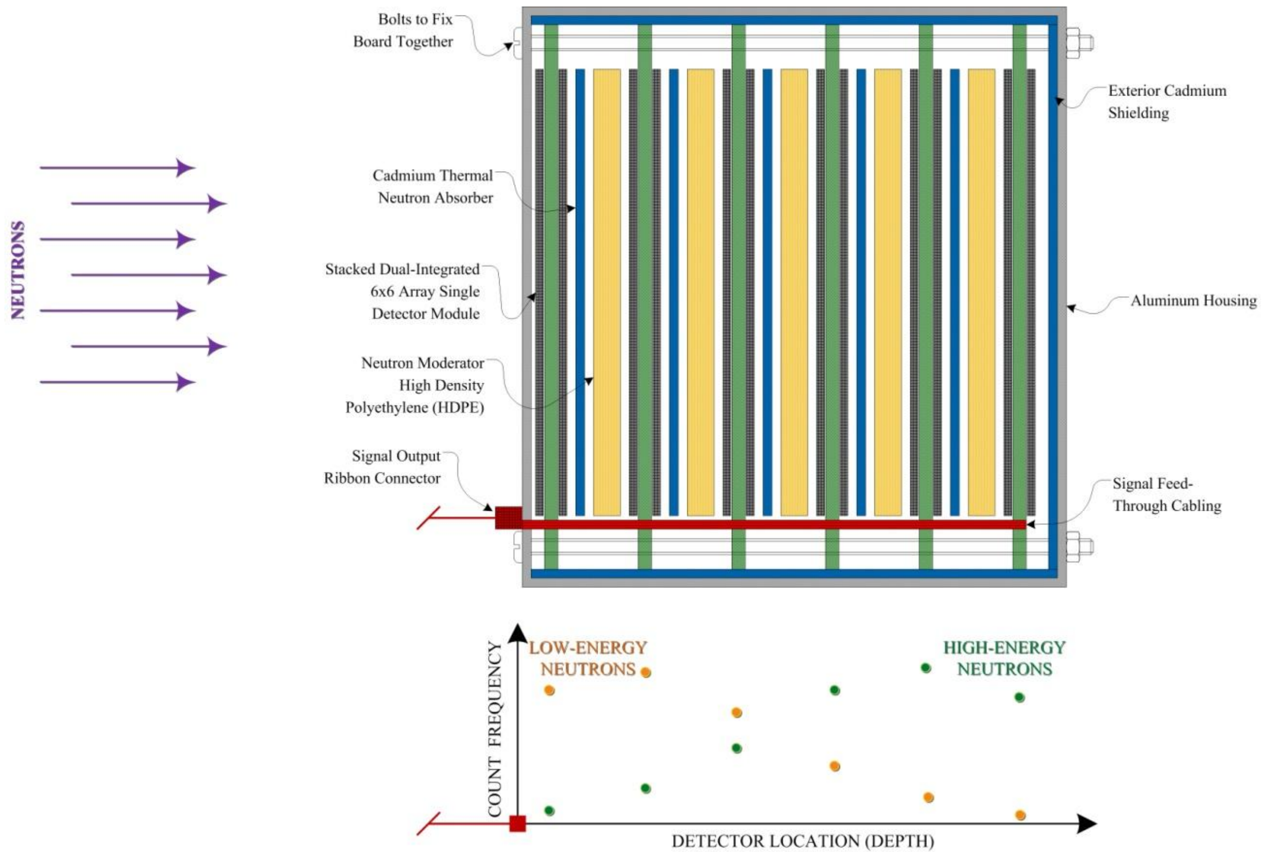

Figure 6.1: Illustration of a cut-section assembly of the neutron energy-spectrum linear-unfolding detector system, utilizing dual-integrated 6x6-arrayed MSNDs, and measures the energy of a neutron based on the depth of interaction within neutron moderating material, e.g. HDPE. For simplicity and ease of view, only six MSNDs are shown, and the NELU detector scale is enlarged.

6.2.5 Space Applications

Ionizing radiation inside the International Space Station (ISS) is produced when high energy heavy ions that make up cosmic rays, collide with the aluminum hull of the ISS, generating a shower of reaction-products into the living quarters. Neutrons are the most prevalent of these particles. Because neutrons are uncharged neutral, they can penetrate farther into human tissue than many other types of radiation and cause severe damage, including nerve damage, DNA damage, and cancer. As such, it is necessary to characterize the neutron dose to an astronaut in real-time. The ISS has been retro-fitted with polyethylene shielding to reduce the neutron production when the ISS is hit by cosmic radiation. The shielding has shown to only reduce the astronaut dose by a few percent. Therefore, there is a dire need to monitor neutron fluence within

the ISS to actively monitor inhabitant dose and electronic hardware damage because of neutron radiation. Because of the limited available power on ISS, such neutron detectors to monitor neutron fluence must be low-power and compact detectors.

Currently, six Bonner Ball Neutron Detector (BBND) systems provide data monitoring on how much neutron radiation is present at various times, allowing a model of real-time exposure to be calculated [127] (see Figure 6.2). Yet, with only six such detectors, limited neutron radiation information is obtained from the BBNDs because of the restriction of detector amount and size. To develop safety measures to protect crewmembers during both long-duration missions on the ISS and during interplanetary exploration, an improved monitoring system must be implemented. MSNDs can be dispersed in the hundreds, each consuming very little power, taking up little space because of compact electronics, and each wirelessly monitoring actively the neutron dose within the ISS. Currently, there are no active neutron monitoring systems for space-suits and space-vehicles, because of power limitations and detector sizes. But, with the MSND technology, many can be incorporated into each space-suit and space-vehicle, thereby alerting the occupants of the ISS and astronauts performing open-space operations when dangerous levels are present.

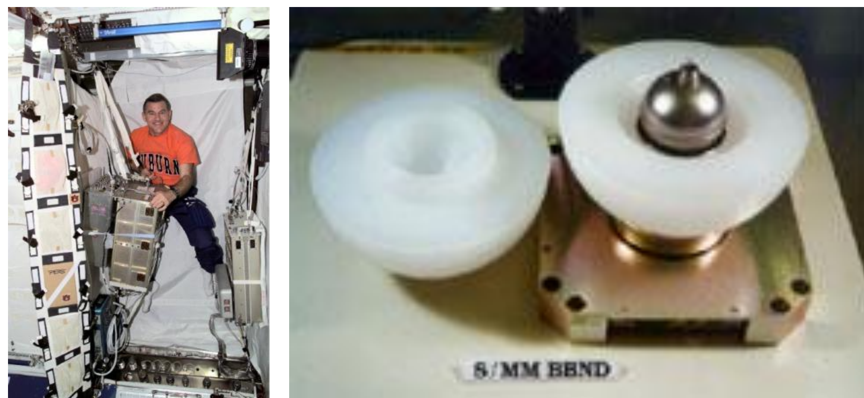

Figure 6.2: (left) Astronaut with Bonner ball neutron detector control unit and (right) detector module in Destiny laboratory. Source is from [127].

6.3 Future Work

To improve the MSND technology, future work should be dedicated to both application environment testing and variant designs for improved MSND operation and fabrication. Potential application environment testing needs to include the following.

- MSND counting characteristics at different operating temperatures (-30C to 200C).
- Packaged MSND drop and mechanical shock testing for high vibration and high g-force environments.
- Mixed radiation-source environment discrimination testing.

Variant designs for improving the MSND operation and fabrication include the following.

- The use of other bulk semiconductor materials, e.g., GaAs and SiC, for specialized applications of MSND.
- Reduce the trench and semiconductor fin sizes to the modeled MSND optimization to increase detection efficiencies of individual and stacked MSNDs.
- Consideration of a Schottky diode structure on silicon to simplify the MSND fabrication process.

A significant MSND design improvement to dramatically decrease the signal integration time is described in the following Section. The design incorporates front and backside interspersed trench etching of the silicon diode to improve the electric potential field strength and decrease the charge sweep-out time to less than a nanosecond.

6.3.1 Dual-Side Etched Interlaced Trench Design

Further enhancement of the conformal diode MSND design, by improving on the flaws of the conformal diode slows charge migration within the silicon microstructure fins, as discussed in Section 5.2.4, will be to fabricate an interlaced, frontside and backside etched MSND. To improve charge capture efficiency and shorten the signal integration time, interlaced microstructures described in Figure 6.3, etched from both sides of the silicon wafer, can be fabricated, and the first such efforts are shown in Figure 6.4. The design, first described in the

literature [121], offers reduced leakage current, zero operation voltage potential, improve charge capture efficiency, and a shortened signal-integration time. The interlaced MSND electric field is uniformly distributed across the silicon detector volume and the signal integration time necessary to collect all the produced charge is dramatically reduced (see Figure 6.5). The single-side etch design has shown a charge collection integration time from 2 to 50 microseconds, whereas the interlaced trench design would be on the order of 1 nanosecond, faster than the collection time of a moderately thin *pin* junction diode [94]. Additionally, in regards to signal integration time, the interlaced trench design is not limited by increased microstructure depth, as in the case of the single-sided design. Another type of dual-side etched MSND design is also shown in Figure 6.3, where the trenches are off-set from each other to decrease loss from neutron streaming and as such, a second stacked MSND is no longer necessary.

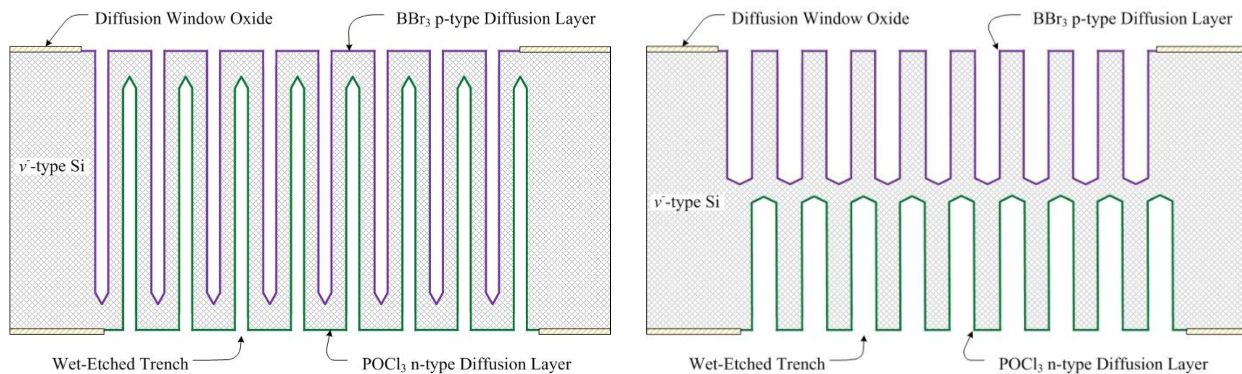

Figure 6.3: Illustrations of advanced microstructure design with (left) interlaced microstructures and (right) opposing microstructures that are etched from both sides of the silicon diode. The interlaced design offers improved charge drifting electric field potential and the opposing design offers improved neutron absorption without the need of a second off-set detector.

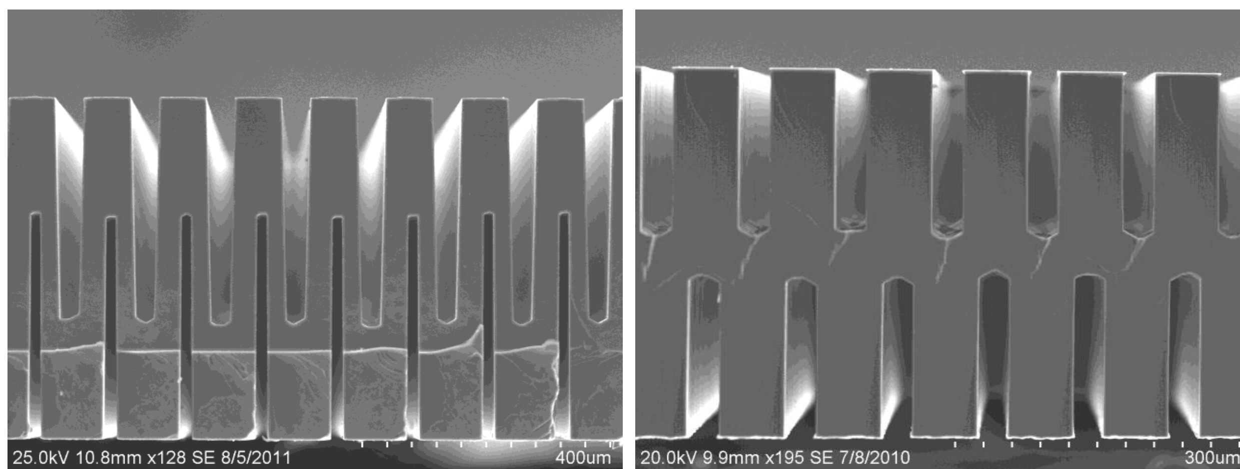

Figure 6.4: SEM pictures of wet-etched advanced microstructure designs with interlaced microstructures (left) that are etched from both sides of the silicon diode to improve charge drifting electric field potential and opposing microstructures (right) to improve neutron detection efficiency.

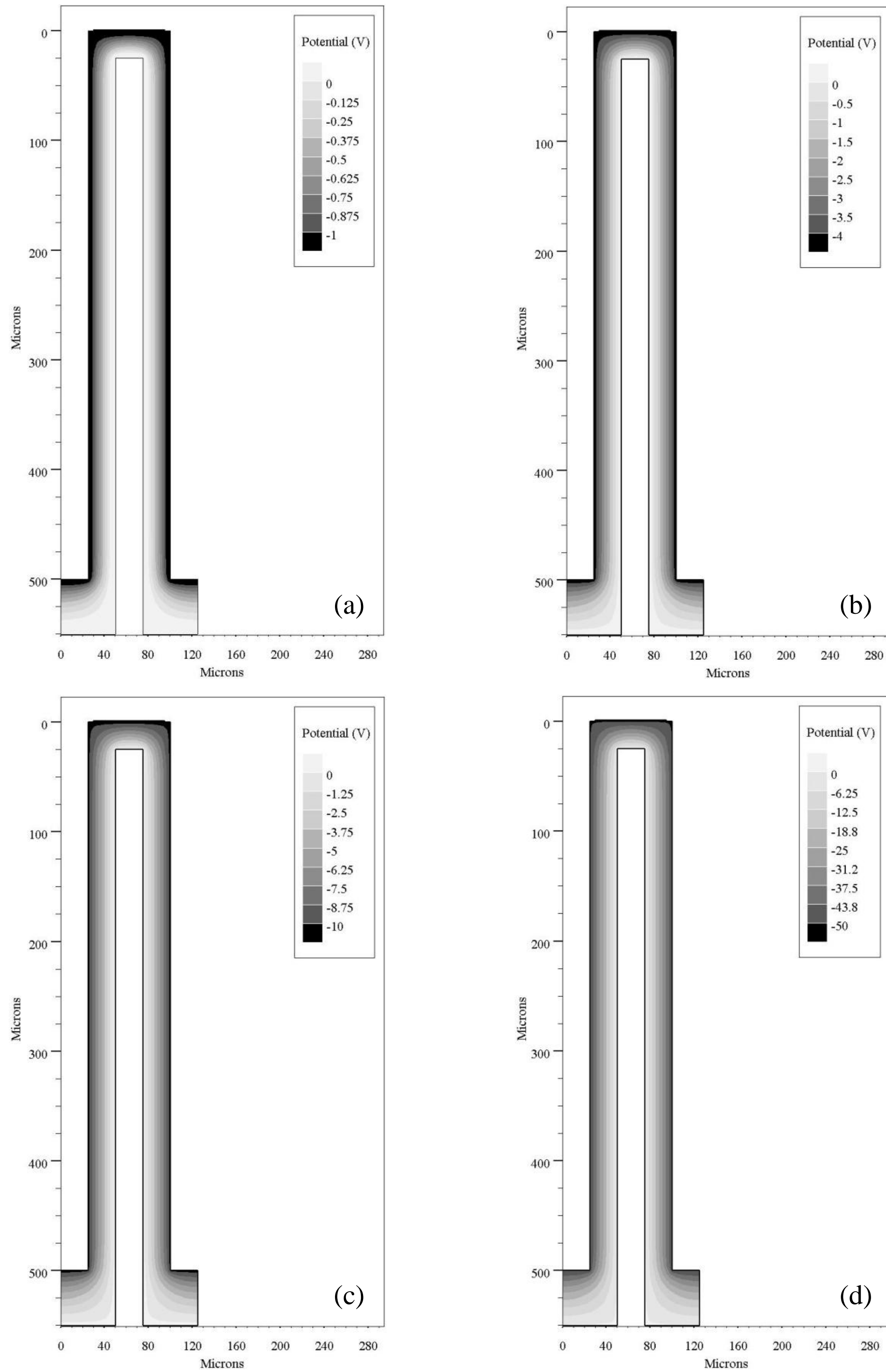

Figure 6.5: Modeled electric potential solution within conformally-diffused 10 kΩ-cm Si, 500-µm deep, 25-µm pitch, front and backside interspersed-trench MSND. Each plot key describes the electric potential gradient within the Si fin for (a) -1 V, (b) -4 V, (c) -10 V, and (d) -50 V of applied bias.

To better understand how the strong electric field scenario affects the interlaced MSND signal induction, a transient solution of current versus time was modeled. Within the diode structure, a single-event-upset was defined as a cloud, 30 μm by 10 μm dia. cylinder, of electron-hole pairs centered midway between the Si fin and at a starting depth of 5 μm from the top surface of the MSND. The amount of charge defined in the simulation was representative of the number of electron-hole pairs generated from the kinetic energy capture from the triton in a 25 μm Si fin (1.23 MeV). A time-transient solution was obtained, which revealed the current resulting at the top electrode of the MSND as a function of time. In the case of a 500 μm deep front and backside interlaced-trench MSND design, it takes 1 nanosecond to collect most of the signal pulse from the MSND (see Figure 6.6). This is a remarkable advantage over many types of neutron detectors which are much slower, e.g., the ^{3}He proportional gas detector which often operates through electron-multiplication avalanching with a representative value of several hundred microseconds for the pulse integration time [4].

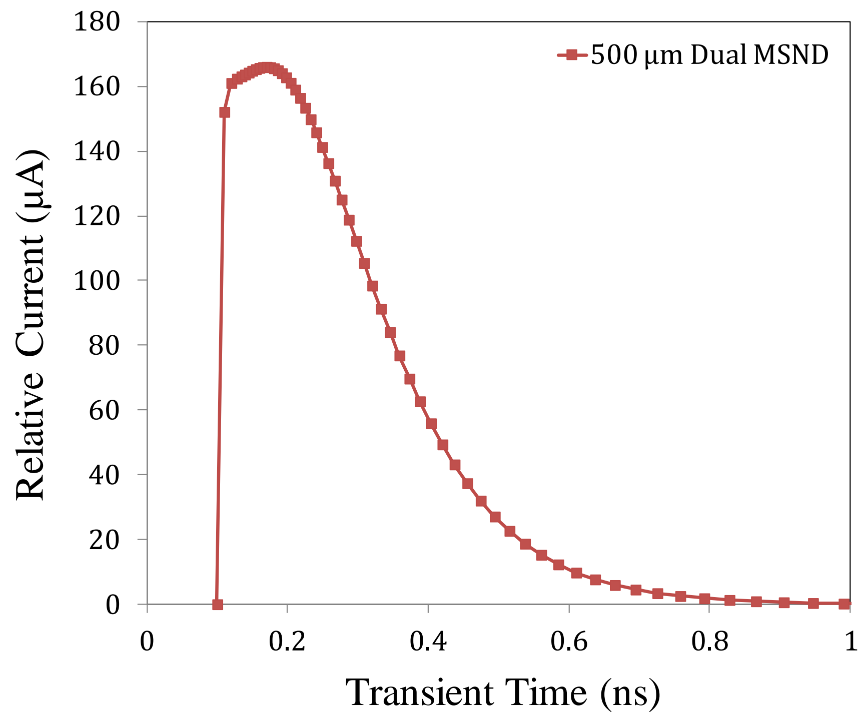

Figure 6.6: Modeled transient solution of current versus time within conformally-diffused 10 kΩ-cm Si, 500-μm deep, 25-μm pitch, front and backside interspersed-trench MSND. The silicon fin is 25 μm in width and is the same modeled geometry and 10 V potential field as shown in Figure 6.5.

LIST OF PUBLICATIONS (NOVEMBER 2011)

Refereed:

1. "Simulation of High Efficiency Dual-Integrated Stacked Microstructured Solid-State Neutron Detectors," S. L. Bellinger, J. K. Shultis, D. S. McGregor, *Nucl. Instrum. Meth. Sect. A*, (2012), *in preparation*.

2. "Arrayed High-Efficiency Dual-Integrated Stacked Microstructured Semiconductor Neutron Detectors," S. L. Bellinger, R. G. Fronk, T. J. Sobering, D. S. McGregor, *Journal of Applied Radiation and Isotopes*, *IRRMA-8 Conference Record*, (2012), *in press*.

3. "Improved High Efficiency Stacked Microstructured Neutron Detectors Backfilled with Nanoparticle 6LiF," S. L. Bellinger, R. G. Fronk, T. J. Sobering, D. S. McGregor, *IEEE Trans. Nucl. Sci.*, vol. 59, no. 1, pp. 167-173, 2012.

4. "Enhanced variant designs and characteristics of the microstructured solid-state neutron detector," S. L. Bellinger, R. G. Fronk, W. J. McNeil, T. J. Sobering, D. S. McGregor, *Nucl. Instr. and Meth.*, vol. A 652, pp. 387-391, 2011.

5. "Microstructured semiconductor neutron detectors," D. S. McGregor, W. J. McNeil, S. L. Bellinger, T. C. Unruh, J. K. Shultis, *Nucl. Instr. and Meth.*, vol. A608, pp. 125-131, 2009.

6. "Improved Fabrication Technique for Microstructured Solid-State Neutron Detectors," S. L. Bellinger, W. J. McNeil, D. S. McGregor, *MRS Spring Meeting*, pp. 57-65, 2009.

7. "Perforated Diode Neutron Detector Modules Fabricated from High-Purity-Silicon," D. S. McGregor, S. L. Bellinger, D. Bruno, W. L. Dunn, W. J. McNeil, E. Patterson, B. B. Rice, J. K. Shultis, T. C. Unruh, *Radiation Physics and Chemistry*, vol. 78, no. 10, pp. 874-881, 2009.

8. "Characteristics of 3D Micro-Structured Semiconductor High Efficiency Neutron Detectors," S. L. Bellinger, W. J. McNeil, T. C. Unruh, D. S. McGregor, *IEEE Trans. Nucl. Sci.*, vol. 56, no. 3, pp. 742-746, 2009.

9. "Design and Operation of a 2D Thin Film Semiconductor Neutron Detector Array for Use as a Beamport Monitor," T. C. Unruh, S. L. Bellinger, D. E. Huddleston, W. J. McNeil, E. Patterson, T. Sobering, R. D. Taylor, D. S. McGregor, *Nucl. Instr. and Meth.*, vol. A604, no. 1-2, pp. 150-153, 2009.

10. "1-D Array of Perforated Diode Neutron Detectors," W. J. McNeil, S. L. Bellinger, T. C. Unruh, C. M. Henderson, P. Ugorowski, B. Morris-Lee, R. D. Taylor, D. S. McGregor, *Nucl. Instr. and Meth.*, vol. A604, pp. 127-129, 2009.

Conference Proceedings:

1. "Arrayed High Efficiency Dual-Integrated Microstructured Semiconductor Neutron Detectors," S. L. Bellinger, R. G. Fronk, T. J. Sobering, D. S. McGregor, *IEEE Nucl. Sci. Sym. Conf. Rec.*, pp. 1281-1284, 2011.

2. "Characteristics of the Stacked Microstructured Solid-State Neutron Detector", S. L. Bellinger, R. G. Fronk, W. J. McNeil, J. K. Shultis, T. J. Sobering, D. S. McGregor, *Proc. SPIE - Int. Soc. Opt. Eng.*, pp. 78050-16, 2010.

3. "High Efficiency Dual-Integrated Stacked Microstructured Solid-State Neutron Detectors," S.L. Bellinger, R. G. Fronk, W. J. McNeil, T. J. Sobering, D. S. McGregor, *IEEE Nucl. Sci. Sym. Conf. Rec.*, pp. 2008-12, 2010.

4. "Variant Designs and Characteristics of Improved Microstructured Solid-State Neutron Detectors," S. L. Bellinger, W. J. McNeil, D. S. McGregor, *IEEE Nucl. Sci. Sym. Conf. Rec.*, pp. 986-989, 2009.

5. "1024-Channel Solid State 1-D Pixel Array for Small Angle Neutron Scattering," W. J. McNeil, S. L. Bellinger, T. C. Unruh, C. M. Henderson, P. B. Ugorowski, W. L. Dunn, R. D. Taylor, B. J. Blalock, C. L. Britton, D. S. McGregor, *IEEE Nucl. Sci. Sym. Conf. Rec.*, pp. 2008-2011, 2009.

6. "PATARA II: a 64-channel solid-state Neutron Detector readout system with integrated analog and digital processing for the SNS," A. G. Antonacci, J. L. Britton, S. C. Bunch, M. N. Ericson, B. J. Blalock, R. Chun, R. Greenwell, D. S. McGregor, L. Crow, L. Clonts, T. Sobering, R. Taylor, W. McNeil, S. Bellinger, C. L. Britton, Jr., *IEEE Nucl. Sci. Sym. Conf. Rec.*, pp. 68-74, 2009.

7. "Characterization of the High-Efficiency Neutron Detector Array (HENDA)," P. Ugorowski, S. Bellinger, L. Crow, C. Henderson, W. L. Dunn, W. J. McNeil, R. D. Taylor, D. S. McGregor, *IEEE Nucl. Sci. Sym. Conf. Rec.*, pp. 1901-1903, 2008.

8. "Micro-Structured High-Efficiency Semiconductor Neutron Detectors," D. S. McGregor, S. L. Bellinger, W. J. McNeil, T. C. Unruh, *IEEE Nucl. Sci. Sym. Conf. Rec.*, pp. 446-448, 2008.

9. "Angular Response of Perforated Silicon Diode High Efficiency Neutron Detectors," S. L. Bellinger, W. J. McNeil, D. S. McGregor, *IEEE Nucl. Sci. Sym. Conf. Rec.*, pp. 1904-1907, 2007.

10. "Preliminary Tests of a High Efficiency 1-D Silicon Pixel Array for Small-Angle Neutron Scattering," W. J. McNeil, S. L. Bellinger, T. Unruh, D. S. McGregor, *IEEE Nucl. Sci. Sym. Conf. Rec.*, pp. 2340-2342, 2007.

11. "Perforated Semiconductor Neutron Detector Modules for Detection of Spontaneous Fission Neutrons," D. S. McGregor, S. L. Bellinger, D. Bruno, S. Cowley, M. Elazegui, W. J. McNeil, E. Patterson, T. Unruh, C. J. Solomon, J. K. Shultis, B. B. Rice, *IEEE Conference on Technologies for Homeland Security: Enhancing Critical Infrastructure Dependability*, pp. 162-167, 2007.

12. "Perforated semiconductor neutron detectors for battery operated portable modules", D.S. McGregor, S.L. Bellinger, W.J. McNeil, J.K. Shultis, T.C. Unruh, *Proc. SPIE - Int. Soc. Opt. Eng.*, pp. 67060N1-67060N12, 2007.

13. "Perforated Semiconductor Neutron Detector Modules," D. S. McGregor, S. L. Bellinger, D. Bruno, W. J. McNeil, E. Patterson, B. B. Rice, *Proc. of 32nd Annual GOMAC Tech Conf.*, 2007.

14. "Wireless Neutron and Gamma Ray Detector Modules for Dosimetry and Remote Monitoring", D. S. McGregor, S. L. Bellinger, D. Bruno, S. Cowley, W. L. Dunn, M. Elazegui, W. J. McNeil, H. Oyenan, E. Patterson, J. K. Shultis, G. Singh, C. J. Solomon, A. Kargar, T. C. Unruh, *IEEE Nucl. Sci. Sym. Conf. Rec.*, pp. 808-812, 2007.

15. "Perforated Diode Fabrication for Neutron Detection," W. J. McNeil, S. L. Bellinger, T. C. Unruh, E. Patterson, A. Egley, D. Bruno, M. Elazegui, A. Streit, D. S. McGregor, *IEEE Nucl. Sci. Sym. Conf. Rec.*, pp. 3732-3735, 2006.

16. "HENDA and PATARA: A solid state neutron detector and a prototype readout chip for the SNS," S. Bunch, J. L. Britton, B. J. Blalock, C. L. Britton, D. S. McGregor, R. Taylor, T. Sobering, D. Huddleston, W. McNeil, T. Unruh, B. B. Rice, S. Bellinger, B. Cooper, L. Crow, *6th International Meeting on Front End Electronics for High Energy, Nuclear, Medical and Space Applications*, May 17-20, Italy, 2006.

17. "Perforated Semiconductor Diodes for High Efficiency Solid State Neutron Detectors," D.S. McGregor, et al., *Presentation Recorded in the Conference Record of the Workshop on Use of Monte Carlo Techniques for Design and Analysis of Radiation Detectors*, Coimbra, Portugal, September 15-17, 2006.

Patents:

- D.S. McGregor, S.L. Bellinger, W.J. McNeil, E.L. Patterson, B.B. Rice, J.K. Shultis, C.J. Solomon, "Non-Streaming High-Efficiency Perforated Semiconductor Neutron Detectors, Methods of Making Same and Measuring Wand and Detector Modules Utilizing Same", US-7855372, Allowed Dec. 21, 2010.

- Steven L. Bellinger, Anthony N. Caruso, Brian Cooper, William L. Dunn, Ryan G. Fronk, Douglas S. McGregor, William H. Miller, Eliot R. Myers, Thomas M. Oakes, Phil B. Ugorowski, John K. Shultis, Tim J. Sobering, “Apparatuses and Methods for the Identification of Free Neutron Properties”, USPTO Provisional No. (TBD – filed under secrecy order 37 CFR 5.2), Filed Oct. 27, 2011.

REFERENCES

[1] J. Chadwick, “The Existence of a Neutron,” pp. 692-708, 1932.

[2] P. J. V. Heerden, *The crystal counter,* Utrecht Dissertation, 1945.

[3] R. V. Babcock, R. E. Davis, S. L. Ruby *et al.*, “Coated Semiconductor Is Tiny Neutron Detector,” *Nucleonics*, no. 17, pp. 116-122, 1959.

[4] G. F. Knoll, *Radiation Detection and Measurement*, 4th ed., New York: Wiley, 2010.

[5] A. Cho, “Helium-3 Shortage Could Put Freeze On Low-Temperature Research,” *AAAS Science,* vol. 326, no. 5954, pp. 778-779, Nov. 6, 2009.

[6] N. Tsoulfanidis, *Measurement and Detection of Radiation*, 3rd ed., Washington, DC: CRC Press, 2010.

[7] D. S. McGregor, M. D. Hammig, H. K. Gersch *et al.*, “Design Considerations for Thin Film Coated Semiconductor Thermal Neutron Detectors, Part I: Basics Regarding Alpha Particle Emitting Neutron Reactive Films,” *Nucl. Instrum. and Meth.,* vol. A500, pp. 272-308, 2003.

[8] R. A. Muminov, and L. D. Tsvang, “High-Efficiency Semiconductor Thermal-Neutron Detectors,” *Soviet Atomic Energy,* vol. 62, no. 4, pp. 316-319, 1987.

[9] J. Schelten, M. Balzhauser, F. Hongesberg *et al.*, “A New Neutron Detector Development Based on Silicon Semiconductor and ^{6}LiF Converter,” *Physica B,* vol. 234-236, pp. 1084-1086, 1997.

[10] J. Schelten, and R. Reinartz, *Neutron Detector*, Patent, U.S.P.T.O., US-58804762, March 9, 1999.

[11] C. P. Allier, *Micromachined Si-well scintillator pixel detectors*, Netherlands: DUP Science, 2001.

[12] D. S. McGregor, R. T. Klann, J. D. Sanders *et al.*, "Recent Results From Thin-Film-Coated Semiconductor Neutron Detectors," *Proc. SPIE - Int. Soc. Opt. Eng.*, pp. 164-182, 2002.

[13] C. P. Allier, R. W. Hollander, P. M. Sarro *et al.*, "Thin photodiodes for a scintillator-silicon well detector," *IEEE Nucl. Sci. Sym. Conf. Rec.*, pp. 198-198, 1998.

[14] C. P. Allier, R. W. Hollander, C. W. E. van Eijk *et al.*, “Thin Photodiodes for a Neutron Scintillator Silicon-Well Detector,” *IEEE Trans. Nucl. Sci.,* vol. 48, no. 4, pp. 1154-1157, Aug., 2001.

[15] D. S. McGregor, R. T. Klann, H. K. Gersch *et al.*, “New Surface Morphology for Low Stress Thin-Film-Coated Thermal-neutron Detectors,” *IEEE Trans. Nucl. Sci.,* vol. 49, no. 4, pp. 1999-2004, Aug., 2002.

[16] D. S. McGregor, R. T. Klann, H. K. Gersch *et al.*, "New surface morphology for low stress thin-film-coated thermal neutron detectors," *IEEE Nucl. Sci. Sym. Conf. Rec.*, pp. 2401-2405, 2001.

[17] J. K. Shultis, and D. S. McGregor, “Efficiencies of Coated and Perforated Semiconductor Neutron Detectors,” *IEEE Nucl. Sci. Sym. Conf. Rec.,* vol. 53, no. 3, pp. 1659-1665, 2006.

[18] J. K. Shultis, and D. S. McGregor, “Efficiencies of Coated and Perforated Semiconductor Neutron Detectors,” *IEEE Nucl. Sci. Sym. Conf. Rec.,* vol. 7, pp. 4569-4574, 2004.

[19] W. J. McNeil, S. L. Bellinger, T. Unruh *et al.*, "Perforated Diode Fabrication for Neutron Detection," *IEEE Nucl. Sci. Sym. Conf. Rec.*, pp. 3732-3735, 2006.

[20] B. B. Rice, *Inductively Coupled Plasma Etching of Silicon and Gallium Arsenide,* M.S. Thesis, Kansas State University, Manhattan, KS, 2006.

[21] S. L. Bellinger, R. G. Fronk, W. J. McNeil *et al.*, "High Efficiency Dual-Integrated Stacked Microstructured Solid-State Neutron Detectors," *IEEE Nucl. Sci. Sym. Conf. Rec.*, pp. 2008-2012, 2010.

[22] S. L. Bellinger, R. G. Fronk, W. J. McNeil *et al.*, "Characteristics of the Stacked Microstructured Solid-State Neutron Detector," *Proc. SPIE - Int. Soc. Opt. Eng.*, pp. 78050-16, 2010.

[23] S. L. Bellinger, R. G. Fronk, W. J. McNeil *et al.*, “Enhanced Variant Designs and Characteristics of the Microstructured Solid-State Neutron Detector,” *Nucl. Instrum. and Meth.,* vol. A652, pp. 387-391, 2011.

[24] S. L. Bellinger, W. J. McNeil, and D. S. McGregor, "Improved Fabrication Technique for Microstructured Solid-State Neutron Detectors," *MRS Spring Meeting*, pp. 57-65, 2009.

[25] S. L. Bellinger, W. J. McNeil, and D. S. McGregor, "Variant Designs and Characteristics of Improved Microstructured Solid-State Neutron Detectors," *IEEE Nucl. Sci. Sym. Conf. Rec.*, pp. 986-989, 2009.

[26] S. L. Bellinger, W. J. McNeil, T. C. Unruh *et al.*, "Angular Response of Perforated Silicon Diode High Efficiency Neutron Detectors," *IEEE Nucl. Sci. Sym. Conf. Rec.*, pp. 1904-1907, 2007.

[27] S. L. Bellinger, W. J. McNeil, T. C. Unruh *et al.*, “Characteristics of 3D Micro-Structured Semiconductor High Efficiency Neutron Detectors,” *IEEE Trans. Nucl. Sci.,* vol. 56, no. 3, pp. 742-746, 2009.

[28] A. M. Conway, T. F. Wang, N. Deo *et al.*, “Numerical Simulations of Pillar Structured Solid State Thermal Neutron Detector: Efficiency and Gamma Discrimination,” *IEEE Trans. Nucl. Sci.,* vol. 56, no. 5, pp. 2802-2807, 2009.

[29] J. Dingley, Y. Danon, N. LiCausi *et al.*, "Optimization of a Novel Solid-State Self Powered Neutron Detector," *Int. Conf. on Math., Comp. Meth., & Reactor Physics*, pp. 952-963, LaGrange Park, 2009.

[30] C. M. Henderson, Q. M. Jahan, W. L. Dunn *et al.*, “Characterization of Prototype Perforated Semiconductor Neutron Detectors,” *Radiation Physics and Chemistry*, no. 79, pp. 144-150, 2010.

[31] Q. Jahan, E. Patterson, B. Rice *et al.*, “Neutron Dosimeters Employing High-efficiency Perforated Semiconductor Detectors,” *Nucl. Instrum. and Meth.,* vol. B263, pp. 183-185, 2007.

[32] N. LiCausi, J. Dingley, Y. Danon *et al.*, "A novel solid state self-powered neutron detector " *Proc. SPIE - Int. Soc. Opt. Eng.*, pp. 707908-12, 2008.

[33] D. S. McGregor, S. L. Bellinger, D. Bruno *et al.*, "Wireless Neutron and Gamma Ray Detector Modules for Dosimetry and Remote Monitoring," *IEEE Nucl. Sci. Sym. Conf. Rec.*, pp. 808-812, 2007.

[34] D. S. McGregor, S. L. Bellinger, D. Bruno *et al.*, "Perforated Semiconductor Neutron Detector Modules for Detection of Spontaneous Fission Neutrons," *IEEE Conference on Technologies for Homeland Security: Enhancing Critical Infrastructure Dependability*, pp. 162-167, Woburn, MA, 2007.

[35] D. S. McGregor, S. L. Bellinger, D. Bruno *et al.*, “Perforated Diode Neutron Detector Modules Fabricated from High-Purity-Silicon,” *Radiation Physics and Chemistry*, no. 78, pp. 195-207, 2009.

[36] D. S. McGregor, S. L. Bellinger, D. Bruno *et al.*, “Perforated Semiconductor Neutron Detector Modules,” *Proc. of 32nd Annual GOMAC Tech Conf.*, 2007.

[37] D. S. McGregor, S. L. Bellinger, D. Bruno *et al.*, "Perforated Semiconductor Neutron Detectors for Battery Operated Portable Modules," *Proc. SPIE - Int. Soc. Opt. Eng.* , pp. 67060N1-67060N12, 2007.

[38] D. S. McGregor, S. L. Bellinger, W. J. McNeil *et al.*, "Micro-Structured High-Efficiency Semiconductor Neutron Detectors," *IEEE Nucl. Sci. Sym. Conf. Rec.*, pp. 446-448, 2008.

[39] W. J. McNeil, “Perforated Diode Neutron Sensors,” Ph.D. Dissertation, Kansas State University, Manhattan, KS, 2010.

[40] W. J. McNeil, S. L. Bellinger, T. C. Unruh *et al.*, "1024-Channel Solid State 1-D Pixel Array for Small Angle Neutron Scattering," *IEEE Nucl. Sci. Sym. Conf. Rec.*, pp. 2008-2011, Orlando, Florida, 2009.

[41] W. J. McNeil, S. L. Bellinger, T. C. Unruh *et al.*, "1-D Array of Perforated Diode Neutron Detectors," *Nucl. Instrum. and Meth.,* vol. A604, pp. 127-129, 2009.

[42] R. J. Nikolic, A. M. Conway, R. Radev *et al.*, "Nine Element Si-based Pillar Structured Thermal Neutron Detector," *Proc. SPIE - Int. Soc. Opt. Eng.*, pp. 78050, 2010.

[43] R. J. Nikolic, A. M. Conway, C. E. Reinhardt *et al.*, "Fabrication of pillar-structured thermal neutron detectors," *IEEE Nucl. Sci. Sym. Conf. Rec.*, pp. 1577-1580, 2007.

[44] R. J. Nikolic, A. M. Conway, C. E. Reinhardt *et al.*, "6:1 Aspect Ratio Silicon Pillar Based Thermal Neutron Detector Filled with ^{10}B," *Appl. Phys. Lett.,* vol. 93, no. 13, pp. 133502-5, 2008.

[45] J. K. Shultis, and D. S. McGregor, "Designs for Micro-Structured Semiconductor Neutron Detectors," *Proc. SPIE - Int. Soc. Opt. Eng.*, pp. 707906-15, 2008.

[46] J. K. Shultis, and D. S. McGregor, "Design and Performance Considerations for Perforated Semiconductor Thermal-Neutron Detectors," *Nucl. Instrum. and Meth.,* vol. A606, pp. 608-636, 2009.

[47] C. J. Solomon, J. K. Shultis, and D. S. McGregor, "Reduced Efficiency Variation in Perforated Neutron Detectors with Sinusoidal Trench Design," *Nucl. Instrum. and Meth.,* vol. A618, pp. 260-265, 2010.

[48] C. J. Solomon, J. K. Shultis, W. J. McNeil *et al.*, "A Hybrid Method for Coupled Neutron-Ion Transport Calculations for ^{10}B and ^{6}LiF Coated and Perforated Detector Efficiencies," *Nucl. Instrum. and Meth.,* vol. A580, pp. 326-330, 2007.

[49] J. Uher, C. Frojdh, J. Jakubek *et al.*, "Characterization of 3D Thermal Neutron Semiconductor Detectors," *Nucl. Instrum. and Meth.,* vol. A576, pp. 32-37, 2007.

[50] T. C. Unruh, "Development of a neutron diffraction system and neutron imaging system for beamport characterization," M.S. Thesis, Kansas State University, Manhattan, KS, 2009.

[51] S. K. Ghandhi, *VLSI Fabrication Principles: Silicon and Gallium Arsenide*, USA: John Wiley & Sons, 1983.

[52] S. M. Sze, *Semiconductor Devices: Physics and Technology*, USA: John Wiley & Sons, 1985.

[53] E. Rutherford, "Bakerian Lecture: Nuclear Constitution of Atoms," *Proceedings of the Royal Society of London,* vol. 97, pp. 374-400, 1920.

[54] P. A. Tipler, and R. A. Llewellyn, *Modern Physics*, p. 508, New York, U.S.A.: W.H. Freeman and Company, 2003.

[55] R. D. Evans, *The Atomic Nucleus*, New York: Krieger, 1958.

[56] P. A. Tipler, and R. A. Llewellyn, "Modern Physics," p. 508, New York, U.S.A.: W.H. Freeman and Company, 2003.

[57] Knolls Atomic Power Laboratory, *Chart of the Nuclides and Isotopes*, 16 ed.: Lockheed Martin Distribution Services, 2002.

[58] J. K. Shultis, and R. E. Faw, *Fundamentals of Nuclear Science and Engineering*, Boca Raton, U.S.A.: CRC Press, 2008.

[59] I. Laue-Langevin, "Neutrons for Science," http://www.ill.eu/, [December, 2010].

[60] G. F. Knoll, *Radioisotope Neutron Sources*, New York: Pergamon Press, 1983.

[61] *Neutron Sciences*, Oak Ridge National Laboratory, http://neutrons.ornl.gov/, [December, 2010].

[62] NIST Center for Neutron Research, http://www.ncnr.nist.gov/resources/n-lengths/elements/si.html, [June, 2010].

[63] L. V. Groshev, A. M. Demidov, V. A. Ivanov *et al.*, "Gamma-rays and conversion electrons from the (n, γ) reaction on gadolinium isotopes," *Izvestiya Akademii Nauk SSSR,* vol. 26, no. 9, pp. 1119-1133, 1962.

[64] Y. Y. Berzin', P. T. Prokof'ev, and G. L. Rezvaya, "Conversion electron spectrum emitted at thermal neutron capture by ^{155}Gd nuclei," *Latvijas PSR Zinatnu Akademijas Vestis, Fizikas un Tehnisko Zinatnu Serija*, no. 6, pp. 3-8, 1968.

[65] Y. Y. Berzin', A. E. Kruminya, L. A. Neiburg *et al.*, "Conversion electron and γ-ray spectra from thermal neutron capture in ^{157}Gd," *Latvijas PSR Zinatnu Akademijas Vestis, Fizikas un Tehnisko Zinatnu Serija*, no. 5, pp. 3-7, 1972.

[66] N. E. Holden, *Helium Isotopic Abundance Variation in Nature.,* BNL-49331, 1993.

[67] E. S. Greiner, and J. A. Gutowski, "Electrical Resistivity of Boron," *Journal of Applied Physics,* vol. 28, no. 11, pp. 1364-1365, 1957.

[68] K. A. Nelson, S. L. Bellinger, J. L. Neihart *et al.*, "Investigation of Aerogel, Saturated Foam, and Foil for Thermal Neutron Detection," *IEEE Nucl. Sci. Sym. Conf. Rec.*, Valencia, Spain, 2011.

[69] I. L. Fowler, "Very Large Boron Trifluoride Proportional Counters," *Rev. Sci. Intrum.,* vol. 34, no. 7, pp. 731-739, 1963.

[70] D. S. McGregor, W. J. McNeil, S. L. Bellinger *et al.*, "Microstructured Semiconductor Neutron Detectors," *Nucl. Instrum. and Meth.,* vol. A608, pp. 125-131, 2009.

[71] S. Normand, B. Mouanda, S. Haan *et al.*, "Discrimination methods between neutron and gamma rays for boron loaded plastic scintillators," *Nucl. Instrum. and Meth.,* vol. A484, no. 1-3, pp. 342-350, May, 2002.

[72] M. V. Prokuronov, A. A. Golubev, V. S. Demidov *et al.*, "A digital method for pulse-shape discrimination between particles," *Instruments and Experimental Techniques,* vol. 49, no. 2, pp. 207-222, 2006.

[73] M. Suffert, "Silicon photodiode readout of scintillators and associated electronics," *Nucl. Instrum. and Meth.,* vol. A322, no. 3, pp. 523-528, Nov., 1992.

[74] A. G. Beyerle, and K. L. Hull, "Neutron Detection With Mercuric Iodide Detectors," *Nucl. Instrum. and Meth.,* vol. A256, no. 2, pp. 377-380, 1987.

[75] D. S. McGregor, J. T. Lindsay, and R. W. Olsen, "Thermal neutron detection with cadmium$_{1-x}$ zinc$_x$ telluride semiconductor detectors," *Nucl. Instrum. and Meth.,* vol. A381, no. 2-3, pp. 498-501, Nov., 1996.

[76] D. S. McGregor, T. C. Unruh, and W. J. McNeil, "Thermal neutron detection with pyrolytic boron nitride," *Nucl. Instrum. and Meth.,* vol. A591, no. 3, pp. 530-533, 2008.

[77] W. C. McGinnis, *Film Implementation of a Neutron Detector (FIND): Proof of Concept Device,* Technical Report 1921, SPAWAR San Diego, 2003.

[78] J. K. Shultis, and D. S. McGregor, "Spectral Identification of Thin-Film-Coated and Solid-Form Semiconductor Neutron Detectors," *Nucl. Instrum. and Meth.,* vol. A517, pp. 180-188, 2004.

[79] J. Uher, S. Pospisil, V. Linhart *et al.*, "Efficiency of composite boron nitride neutron detectors in comparison with helium-3 detectors," *Appl. Phys. Lett.,* vol. 90, no. 12, pp. 124101-2, 2007.

[80] P. A. Dowben, A. N. Caruso, S. Balkir *et al.*, "The all boron carbide diode neutron detector: Comparison with theory," *Mater. Sci. Eng. B, Solid-State Mater. Adv. Technol.,* vol. 135, no. 2, pp. 129-133, 2006.

[81] *Neutron Detectors,* 18, International Atomic Energy Agency, Bibliographical Series, Vienna, 1966.

[82] W. Shockley, "Currents to Conductors Induced by a Moving," *Journal of Applied Physics,* vol. 9, pp. 635-636, 1938.

[83] S. Ramo, "Currents Induced by Electron Motion," *Proceedings of the IRE,* vol. 27, pp. 584-585, 1939.

[84] J. K. Shultis, and D. S. McGregor, *Calculation of Ion Energy-Deposition Spectra in Silicon, Lithium-Fluoride, Boron, and Boron Carbide,* Engineering Experiment Station 299, Manhattan, Kansas 66506, 2004.

[85] S. M. Sze, and K. N. Kwok, *Physics of semiconductor devices*, Hoboken, NJ, USA: Wiley-Interscience, 2007.

[86] K. E. Bean, and R. J. Lawson, "Application of Silicon Crystal Orientation and Anisotropic Effects to the Control of Charge Spreading in Devices," *IEEE Journal of Solid-State Circuits,* vol. SC-9, no. 3, pp. 111-117, June, 1974.

[87] NIST Ionizing Radiation Division, *Standard Reference Database 126*, http://physics.nist.gov/PhysRefData/XrayMassCoef/ElemTab/z14.html, [Nov., 2011].

[88] D. S. McGregor, and R. T. Klann, *Pocked Surface Neutron Detector*, Patent, U.S.P.T.O., US-6545281, April 8, 2003.

[89] P. G. Neudeck, "Silicon Carbide Technology," *The VLSI Handbook*, NASA Glenn Research Center, United States of America: CRC Press LLC, 2006.

[90] J. K. Shultis, and R. E. Faw, *Radiation Shielding*, Upper Saddle River, N.J., U.S.A.: Prentice Hall PTR, 1996.

[91] C. J. Solomon, *Analysis and characterization of perforated neutron detectors,* Masters Thesis, Manhattan, KS, 2007.

[92] D. S. McGregor, and J. K. Shultis, "Reporting Detection Efficiency for Semiconductor Neutron Detectors: A Need for a Standard," *Nucl. Instrum. and Meth.,* vol. A632, no. 1, pp. 167-174, 2011.

[93] J. K. Shultis, and D. S. McGregor, "Efficiencies of Coated and Perforated Semiconductor Neutron Detectors," *IEEE Trans. Nucl. Sci.,* vol. 53, no. 3, pp. 1659-65, June, 2006.

[94] A. Coche, and P. Siffert, "N-P Detectors," *Semiconductor Detectors*, pp. 103-148, Amsterdam, Netherlands: North-Holland Publishing Company, 1968.

[95] G. Lutz, *Semiconductor Radiation Detectors*, Munich, Germany: Springer-Verlag Berlin Heidelberg, 1999.

[96] S. Campbell, *Fabrication Engineering at the Micro- and Nanoscale*, New York, U.S.A.: Oxford University Press, 2008.

[97] F. Marty, L. Rousseau, B. Saadany *et al.*, "Advanced etching of silicon based on deep reactive ion etching for silicon high aspect ratio microstructures and three-dimensional micro- and nanostructures," *Microelectronics Journal,* vol. 36, no. 7, pp. 673-677, 2005.

[98] F. Larmer, and A. Schilp, *Method of anisotropically etching silicon*, Patent, U.S.P.T.O., US-5501893, March 26, 1996.

[99] *PlasmaProNGP®1000 Large Batch Next Generation Plasma System*, Oxford Instruments, http://www.oxford-instruments.com/products/etching-deposition-growth/tools/tools/NGP1000/Pages/NGP1000.aspx, [Febuary, 2011].

[100] K. E. Bean, "Anisotropic Etching of Silicon," *IEEE Trans. on Electron Devices,* vol. ED-25, no. 10, pp. 1185-1193, 1978.

[101] H. Seidel, L. Csepregi, A. Heuberger *et al.*, "Anisotropic Etching of Crystalline Silicon in Alkaline Solutions," *J. Electrochem. Soc.,* vol. 137, no. 11, pp. 3612-3626, Nov., 1990.

[102] H. Lim, and Y. Kim, "Novel Fabrication of Comb Actuator Using Reactive Ion Etching of Polysilicon and (110) Si Anisotropic Bulk Ethcing in KOH," *Jpn. J. Appl. Phys.,* vol. 37, no. 12B, pp. 7086-7092, 1998.

[103] D. L. Kendall, and G. R. de Guel, *Micromachining and Micropackaging of Transducers*, Amsterdam: Elsevier, 1985.

[104] K. Sato, M. Shikida, T. Yamashiro *et al.*, "Anisotropic etching rates of single-crystal silicon for TMAH water solution as a function of crystallographic orientation," *Sensors and Actuators A (Physical),* vol. A73, no. 1-2, pp. 131-137, 1999.

[105] E. D. Haberer, *Appl. Phys. Lett.*, no. 76, pp. 3941, 2000.

[106] W. J. Price, *Nuclear Radiation Detection*, New York: McGraw-Hill, 1964.

[107] J. T. Baker Microelectronic Materials, "Advances in Cleaning Technologies Using JTB-100 in the BakeClean Process," http://www.mallbaker.com/micro/documents/performance/lit%204927.pdf, [Aug., 2009].

[108] W. van Gelder, and V. E. Hauser, "The Etching of Silicon Nitride in Phosphoric Acid with Silicon Dioxide as a Mask," *J. Electrochem. Soc.,* vol. 114, no. 8, pp. 869-872, 1967.

[109] I. Zubel, and M. Kramkowska, "Analysis of Interaction of Surfactant Molecules with Si (hkl) Planes on the Basis of Anisotropic Etching in Alkaline Solutions," *Proceedings of the III National Conference on Nanotechnology NANO*, pp. S-105-S107, 2009.

[110] J. Ya-Min Lee, "Reduction of Leakage Current of Large-Area High-Resistivity Silicon p-i-n Photodiodes for Detection at 1.06 pm," *IEEE Trans. on Electron Devices,* vol. ED-28, no. 4, pp. 412-416, April, 1981.

[111] G. Cao, *Nanostructures and Nanomaterials - Synthesis, Properties and Applications*: World Scientific, 2004.

[112] S. L. Bellinger, R. G. Fronk, T. J. Sobering *et al.*, "Improved High Efficiency Stacked Microstructured Neutron Detectors Backfilled with Nanoparticle ^{6}LiF," *IEEE Trans. Nucl. Sci.,* vol. 59, no. 1, pp. 167-173, 2012.

[113] S. Friedlander, *Smoke, Dust, and Haze: Fundamentals of Aerosol Dynamics*, New York: Oxford, 2000.

[114] S. Cingarapu, "Synthesis of CdSe Quantum Dots by Evaporation of Bulk CdSe Using SMAD and Digestive Ripening Processes," *Chemistry of Materials,* vol. 21, no. 7, pp. 1248-1252, 2009.

[115] S. Stobbe, "Frequency Dependence of the Radiative Decay Rate of Excitons in Self-Assembled Quantum Dots: Experiment and Theory," *Phys. Rev. B, Condens. Matter Mater. Phys.,* vol. 80, no. 15, pp. 155307, 2009.

[116] Bi-CMOS Foundry, http://www.bicmosfoundry.com/, [April, 2011].

[117] Kansas State University, "Semiconductor Materials And Radiological Technologies (S.M.A.R.T.) Laboratory," http://www.mne.ksu.edu/research/centers/SMARTlab,

[118] R. F. Lever, and H. M. Demsky, "Water vapor as an oxidant in BBr3 open-tube silicon diffusion systems," *IBM J. Res. Dev.*, no. 18, pp. 40-46, 1974.

[119] Halliday, Resnick, and Walker, *Fundamentals of Physics*, Danvers, U.S.A.: John Wiley & Sons, Inc., 2001.

[120] Bureau of Radiological Health, *Radiological Health Handbook*, Washington, D.C., United States of America: U.S. Government Printing Office, 1970.

[121] D. S. McGregor, and R. T. Klann, *High-Efficiency Neutron Detectors and Methods of Making the Same*, Patent, U.S.P.T.O., US-7164138, January 16, 2007.

[122] *TCAD Software*, SILVACO, www.silvaco.com, [May, 2011].

[123] J. F. Ziegler, "The Stopping and Range of Ions in Matter SRIM," http://www.srim.org, [Aug. 2011, Ver. 2006.02].

[124] M. S. Gordon, P. Goldhagen, K. P. Rodbell *et al.*, "Measurement of the flux and energy spectrum of cosmic-ray induced neutrons on the ground," *IEEE Trans. Nucl. Sci.,* vol. 51, no. 6, pp. 3427-3434, 2004.

[125] R. L. Walsh, "Spin-Dependent Calculation of Fission Neutron Spectra and Fission Spectrum Integrals for Six Fissioning Systems," *Nucl. Sci. Eng.*, no. 102, pp. 119-133, 1989.

[126] R. B. Schwartz, and C. M. Eisenhauer, "The Design and Construction of a D_2O-Moderated ^{252}Cf Source for Calibrating Neutron Personnel Dosimeters Used at Nuclear Power Reactors," *Division of Siting, Health and Safeguards Standards, NIST*, 1979.

[127] "Bonner Ball Neutron Detector (BBND)," http://www.nasa.gov/mission_pages/station/research/experiments/BBND.html, [September 10, 2011].

[128] J. F. Ziegler, and J. P. Biersack, "Stopping and Range of Ions in Matter," SRIM-2000.40, 2002.

[129] *MatLab*, MathWorks, http://www.mathworks.com/products/matlab/, [Version, 2006b].

APPENDIX A - MSND MODEL DETAIL

A. 1 Empirical Fits for ^{6}LiF Ion Data

To estimate the ion energy deposited in each material structure region, all the ions are assumed to travel approximately in straight lines. This assumption is based on the ions of boron having heavy mass and high kinetic energy, unlike that of the easily scattered electron. Energy straggling and scattering events will be ignored for this simulation because of the complex nature of applying these physics. From the straight line assumption, the energy deposited in the separate microstructured regions of ^{6}LiF and silicon is directly related to the path-length of the ion through the material of each region from beginning to end, which may be more than once because of the mirror reflection at the unit cell boundary. Because the size of the unit cell may be smaller than the total path length of a specific ion (particularly the higher energy triton ion), the ion was reflected at the unit cell boundary to account for the additional travel in the total MSND structure (see Figure A.1). This method simplifies individual structure definitions within the simulation code by reducing the structure boundary description. Finally, the ion kinetic energy deposited in the silicon detector region calculated over every path-length segment, is summed with the energy deposited by its ion production pair and tallied in the respective energy bin to simulate the detector response spectra. [84]

To calculate the approximate energy lost over each path-length segment, two empirical functions were used. The first is the mean residual energy $\overline{E}_m^i(x)$, which is the residual energy of an ion of a specific type *i*, after it travels some distance *x* in material *m* [84]. The mean residual energy empirical function was developed by *Shultis et al.*, through the use of the SRIM code [128], for silicon and ^{6}LiF-converter materials [84]. The empirical formulas developed for the alpha and triton ^{6}Li reaction-product ions specific residual-energy after a specified path-length *x*

(μm) in silicon are given by Eqs. A1.1 and A1.2, respectively, with corresponding fitting parameters in Table A1.1.

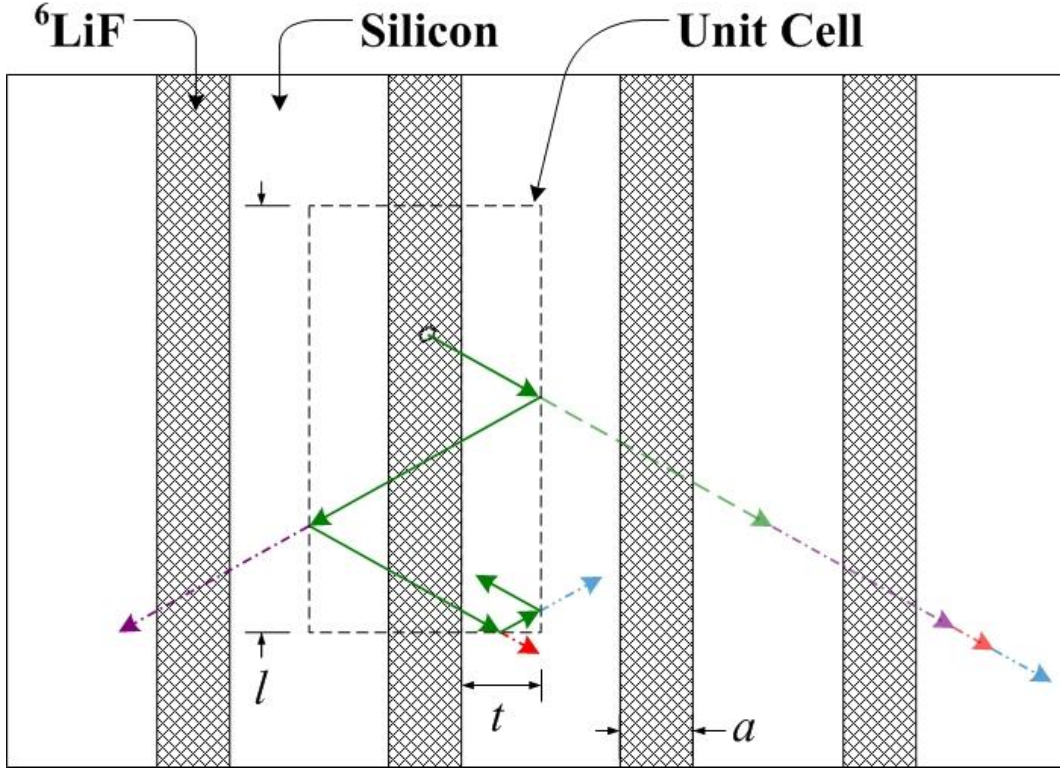

Figure A.1: Illustrated is the unit cell boundary for each microstructured pattern. Notice that because of the symmetry of the unit cell, an ion can be mirrored (shown with arrows in the straight trench pattern illustration) at the boundary and still travel through the same amount of material as if the boundary were not present. The unit cell boundary for the straight trench pattern is aligned to the half thickness t of the silicon fin, which is on either side of the solid ^{6}LiF backfill material. The length l of the unit cell is arbitrary and defined in the simulation as l = 3(2t+a).

$$\overline{E}_{^4\text{He}}(x) = \frac{a + cx + ex^2}{1 + bx + dx^2 + fx^3} \quad \text{(A1.1)}$$

$$\overline{E}_{^3\text{H}}(x) = \exp\left[\frac{a + cx + ex^2}{1 + bx + dx^2}\right] \quad \text{(A1.2)}$$

Table A1.1: Parameters for fitting the empirical formulas for the ^{6}Li residual ion energies in silicon, *E(x)* [84].

Parameter	^{4}He [Eq. (A1.1)] (2.0553MeV)	^{3}H [Eq. (A1.2)] (2.728MeV)
a	2.0549684169	0.99849937868
b	-0.1483764308	-0.03278510295
c	-0.5570727178	-0.04902551060
d	-0.0005753511	0.00022141343
e	0.0377800136	0.00054282700
f	0.0007588408	--

The empirical formula developed for the alpha and triton ^{6}Li reaction-product ions specific residual-energy after a specified path-length x (μm) in LiF is given by Eq. A1.1 and Eq. A1.2, respectively, with corresponding fitting parameters in Table A1.2.

Table A1.2: Parameters for fitting the empirical formula for the ^{6}Li residual ion energies in LiF, *E(x)* [84].

Parameter	^{4}He [Eq. (A1.1)] (2.0553MeV)	^{3}H [Eq. (A1.2)] (2.728MeV)
a	2.045795872242	1.002503409342
b	-0.161868152261	-0.043787370382
c	-0.665680395107	-0.065185375563
d	-0.000407316315	0.000410451552
e	0.054192529543	0.000957069819
f	0.001694213790	--

Next, the second function to determine the deposited energy in each material region, is to know the path-length segment in material m for some type i ion, in which to obtain a mean residual energy E. This path-length function is the inverse of the residual energy $\overline{E}^{\,i}_{m}(x)$, and is expressed as $\overline{X}^{\,i}_{m}(E)$. With this collective information, the residual energy can be calculated with

Eq. A1.1 and Eq. A1.2, from any residual energy state (note that these equations only give the residual energy from the path-length starting at the original energy of the ion, that is why the additional path-length estimation is necessary). The empirical formulas developed for the alpha and triton ^{6}Li reaction products ions' specific path-length traveled X (μm) after a specified residual energy E (MeV) in silicon are given by Eq. A1.3 and Eq. A1.4, respectively, with corresponding fitting parameters in Table A1.3.

$$\overline{X}_{^4\mathrm{He}}\left(E\right) = a + b\sqrt{E} + cE + dE^{3/2} + eE^2 + fE^{5/2} + gE^3 \qquad (A1.3)$$

$$\overline{X}_{^3\mathrm{H}}\left(E\right) = a - bE + cE^2 + dE^2\ln E + e\sqrt{E}\ln E \qquad (A1.4)$$

Table A1.3: Parameters for fitting the empirical formula for the path length to reach energy *E*, *X(E)*, in silicon for ions produced by the ^{6}Li neutron reaction [84].

Parameter	^{4}He [Eq. (A1.3)] (2.0553MeV)	^{3}H [Eq. (A1.4)] (2.728MeV)
a	7.650654782456231	42.55432730826800
b	-2.951907906029242	6.126822912741065
c	-3.226254043595208	-5.405288206496186
d	12.90757367270686	1.274522449649497
e	-19.00554784825017	2.744516841023055
f	10.85346324881674	--
g	-2.337319132539310	--

Finally, the empirical formulas developed for the alpha and triton ^{6}Li reaction products ions' specific path-length traveled X (μm) after a specified residual energy E (MeV) in LiF are given by Eq. A1.3 and Eq. A1.4, respectively, with corresponding fitting parameters in Table A1.4.

Table A1.4: Parameters for fitting the empirical formula for the path length to reach energy E, $X(E)$, in LiF for ions produced by the ^{6}Li neutron reaction [84].

Parameter	^{4}He [Eq. (A1.3)] (2.0553MeV)	^{3}H [Eq. (A1.4)] (2.728MeV)
a	6.312636231356	33.054989509315
b	-3.594256350143	-6.885172032726
c	1.968648983630	-2.727479733376
d	-1.822537261104	0.312521118012
e	0.136384942661	2.194886238813
f	-0.128391568854	--
g	0.037737798916	--

With these empirical fitting equations, the ion energy deposited in the silicon detector, along with the entire microstructure matrix, can be approximated through Monte Carlo simulation. After the random interaction site (x_i, y_i, z_i) and the reaction product directions Ω_i have both been determined, through the previously discussed process, the charged ion energy deposition must be tracked and measured. To do this, the ion's position is incrementally changed through small steps, in the specified direction and through a specified region (at the start, it is LiF). Along these increments, the energy deposited in the region is calculated by summing the increments and using Eq. A1.1, where the distance x is the summed increments plus the virtual traveled distance from previously deposited energy, Eq. A1.3. At the start, $X = 0$, because no previous energy has been lost. When the ion either exits the material region (or has lost all its energy or exits the detector z-plane, for both it is killed), the deposited energy is recorded and the new region specifications are defined through the X and E empirical formulas, and again the ion moves through the region incrementally. Through this incremental integration, the deposited energy can be accumulated in each region, by back-tracking how much energy was deposited in previous regions and applying that information to the X and E empirical formulas to initialize the ion parameters in each new region the ion has entered. Finally, the unit cell is designed to mirror particles that exit the unit cell boundaries, such that a single unit cell simulates the entire detector, which is composed of an array of unit cells. This is easily done by logically changing the sign of the corresponding direction cosine of the ion in response to unit cell boundary plane

that it has crossed. So, if the ion moves past the y-axis parallel plane, the x-direction cosine value is changed so as to mirror the ion back into the unit cell. Finally, the energy of the two reaction products are summed and tallied in respective energy bins for each simulated neutron absorption event. Once this simulation has been performed for many histories, an approximate ion energy-deposition (pulse-height) spectrum is developed for the specific microstructured pattern.

A. 2 Gaussian Averaging of the Simulated Spectra

The ion energy-deposition spectra obtained from the simulation are ideal and do not include the varying effects from energy straggle, detector noise, other background ionization (gamma-rays), ion scattering, and other stochastic measuring effects. Therefore, to better simulate an expected multi-channel analyzer recorded spectrum, the simulated spectra can be post-processed with a Gaussian averaging function, which is described in previous literature [84]. For the simulated spectra calculated, a standard deviation of σ = 20 keV, typical for silicon based detectors, was assumed [84]. The Gaussian averaging function (a normal distribution), is defined by the normal probability density function (PDF) in Eq. A2.1,

$$f\left(x\,|\,\mu,\sigma\right)=\frac{1}{\sqrt{2\pi}\cdot\sigma}\exp\left[\frac{-\left(x-\mu\right)^{2}}{2\sigma^{2}}\right] \qquad \textit{(A2.1)}$$

where σ is the standard deviation, and μ is the mean. For simplicity, $\mu = 0$, such that a standard normal distribution is used to smooth the simulated spectra. The integration of the standard normal distribution of the probability an ion deposits some energy in *dE* about *E*, centered over each recorded energy bin in the simulated pulse-height spectrum, will approximately smooth the counts from the centered energy bin to adjacent bins. Hence, the counts in the energy bins are averaged according to the standard deviation of the silicon detector energy variance spreading physics.

To operate the smoothing function on the tallied-histogram ion energy-distribution spectra, the number of counts in each energy bin are spread across adjacent energy bins according to the cumulative density function (CDF) in Eq. A2.2,

$$CDF = \int_{E_c-3\sigma}^{E_c+3\sigma} f \quad E \,|\, \sigma \quad dE = \int_{E_c-3\sigma}^{E_c+3\sigma} \frac{1}{\sqrt{2\pi}\cdot\sigma} \exp\left[\frac{- \quad E_c \quad ^{2}}{2\sigma^{2}}\right] dE \qquad \textit{(A2.2)}$$

where, E_c is the center of the energy bin to be operated on, and the integration range is limited to $\pm 3\ \sigma$ of which is 99.9% of the energy-distribution spread. This is illustrated in Figure A2.1. The smoothing operation is accomplished with an algorithm based on matrix operations, where the ion energy-distribution spectrum is multiplied by segmented parts of the PDF, which have been segmented into the energy bins of a set size within the spectrum. Hence, by multiplying the ion energy-distribution spectrum by each cumulative segment of the PDF, a 2D array is constructed of each energy bin and is smoothed by the PDF over adjacent bin energies. This is accomplished by the 2D array being diagonalized through the shifting of each increasing row over one bin length, thereby each bin column can be summed into an integrated smoothed spectrum.

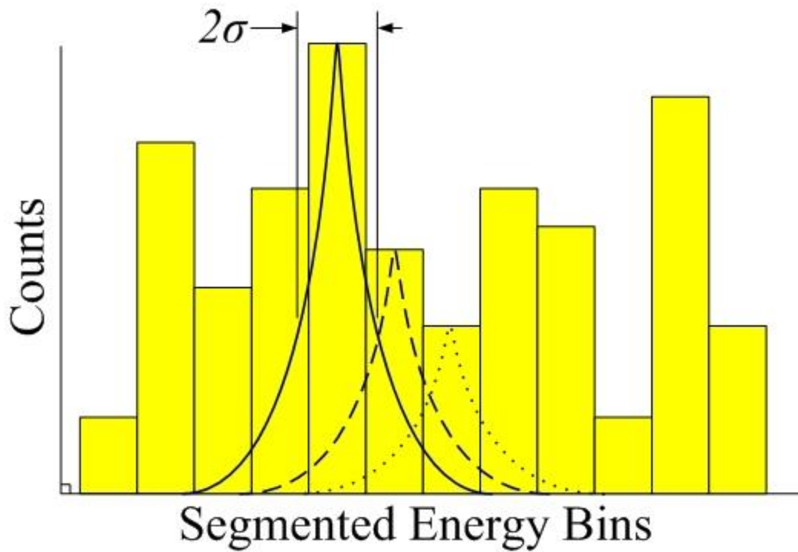

Figure A2.1: Illustration of the Gaussian smoothing process, where the count in each energy bin is re-distributed across adjacent bins according to the standard normal distribution. This operation smoothes the simulated spectra to better approximate the spectral form because of *non-ideal measurement effects.*

A. 3 MSND Neutron-Response Model Simulation *MatLab*™ Code

The MSND simulation *MatLab*™ R2006b code [129] is given. The code operates on Monte Carlo iterations of individual neutron absorption events and continuance of reaction product particle ray-tracing with ion-energy deposition tracking along the ray.

<u>Primary Code</u>:

```
clear all; clc; close all; clear global;


%%  STACKED DEVICES
%PreAllocate
EfficiencyTop=zeros(4,5,9);
EfficiencyBottom=zeros(4,5,9);
EfficiencyStacked=zeros(4,5,9);

%Top Device
for i=1:4
%Histories
    n = 3e4;
%Depth Variables
    if (i==1)
    DepthTop = 90;
    DepthBottom = DepthTop;
    end
    if (i==2)
    DepthTop = 175;
    DepthBottom = DepthTop;
    end
    if (i==3)
    DepthTop = 350;
    DepthBottom = DepthTop;
    end
    if (i==4)
    DepthTop = 500;
    DepthBottom = DepthTop;
    end
tic
for k=1:5  %5 different cell widths (Wcell=a+t), 20, 40, 60, 80, 100 um
    WcellT=20+20*(k-1);
    WcellB=WcellT;
for m=1:9  %9 different D/Wcell, 0.1, 0.2, ..., 0.9
%Dim. Variables
    fraction = m/10;
    WT=fraction*WcellT;
    WB=fraction*WcellB;
```

```
%Initialize
    TotalnTop = 0;
    TotalECumTop=0;
    TotalnBottom = 0;
    TotalECumBottom = 0;
    save ('TotalEnergySi_Stacked_Top', 'TotalECumTop', 'TotalnTop')
    save ('TotalEnergySi_Stacked_Bottom','TotalECumBottom','TotalnBottom')
%% Start Simulation
for j=1:1
%tic
%Top Device
    load ('TotalEnergySi_Stacked_Top', 'TotalECumTop', 'TotalnTop')
    [TotalEnergyDep] = CBSFunc(n,WT,WcellT,DepthTop);
    TotalECumTop = cat(2,TotalECumTop,TotalEnergyDep);
    TotalnTop=TotalnTop+n;
    save ('TotalEnergySi_Stacked_Top', 'TotalECumTop', 'TotalnTop')
%Bottom Device
    load ('TotalEnergySi_Stacked_Bottom','TotalECumBottom','TotalnBottom')
    [TotalEnergyDep] = CBSFunc2(n,WB,WcellB,DepthBottom);
    TotalECumBottom = cat(2,TotalECumBottom,TotalEnergyDep);
    TotalnBottom=TotalnBottom+n;
    save ('TotalEnergySi_Stacked_Bottom','TotalECumBottom','TotalnBottom')
%toc
end
%% Endsimulation
%% Compile top and bottom device data
    load ('TotalEnergySi_Stacked_Top', 'TotalECumTop', 'TotalnTop')
    load ('TotalEnergySi_Stacked_Bottom','TotalECumBottom','TotalnBottom')
    TotalECum = cat(2,TotalECumTop, TotalECumBottom);
    Totaln = TotalnTop;

%% Calculate Efficiency (LLD cutoff energy 300keV)
EfficiencyTop(i,k,m)=DeviceEfficiency(TotalECumTop, Totaln);
EfficiencyBottom(i,k,m)=DeviceEfficiency(TotalECumBottom, Totaln);
EfficiencyStacked(i,k,m)=DeviceEfficiency(TotalECum, Totaln);
end
end
toc
end
%% Build Efficiency Table
save ('EfficiencyTop_LiF_Trench', 'EfficiencyTop')
save ('EfficiencyBottom_LiF_Trench', 'EfficiencyBottom')
save ('EfficiencyStacked_LiF_Trench', 'EfficiencyStacked')
```

Subroutine - Top Device Code:

```
function [TotalEnergyDep] = CBSFunc(no,W,UnitCell,Depth)
rand('state',sum(100*clock));    %Generate random numbers everytime ran
%% MATERIAL PROPERTIES & UNIT CELL SETUP
L = 50.0;                % Length of Unit Cell, based on longest range in Si
WaferThick = 650.0;      % Wafer Thickness (um)
Sigma = 57.53;           % Att. Length of Lithium-6 Fluoride (1/mfp) (cm^-1)
LLD = 0.001;             % 1keV
%% NEUTRON ABSORPTION SAMPLING ON UNIT CELL
S = exp(-Sigma*Depth/(10^4));   % Neutron Transmission
Pcrod = 1 - S;                  % Probability Neutron Interacts
n =  int16(no*Pcrod);     % Trim history number to reflect interaction Prob.
nT = int16(no*S);         % Percentage of neutron Transmission
% z is an array of random sampling from CDF interaction depth.
z =(10^4)*log(1-Pcrod.*rand(1,n))/(-Sigma);

%% REMOVING NON-INTERACTING NEUTRONS
 % rand(1,n)creates a 1xn array of random numbers (0-1)
CSUCx = UnitCell*(rand(1,n));  % Sample neutron origin on unit cell x-Loc
CSUCy = L*(rand(1,n));  % Sample neutron origin on unit cell y-Loc
% Track 2D Projected Location of neutron Trimming
    binaryA = (CSUCx >= (UnitCell/2-W/2) & CSUCx <= (UnitCell/2+W/2));
    TrimX = binaryA.*CSUCx;
    TrimX = TrimX(TrimX ~=0);
    TrimY = binaryA.*CSUCy;
    TrimY = TrimY(TrimY ~=0);
    TrimZ = binaryA.*z;
    TrimZ = TrimZ(TrimZ ~=0);
    n = numel(TrimX);    %Trim history number, dep. on neut. interact

%% DIRECTION SAMPLING FOR CHARGE PARTICLE RAY TRACKING
[Dirx,Diry,Dirz] = Direction(n);
%% DEPOSITED ENERGY IN Si 1ST PARTICLE TILL DEATH
% Trace 1st particle He through silicon
alpha = 2.05;  %MeV
[Part_a_Energy]=AllocateEnergy(alpha,n);
type=1;
[EnergyDep_Si_1] = EnergyDepSi(Part_a_Energy,n,type,Dirx,Diry,Dirz,...
    TrimX,TrimY,TrimZ,W,UnitCell,Depth,WaferThick,L,LLD);
clear functions
%% DEPOSITED ENERGY IN Si 2nd PARTICLE TILL DEATH
% Trace 2nd particle Triton through silicon
Triton = 2.73;  %MeV
[Part_T_Energy]=AllocateEnergy(Triton,n);
type=2;
[EnergyDep_Si_2] = EnergyDepSi(Part_T_Energy,n,type,-Dirx,-Diry,-Dirz,...
    TrimX,TrimY,TrimZ,W,UnitCell,Depth,WaferThick,L,LLD);
clear functions
%% CALCULATE AND GRAPH DETECTOR SPECTRUM
TotalEnergyDep = EnergyDep_Si_1 + EnergyDep_Si_2;
```

Subroutine - Bottom Device Code:

```
function [TotalEnergyDep] = CBSFunc2(no,W,UnitCell,Depth)
rand('state',sum(100*clock));    %Generate random numbers everytime ran
%% MATERIAL PROPERTIES & UNIT CELL SETUP
L = 50.0;                  % Length of Unit Cell, based on longest range in Si
WaferThick = 650.0;        % Wafer Thickness (um)
Sigma = 57.53;             % Att. Length of Lithium-6 Fluoride (1/mfp) (cm^-1)
LLD = 0.001;               % 1keV
%% NEUTRON ABSORPTION SAMPLING ON UNIT CELL
S = exp(-Sigma*Depth/(10^4));    % Neutron Transmission
Pcrod = 1 - S;                   % Probability Neutron Interacts
n =  int16(no*Pcrod);      % Trim history number to reflect interaction Prob.
nT = int16(no*S);          % Percentage of neutron Transmission

%% REMOVING NON-INTERACTING NEUTRONS
 % rand(1,n)creates a 1xn array of random numbers (0-1)
xLoc = UnitCell*(rand(1,no));  % Sample neutron origin on unit cell x-Loc
yLoc = L*(rand(1,no));  % Sample neutron origin on unit cell y-Loc
% Sample only interacted n
binaryI = cat(2,ones(1,n),zeros(1,no-n));
CSUCx = xLoc .* binaryI;
CSUCy = yLoc .* binaryI;

% Track 2D Projected Location of neutron Trimming
    binaryA = (CSUCx >= (UnitCell/2-W/2) & CSUCx <= (UnitCell/2+W/2));
    TrimX = binaryA.*CSUCx;
    % Trim previous detector abs. from Stacked Det.2 neutron flux
    xLoc  = xLoc - TrimX;
    xLoc  = xLoc(xLoc ~=0);
    TrimY = binaryA.*CSUCy;
    % Trim previous detector abs. from Stacked Det.2 neutron flux
    yLoc =  yLoc - TrimY;
    yLoc  = yLoc(yLoc ~=0);
    nL    = numel(yLoc);

% Shift neutron flux to shift upper det. for off set stacking
for i=1:nL
    if (xLoc(i) < UnitCell/2)
        xLoc(i) = xLoc(i) + UnitCell/2;
    else
        xLoc(i) = xLoc(i) - UnitCell/2;
    end
    if (yLoc(i) < L/2)
        yLoc(i) = yLoc(i) + L/2;
    else
        yLoc(i) = yLoc(i) - L/2;
    end
end

% Re-randomize position matrix and Sample only interacted n
s = rand('state');
xLoc = randintrlv(xLoc,s);
yLoc = randintrlv(yLoc,s);
```

```
%%  TRIM 2ND STACK DETECTOR NEUTRON INTERACTIONS
% Re-Track 2D Projected Location of neutron Trimming
    binaryA = (xLoc >= (UnitCell/2-W/2) & xLoc <= (UnitCell/2+W/2));
    TrimX = binaryA.*xLoc;
    TrimX = TrimX(TrimX ~=0);
    TrimY = binaryA.*yLoc;
    TrimY = TrimY(TrimY ~=0);
    no = numel(TrimX);
    n =  int16(no*Pcrod);% Trim history number to reflect interaction Prob.
    binaryI = cat(2,ones(1,n),zeros(1,no-n));
    TrimX = TrimX .* binaryI;
    TrimX = TrimX(TrimX ~=0);
    TrimY = TrimY .* binaryI;
    TrimY = TrimY(TrimY ~=0);
    % z is an array of random sampling from CDF interaction depth.
    TrimZ =(10^4)*log(1-Pcrod.*rand(1,n))/(-Sigma);

%% DIRECTION SAMPLING FOR CHARGE PARTICLE RAY TRACKING
[Dirx,Diry,Dirz] = Direction(n);
%% DEPOSITED ENERGY IN Si 1ST PARTICLE TILL DEATH
% Trace 1st particle He through silicon
alpha = 2.05;  %MeV
[Part_a_Energy]=AllocateEnergy(alpha,n);
type=1;
[EnergyDep_Si_1] = EnergyDepSi(Part_a_Energy,n,type,Dirx,Diry,Dirz,...
    TrimX,TrimY,TrimZ,W,UnitCell,Depth,WaferThick,L,LLD);
clear functions
%% DEPOSITED ENERGY IN Si 2nd PARTICLE TILL DEATH
% Trace 2nd particle Triton through silicon
Triton = 2.73;  %MeV
[Part_T_Energy]=AllocateEnergy(Triton,n);
type=2;
[EnergyDep_Si_2] = EnergyDepSi(Part_T_Energy,n,type,-Dirx,-Diry,-Dirz,...
    TrimX,TrimY,TrimZ,W,UnitCell,Depth,WaferThick,L,LLD);
clear functions
%% CALCULATE AND GRAPH DETECTOR SPECTRUM
TotalEnergyDep = EnergyDep_Si_1 + EnergyDep_Si_2;
```

Subroutine - Track Particle Through MSND Code:

```
function [EnergyDep_Si] = EnergyDepSi(ResEnergy,n,type,Dirx,Diry,Dirz,...
    Posx,Posy,Posz,W,UnitCell,Depth,WaferThick,L,LLD)
%Allocate Arrays for testing
EnergyDep_Trench = 2.05*(ones(1,n));
EnergyDep_Trench2 = 2.73*(ones(1,n));
EnergyDep_Si = zeros(1,n);
ResEnergy2 = zeros(1,n);

T1=(UnitCell/2-W/2);
T2=(UnitCell/2+W/2);

Path = 1.0e-3;  %Path Length Stepping by unit step (micron)
for i=1:n
%%  Alpha Ion 2.05 MeV
    if(type == 1)
        while ((Posz(i)>0)&&(Posz(i)<=WaferThick)&&(ResEnergy(i)>LLD))
        %Check if in LiF Trench
        %Determine Residual Energy after removed from LiF Trench

        if((Posx(i)>=T1)&&(Posx(i)<=T2)&&(ResEnergy(i)>LLD)&&...
                (Posy(i)>=0)&&(Posy(i)<=L)&&(Posz(i)>=0)&&(Posz(i)<=Depth))
            %Find Extra Path-Length to compensate Residual Energy Equation
            %Parameters from Shultis's "Path-Length to Reach Residual
            %Energy in Li-6F" Empirical Formula
            a=6.312636231356; b=-3.594256350143; c=1.968648983630; ...
                d=-1.822537261104; e=0.136384942661; f=-0.128391568854;...
                g=0.037737798916;
            Rx = a+b*sqrt(ResEnergy(i))+c*ResEnergy(i)+...
                d*ResEnergy(i)^(3/2)+e*ResEnergy(i)^2+...
                f*ResEnergy(i)^(5/2)+g*ResEnergy(i)^3;
            Rx = (Rx>=0)*Rx;
            %Track Energy
            dx=0;
            while ((ResEnergy(i)>LLD)&&(Posx(i)>=T1)&&(Posx(i)<=T2)&&...
                    (Posy(i)>=0)&&(Posy(i)<=L)&&(Posz(i)>=0)&&...
                    (Posz(i)<=Depth))

                x=Posx(i);y=Posy(i);z=Posz(i); %Keep track of last position
                Posx(i) = (Path)*Dirx(i)+Posx(i);
                Posy(i) = (Path)*Diry(i)+Posy(i);
                Posz(i) = (Path)*Dirz(i)+Posz(i);
                dx=sqrt((x-Posx(i))^2+(y-Posy(i))^2+...
                    (z-Posz(i))^2)+dx; %Measure Inc. Dist. Traveled
                %Parameters from Shultis's
                %"Residual Energy in LiF" Empirical Formula
                a=2.045795872242; b=-0.161868152261; c=-0.665680395107;...
                    d=-0.000407316315; e=0.054192529543; f=0.00169421379;
                %Empirical Formula for Residual Energy after Trench
                ResEnergy(i)=(a+c*(dx+Rx)+e*(dx+Rx)^2)/(1+b*(dx+Rx)+...
                    d*(dx+Rx)^2+f*(dx+Rx)^3);
                ResEnergy2(i)=(a+c*(dx+Rx+0.1)+e*(dx+Rx+0.1)^2)/...
                    (1+b*(dx+Rx+0.1)+d*(dx+Rx+0.1)^2+f*(dx+Rx+0.1)^3);
                ResEnergy(i) =((ResEnergy(i)-...
                    abs(ResEnergy2(i)))>0)*ResEnergy(i);
```

```
    end
        EnergyDep_Trench(i) = EnergyDep_Trench(i)-ResEnergy(i);
end

%Parameters from Shultis's
%"Path-Length to Reach Residual Energy in Si" Empirical Formula
if((ResEnergy(i)>LLD))
    a=7.650654782456231; b=-2.951907906029242; ...
        c=-3.226254043595208; d=12.90757367270686; ...
        e=-19.00554784825017; f=10.85346324881674; ...
        g=-2.337319132539310;
    Rx = a+b*sqrt(ResEnergy(i))+c*ResEnergy(i)+...
        d*ResEnergy(i)^(3/2)+e*ResEnergy(i)^2+...
        f*ResEnergy(i)^(5/2)+g*ResEnergy(i)^3;
    Rx = (Rx>=0)*Rx;
end

    %Track Energy
    dx=0;   %Initialize
    Res_E_Si = ResEnergy(i);   %Energy before lost in Si

    %Parameters from Shultis's "Residual Energy in Si"
    %Empirical Formula
    a=2.0549684169; b=-0.1483764308; c=-0.5570727178; ...
        d=-0.0005753511; e=0.0377800136; f=0.0007588408;

while (((ResEnergy(i)>LLD)&&(Posx(i)<=T1)&&(Posx(i)>=0)&&...
        (Posz(i)>=0)&&(Posz(i)<=WaferThick)&&...
        (Posy(i)>=0)&&(Posy(i)<=L))||((ResEnergy(i)>LLD)&&...
        (Posx(i)>=T2)&&(Posx(i)<=UnitCell)&&(Posz(i)>=0)&&...
        (Posz(i)<=WaferThick)&&(Posy(i)>=0)&&(Posy(i)<=L))||...
        ((ResEnergy(i)>LLD)&&(Posz(i)>Depth)&&...
        (Posz(i)<=WaferThick)&&(Posx(i)>=0)&&...
        (Posx(i)<=UnitCell)&&(Posy(i)>=0)&&(Posy(i)<=L)))

        x=Posx(i);y=Posy(i);z=Posz(i);%Keep track of last position
        Posx(i) = (Path)*Dirx(i)+Posx(i);
        Posy(i) = (Path)*Diry(i)+Posy(i);
        Posz(i) = (Path)*Dirz(i)+Posz(i);
        %Measure Inc. Dist. Traveled
        dx = sqrt((x-Posx(i))^2+(y-Posy(i))^2+(z-Posz(i))^2) + dx;
        %Shultis's "Residual Energy in Si" Empirical Formula
        ResEnergy(i)=(a+c*(dx+Rx)+e*(dx+Rx)^2)/(1+b*(dx+Rx)+...
            d*(dx+Rx)^2+f*(dx+Rx)^3);
        ResEnergy2(i)=(a+c*(dx+Rx+0.1)+e*(dx+Rx+0.1)^2)/...
            (1+b*(dx+Rx+0.1)+d*(dx+Rx+0.1)^2+f*(dx+Rx+0.1)^3);
        ResEnergy(i) =((ResEnergy(i)-...
            abs(ResEnergy2(i)))>0)*ResEnergy(i);
end
```

```
        %Mirror off UnitCell walls to account for cross-cell energy deposit
        if(((Posx(i)<0)||(Posx(i)>UnitCell)||(Posy(i)<0)||(Posy(i)>L))&&...
                ((ResEnergy(i)>LLD)&&(Posz(i)>=0)&&(Posz(i)<=WaferThick)))
           %Mirror by Change Direction
           if((Posy(i)<0)||(Posy(i)>L))
                Diry(i)=-Diry(i);
                %Move everything back one unit,
                %so as to still be in Unit Cell
                Posx(i) = (Path)*(-Dirx(i))+Posx(i);
                Posy(i) = (Path)*(Diry(i))+Posy(i);
                Posz(i) = (Path)*(-Dirz(i))+Posz(i);
           elseif((Posx(i)<0)||(Posx(i)>UnitCell))
                Dirx(i)=-Dirx(i);
                %Move everything back one unit,
                %so as to still be in Unit Cell
                Posx(i) = (Path)*(Dirx(i))+Posx(i);
                Posy(i) = (Path)*(-Diry(i))+Posy(i);
                Posz(i) = (Path)*(-Dirz(i))+Posz(i);
           end
        end
        %Sum energy loss in Si
        EnergyDep_Si(i) = Res_E_Si - ResEnergy(i) + EnergyDep_Si(i);
        end
    end


%%  Triton Ion 2.73 MeV
    if(type == 2)
        while ((Posz(i)>0)&&(Posz(i)<=WaferThick)&&(ResEnergy(i)>LLD))
        %Check if in LiF Trench
        %Determine Residual Energy after removed from LiF Trench
        if((Posx(i)>=T1)&&(Posx(i)<=T2)&&(ResEnergy(i)>LLD)&&...
                (Posy(i)>=0)&&(Posy(i)<=L)&&(Posz(i)>=0)&&(Posz(i)<=Depth))
            %Find Extra Path-Length to compensate Residual Energy Equation
            %Parameters from Shultis's "Path-Length to Reach Residual
            %Energy in LiF" Empirical Formula
            a=33.054989509315; b=-6.885172032726; c=-2.727479733376; ...
                d=0.312521118012; e=2.194886238813;
            Rx = a+b*ResEnergy(i)+c*ResEnergy(i)^2+d*ResEnergy(i)^2*...
                log(ResEnergy(i))+e*ResEnergy(i)^(0.5)*log(ResEnergy(i));
            Rx = (Rx>=0 && Rx<34.7)*Rx + (Rx>=34.7)*34.7;

            %Track Energy
            dx=0;
            while ((ResEnergy(i)>LLD)&&(Posx(i)>=T1)&&(Posx(i)<=T2)&&...
                    (Posy(i)>=0)&&(Posy(i)<=L)&&(Posz(i)>=0)&&...
                    (Posz(i)<=Depth))

                x=Posx(i);y=Posy(i);z=Posz(i);%Keep track of last position
                Posx(i) = (Path)*Dirx(i)+Posx(i);
                Posy(i) = (Path)*Diry(i)+Posy(i);
                Posz(i) = (Path)*Dirz(i)+Posz(i);
                %Measure Inc. Dist. Traveled
                dx=sqrt((x-Posx(i))^2+(y-Posy(i))^2+(z-Posz(i))^2)+dx;
                %Parameters from Shultis's
```

```
        %"Residual Energy in LiF" Empirical Formula
        a=1.002503409342; b=-0.043787370382; c=-0.065185375563;...
            d=0.000410451552; e=0.000957069819;
        %Empirical Formula for Residual Energy after Trench
        ResEnergy(i)=exp((a+c*(dx+Rx)+e*(dx+Rx)^2)/(1+b*(dx+Rx)+...
            d*(dx+Rx)^2));
        ResEnergy2(i)=exp((a+c*(dx+Rx+0.1)+e*(dx+Rx+0.1)^2)/...
            (1+b*(dx+Rx+0.1)+d*(dx+Rx+0.1)^2));
        ResEnergy(i) =((ResEnergy(i)-abs(ResEnergy2(i)))>0)*...
            ResEnergy(i);
    end
        EnergyDep_Trench2(i) = EnergyDep_Trench2(i)-ResEnergy(i);
end
%Parameters from Shultis's "Path-Length to Reach Residual
%Energy in Si" Empirical Formula
if((ResEnergy(i)>LLD))
    a=42.554327308268; b=6.126822912741065; ...
        c=-5.405288206496186; d=1.274522449649497;...
        e=2.744516841023055;
    Rx = a-b*ResEnergy(i)+c*ResEnergy(i)^2+d*ResEnergy(i)^2*...
        log(ResEnergy(i))+e*ResEnergy(i)^(0.5)*log(ResEnergy(i));
    Rx = (Rx>=0 && Rx<42.9)*Rx + (Rx>=42.9)*42.9;
end

    %Track Energy
    dx = 0;      %intialize
    Res_E_Si = ResEnergy(i);   %Energy before lost in Si

    %Parameters from Shultis's
    %"Residual Energy in Si" Empirical Formula
    a=0.99849937868; b=-0.03278510295; c=-0.04902551060;...
        d=0.00022141343; e=0.000542827;

while (((ResEnergy(i)>LLD)&&(Posx(i)<=T1)&&(Posx(i)>=0)&&...
        (Posz(i)>=0)&&(Posz(i)<=WaferThick)&&...
        (Posy(i)>=0)&&(Posy(i)<=L))||((ResEnergy(i)>LLD)&&...
        (Posx(i)>=T2)&&(Posx(i)<=UnitCell)&&(Posz(i)>=0)&&...
        (Posz(i)<=WaferThick)&&(Posy(i)>=0)&&(Posy(i)<=L))||...
        ((ResEnergy(i)>LLD)&&(Posz(i)>Depth)&&...
        (Posz(i)<=WaferThick)&&(Posx(i)>=0)&&...
        (Posx(i)<=UnitCell)&&(Posy(i)>=0)&&(Posy(i)<=L)))

    x=Posx(i);y=Posy(i);z=Posz(i);    %Keep track of last position
    Posx(i) = (Path)*Dirx(i)+Posx(i);
    Posy(i) = (Path)*Diry(i)+Posy(i);
    Posz(i) = (Path)*Dirz(i)+Posz(i);
    %Measure Inc. Dist. Traveled
    dx = sqrt((x-Posx(i))^2+(y-Posy(i))^2+(z-Posz(i))^2) + dx;
    %Shultis's "Residual Energy in Si" Empirical Formula
    ResEnergy(i)=exp((a+c*(dx+Rx)+e*(dx+Rx)^2)/(1+b*(dx+Rx)+...
        d*(dx+Rx)^2));
    ResEnergy2(i)=exp((a+c*(dx+Rx+0.1)+e*(dx+Rx+0.1)^2)/...
        (1+b*(dx+Rx+0.1)+d*(dx+Rx+0.1)^2));
    ResEnergy(i) =((ResEnergy(i)-abs(ResEnergy2(i)))>0)*...
        ResEnergy(i);
end
```

```
        %Mirror off UnitCell walls to account for cross-cell energy deposit
        if(((Posx(i)<0)||(Posx(i)>UnitCell)||(Posy(i)<0)||(Posy(i)>L))&&...
                ((ResEnergy(i)>LLD)&&(Posz(i)>=0)&&(Posz(i)<=WaferThick)))
          %Mirror by Change Direction
           if((Posy(i)<0)||(Posy(i)>L))
                Diry(i)=-Diry(i);
                %Move everything back one unit,
                %so as to still be in Unit Cell
                Posx(i) = (Path)*(-Dirx(i))+Posx(i);
                Posy(i) = (Path)*(Diry(i))+Posy(i);
                Posz(i) = (Path)*(-Dirz(i))+Posz(i);
           elseif((Posx(i)<0)||(Posx(i)>UnitCell))
                Dirx(i)=-Dirx(i);
                %Move everything back one unit,
                %so as to still be in Unit Cell
                Posx(i) = (Path)*(Dirx(i))+Posx(i);
                Posy(i) = (Path)*(-Diry(i))+Posy(i);
                Posz(i) = (Path)*(-Dirz(i))+Posz(i);
           end
        end
        %Sum energy loss in Si
        EnergyDep_Si(i) = ((Res_E_Si - ResEnergy(i))>0)*(Res_E_Si - ...
            ResEnergy(i)) + EnergyDep_Si(i);
        end
    end
%% End Loop
end
```

Subroutine - Particle Direction Code:

```
function [Dirx,Diry,Dirz] = Direction(n)
Theta = (2*pi).*rand(1,n);
Dirz = -1 + 2.*rand(1,n);
DirxDiry = (1-Dirz.^2).^(0.5);
Dirx = DirxDiry.*sin(Theta);
Diry = DirxDiry.*cos(Theta);
```

Subroutine - MSND Efficiency Code:

```
function [Efficiency] = DeviceEfficiency(TotalECum, Totaln)
%% MEASURE SPECTRUM TOTAL COUNTS ABOVE THRESHOLD (TLLD)
TLLD=.3;%MeV, Lower Level Disc.
E = 5;              %MeV, Energy Max
chn = 256;          %256 Bin Channels
BinE = E/chn;       %MeV/chn center of bin
x = 0:(BinE):5;
Spec = histc(TotalECum,x);   %Split up into var. seperate bins
% Sum spectrum from TLLD and up
CountNeutronSum = sum(Spec(ceil(TLLD/BinE):chn));
% Account for mid-Bin remainder
CountNeutronSum = Spec(ceil(TLLD/BinE))*...
    (ceil(TLLD/BinE)-TLLD/BinE) + CountNeutronSum;
Efficiency = CountNeutronSum/Totaln;  % fractional

clear all; clc; close all; clear global;
```

Data Module - MSND Efficiency Table Code:

```
%% Build Efficiency Table
load ('EfficiencyTop_LiF_Trench', 'EfficiencyTop')
load ('EfficiencyBottom_LiF_Trench', 'EfficiencyBottom')
load ('EfficiencyStacked_LiF_Trench', 'EfficiencyStacked')

%Arrange Data
for i=1:4 %Depths 10, 20, 40, 60 microns 1:4 respectively
%     TableTop=['TableTop',num2str(i)];
%     TableBottom=['TableBottom',num2str(i)];
%     TableStacked=['TableStacked',num2str(i)];

for k=1:5  %5 different cell widths (Wcell=a+t), 4, 6, 8, 10, 12 um
for m=1:9  %9 different D/Wcell, 0.1, 0.2, ..., 0.9

TableTopArray((m+(i-1)*9),k) = EfficiencyTop(i,k,m)*100;
TableBottomArray((m+(i-1)*9),k) = EfficiencyBottom(i,k,m)*100;
TableStackedArray((m+(i-1)*9),k) = EfficiencyStacked(i,k,m)*100;

end
end
save ('TableTop.txt', 'TableTopArray', '-ascii');
save ('TableBottom.txt', 'TableBottomArray', '-ascii');
save ('TableStacked.txt', 'TableStackedArray', '-ascii');
end
```

Data Module - Stacked MSND Spectrum Code:

```
clear all; clc; close all; clear global;format long;

%%  STACKED DEVICES
for i=1:100
tic
n = 3e4;                   %Histories
DepthTop = 250;            %Depth of Trench
WTop = 14;                 %Width of Trench
UnitCellTop = 20;           %Width of Unit Cell

%TotalnTop = 0;
%TotalECumTop = 0;
load TotalEnergySiLiFTrench_Stacked_Top5 TotalECumTop TotalnTop
[TotalEnergyDep] = CBSFunc(n,WTop,UnitCellTop,DepthTop);
TotalECumTop = cat(2,TotalECumTop,TotalEnergyDep);
TotalnTop=TotalnTop+n;
save ('TotalEnergySiLiFTrench_Stacked_Top5', 'TotalECumTop',
'TotalnTop','WTop','UnitCellTop','DepthTop')
toc
end

clear all

for i=1:100
tic
n = 3e4;                    %Histories
DepthBottom = 250;          %Depth of Trench
WBottom = 14;               %Width of Trench
UnitCellBottom = 20;         %Width of Unit Cell

%TotalnBottom = 0;
%TotalECumBottom = 0;
load TotalEnergySiLiFTrench_Stacked_Bottom5 TotalECumBottom
[TotalEnergyDep] = CBSFunc2(n,WBottom,UnitCellBottom,DepthBottom);
TotalECumBottom = cat(2,TotalECumBottom,TotalEnergyDep);
save ('TotalEnergySiLiFTrench_Stacked_Bottom5', 'TotalECumBottom',
'DepthBottom','WBottom','UnitCellBottom')
toc
end
load TotalEnergySiLiFTrench_Stacked_Top5 TotalECumTop TotalnTop
load TotalEnergySiLiFTrench_Stacked_Bottom5 TotalECumBottom
TotalECum = cat(2, TotalECumTop, TotalECumBottom);
Totaln = TotalnTop;
save ('TotalEnergySiLiFTrench_Stacked5', 'TotalECum', 'Totaln')
%
clear all;
```

Data Module - Stacked MSND Gaussian Smear Code:

```
clc; clear all; close all;

%% TOP DETECTOR

load TotalEnergySiLiFTrench_Stacked_Top1 TotalECumTop TotalnTop ...
    WTop UnitCellTop DepthTop

%% INITIAL CONDITIONS
E = 5;               %MeV, Energy Max
chn = 256;           %256 Bin Channels
sigma = 20/1000;     %MeV, Si Det. known to have 20keV sigma
BinE = E/chn;        %MeV/chn center of bin
SigmaChn = E/sigma; %How many channels are evenly spaced for var. channels
VarBins = 5;
x = 0:(BinE):5;
VarHist = histc(TotalECumTop,x);   %Split up into var. seperate bins

%% FIND SPREADING MATRIX, NORMAL CDF DISTRIBUTION
for i = 1:VarBins+1
p = normcdf([-i*sigma*SigmaChn/chn i*sigma*SigmaChn/chn],0,sigma);
SpreadMatI(i) = (p(2) - p(1));
end
SpreadMat = SpreadMatI;
for i = 1:VarBins
SpreadMat(i+1) = (SpreadMatI(i+1) - SpreadMatI(i))/2;
end
for i = 1:(VarBins)
Spread(i) = SpreadMat((VarBins+1)-i);
Spread((VarBins-1)+i) = SpreadMat(i);
end
%% ARRANGE HISTOGRAM MATRIX INTO CODED VAR BINS
HistSpread = zeros(((VarBins-1)+VarBins),chn+((VarBins-1)+VarBins));
for i = 1:((VarBins-1)+VarBins)
    for j = 1:chn
    HistSpread(i,j) = VarHist(j).*Spread(i);
    end
end
% HistSpreadRow = reshape(HistSpread,1,((VarBins-1)+VarBins)*chn);   %Reshape
matrix to combine
%% ARRANGE HISTOGRAM MATRIX INTO CODED VAR BINS
HistSmooth = zeros(((VarBins-1)+VarBins),chn+((VarBins-1)+VarBins));
for i = 1:((VarBins-1)+VarBins)
    for j = 1:chn
        HistSmooth(i,j+(i-1)) = HistSpread(i,j);
    end
end
% Sum the Arranged Matrix and move to the right
HistSmooth = sum(HistSmooth);
Smoothed_Spectrum = circshift(HistSmooth, [0, -(VarBins-1)]);
SmoothedSpectTop = zeros(1,chn);
for i = 1:(chn+1)
    SmoothedSpectTop(i) = Smoothed_Spectrum(i);
end
x = 0:BinE:E;
```

```
%%  BOTTOM DETECTOR

load TotalEnergySiLiFTrench_Stacked_Bottom1 TotalECumBottom


%% INITIAL CONDITIONS
E = 5;              %MeV, Energy Max
chn = 256;          %256 Bin Channels
sigma = 20/1000;    %MeV, Si Det. known to have 20keV sigma
BinE = E/chn;       %MeV/chn center of bin
SigmaChn = E/sigma; %How many channels are evenly spaced for var. channels
VarBins = 5;
x = 0:(BinE):5;
VarHist = histc(TotalECumBottom,x);   %Split up into var. seperate bins

%% FIND SPREADING MATRIX, NORMAL CDF DISTRIBUTION
for i = 1:VarBins+1
p = normcdf([-i*sigma*SigmaChn/chn i*sigma*SigmaChn/chn],0,sigma);
SpreadMatI(i) = (p(2) - p(1));
end
SpreadMat = SpreadMatI;
for i = 1:VarBins
SpreadMat(i+1) = (SpreadMatI(i+1) - SpreadMatI(i))/2;
end
for i = 1:(VarBins)
Spread(i) = SpreadMat((VarBins+1)-i);
Spread((VarBins-1)+i) = SpreadMat(i);
end
%% ARRANGE HISTOGRAM MATRIX INTO CODED VAR BINS
HistSpread = zeros(((VarBins-1)+VarBins),chn+((VarBins-1)+VarBins));
for i = 1:((VarBins-1)+VarBins)
    for j = 1:chn
    HistSpread(i,j) = VarHist(j).*Spread(i);
    end
end
% HistSpreadRow = reshape(HistSpread,1,((VarBins-1)+VarBins)*chn);   %Reshape
matrix to combine
%% ARRANGE HISTOGRAM MATRIX INTO CODED VAR BINS
HistSmooth = zeros(((VarBins-1)+VarBins),chn+((VarBins-1)+VarBins));
for i = 1:((VarBins-1)+VarBins)
    for j = 1:chn
        HistSmooth(i,j+(i-1)) = HistSpread(i,j);
    end
end
% Sum the Arranged Matrix and move to the right
HistSmooth = sum(HistSmooth);
Smoothed_Spectrum = circshift(HistSmooth, [0, -(VarBins-1)]);
SmoothedSpectBottom = zeros(1,chn);
for i = 1:(chn+1)
    SmoothedSpectBottom(i) = Smoothed_Spectrum(i);
end
x = 0:BinE:E;
```

```
%% TOTAL SUMMED DETECTORS

load TotalEnergySiLiFTrench_Stacked1 TotalECum


%% INITIAL CONDITIONS
E = 5;              %MeV, Energy Max
chn = 256;          %256 Bin Channels
sigma = 20/1000;    %MeV, Si Det. known to have 20keV sigma
BinE = E/chn;       %MeV/chn center of bin
SigmaChn = E/sigma; %How many channels are evenly spaced for var. channels
VarBins = 5;
x = 0:(BinE):5;
VarHist = histc(TotalECum,x);   %Split up into var. seperate bins

%% FIND SPREADING MATRIX, NORMAL CDF DISTRIBUTION
for i = 1:VarBins+1
p = normcdf([-i*sigma*SigmaChn/chn i*sigma*SigmaChn/chn],0,sigma);
SpreadMatI(i) = (p(2) - p(1));
end
SpreadMat = SpreadMatI;
for i = 1:VarBins
SpreadMat(i+1) = (SpreadMatI(i+1) - SpreadMatI(i))/2;
end
for i = 1:(VarBins)
Spread(i) = SpreadMat((VarBins+1)-i);
Spread((VarBins-1)+i) = SpreadMat(i);
end
%% ARRANGE HISTOGRAM MATRIX INTO CODED VAR BINS
HistSpread = zeros(((VarBins-1)+VarBins),chn+((VarBins-1)+VarBins));
for i = 1:((VarBins-1)+VarBins)
    for j = 1:chn
    HistSpread(i,j) = VarHist(j).*Spread(i);
    end
end
% HistSpreadRow = reshape(HistSpread,1,((VarBins-1)+VarBins)*chn);   %Reshape
matrix to combine
%% ARRANGE HISTOGRAM MATRIX INTO CODED VAR BINS
HistSmooth = zeros(((VarBins-1)+VarBins),chn+((VarBins-1)+VarBins));
for i = 1:((VarBins-1)+VarBins)
    for j = 1:chn
        HistSmooth(i,j+(i-1)) = HistSpread(i,j);
    end
end
% Sum the Arranged Matrix and move to the right
HistSmooth = sum(HistSmooth);
Smoothed_Spectrum = circshift(HistSmooth, [0, -(VarBins-1)]);
SmoothedSpectTotal = zeros(1,chn);
for i = 1:(chn+1)
    SmoothedSpectTotal(i) = Smoothed_Spectrum(i);
end
x = 0:BinE:E;
```

```
figure(1)
axes('FontSize',16,'FontName','Times New Roman');

semilogy(x,SmoothedSpectTop,':m',x,SmoothedSpectBottom,'--c', x,
SmoothedSpectTotal,'-k','LineWidth',5);
ylim([1,10^5]);

axis square;

title({'LiF STRAIGHT TRENCH ENERGY SPECTRUM';'STACKED DETECTORS';[' Depth =
',num2str(DepthTop),...
    ',  Trench Width = ',num2str(WTop),',  Unit Cell Width =
',num2str(UnitCellTop),'    (Dim. in microns)']},...
     'FontWeight','bold',...
    'FontSize',12,...
    'FontName','Times New Roman');

% Create xlabel
xlabel('ENERGY DEPOSITED IN SILICON (MeV)','FontWeight','bold',...
    'FontSize',12,...
    'FontName','Calisto MT');

% Create ylabel
ylabel('NUMBER OF INTERACTIONS','FontWeight','bold','FontSize',12,...
    'FontName','Calisto MT');

% Legend in Top Right Corner
legend('Top Detector','Bottom Detector','Summed Detector',1);
```

Data Module - Efficiency of Stacked MSND Code:

```
clc; clear all; close all;

load TotalEnergySiLiFTrench_Stacked TotalECum Totaln
load TotalEnergySiLiFTrench_Stacked_Top WTop DepthTop UnitCellTop
%% MEASURE SPECTRUM TOTAL COUNTS ABOVE LLD
for i=1:11
    if(i<2)
        LLD = 0.05;
    else
        LLD = 0.1*(i-1);%MeV, Lower Level Disc.
    end
LLDx(i) = LLD;
E = 5;                %MeV, Energy Max
chn = 256;            %256 Bin Channels
BinE = E/chn;         %MeV/chn center of bin
x = 0:(BinE):5;
Spec = histc(TotalECum,x);   %Split up into var. seperate bins
% Sum spectrum from LLD and up
CountNeutronSum = sum(Spec(ceil(LLD/BinE):chn));
% Account for mid-Bin remainder
CountNeutronSum = Spec(ceil(LLD/BinE))*...
    (ceil(LLD/BinE)-LLD/BinE) + CountNeutronSum;
Eff(i) = CountNeutronSum/Totaln*100;  % in percent
end

figure(1)
axes('FontSize',16,'FontName','Times New Roman');
plot(LLDx,Eff,'-ko','MarkerFaceColor','b','LineWidth',2);
ylim([0,55]);
axis square;
title({'LiF  STRAIGHT  TRENCH  INTRINSIC  EFFICIENCY';'STACKED  DEVICE';...
    [' Depth = ',num2str(DepthTop),',  Trench Width = ',num2str(WTop),...
    ',  Unit Cell Width = ',num2str(UnitCellTop), '  (Dim. in
microns)']},'FontWeight','bold',...
    'FontSize',12,...
    'FontName','Times New Roman');

xlabel('LLD  ENERGY
(MeV)','FontWeight','bold','FontSize',12,'FontName','Calisto MT');
ylabel('INTRINSIC  EFFICIENCY
(%)','FontWeight','bold','FontSize',12,'FontName','Calisto MT');
```

APPENDIX B - MSND FABRICATION DETAIL

B. 1 MSND Fabrication Process Detail: Single Sided Device

Wafer specifications detail:

Silicon wafers, per SEMI Prime, P/P 4"Ø×525±25µm, with a 2.5um oxide on both sides, FZ Si:P[110], Ro=(5,000-10000) Ohm-cm, n-type Dual-side-polished, two SEMI Flats @ [111], Primary Flat @ [111], Secondary Flat @ [111] that is 70.53º CW from Primary.

Process 1: Diffusion Window Patterned

Diffusion window masked with thin negative photoresist on topside of wafer, align masking pattern to the side of the square diffusion window to the [111] primary flat and center 6x6 MSND array in center of 100mm wafer (see Figures. B.1.1 & B.1.2).

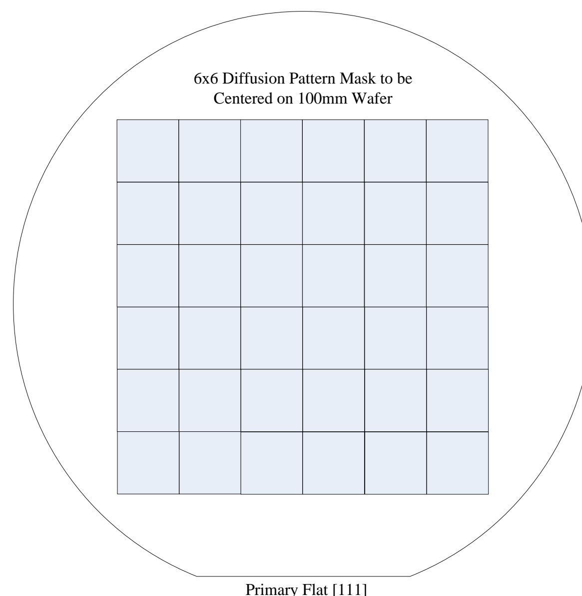

Figure B.1.1: Photoresist mask diffusion window pattern centered on 100mm wafer.

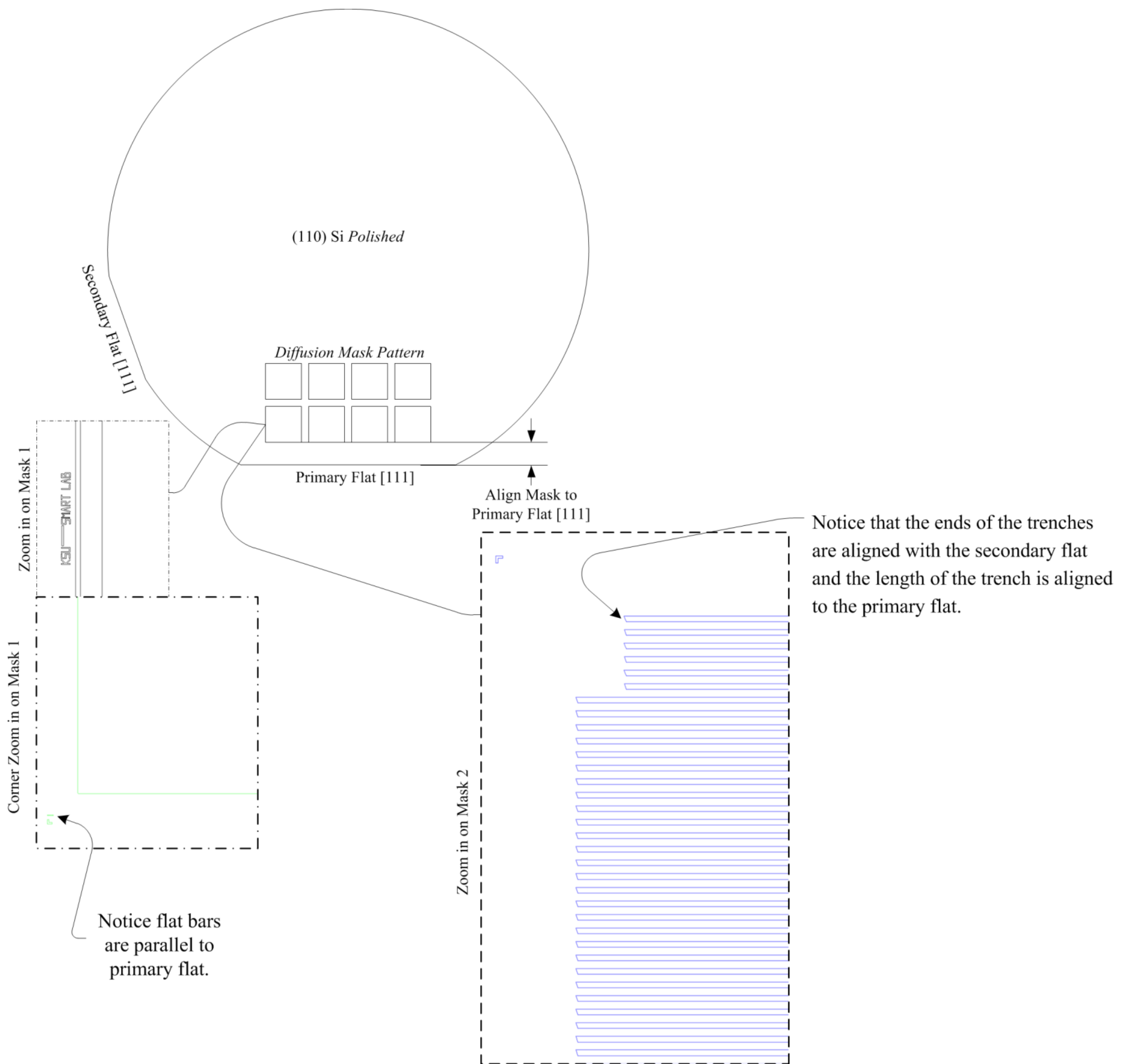

Figure B.1.2: Diffusion window negative photoresist patterning of frontside of silicon wafer. Notice the alignment of the mask pattern to the primary flat.

Process 2: Diffusion Window Partial Oxide Removal

BOE wafers until the oxide in the diffusion windows have been partially removed to 1.75 microns thick (~0.75 micron removal). Apply thick negative photoresist to backside of wafer and dry cure. Apply negative thin photoresist to frontside of wafer (may need dehydration and HMDS primer) and align Single Sided Straight Trench Pattern to diffusion window pattern alignment marks (smallest allowable proximity width between mask and wafer). Develop photoresist and BOE Trench Pattern until strait trenches show hydrophobic activity. Remove all photoresist and O_2 Ash for 1hr.

Process 3: KOH wet etch frontside (DRIE may be used, but suffers increased cost)

A KOH wet etch will then be done, etching the single-sided masked pattern trenches 475um deep, but no more. Slow DI rinse for 3 min.

Process 4: Microstructured Diode Diffusion (liquid BBr_3 source)

Apply thick negative photoresist to backside of wafer and dry cure. BOE Wafers until diffusion window trench masking oxide is removed and shows hydrophobic activity. Remove all photoresist and O_2 Ash for 1hr. Clean wafers (preferably the death etch HNO_3, HF, H_2O (*Robbins & Schwartz*), to fully remove residual potassium ~0.1 micron silicon removal), then RCA (or comparable) clean wafers, and diffuse a 0.3 micron shallow p-type (BBr_3) layer on frontside of wafer, *with an extended sourcing time*. BOE remove boron diffusion film.

Process 5: Microstructured Diode Metal Contact Photoresist Masking

Apply thick (SU8 ~30 micron thickness) negative photoresist to frontside of wafer and dry cure. BOE Wafers until backside oxide is removed and shows hydrophobic activity. Remove all photoresist and O_2 Ash for 1hr. Apply thick (SU8 ~30 micron thickness) negative photoresist to frontside of wafer and align Metal Contact Pattern to diffusion window pattern alignment marks and expose for liftoff undercut development. Develop photoresist and BOE for 2 min.

Process 6: Metallization

BOE residual native oxide in contact windows and apply [**Ti (10%) / W (90%)**] **Ti/W** (1000Å) / **Al** (4kÅ) to both sides of wafer. Lift-off metal.

B. 2 MSND Fabrication Process Detail: Dual Sided Device

Wafer specifications detail:

Silicon wafers, per SEMI Prime, P/P 4"Ø×525±25µm, with a 2.5um oxide on both sides, FZ Si:P[110], Ro=(5,000-10000) Ohm-cm, n-type Dual-side-polished, two SEMI Flats @ [111], Primary Flat @ [111], Secondary Flat @ [111] that is 70.53º CW from Primary.

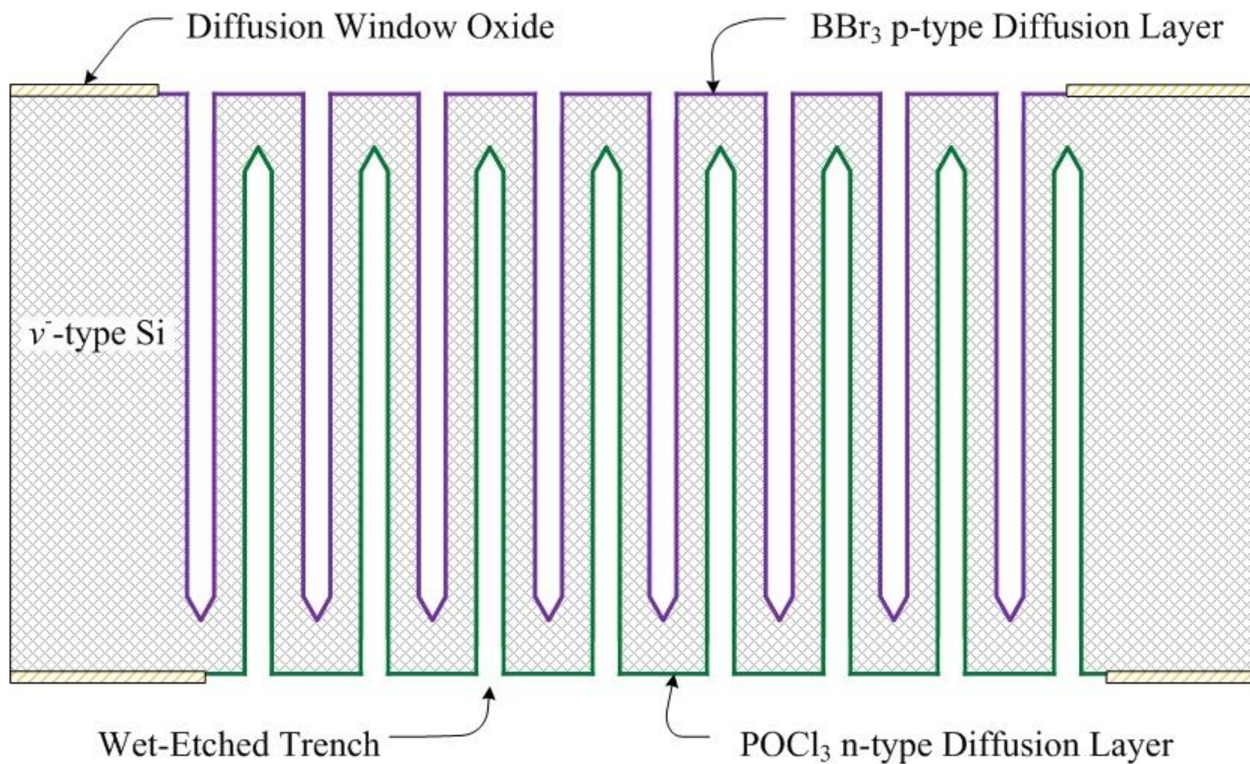

Figure B.2.1: Illustration of advanced microstructure design with interlaced microstructures that are etched from both sides of the silicon diode to improve charge drifting electric field potential.

Process 1: Diffusion Window Patterned

Note: Dual Sided Alignment and Photoresist Processing will be required; therefore, an Oven Bake Photoresist processing is necessary.

Diffusion window masked with thin negative photoresist on topside (polished side) of wafer, align masking pattern to the side of the square diffusion window to the [111] primary flat and center 6x6 MSND array in center of 100mm wafer (see Figures B.1.1 & B.1.2). Then, another diffusion window (same as topside) is masked with thin negative photoresist on the backside of wafer, where the wafer is flipped with the primary flat on the same side as the topside. The backside diffusion window pattern is then aligned to the frontside pattern identically with dual-side alignment optics and then normally offset away (towards wafer center) from the primary flat by 60 microns (see Figure B.2.2). The offset direction is normal to the [111] primary flat.

Process 2: Diffusion Window Partial Oxide Removal

Note: Dual Sided Photoresist Processing will be required, therefore Oven Bake Photoresist processing is necessary.

BOE wafers until the oxide in the diffusion windows have been partially removed to 1.75 microns thick (~0.75 micron removal) - residual photoresist may need to be removed to apply second photoresist masking layer, else apply on-top of diffusion window photoresist mask. Apply thin negative photoresist to backside of wafer (may need dehydration and HMDS primer) and align Dual Sided Straight Trench Pattern to diffusion window pattern alignment marks (smallest allowable proximity width between mask and wafer). Develop photoresist and apply thin negative photoresist to frontside of wafer (may need dehydration and HMDS primer) and again align Straight Trench Pattern to diffusion window pattern alignment marks. Develop photoresist and BOE Trench Pattern until straight trenches show hydrophobic activity. Remove all photoresist and O_2 Ash for 1hr.

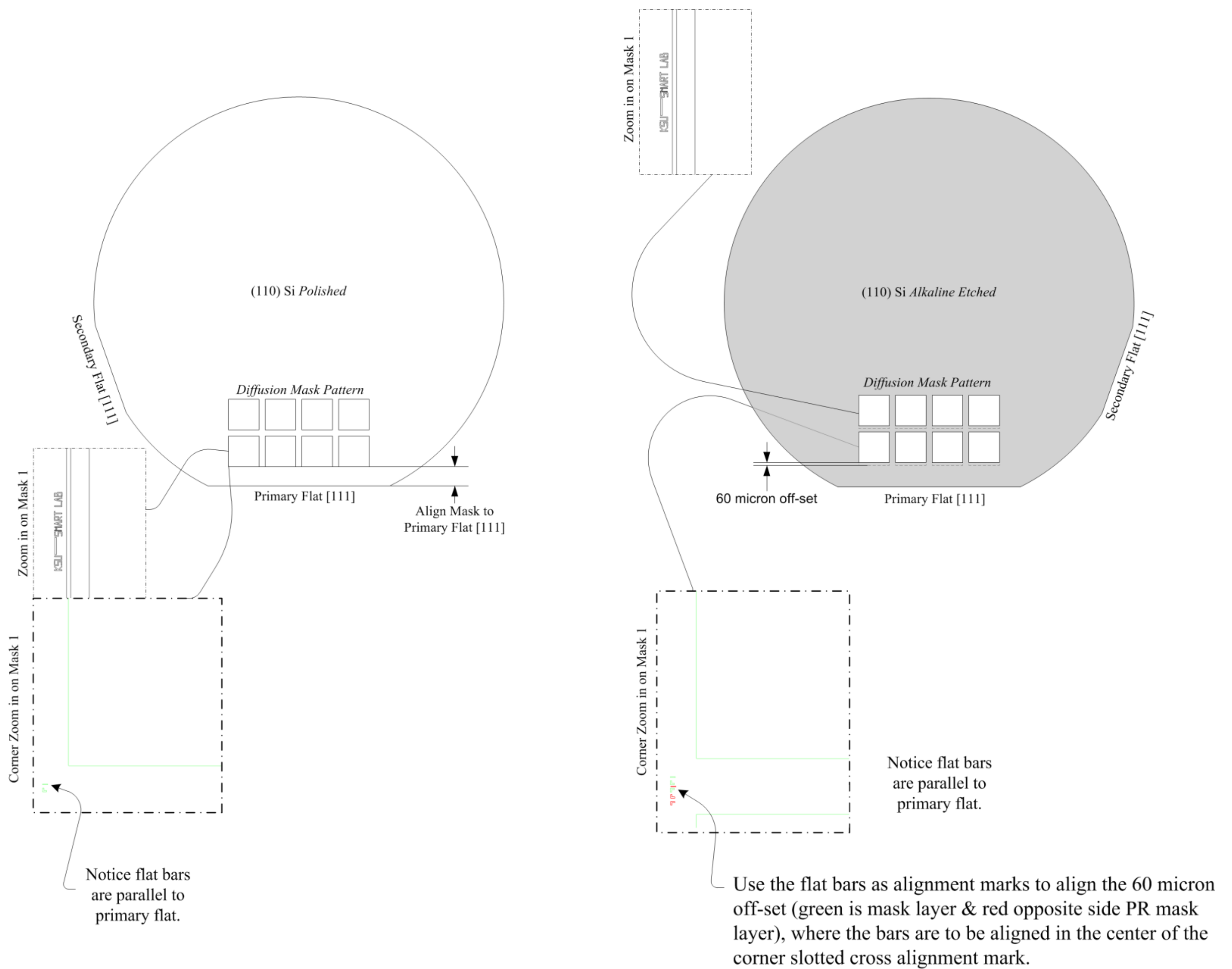

Figure B.2.2: Diffusion window negative photoresist patterning of front- and back-side of silicon wafer. Notice the alignment of the mask pattern to the primary flat (left picture) and the 60 micron offset of the backside pattern to adjust for dual-sided interdigitated trench microstructure alignment with equilateral trench width and spacing with a pitch of 120 microns (right picture). Alignment mark is present in diffusion mask for alignment of offset of 60 microns.

Process 3: KOH wet etch front- and back-side

A KOH wet etch will then be done, etching the single and dual sided masked pattern trenches 475um deep, but no more. BOE Wafers until diffusion window oxide is removed and shows hydrophobic activity.

Process 4: Grow 0.5 micron oxide on wafer

Clean wafers (preferably the death etch HNO_3, HF, H_2O (*Robbins & Schwartz*), to fully remove residual potassium ~0.1 micron silicon removal), then RCA (or comparable) clean wafers, then grow 0.5 micron wet oxide on wafer.

Process 5: Remove backside oxide on wafer

Apply thick (~20-30 micron) photoresist on frontside of wafer and cure slowly to keep trenches from bubbling photoresist. BOE Wafers until backside diffusion window oxide is removed and shows hydrophobic activity. Remove all photoresist and O_2 Ash for 1hr.

Process 6: Microstructured Diode Diffusion (liquid source)

RCA (or comparable) clean wafers and diffuse a 0.2 micron shallow n-type ($POCl_3$) layer on the backside of wafers, *with an extended sourcing time*. BOE Wafers until frontside oxide is removed and frontside diffusion windows show hydrophobic activity. RCA clean wafers and diffuse a 0.3 micron shallow p-type (BBr_3) layer on frontside of wafer, *with an extended sourcing time*. Remove boron diffusion film.

Process 7: Microstructured Diode Metal Contact Photoresist Masking

Apply thick negative photoresist (~20-30 micron) to backside of wafer and align Metal Contact Pattern to diffusion window pattern alignment marks and expose for liftoff undercut development. Develop photoresist and apply negative photoresist to frontside of wafer and again align Metal Contact Pattern to diffusion window pattern alignment marks and expose for liftoff undercut development.

Or, no Photoresist.

Index wafer and align in a shadow mask in an evaporation system. Coat entire individual MSND (over microstructures).

Process 8: Metallization

BOE residual native oxide in contact windows and apply [**Ti (10%) / W (90%)**] **Ti/W** (1000Å) / **Al** (4kÅ) to both sides of wafer. Lift-off metalized photoresist.

B. 3 MSND Fabrication Process *Run Card*: Dual Sided Device

PART **Microstructured Diode Design**
RUN NO: ____________
START DATE:__________
FINISH BY. (DATE):________

Starting Material :N-TYPE <110> 5K - 10KΩ-cm
2 micron Initial Oxide

OP NO	OPERATION	SPEC NO	IN	OUT	DATE	TIME	OPR
0100	**First Mask on front (MASK ID: 1cm SQ DIFF DUAL SIDED)**						
	Hardbake 30 mins. / 115ºC	412-xxxx	________	________	________	________	________
	(-) Resist Coat & Bake	412-0002	________	________	________	________	________
	(Standard program)						
	Align (PE#__________)	412-0019	________	________	________	________	________
	Exposure:________( )		TW #:__________				
	Batch Develop	412-0009	________	________	________	________	________
	Develop Inspect	412-0012	________	________	________	________	________
0200	**First Mask on back (MASK ID: 1cm SQ DIFF DUAL SIDED)**						
	Hardbake 30 mins. / 115ºC	412-xxxx	________	________	________	________	________
	(-) Resist Coat & Bake	412-0002	________	________	________	________	________
	Make sure there is a 60 Miron Offset in alignment towards the center of wafer						
	Align (PE#__________)	412-0019	________	________	________	________	________
	Exposure:________( )		TW #:__________				
	Batch Develop	412-0009	________	________	________	________	________
	Develop Inspect	412-0012	________	________	________	________	________
0300	**BOE Etch on Front side & Back side**						
	Hard Bake (30 min/145ºC)	413-0001	________	________	________	________	________
	Descum	413-0003	________	________	________	________	________
	BOE Etch	413-0010	________	________	________	________	________
	TW Etch Time:______		TW Tox:__________(>17500A) TW#________				
	Lot Etch Time:__________		Lot Tox:__________ (>17500A)				
	Etch Inspect	413-0010	________	________	________	________	________
	Resist Strip	413-0007	________	________	________	________	________
	Final Inspect	413-0017	________	________	________	________	________
0400	**Second Mask (Dual Sided Trench Pattern)on back[MASK ID: 1cm SQ ST TRENCH DUAL SIDED]**						
	LP III Vapor Prime	412-0005	________	________	________	________	________
	(-) Resist Coat & Bake	412-0002	________	________	________	________	________
	Align (PE#__________)	412-0019	________	________	________	________	________
	Exposure:________( )		TW #:__________				
	Batch Develop	412-0009	________	________	________	________	________
	Develop Inspect	412-0012	________	________	________	________	________

OP NO	OPERATION	SPEC NO	IN	OUT	DATE	TIME	OPR
0500	**Second Mask (Dual Sided Trench Pattern)on front [MASK ID: 1cm SQ ST TRENCH DUAL SIDED]**						
	LP III Vapor Prime	412-0005					
	(-) Resist Coat & Bake	412-0002					
	Align (PE#__________)	412-0019					
	Exposure:________( )		TW #:__________				
	Batch Develop	412-0009					
	Develop Inspect	412-0012					
0600	**BOE Etch on Front side & Back side**						
	Hard Bake (30 min/145ºC)	413-0001					
	Descum	413-0003					
	BOE Etch	413-0010					
	TW Etch Time:______		TW Tox:__________			TW#________	
	Lot Etch Time:__________		Lot Tox:__________				
	Etch Inspect	413-0010					
	Resist Strip in Asher for 1 hour	413-0007					
	Final Inspect	413-0017					
	Note: BOE until oxide has been removed in the Trench Pattern						
0700	**KOH Etch on Front side and Back Side**						
	KOH Etch (475 microns deep)	413-0001					
	Descum	413-0003					
	BOE Etch	413-0010					
	TW Etch Time:______		TW Tox:__________			TW#________	
	Lot Etch Time:__________		Lot Tox:__________				
	Etch Inspect	413-0010					
	Final Inspect	413-0017					
	NOTE: BOE until oxide is removed in diff. window around trenches, but not through the diffusion window masking oxide						
0800	**Oxidation**						
	Visually inspect wfrs under UV						
	Wafer Rinse	411-0029					
	Pre Ox-Clean	411-0014					
	RCA Clean						
	Oxidation	411-0070					
	Furnace #:___________(1)	Set Pt #1 = 900ºC			Set PT #2 = 1050ºC		
		Standard Preheat in N_2			Push in O2		
		T1 =	15 min	O_2		Ramp Up	
		T2 =	80 min	$H_2 + O_2$			
		T3 =	10 min	O_2			
		T4 =	30 min	N_2		Ramp Down	
	Product Tox:__________ (5000+/- 500 A))						
0900	**BOE Etch on Back side**						
	(-) Resist Coat & Bake on the front	412-0002					
	Hard Bake (30 min/145ºC)	413-0001					
	Descum	413-0003					
	BOE Etch	413-0010					
	TW Etch Time:______		TW Tox:__________			TW#________	
	Lot Etch Time:__________		Lot Tox:__________				
	Etch Inspect	413-0010					
	Resist Strip in Asher for 1 hour	413-0007					
	NOTE: BOE until oxide is removed in diff. windows around trenches but not through the diffusion window masking oxide						

OP NO	OPERATION	SPEC NO	IN	OUT	DATE	TIME	OPR
1000	**$POCl_3$ <u>Diffuse</u> on Backside**	(Add P-type test wafer, 5 to 20 ohm-cm resistivity)					
	Pre-Diffusion Clean	411-0014	________	________	________	________	________
	RCA I and RCA II Clean		________	________	________	________	________
	POCl3 Dope	414-xxxx	________	________	________	________	________
	Furnace #_____ (2)	Set Pt #1 = 800ºC		Set Pt #2 = 950ºC		Set Pt #3 = 1000ºC	
		Standard Preheat and Push in					
		T1 =	15 min	N_2		Ramp Up	
		T2 =	20 min	$N_2 + O_2 + POCl_3$		Source	
		T3 =	30 min	N_2		Ramp Up	
		T4 =	60 min	N_2		Ramp Down	
	10:1 HF DIP 30 Seconds	411-0006	________	________	________	________	________
	TW Sheet Resistance:__________	(1 to 5 ohm/sq)					
1100	**<u>Resist Coat</u> on back to protect $POCL_3$**						
	Hard Bake (30 min/145ºC)	412-0005	________	________	________	________	________
	(-) Resist Coat & Bake	412-0002	________	________	________	________	________
1200	**<u>BOE</u> Etch on Front side till Hydrophobic Activity is seen**						
	Hard Bake (30 min/145ºC)	413-0001	________	________	________	________	________
	Descum	413-0003	________	________	________	________	________
	BOE Etch	413-0010	________	________	________	________	________
	TW Etch Time:______		TW Tox:__________			TW#________	
	Lot Etch Time:__________		Lot Tox:__________				
	Etch Inspect	413-0010	________	________	________	________	________
	Resist Strip in Asher	413-0007	________	________	________	________	________
1300	**BBR_3 <u>Diffuse</u> on Frontside**		**ADD N TYPE TEST WAFER , 2-8 Ohm cm**				
	Pre-Clean	411-0014	________	________	________	________	________
	ISO Predeposition	411-xxxx	________	________	________	________	________
	Furnace #: 11	Set Pt #1 = 800ºC			Set PT #2 = 1025ºC		
					Set PT #3 = 1125ºC		
		Standard Preheat and Push in (N2)					
		T1 =	20 min	N2 @ 75mm		Ramp up to 1025ºC	
		T2 =	5 min	N2 @ 75mm + LO2 @ 105mm			
		T3 =	60 min	N2+LO2+BBR3			
				N2 @ 75mm, LO2 @ 105mm, BBR3 @ 55m			
		T4 =	15 min	N2 @ 75mm + LO2 @ 105mm			
		T5 =	10 min	N2 ramp up to 1125ºC			
		T6 =	45 min	N2			
		T7 =	60 min	N2 Ramp down to 800ºC			
	Flowmeters used:	N2:	R-215-C	SS Float			
		O2:	R-215-D	SS Float			
		BBR3:	R-215-D	SS Float			
	10:1 HF Dip 30 Seconds	411-xxxx	________	________	________	________	________
	(Dip immediately)						
	TW Rs =__________ Ω/Sq		Target Rs = 3 - 8 Ω/Sq				

OP NO	OPERATION	SPEC NO	IN	OUT	DATE	TIME	OPR

1400 **LTO** Include TW from above. This step has to be done **immediately** after predep.

	LTO	411-xxxx	________	________	________	________	________

Furnace # 9 — Set Pt #1 = 800ºC
Standard Preheat and Push in

T1 =	6 min	O_2	Dry Ox
T2 =	20 min	$O_2 + H_2$	Wet Ox
T3 =	6 min	N_2	Purge

	10:1 HF Dip 3 Minutes	411-xxxx	________	________	________	________	________

TW Rs =__________ Ω/Sq — Target Rs = 3.0 - 10 Ω/Sq

1500 **BORON Drive-In** **Include earlier TW . Do not clean wafers.**

	Boron Drive	411-xxxx	________	________	________	________	________

Furnace #: 9 — Set Pt #1 = 800ºC — Set Pt #2 = 1125ºC
Standard Preheat and Push in

T1 =	5 min	N_2 @ 75mm	
T2 =	32 min	N_2 / O_2	Ramp Up 90% N_2 (75mm)/
T3 =	40 min	N_2 / O_2	10% O_2 (12mm)
T4 =	35 min	$O_2 + H_2$	O2= 40mm, H2=25mm
T5 =	15 min	N_2	
T6 =	64 min	N_2	Ramp down

TW Tox__________ (6000 ± 600Å)

TW Rs =__________ Ω/Sq — Target Rs = 4.5 - 10.0 Ω/Sq

1600 **Third Mask(Lift Off PR Mask) on Back [MASK ID: 1cm SQ METAL DUAL SIDED]**

	LP III Vapor Prime	412-0005	________	________	________	________	________
	(-) Resist Coat(20-30u) & Bake (	412-0002	________	________	________	________	________
	Align (PE#__________)	412-0019	________	________	________	________	________
	Exposure:________( )		TW #:__________				
	Batch Develop	412-0009	________	________	________	________	________
	Develop Inspect	412-0012	________	________	________	________	________

1700 **Third Mask(Lift Off PR Mask) on Front [MASK ID: 1cm SQ METAL DUAL SIDED]**

	LP III Vapor Prime	412-0005	________	________	________	________	________
	(-) Resist Coat(20-30u) & Bake	412-0002	________	________	________	________	________
	Align (PE#__________)	412-0019	________	________	________	________	________
	Exposure:________( )		TW #:__________				
	Batch Develop	412-0009	________	________	________	________	________
	Develop Inspect	412-0012	________	________	________	________	________

OP NO	OPERATION	SPEC NO	IN	OUT	DATE	TIME	OPR
1800	**<u>BOE</u> Etch until Drive in Oxide has been removed**						
	Hard Bake (30 min/145ºC)	413-0001	________	________	________	________	________
	Descum	413-0003	________	________	________	________	________
	BOE Etch in Contact Windows	413-0010	________	________	________	________	________
	TW Etch Time: 2 to 5 minutes		TW Tox:__________(<100A)			TW#________	
	Lot Etch Time:__________		Lot Tox:__________ (<100 A)				
	Etch Inspect	413-0010	________	________	________	________	________
	Final Inspect	413-0017	________	________	________	________	________

01900 **METAL DEP**

[Ti(10%)/ W(90%)] (1000A)/ Al (10,000A) on Both Sides

2000 **METAL LIFT OFF**

Strip lift-off photoresist

APPENDIX C - *SILVACO* MODEL INPUT CODE

C. 1 *Silvaco* TCAD Potential Model Input Code

Given is the TCAD Deckbuild™ input file for potential distribution simulation loading the 3-dimensional 5 μm mesh and 2 μm z-plane mesh of the MSND geometry created in DevEdit3D™ and pictured in Figures 5.16, 5.17, and 5.18. The anode is on the topside of the Si fin and the cathode is defined on the bottom of the MSND. The silicon bulk n-type resistivity is 10 kΩ-cm (phosphorus doping of 4.174×10^{11} cm^{-3}). The conformal junction is defined with a Gaussian distribution of 0.2 and a boron doping of $1{\times}10^{20}$ cm^{-3}.

```
go atlas
mesh infile=10000_Ohmcm_100_3d_S.str
contact all neutral
#solving method
models bbt.std consrh fldmob
method newton autonr carriers=2 climit=1e-3
#Initializing Solve
solve initial
solve previous
solve vanode=0 vcathode=0 vstep=0.1 vfinal=2.00 name=cathode
solve vanode=0 vcathode=2 vstep=0.2 vfinal=25.00 name=cathode
save outfile=pot_res_100.str
quit
```

C. 2 *Silvaco* TCAD Single Event Upset Model Input Code

Given is the TCAD Deckbuild™ input file for single-event-upset simulation loading the 3-dimensional MSND geometry and potential solution found in Section 5.2.4 and as pictured in Figures 5.16, 5.17, and 5.18. The anode is on the topside of the Si fin and the cathode is defined on the bottom of the MSND. The silicon bulk n-type resistivity is 10 kΩ-cm (phosphorus doping of 4.174×10^{11} cm^{-3}). The conformal junction is defined with a Gaussian distribution of 0.2 and boron doping of 1×10^{20} cm^{-3}.

```
go atlas
mesh infile=10000_Ohmcm_100_3d_S.str
load infile=pot_res_100.str MASTER
method halfimpl dt.min=1e-10 #min time step
log outfile=TMSND_100seu.log
#Solve initial
solve tfinal=1e-7 tstep=5e-8
#Single Event Upset (SEU) Track
singleeventupset entry="22,25,5" exit="43,5,5" radius=5 density=1e14
solve tfinal=1e-6 tstep=5e-8
solve tfinal=1e-5 tstep=2e-7
tonyplot TMSND_100seu.log
quit
```

APPENDIX D - KSU ^{252}CF SOURCE DETAIL

D. 1 Californium-252 Radiological Specifications†

DECAY SCHEME

Californium-252 decays by alpha emission (97%) and by spontaneous fission (3%), as shown in Table I and Figure 1.

Table I

Decay Properties of ^{252}Cf

	Alpha Decay	*Spontaneous Fission*	*Total*
Specific activity, disintegrations or fissions per gram per second	1.92×10^{13}	6.14×10^{11}	1.98×10^{13}
Curies per gram[a]	519.4	16.6	536.0
Half-life, years	2.731	85.5	2.646[b]
Decay heat, watts/gram	18.8	19.7	38.5

a A curie of any radioactive material is that amount which undergoes 3.7×10^{10} disintegrations/second.

b Actually not a total, but rather an effective half-life, given by $T_{eff} = T_{\alpha} T_{SF}/(T_{\alpha} + T_{SF})$.

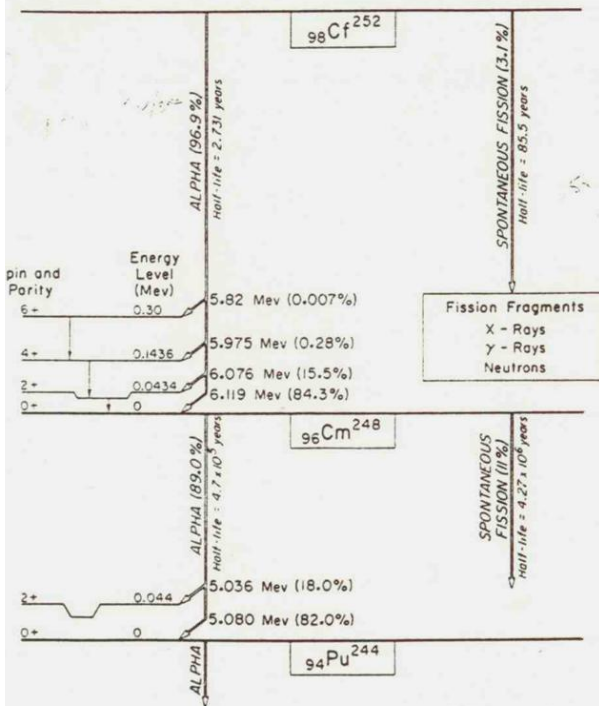

FIG. 1 Decay Scheme for ^{252}Cf

Nuclear Properties of ^{252}Cf

Mode of decay	
Alpha emission	96.9%
Spontaneous fission	3.1%
Half-life	
Alpha decay	2.731 ±0.007 years
Spontaneous fission	85.5 ±0.5 years
Effective (α and SF)	2.646 ±0.004 years
Neutron emission rate	2.31×10^{12} neutrons per second per gram
Neutrons emitted per spontaneous fission	3.76
Average neutron energy	2.348 million electron volts
Average alpha particle energy	6.117 million electron volts
Gamma emission rate (exclusive of internal conversion X-rays)	1.3×10^{13} photons per second per gram
Dose rate at one meter in air	
Neutron	2.2×10^{3} rem per hour per gram
Gamma	1.6×10^{2} rads per hour per gram
Decay heat	
From alpha decay	18.8 watts per gram
From fission	19.7 watts per gram
Source volume (excluding void space for helium)	< 1 cm^3 per gram

Table II

Gamma Rays from ^{252}Cf Alpha Decay Process

Energy, Mev	Abundance, photons/(sec)(gram)
0.043	2.8×10^{9}
0.100	2.0×10^{9}
0.156	4.0×10^{8}

Table III

Gamma Rays from Spontaneous Fission of ^{252}Cf

photons/(sec)(gram)

Energy, Mev	*Prompt Gamma Rays*	*Gamma Rays from Equilibrium Fission Products*	*Total*
0 - 0.5	3.3×10^{12}	1.3×10^{12}	4.6×10^{12}
0.5 - 1.0	1.7×10^{12}	4.0×10^{12}	5.7×10^{12}
1.0 - 1.5	7.7×10^{11}	9.1×10^{11}	1.7×10^{12}
1.5 - 2.0	4.2×10^{11}	3.5×10^{11}	7.7×10^{11}
2.0 - 2.5	2.2×10^{11}		2.2×10^{11}
2.5 - 3.0	1.1×10^{11}		1.1×10^{11}
3.0 - 3.5	5.6×10^{10}		5.6×10^{10}
3.5 - 4.0	3.0×10^{10}		3.0×10^{10}
4.0 - 4.5	1.7×10^{10}		1.7×10^{10}
4.5 - 5.0	8.2×10^{9}		8.2×10^{9}
5.0 - 5.5	4.9×10^{9}		4.9×10^{9}
5.5 - 6.0	1.8×10^{9}		1.8×10^{9}
6.0 - 6.5	1.0×10^{9}		1.0×10^{9}
Total	6.6×10^{12}	6.6×10^{12}	1.3×10^{13}

Table IV

Neutrons From Spontaneous Fission Of ^{252}Cf

Energy, Mev	*Neutrons/(sec)(gram)*
10.0 - 14.92	8.28×10^{9}
6.70 - 10.00	6.42×10^{10}
5.49 - 6.70	8.19×10^{10}
4.49 - 5.49	1.26×10^{11}
3.68 - 4.49	1.68×10^{11}
3.01 - 3.68	2.0×10^{11}
2.02 - 3.01	4.36×10^{11}
0.91 - 2.02	6.98×10^{11}
0.41 - 0.91	3.36×10^{11}
0.11 - 0.41	1.56×10^{11}
0.015 - 0.11	2.74×10^{10}
0.0 - 0.015	0
Total	2.3×10^{12}

†Data sourced from KSU Triga Reactor Library.

D. 2 KSU ^{252}Cf Assay[†]

Table 1. Source fabrication information for SR-Cf-331

Neutron Source	SR-Cf-331
Sample Identification	CX-CF115
Date of Analysis	February 17, 1978
Nuclide	Isotopic Composition (atom %)
^{249}Cf	2.218
^{250}Cf	8.513
^{251}Cf	2.247
^{252}Cf	86.918
^{253}Cf	0.082
^{254}Cf	0.024
Date of Final Purification	November 3, 1982
Date of Californium Assay	December 31, 1992
Calculated Fraction of Neutrons from ^{252}Cf	0.86926[a]
^{252}Cf Content, μg	23.56[a]

[a]Value decayed to August 31, 2005

[†]Data sourced from KSU Triga Reactor Library.